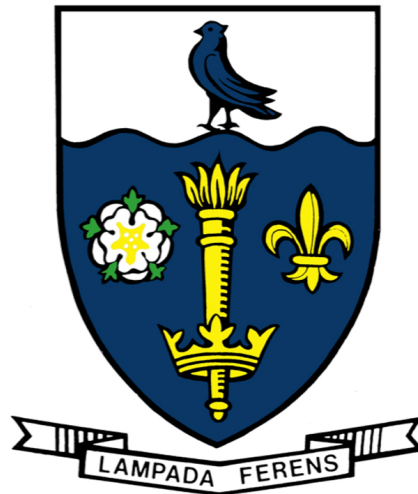


# The First Holistic View of Minor Mergers of Galaxy Clusters



**Alexander James Sheardown, MPhys. (Hons.)**

Department of Physics and Mathematics  
University of Hull

This thesis is submitted for the degree of  
*Doctor of Philosophy*

## **Declaration**

I submit this thesis for the fulfilment of the degree of Doctor of Philosophy from the University of Hull. I hereby declare that except where reference is made to the work of others, the work presented in this thesis is original, carried out under the supervision of Dr. Elke Roediger and Prof. Brad Gibson, and has not been previously submitted for examination for any other award. Chapter 3 has been published in *The Astrophysical Journal* as Sheardown et al. (2018) and Chapter 4 has also been published in *The Astrophysical Journal* as Sheardown et al. (2019). Though not my original work, Chapter 5 presents a description of work being conducted by my supervisor Dr. Elke Roediger and MSc student Thomas Fish at the University of Hull written in my words. This work will take the form of two publishable papers - Roediger et al. (in preparation) and Fish et al. (in preparation) of which I will be a co-author of. This work is based on a result from my work detailed in Chapter 3 and thus is included in my thesis.

Alexander James Sheardown, MPhys. (Hons.)

September 2019

## Acknowledgements

Here I would like to take the opportunity to thank the people who have supported me throughout my PhD or who have provided me with help and guidance throughout my academic studies to get me to where I am today. First and foremost, I want to say a huge thank you to my supervisor Elke Roediger for being the best supervisor a student could ask for. Her constant support, understanding and encouragement has made this PhD journey a much easier and enjoyable ride. I will take your guidance and advice with me into whatever I decide to do next in my career.

From an academic standpoint there are several people I would like to extend thanks to. Firstly, I want to thank Brad Gibson for giving me the opportunity to do this PhD and to be a part of the incredible E.A. Milne Centre team, for which I am forever grateful, and also for his support throughout my PhD as my second supervisor. I would like to thank my undergraduate degree supervisor Howard Snelling and Ali Adawi for their guidance throughout my time as an undergraduate, and also Kevin Pimblet for giving me the opportunity to do my first astrophysics based research project and preparing me for a research role. I also would like to thank Ralph Kraft and Yuanyuan Su at the CfA for their constructive conversations over Skype and for their help and support during my PhD, it was a pleasure to be a part of several papers with you. I would also like to thank my fellow PhD students who I spent time with in the office. Although I tended to keep myself to myself, you guys made the long days in the office enjoyable and a little easier to get through. Additionally, I would like to thank my AS level physics teacher Steve Stow for providing me with my first real introduction to physics and for helping me during my early years as an undergraduate. I also thank my A level sport teacher James Morris for giving me advice on exam preparation and work organisation which I have taken on board throughout my academic studies, I put a lot of my success down to this.

Finally, I would like to thank my friends and family for their continued love and support throughout my PhD, with a special mention to my girlfriend Hazel. Particularly, I want to say a big thank you to my parents who have always been there for my every need and given me the platform to succeed, I can't thank you enough.

## Abstract

Utilising hydrodynamic + N-body simulations, we present the first holistic view of minor mergers of galaxy clusters. A minor merger describes the merging of a main cluster and a less massive subhalo, this could be a subcluster, group or an elliptical galaxy. Throughout the minor merger, we consider simultaneously both the evolution of the subhalo atmosphere via gas stripping and other processes, along with the evolution of gas sloshing and shocks in the main cluster atmosphere. These merger features, and others, are recorded in the intra-cluster medium (ICM) of the cluster and are thus embedded in X-ray observations. The X-ray band is the focus of our analysis although other wavelengths are discussed. We direct our attention on the Fornax Cluster and the infall of its elliptical galaxy NGC 1404, constructing a tailored simulation of this system. By comparing our simulated data to observations of the cluster, we are able to constrain its previous 1.1 – 1.3 Gyr history, showing that a second or third infall of NGC 1404 into Fornax reproduces all the main observed merger features in both objects, ruling out the possibility of a first infall. Additionally, we are further able to make predictions for other possible observed merger features in Fornax. We also provide an outlook on a side project based on this work which analyses the globular cluster content observed in NGC 1404 and the central BCG galaxy in Fornax. Analysing these and further minor cluster merger simulations in a broader context, we identify a new class of gas tail, which we term slingshot tail. Gas tails of galaxies and subhalo's are generally accredited to ram pressure stripping which produces an orderly head-tail like morphology with the tail pointing in the direction of the recent orbital path. In contrast, slingshot tails form as a subhalo moves away from pericentre toward apocentre during a merger. Here, the gas in the tail slingshots as the subhalo rapidly decelerates, resulting in a tail that can point perpendicular or even opposite to the subhalo's direction of motion. We also find that the flow patterns associated with slingshot tails are highly irregular. Therefore naively applying the ram pressure scenario to a gas tail should be cautioned, as the tail direction can be misleading and can also lead to incorrect conclusions regarding properties of the subhalo and the surrounding ICM. Applying this new understanding, we attempt to explain some examples of gas tails reported in literature. Finally, building on the detection of a stolen atmosphere feature of NGC 1404 in the Fornax merger simulations, we present a description of work being conducted by Dr Elke Roediger and Thomas Fish which provides the theory behind the feature and also provides a comparison between stagnation point methods which are used to estimate the infall velocity of NGC 1404.

# Table of contents

<b>List of figures</b>	<b>xv</b>
<b>List of tables</b>	<b>xix</b>
<b>1 Introduction</b>	<b>1</b>
1.1 Preface . . . . .	1
1.2 Cosmology . . . . .	1
1.3 Galaxy Clusters and Galaxies . . . . .	4
1.3.1 Galaxy Clusters . . . . .	4
1.3.2 Galaxies . . . . .	7
1.4 X-ray Observations of Galaxy Clusters . . . . .	8
1.5 The Intra-Cluster Medium (ICM) . . . . .	11
1.5.1 Plasma or Fluid? . . . . .	11
1.5.2 Microphysics and Transport Processes . . . . .	12
1.5.3 Probes for ICM Transport Processes . . . . .	14
1.5.4 Enrichment of the ICM . . . . .	15
1.6 Mergers of Galaxy Clusters . . . . .	16
1.6.1 Merger Basics . . . . .	16
1.6.2 Outline of Minor Merger Phases . . . . .	17
1.6.3 Energy Dissipation and Shocks in Mergers . . . . .	18
1.6.4 Gas Sloshing and Cold Fronts in Mergers . . . . .	20
1.6.5 Simulations of Cluster Mergers . . . . .	21
1.7 Gas Stripping of Cluster Galaxies, Groups and Subclusters . . . . .	22
1.8 Outline of this Work . . . . .	24
<b>2 Simulation Method</b>	<b>27</b>
2.1 Preface . . . . .	27
2.2 Flow Descriptions . . . . .	27
2.3 FLASH code and The yt Project . . . . .	29
2.3.1 Hydrodynamics in FLASH . . . . .	30
2.3.2 Dark Matter Particles and Gravity in FLASH . . . . .	31
2.4 Generating Model Clusters . . . . .	32
2.5 Simulation Resolution . . . . .	34
2.6 Preliminary Simulations . . . . .	36

2.6.1	Wind Tunnel . . . . .	36
2.6.2	Gas Cloud Stripping . . . . .	38
2.6.3	Galaxy Stripping . . . . .	43
2.6.4	Rigid Potential Merger Simulations . . . . .	45
<b>3</b>	<b>The Recent Growth History of the Fornax Cluster Derived from Simultaneous Sloshing and Gas Stripping: Simulating the Infall of NGC 1404</b>	<b>49</b>
3.1	Prologue . . . . .	49
3.2	Abstract . . . . .	49
3.3	Introduction . . . . .	50
3.4	Setting the Scene: NGC 1404 and the Fornax Cluster . . . . .	52
3.5	Simulation Setup . . . . .	54
3.5.1	Initial Conditions . . . . .	54
3.5.2	Metallicity Profiles . . . . .	57
3.5.3	FLASH - The Simulation Code . . . . .	59
3.5.4	Simulation Design . . . . .	60
3.6	Results . . . . .	61
3.6.1	Overall Merger History . . . . .	61
3.6.2	Second + Third Infall . . . . .	64
3.6.3	Evolution of Fornax . . . . .	67
3.6.4	Predictions . . . . .	70
3.7	Discussion . . . . .	74
3.7.1	Merging History . . . . .	74
3.7.2	Enrichment Processes . . . . .	75
3.7.3	Importance of Dynamical Friction . . . . .	75
3.7.4	NGC 1404 as a Test Case for ICM Plasma Physics . . . . .	76
3.7.5	Globular Cluster Debate . . . . .	76
3.8	Summary . . . . .	77
3.9	Acknowledgments . . . . .	78
<b>4</b>	<b>A New Class of X-Ray Tails of Early-Type Galaxies and Subclusters in Galaxy Clusters - Slingshot Tails vs Ram Pressure Stripped Tails</b>	<b>79</b>
4.1	Prologue . . . . .	79
4.2	Abstract . . . . .	79
4.3	Introduction . . . . .	80
4.4	Simulations . . . . .	81
4.5	Ram Pressure Stripped Tail vs Slingshot Tail . . . . .	83
4.6	Slingshot Tails . . . . .	85
4.6.1	Arc-Shaped Tails . . . . .	85
4.6.2	Overrun Tails . . . . .	87
4.7	Flow Patterns of Slingshot Tails . . . . .	89
4.8	Observable Features of Slingshot Tails . . . . .	92

4.9	Classifying Some Known X-ray Tails . . . . .	93
4.9.1	LEDA 87745 in Hydra A . . . . .	94
4.9.2	NGC 7618 and UGC 12491 . . . . .	96
4.9.3	NGC 4839 Group in Coma . . . . .	96
4.9.4	NGC 4472/M49 and NGC 4649/M60 in Virgo . . . . .	97
4.9.5	Abell 85 . . . . .	98
4.9.6	Abell 1644 . . . . .	99
4.9.7	Abell 2744 . . . . .	101
4.10	Conclusion . . . . .	102
4.11	Acknowledgments . . . . .	103
<b>5</b>	<b>Stolen Atmosphere Theory - Assessing Stagnation Point Methods and the Stolen Atmosphere Effect in Tailored Simulations of a Minor Cluster Merger</b>	<b>105</b>
5.1	Prologue . . . . .	105
5.2	Introduction . . . . .	105
5.3	Current Stagnation Point Methods . . . . .	107
5.4	Stagnation Point Method Including The Stolen Atmosphere Effect . . . . .	108
5.4.1	Incompressible Model . . . . .	108
5.4.2	Compressible Model . . . . .	110
5.5	Comparing Stagnation Point Models in a Minor Merger Simulation . . . . .	112
5.5.1	Results . . . . .	114
5.6	Discussion and Conclusion . . . . .	116
<b>6</b>	<b>Concluding Remarks and Future Work</b>	<b>119</b>
6.1	The New, Holistic View of a Minor Merger . . . . .	119
6.1.1	Initial Conditions . . . . .	119
6.1.2	First Infall . . . . .	119
6.1.3	First Pericentre to First Apocentre . . . . .	120
6.1.4	Second Infall . . . . .	121
6.1.5	Second Pericentre to Second Apocentre . . . . .	121
6.1.6	Implications . . . . .	121
6.2	Future Work . . . . .	123
6.2.1	The Globular Cluster Content of NGC 1404 and NGC 1399 . . . . .	123
6.2.2	Probing the Viscosity of the ICM . . . . .	125
6.2.3	Deeper Analysis on Slingshot Tails . . . . .	125
6.2.4	Observational Aids for Minor Merger Interpretation . . . . .	125
6.2.5	Predicting Future High-Resolution X-ray Observations . . . . .	126
6.2.6	Summary of Future Work . . . . .	128
	<b>References</b>	<b>129</b>
	<b>Appendix A Characteristics of Fluid Flow</b>	<b>145</b>

# List of figures

1.1	SDSS map of the Large Scale Structure of the Universe . . . . .	4
1.2	Optical Image of Abell 370 . . . . .	5
1.3	A merger tree for the growth of a brightest cluster galaxy (BCG) . . . . .	6
1.4	Composite X-ray and Optical images of the galaxy clusters Abell 262, Abell 383, Abell 1413 and Abell 2399 . . . . .	10
1.5	A set of 6 composite X-ray and optical images of galaxy cluster mergers .	16
1.6	First infall merger phase . . . . .	18
1.7	Apocentre merger phase . . . . .	19
1.8	Second infall merger phase . . . . .	19
1.9	XMM-Newton observation of Abell 2142 taken from Rossetti et al. (2013)	21
1.10	Chandra image of M89 . . . . .	23
2.1	Snapshots from a minor merger cluster simulation showing the refinement grid . . . . .	35
2.2	Mach 3 wind tunnel with a step simulation setup . . . . .	36
2.3	Simulation snapshots of a Mach 3 wind tunnel with a step . . . . .	37
2.4	Simulation snapshots of a Mach 3 wind flowing around a rigid domain . .	37
2.5	Simulation snapshots of subsonic stripping of gas cloud . . . . .	39
2.6	Simulation snapshots of supersonic stripping of a gas cloud . . . . .	41
2.7	Comparison of levels of refinement for subsonic gas cloud stripping . . .	42
2.8	Simulation snapshots of galaxy stripping . . . . .	44
2.9	Snapshots from a rigid potential merger between a cluster and a galaxy. .	46
3.1	XMM image of Fornax taken from Su et al. (2017d) and Chandra mosaic of Fornax taken from Su et al. (2017a) . . . . .	51
3.2	Comparison of simulated and observed ICM profiles for the Fornax cluster from the V0 and V2 simulations . . . . .	55
3.3	Cumulative mass profile for our model Fornax cluster compared to cumu- lative stellar mass of NGC 1399, converted from K-Band luminosity . . .	56
3.4	Comparison of simulated and observed gas atmosphere profiles for NGC 1404 from the V0 and V2 simulations . . . . .	58
3.5	Cumulative mass profile for our model NGC 1404 compared to cumulative stellar mass of NGC 1404, converted from K-Band luminosity . . . . .	58
3.6	Initial metallicity profiles in Fe solar abundance for Fornax and NGC 1404	59

3.7	Electron density snapshots in the orbital plane for the overall evolution of the infall of NGC 1404 into Fornax . . . . .	62
3.8	Temperature slices in the orbital plane for the overall evolution of the infall of NGC 1404 into Fornax . . . . .	63
3.9	Comparison of the best match stage for all 3 simulations . . . . .	65
3.10	X-ray photon emissivity projections for the V2 simulation . . . . .	68
3.11	Velocity and metallicity snapshots from the V0, V1 and V2 simulations . . . . .	69
3.12	Comparing XMM image of Fornax to a mock X-ray images of the V2 simulation . . . . .	71
3.13	Comparing galactic gas fraction slices between first and second infall . . . . .	72
3.14	Comparing Chandra image of NGC 1404 to an X-ray photon emissivity projection of the galaxy in the V2 simulation . . . . .	74
3.15	Comparing Chandra derived temperature map of NGC 1404 to the simulated galaxy in the V2 simulation . . . . .	75
4.1	A cartoon image showing a clear distinction between the two slingshot tail forms . . . . .	84
4.2	Evolution of a 1:10 and a 1:3 cluster merger . . . . .	86
4.3	X-ray photon intensity field projections for the different slingshot tail forms . . . . .	88
4.4	Flow patterns in and around secondaries with <i>overrun slingshot tails</i> . . . . .	90
4.5	Flow patterns in and around secondaries with <i>arc-shaped slingshot tail</i> . . . . .	91
4.6	Comparing an XMM/EPIC mosaic image of Hydra A taken from De Grandi et al. (2016) to a simulated image . . . . .	94
4.7	Comparing a Chandra image of NGC 7618 and UGC 12491 taken from Roediger et al. (2012) to simulated images . . . . .	95
4.8	Comparing an XMM-Newton image of Coma taken from Lyskova et al. (2019) to a simulated image . . . . .	97
4.9	XMM-Newton image of M49 taken from Kraft et al. (2011) and Chandra image of M60 taken from Wood et al. (2017) . . . . .	98
4.10	Chandra image of Abell 85 taken from Ichinohe et al. (2015) . . . . .	99
4.11	Chandra image of Abell 1644 taken from Johnson et al. (2010) . . . . .	100
4.12	Chandra image of Abell 2744 taken from Owers et al. (2011b) . . . . .	101
5.1	Schematic for data collection for stagnation point analysis of the galaxy . . . . .	113
5.2	Estimated infall velocity of NGC 1404 from the V2 simulation comparing stagnation point methods . . . . .	115
6.1	A Simulated Athena WFI 3x3 30ks mosaic observations of the Fornax Cluster from the V2 simulation at the best observed timestep in the 0.5-2.0 keV energy band . . . . .	126
6.2	A mock 200 ks Athena X-IFU observation of NGC 1404 from the V2 simulation . . . . .	127
A.1	Laminar flow around a sphere taken from van Dyke & White (1982) . . . . .	146

A.2	Turbulent flow from a water jet taken from Dimotakis et al. (1983) . . . . .	147
A.3	Optical image of the Crab Nebula . . . . .	148
A.4	KHI of stratified shear flow taken from Thorpe (1971) . . . . .	149
A.5	Flow past a circular cylinder from van Dyke & White (1982) . . . . .	150
A.6	von Karman vortex street taken from van Dyke & White (1982) . . . . .	150

# List of tables

2.1	Parameters for the mass, temperature and gas profiles for the cluster and galaxy for the rigid gravitational potential merger. These parameters were chosen to provide a close match to the Fornax Cluster and NGC 1404. . .	46
3.1	Fornax Cluster Model Parameters . . . . .	56
3.2	NGC 1404 Model Parameters . . . . .	57
3.3	Simulation Runs . . . . .	61
6.1	Summary of the Minor Binary Merger Phases. SA - stolen atmosphere, DBS - detached bow shock. . . . .	122

# Chapter 1

## Introduction

### 1.1 Preface

In this first chapter, a broad overview of the current astrophysics landscape relevant to the physics of galaxy clusters is presented in order to prepare the reader for the rest of the thesis. After outlining the cosmological background, particular focus is placed on the properties of galaxy clusters, the characteristics of the hot cluster gas and the physical processes at work during the mergers of clusters.

### 1.2 Cosmology

In the late 1920s whilst working at Mount Wilson Observatory, Edwin Hubble began collecting measurements for the recessional velocity of galaxies. Hubble was aware of work by Vesto Slipher a decade previous, who was the first to measure the Doppler shift of spectral lines in galaxies to determine their radial velocity (Slipher, 1917). Slipher had found that a small number of galaxies were moving toward the Milky Way, i.e, their spectra appears blue-shifted, but found that several galaxies were in fact moving away at high velocities, i.e., their spectra appears red-shifted. Significantly, Hubble found a positive linear correlation between the distance of a galaxy and its recessional velocity. This implied that the further away a galaxy is, the greater its recessional velocity (Hubble, 1929). This became known as Hubble's Law, and provided the first observational evidence for an expanding universe which had been theorised by Friedmann (1922) and also later by Lemaître (1931). Much later in 1998, observations of a Type 1a supernova by Perlmutter et al. (1998) showed that the expansion of the universe is in fact accelerating. As well as Alexander Friedmann and Georges Lemaître, both Howard Robertson and Arthur Walker worked on an expanding universe theory. The culmination of work by these physicists resulted in a cosmological model which describes the universe known as the Friedmann-Lemaître-Roberston-Walker model (FLRW model) based on the postulates of an expanding, isotropic and homogeneous universe. For a comprehensive review of modern cosmology see e.g. Mukhanov (2005); Weinberg (2008). As the universe is expanding, the FLRW model reveals that in the past, the universe must have been smaller

and hotter, such that as the universe expands in time, it also cools. Crucially, the universe is not perfectly homogeneous and has been observed to be seeded with inhomogeneities. These inhomogeneities are of the utmost importance as they allowed cosmic structure (e.g. galaxies and galaxy clusters) to form via gravitational collapse.

Following the expansion of the universe back in time results in the formulation of the hot Big Bang Theory - the leading theory which provides an explanation for the origin of the universe. The hot Big Bang theory states that the universe began from an incredibly dense hot state and has expanded and cooled over time. Both Gamow (1948) and Alpher & Herman (1948) discovered that the hot Big Bang Theory predicted an afterglow of radiation with a blackbody spectrum, which would have been produced during the early evolution of the universe, with an estimated temperature between 5K to 50K. During the infancy of the universe, atoms could not form due to the extreme temperatures and density. In this period, the universe was in thermal equilibrium, as matter in the form of highly ionised plasma was constantly absorbing and re-emitting photons by Compton scattering, making the universe opaque to light. However as the universe continued to expand, it also cooled. Around 380,000 years after the Big Bang, the universe had cooled enough to a temperature of around 3000 K such that the ions and electrons in the plasma could recombine to form atoms. This is known as the epoch of recombination and now allowed photons to travel freely as they were no longer scattered. These first photons emitted at the epoch of recombination are the predicted afterglow, now known as the cosmic microwave background (CMB). Arno Penzias and Robert Wilson discovered the first observational evidence of the CMB by noticing a mysterious noise in their radio data, corresponding to a temperature excess of  $\sim 3.5\text{K}$  (Penzias & Wilson, 1965). Penzias and Wilson were aware of work being done by Dicke et al. (1965) who were in the process of searching for the CMB and therefore attributed this temperature excess to be evidence of the CMB. The CMB was mapped with high precision by a series of missions including COBE and WMAP (Hinshaw et al., 2007; Mather et al., 1994), revealing a temperature of 2.7K and a perfect blackbody spectrum, which appears isotropic apart from some very small directional anisotropies. The latter are of the utmost significance as they trace the density fluctuations that provided seeds for gravitational instability for the first stars and galaxies to form. The Big Bang Model also predicts the concentration of primordial elements which were formed when the first atoms were made (Big Bang Nucleosynthesis), this included helium, deuterium and lithium. The abundances of these atoms are dependent on the baryon to photon ratio and observational results have found that the observed abundances for each of these atoms match the predicted values from the Big Bang model (Tytler et al., 2000). Thus, the CMB, Hubble's Law, and the abundance of primordial elements all provide significant evidence for the hot Big Bang theory.

The hot Big Bang theory of cosmology requires an incredibly tight set of initial values which causes two problems to arise. Firstly, the observed homogeneity of the universe is hard to explain, in particular the thermal equilibrium state of the CMB. This is because there are regions of the universe which are separated by more than size of the cosmological horizon (this is the distance a photon has travelled since the Big Bang) which means that

they have had no causal contact during the lifetime of the universe and thus should not be in thermal equilibrium. This is known as the horizon problem. Secondly, its also hard to explain why the universe needs to be so accurately fine tuned to produce the observed flatness of the universe, as any small deviations from these values severely changes the topology of the universe, this is known as the flatness problem. However, Guth (1981) proposed an inflation model for the early universe which offers a solution to the horizon and flatness problems. Guth showed that they would disappear if the universe underwent a rapid phase of exponential expansion by which the universe super-cooled by 28 or more orders of magnitude below the critical temperature which would be required for a phase transition. The inflation model can be probed by way of gravitational waves, these are ripples in space-time generated by an extreme acceleration of mass. During the period of inflation, gravitational waves are theorised to have been produced due to the rapid expansion, these are known as primordial gravitational waves (these waves are also expected to be produced in the period between the end of inflation and the start of Big Bang Nucleosynthesis Ricciardone 2017). The recent ground breaking detection of gravitational waves by way of binary black hole mergers (Abbott et al., 2016) provides future potential to detect primordial gravitational waves and therefore offer a significant insight into the inflationary period of the universe.

In Guth's model, the universe initially contained a sea of quantum fluctuations which as a result of the inflation period caused them to be amplified to macroscopic scales. These albeit very small macroscopic fluctuations in density and temperature are observed in maps of the CMB as the CMB anisotropies mentioned above. The now macroscopic size fluctuations were regions of overdense dark matter and gas which were able to collapse under the force of gravity to form the first stars and galaxies. Models for the formation of galaxies such as those developed by Rees & Ostriker (1977) and White & Rees (1978), propose that as the dark matter collapses to form a dark matter halo, gas is then attracted toward their deep gravitational potential wells which becomes heated to the virial temperature. The gas then cools radiatively and condenses at the centre of the dark matter halo to form the galaxy. Thus the statistical properties of the initial fluctuations should still be imprinted on the distribution of galaxies throughout the universe.

Redshift surveys such as the 2 Degree Field (2dF) survey (Colless et al., 2001) and the Sloan Digital Sky Survey SDSS (York et al., 2000) have been able to quantify the distribution of galaxies in the local universe. Maps produced by these surveys show that galaxies trace the clear web-like structure of the universe. This can be seen in the wedge plot from SDSS shown in Figure 1.1. Galaxies are preferentially found in high density regions such as clusters or groups which are located at intersections of long filaments of galaxies. It is thought that the growth of clusters is established by the feeding of galaxies from these filaments (e.g. see Fadda et al. 2008). Spanning the regions between clusters and filaments are vast regions of empty space known as voids where no or significantly low fractions of galaxies reside. Large scale cosmological simulations such as the Millennium (Springel et al., 2005) and Illustris (Vogelsberger et al., 2014) simulations have successfully been able to replicate the web-like structure of the universe. This

demonstrates how modelling simulations such as the latter and comparing to observations can effectively be used to probe the cosmology of the universe. In this regard, galaxy clusters offer a wealth of opportunity to constrain cosmology, they represent the largest structures in the universe which have grown hierarchically overtime, governed by the underlying cosmology. For example, cluster counts or cluster gas mass fractions can be used to constrain cosmological parameters, and comparisons of cluster mass distributions at low and high redshifts can probe the formation rates of cosmic structure which can provide constraints on cosmological models (see Allen et al. 2011; Vikhlinin et al. 2009b; Voit 2005 for detailed reviews on the importance of galaxy clusters to cosmology). In particular, simulations which model the mergers of galaxy clusters can be used to test physical models of dark matter or the plasma atmospheres of clusters. Furthermore, simulations of mergers can be used to understand the mass assembly of clusters by studying merger timescales and how the mass is accumulated.

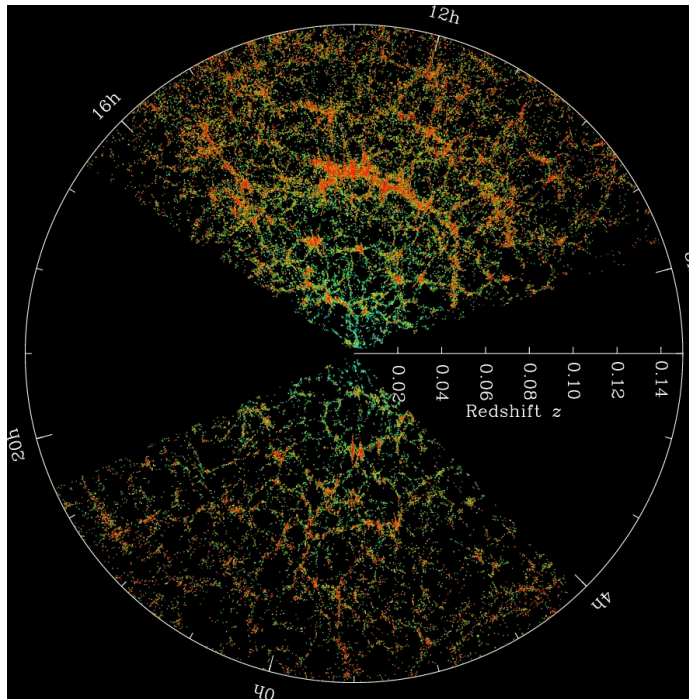


**Fig. 1.1:** Large Scale Structure of the universe revealed by The Sloan Digital Sky Survey (SDSS). Obtained from <https://www.sdss.org/>

## 1.3 Galaxy Clusters and Galaxies

In this section, the main properties of galaxy clusters and galaxies are provided to introduce the reader to the systems that are involved in minor mergers.

### 1.3.1 Galaxy Clusters

Galaxy clusters are the largest virialised structures found in the universe with typical masses between  $10^{13} M_{\odot}$  -  $10^{15} M_{\odot}$ , on scales spanning a few Mpc across, containing hundreds to thousands of galaxies. Clusters can essentially be thought of as closed box

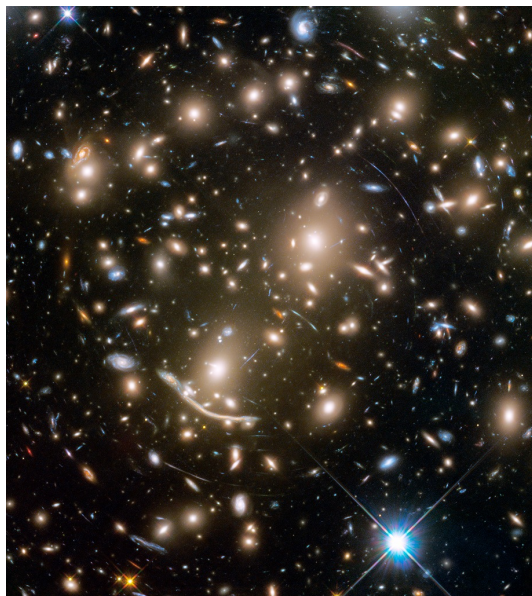


**Fig. 1.2:** Optical image of the galaxy cluster Abell 370. Image credit: NASA, ESA, Jennifer Lotz and the HFF Team (STScI). Obtained from <https://apod.nasa.gov/apod/ap170506.html>

systems, due to their deep gravitational potential wells which traps the majority of matter inside them. In 1933, Fritz Zwicky calculated the radial velocity of galaxies in the volume of the Coma cluster and applied the virial theorem to estimate the total cluster mass. Zwicky found that the cluster is more than an order of magnitude more massive than was expected as based on its luminosity and proposed that this missing mass was dark matter (Zwicky, 1933). Smith & Sinclair (1936) affirmed this result by performing the same analysis on the Virgo Cluster.<sup>1</sup> Measurements of flat rotation curves of galaxies gave the first indication that the vast majority of matter in the universe is in the form of dark matter and is not baryonic. For galaxy clusters, approximately 80 % of the total mass is due to dark matter. The remaining  $\sim 20$  % corresponds to a baryonic component, the majority of which is dominated by the hot cluster gas known as the intra-cluster medium (ICM), see Section 1.5. The cluster galaxies themselves only provide a small fraction of the total baryonic mass.

Through optical observations, clusters were first identified as large over densities of galaxies. Abell (1958) provided the first catalog of galaxy clusters based on optical observations. Figure 1.2 shows an optical image of the galaxy cluster Abell 370 which contains several hundred galaxies. This cluster is dominated by the two large elliptical galaxies in the centre of the image. Galaxy clusters typically contain a high fraction

---

<sup>1</sup>Further insights into dark matter are found by analysing rotation curves of galaxies. Rotation curves characterise the orbital circular velocity of stars or clouds of gas over the radius of the galaxy. As velocity is controlled by the mass, it allows for an indirect way to estimate the mass of the galaxy through Newtons Laws. The prediction from observing the visible disk of galaxies was to expect the rotation curve to decrease as the radius from the galaxy centre increased, this is the Keplerian expectation as is observed with the planets in the solar system. Rather notably, Rubin & Ford (1970) derived the rotation curve for the nearby Andromeda galaxy (M31) by measuring the hydrogen 21cm line in gas clouds and found that the rotation curve did not decrease with increasing radius but instead remained flat. The flat rotation curve meant that the mass of the galaxy increased with radius. The discrepancy between the Keplerian expectation and the flat rotation curve can be explained by the presence of dark matter in a spherical halo which is much larger than the visible disk of the galaxy. The dark matter halo would account for  $\sim 90\%$  of the total galaxy mass.

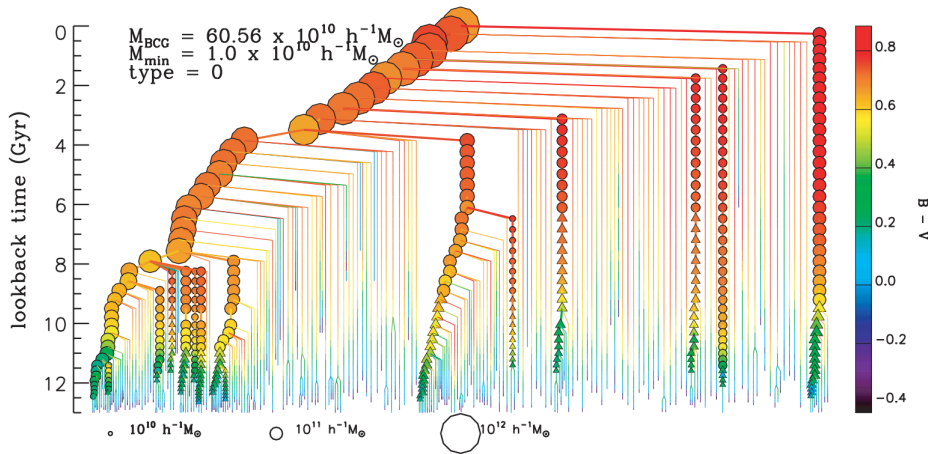


**Fig. 1.3:** Figure taken De Lucia & Blaizot (2007). A merger tree for the growth of a brightest cluster galaxy (BCG). Each symbol represents dark matter halo at that moment in time and are colour-coded as a function of B-V magnitude colour. The size of the halo scales with the stellar mass.

of elliptical galaxies, and at the very centre of the cluster there typically lies a giant elliptical galaxy known as the brightest cluster galaxy (BCG), which sits at the bottom of the clusters gravitational potential well. A BCG or also known as cD galaxies are the largest and brightest galaxies in the cluster and contain a large diffuse halo of stars. Many galaxy clusters contain substructure and hence can be split into smaller structures known as subclusters (Jones & Forman, 1999). Like their larger counterpart, subclusters are generally centred on a BCG and their presence in a cluster may indicate a merger is underway (Barrena et al., 2007; Drinkwater et al., 2001; Hwang & Lee, 2009; Ichinohe et al., 2015; Kravtsov & Borgani, 2012a).

Although often approximated as relaxed systems, galaxy clusters are dynamically young entities which are frequently subjected to mergers (Cohn & White, 2005) and are found to have typically undergone one major merger within the last  $\sim 5$  Gyr. In the framework of the cold dark matter model ( $\Lambda$ CDM) and driven by the force of gravity, galaxy clusters form through a hierarchical sequence of mergers and accretion of smaller sub-systems, such as subclusters, galaxy groups and galaxies, and continue to grow in this way (Kravtsov & Borgani, 2012a; White & Rees, 1978). Based on the hierarchical growth of galaxies and clusters, the Press-Schechter formalism (Press & Schechter, 1974) and extended versions by, e.g., Bond et al. (1991) and Lacey & Cole (1993) provide an analytical model to calculate the abundance of dark matter haloes as a function of mass for a given redshift. This formalism has been shown to catch many main features for the hierarchical build up of dark matter haloes in cosmological N-body simulations (Lacey & Cole, 1994). The Press-Schechter formalism can be used to estimate the rates of cluster mergers as a function of the cluster mass and can thus be used to understand the growth history of haloes and clusters. This is often pictured by a ‘merger tree’ which shows the growth of a dark matter halo through sequential merging in time to the final halo at the present epoch. A good example of a merger tree for the hierarchical growth of a BCG is shown in Fig. 1.3. As shown here, the dark matter halo of the BCG at the present epoch attains it’s mass through the culmination of many smaller mergers.

To quantify the boundary of galaxy clusters, the common prescription is to select the radius which encapsulates a total mass density of  $200 \rho_c$ , where  $\rho_c$  is the critical density of the universe. This radius is referred to as  $R_{200}$  and is approximately the virial radius of the cluster. Recent work however has suggested that the splashback radius (the radius of the first apocentre point a subhalo reaches during a cluster merger) may provide a more accurate physical representation for the cluster dark matter halo (More et al., 2015; Walker et al., 2019).

### 1.3.2 Galaxies

The first galaxies were born a few 100 million years after the Big Bang with the earliest known galaxy to date existing 400 million years after the Big Bang, at a redshift of  $z = 11.1$  (Oesch et al., 2016). Edwin Hubble discovered in his observations that there were distinct differences in the morphological properties of galaxies. Hubble had observed spiral galaxies - these are galaxies which are comprised of a flat disk with spiral arms which can vary depending on whether or not they have a central bar structure or how tightly wound the arms are. For elliptical galaxies - these are galaxies which have a smooth ellipsoidal appearance - Hubble found that they varied in terms of their eccentricity. In 1926, Hubble established the Hubble sequence which classified galaxies into three broad morphological categories; spiral, elliptical and lenticular (Hubble, 1926). The Hubble sequence is also referred to as a 'tuning fork' due to its shape, starting on the left (the handle) with elliptical galaxies ordered by their eccentricity, moving along the sequence it splits spiral galaxies into barred and unbarred types, ordered by the tightness of their arms. At the joint where the sequence splits from the handle lies lenticular galaxies, these are galaxies which have a disk shape like spiral galaxies but do not have spiral arms (lenticular and spiral galaxies are often referred to as disk galaxies). Spiral galaxies are also referred to as late-type galaxies and are generally star forming galaxies due to their large amounts of cold gas, high star formation rates and blue colour. Elliptical galaxies can also be referred to as early-type galaxies and in contrast to spiral galaxies, their star formation has been shut down. This is evidenced by their redder colour due to old populations of stars (in comparison to the younger average age of stars in spiral galaxies) and a sparse inter-stellar medium. For a more detailed review of galaxies see e.g. Binney & Merrifield (1998).

Every galaxy is thought to have a supermassive black hole (SMBH) at its core. A black hole represents a singularity in space-time which has an immense gravitational attraction and is characterised by an event horizon, this resembles a boundary where a photon inside the event horizon cannot escape the gravitational pull of the black hole. A special class of galaxy is known where the black hole at its core is actively accreting matter. As this matter falls toward the black hole, a significant amount of radiation is produced making the core of the galaxy incredibly luminous compared to the rest of the galaxy. The radiation is produced by converting gravitational potential energy into kinetic energy and is emitted across all wavelengths, in particular in their radio and X-ray spectra. These types of cores or nuclei are known as active galactic nuclei (AGN) and thus these galaxies are referred

to as active galaxies. Seyfert (1943) was the first to observe such galaxies with broad emission lines, therefore these galaxies are specified as Seyfert galaxies. Additionally, as found by Baade & Minkowski (1954), some active galaxies appear star-like (quasi-stellar) and emit strongly in the radio spectrum, these galaxies are known as quasi-stellar radio sources or quasars. BCG galaxies which have an AGN are thought to play a crucial role in thermal regulation of gas in the cluster core as they can balance radiative losses in the cluster (this is detailed further in Section 1.4.)

The life of any subcluster, group or galaxy that resides in the cluster environment, is far from monotonous. Particularly the interplay between such a body and the ICM gas it must traverse is a key ingredient in both its own evolutionary picture but also the overall cluster evolution. Dressler (1980) determined a relationship between the morphology of a galaxy and its location in a cluster, termed the morphology-density relationship. Dressler (1980) found that there is a higher frequency of early-type galaxies located in denser cluster environments in comparison to late-type galaxies, whereas there is a higher frequency of late-type galaxies in low density regions. This result indicated that the cluster environment plays a significant role in the evolution of a cluster galaxy. For example, a late-type galaxy moving toward higher density regions of the cluster faces many physical interactions which are at work to remove its gas atmosphere and shut down star formation, transforming the late-type galaxy into an early-type galaxy. These interactions include harassment, ram pressure stripping and cluster tidal effects (Balogh et al., 2000; Bialas et al., 2015; Boselli et al., 2016; Byrd & Valtonen, 1990; Larson et al., 1980; Moore et al., 1996; Peng et al., 2015). However, late-type galaxies have been observed in the core regions of galaxy clusters which are being subjected to ram pressure stripping (see Section 1.7 for further details on ram pressure stripping). Crucially, the ram pressure stripped tails of these galaxies are found to be locations of vigorous starbursts, i.e., locations which have a significant increase in star formation rate - these galaxies are known as jellyfish galaxies (Ebeling et al., 2014; McPartland et al., 2016). Therefore, the cluster environment can also act to increase star formation in galaxies.

Redshift surveys of the nearby universe indicate that most galaxies are found to be clumped together forming galaxy groups (Geller & Huchra, 1983; Tully & Brent, 1987) and are characteristically different to the larger galaxy clusters (Paul et al., 2017). Galaxy groups contain between 20 - 50 galaxy members (Mulchaey, 2000), therefore groups are smaller in size and lower in mass compared to the larger galaxy clusters. Groups are also cooler as they don't contain the hot ICM of clusters, and therefore temperatures typically range between 0.3 - 2.0 keV (Mulchaey, 2000). Using scaling laws Paul et al. (2017) state that they can clearly classify groups from clusters using mass, as they place an upper limit on group mass of  $\sim 8 \times 10^{13} M_{\odot}$ .

## 1.4 X-ray Observations of Galaxy Clusters

Observations of the Virgo Cluster by Byram et al. (1966) provided the first example of X-ray emission from galaxy clusters. This was followed a few years later by the first

X-ray catalog of clusters established by Giacconi et al. (1972) using the UHURU satellite. Many decades later, X-ray telescopes such as ROSAT, Chandra and XMM-Newton have all provided a wealth of information regarding the X-ray properties of clusters. Forman & Jones (1982) provided an early review on X-ray images of clusters, followed a few years later by Sarazin (1986) who provided an early review of the X-ray emission from clusters. The X-ray emission reveals that galaxy clusters are incredibly luminous systems with X-ray luminosities ranging between  $L_x 10^{43} - 10^{45}$  erg/s (Sarazin, 1986). The X-ray emission is spatially extended, meaning that the emission does not originate from cluster galaxies, but from the cluster itself. This X-ray emission is the dominant baryonic component in galaxy clusters, it is a hot, fully ionised, magnetised plasma that permeates throughout the whole cluster known as the intra-cluster medium (ICM) (see Section 1.5 for further details). Figure 1.4 shows composite X-ray and optical images of several galaxy clusters revealing the presence of the ICM in the X-ray.

The majority of the X-ray emission is produced via thermal bremsstrahlung. This occurs due to the ions in the plasma which have a positive charge, deflecting and accelerating the negatively charged electrons due to Coulomb forces which in the process causes the emission of an X-ray photon. However, X-ray radiation can be produced by free bound recombination when an electron recombines with an ion (Böhringer & Werner, 2010).

The X-ray photon emissivity is proportional to the square of the gas density, thus the central regions of clusters are the dominant feature of X-ray images due to their high densities. Consequently, this means that the outer regions of the cluster are more difficult to observe due to the lower surface brightness. Measurements for the density and temperature of the ICM can accurately be made through the use of X-ray spectroscopy. The cores of galaxy clusters contain a high central gas density, ranging from  $10^{-3}\text{cm}^{-3}$  to  $10^{-1}\text{cm}^{-3}$ , with the ICM temperature in these regions ranging between 1-10 keV. Moving away from the core, the cluster gas density decreases towards the outskirts, decreasing down to values of  $10^{-5}\text{cm}^{-3}$  or even lower (Böhringer & Werner, 2010).

Based on the characteristics of the X-ray emission, galaxy clusters have traditionally been split into two different cases, those with a cool core and those without a cool core. Cool core clusters are considered to be regular dynamically relaxed systems as they have a smooth X-ray brightness distribution which peaks in the very centre on the BCG galaxy in a region of condensed cooler gas. Non cool core clusters lack the pronounced cool core, which is thought to have been disrupted by mergers (Burns et al., 2008). Recent work by Mittal et al. (2009) and Hudson et al. (2010) however finds that galaxy clusters may be better split into three different regimes, those with a strong cool-core (SCC), weak cool-core (WCC) or a non-cool-core (NCC). These authors characterise clusters by their central cooling times, entropy and temperature profiles. Their results find that SCC clusters have very short central cooling times ( $t_{cool} < 1.0$  Gyr) and a low central entropy with a systematic drop in temperature which is centred on  $0.4 T_{vir}$ . WCC clusters on the other hand show an enhanced central entropy with a moderate central cooling time ( $t_{cool}$  between 1.0 - 7.7 Gyr) and a flat temperature profile or with a slight decrease in temperature towards

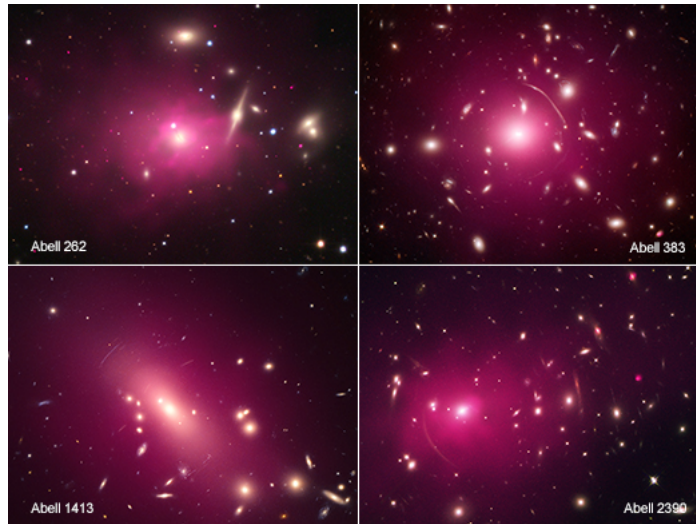


**Fig. 1.4:** Composite X-ray and Optical images of the galaxy clusters Abell 262, Abell 383, Abell 1413 and Abell 2399. In the X-ray (red colour) the intra-cluster medium is revealed to pervade throughout the cluster. For the X-ray images, credit NASA/CXC/Cinestav/T.Bernal et al. For the optical image of Abell 262, credit Adam Block/Mt. Lemmon SkyCenter/U. Arizona. For the other optical images credit NASA/STScI. Image obtained from <http://chandra.harvard.edu/photo/2017/clusters>

the centre. NCC clusters have high central entropies and long central cooling times ( $t_{cool} > 7.7$  Gyr) with temperature profiles which are flat or increase towards the centre.

As the ICM strongly emits X-rays it should in theory be losing thermal energy and therefore be cooling. The cooling gas will become denser and in the process will exert less pressure. In consequence, it should therefore not be able to support the outer layers of gas in the cluster. This would result in a subsonic flow of gas inwards toward the centre of the cluster creating a flow of cooled gas, i.e. a cooling flow (Fabian, 1994). However from X-ray observations of clusters, the data shows that there is not as much cool gas present in the cores than is predicted from their X-ray emission - this is known as the cooling flow problem (Peterson et al. 2003; Molendi et al. 2016; Hoffer et al. 2012; Donahue et al. 2000). However, it has been suggested that active galactic nuclei (AGN) can solve the problem through mechanical feedback (Gaspari et al., 2013; Guo et al., 2008; Mittal et al., 2009). This idea suggests that the energy an AGN transfers into the surrounding cluster gas by its expelling of radio jets can balance the radiative losses due to X-ray emission. Other solutions have been proposed to solve the cooling flow problem such as feedback from supernovae (Mathews & Brighenti, 2003) and thermal conduction which causes heat to flow from the outskirts of clusters inward towards the centre (Parrish et al., 2009; Voigt & Fabian, 2004). Significantly, Sharma et al. (2012) showed that cold filaments which condense out of the hot ICM due to thermal instabilities have a significant impact on feedback regulation in clusters. In particular, the latter can provide the fuel for black hole or stellar feedback which can provide thermal support to the cluster gas.

## 1.5 The Intra-Cluster Medium (ICM)

### 1.5.1 Plasma or Fluid?

The ICM is a highly ionised magnetised plasma, with typical temperatures ranging between 1 - 10 keV (Sarazin, 1986). The ICM plasma is weakly collisional and magnetised (Schekochihin & Cowley, 2006), with a Debye length of  $\lambda_d \approx 10^5$  m (ZuHone & Roediger, 2016). The most abundant element by far in the plasma is hydrogen, with a small fraction of helium and metals (Sarazin, 1986). As mentioned, the ICM strongly emits X-ray radiation. The plasma X-ray emission can be clearly explained by the coronal approximation (Mewe, 1999). This approximation is based on the assumptions that; photons in the plasma are free to move and do not interact with electrons and ions, all the electrons in atoms are in their ground state, and the plasma is locally relaxed to a Maxwellian distribution centred on a common temperature (Peterson & Fabian, 2006). The latter is only true if the time scale for equilibration is shorter than typical dynamical time scales of the cluster, such as the cluster cooling time. From Sarazin (1986), the proton equilibration time scale is  $\approx 1.4 \times 10^6$  yr, the electron equilibration time scale is  $\approx 6.2 \times 10^8$  yr. As the typical cluster cooling time is  $8.5 \times 10^{10}$  yr (Hudson et al., 2010), the equilibration timescales are shorter, thus satisfying the condition. These assumptions allow for collisional equilibrium to be reached as the collisional ionisation processes become balanced with recombination processes. However this notion may not hold in the cluster outskirts as the gas density is much lower, thus lowering the number of collisions. In result, this produces an optically thin plasma, i.e. radiation can escape the plasma without interacting with it, that is in collisional equilibrium.

In the absence of a magnetic field, the mean free path of electrons and ions in the ICM plasma is determined by Coulomb collisions. Based on Spitzer & L. (1956), Sarazin (1986) show that the mean free path of electrons ( $\lambda_e$ ) and ions ( $\lambda_i$ ) in a Maxwellian plasma is given by,

$$\lambda_e = \lambda_i = \frac{3^{3/2}(kT_e)^2}{4\pi^{1/2}n_e e^4 \ln \Lambda} \approx 23 \text{ kpc} \left( \frac{T}{10^8 \text{ K}} \right)^2 \left( \frac{n_e}{10^{-3} \text{ cm}^{-3}} \right)^{-1} \quad (1.1)$$

where  $k$  is the Boltzmann constant,  $T_e$  is electron temperature,  $n_e$  is electron density,  $e$  is the elementary charge and  $\Lambda$  is the Coulomb logarithm. This mean free path of 23 kpc is much less than the size of a cluster,  $\sim 1$  Mpc, thus it is reasonable to treat the ICM as a collisional fluid.

However, simulations of galaxy clusters using hydrodynamics resolve structures down to pc scales (as is the case in this thesis). Therefore, the mean free path must be much lower for this fluid approximation to be true. Significantly, as the ICM plasma is threaded with weak magnetic fields, it is subjected to plasma instabilities generated by turbulent motions (Schekochihin & Cowley, 2006). In the magnetic field of the ICM plasma, electrons and ions follow helical orbits as they gyrate around the magnetic field lines, for example, a typical electron Larmor radius is  $r_g \approx 3 \times 10^8$  cm (Sarazin, 1986). Crucially, these

plasma instabilities are found to peak at scales which are near the gyroradius which causes scattering and collisions on scales much smaller than the Coulomb mean free path, i.e. the effective mean free path is reduced (Brunetti & Lazarian, 2011; Schekochihin & Cowley, 2006). Thus, it is believed that the presence of the magnetic field in the ICM plasma and the small Larmor radius ensures that the ICM behaves as a fluid. This reduced mean free path is supported by the fact that on small scales, the ICM displays many fluid like features such as shocks (Fabian et al., 2003, 2006; Kraft et al., 2012), bubbles (Churazov et al., 2001; Su et al., 2017c), and gas tails of galaxies (Boselli et al., 2016; Randall et al., 2008a). Furthermore, numerical simulations of astrophysical systems using hydrodynamics can replicate the observed features seen in the ICM (see Roediger et al. 2015a). As the mean free path for ions and electrons in the ICM is small, local gas properties are determined by transport processes such as thermal conduction and viscosity.

Due to the hot plasma of the ICM, an interesting effect arises. Sunyaev & Zeldovich (1972) predicted that the movement of the hot free electrons in the ICM plasma causes inverse Compton scattering of cosmic microwave background (CMB) photons which pass through the cluster to higher energies, distorting the CMB spectrum in the process. This is known as the thermal Sunyaev & Zeldovich effect and has been observed in many clusters (see Carlstrom et al. 2002). The scattering of the CMB photons is proportional to the electron pressure integrated along the line of sight. In addition, the distorting of the scattered CMB photons due to the SZ effect can be Doppler shifted due to the bulk motions of the ICM, this is known as the kinetic SZ effect (Sunyaev & Zeldovich, 1980). Thus the SZ effect provides an independent way to measure ICM properties. Measuring these distortions in the spectrum of the CMB allows researchers to study a wealth of features, such as the thermal pressure of the ICM, density perturbations in the universe and also allows for measurements of the peculiar velocities of clusters.

## 1.5.2 Microphysics and Transport Processes

An important aspect of ICM microphysics is the magnetic field. From radio-relic observations, the magnitude of the ICM magnetic field is measured to be on the order of a few  $\mu\text{G}$  (Bonafede et al., 2009, 2010; Ferrari et al., 2008) and is embedded in the ICM on scales on the order of tens of kpc or less. The origin of the magnetic field and its amplification is still an open question in astrophysics. One possible pathway for the origin of the magnetic field is through galactic outflows (Donnert et al., 2009) which can then be amplified by cluster mergers and turbulence (Dubois & Teyssier, 2008; Ryu et al., 2012). Another proposed scenario by Ryu et al. (2008) involves a turbulent dynamo model in the ICM which amplifies magnetic fields from small seeded fields, which would give rise to the observed magnetic field magnitudes. Further, Kunz et al. (2014); St-Onge & Kunz (2018) propose that the magnetic field arises through plasma instabilities which can amplify the magnetic field to macroscopic scales. Significantly, even though the ICM is magnetised, the thermal pressure is much larger than the magnetic pressure and therefore dominates the ICM dynamics. Therefore, hydrodynamics can be used as a first approximation when

performing simulations of galaxy clusters. As demonstrated in the previous subsection, the Larmor radius for electron and ions is significantly shorter than their mean free paths. In consequence the diffusion of momentum and heat is strongly anisotropic (Braginskii, 1965), therefore magnetic fields may play a role in potentially suppressing thermal conduction and viscosity in the ICM (Chen et al., 2017; Vikhlinin & Markevitch, 2002; ZuHone et al., 2011). However in regards to the mergers of galaxy clusters, Brzycki and ZuHone (submitted) conducted a parameter space exploration for the effects of magnetic fields in mergers to find that they do not have a significant effect on the merger driven gas dynamics.

Another important aspect of the ICM microphysics is turbulence. Cluster mergers induce large bulk velocities in the ICM on the order of  $1000 \text{ km s}^{-1}$  producing turbulence in the cluster gas. For example, during a cluster merger, an infalling subcluster or galaxy produces Kelvin-Helmholtz instabilities (KHI) along its sides, at the interface between the bulk flow of the galaxy and the ICM, which strips its gaseous atmosphere. These KHIs drive the production of turbulent eddies in the gas as it is stripped away, resulting in the redistribution of kinetic energy produced by merger throughout the cluster. AGN feedback is also thought to provide an injection of kinetic energy into a cluster which drives turbulence in the ICM (Gaspari, 2015). The kinetic energy is dissipated into heat and therefore has a significant impact on the thermal state of the ICM gas. However, the exact properties of turbulence in the ICM remain unclear, as there is still the open question of how turbulent is the ICM? At present, measurements for the gas velocities in the ICM are very difficult, as the energy resolution required to do this is unavailable with current X-ray telescopes. However, constraints on turbulence can be put in place by observing thermal Sunyaev-Zeldovich (SZ) effect fluctuations and surface brightness fluctuations (Churazov et al., 2012; Khatri & Gaspari, 2016; Zhuravleva et al., 2014). However, in the brief moments it was active, the Hitomi satellite, with its increased energy resolution, was able to measure a line-of-sight ICM velocity dispersion from the Perseus Cluster core of  $150 \text{ km s}^{-1}$  (Collaboration et al., 2016) demonstrating that future high resolution telescopes can probe the level of turbulence in the ICM.

Transport processes in the ICM relate to the characteristics of its thermal conduction and viscosity. These two elements crucially effect the level of diffusion, and the redistribution and dissipation of energy in a cluster, and therefore play a pivotal role in a cluster's overall thermal state and it's subsequent evolution (Fabian et al., 2005). Further, the ability to constrain transport processes in the ICM is a critical factor in determining the gas stripping of galaxies (Nulsen, 1982). At present, the level of the effective viscosity and thermal conductivity of the ICM is an open question. In regards to level of viscosity, it has been reported that the morphology of cavities produced by AGN can be explained by a viscous ICM (Fabian et al., 2003). However, there is substantial evidence that the ICM viscosity is suppressed relative to the Spitzer value (this is the coefficient of viscosity for an unmagnetised, ionised plasma Braginskii 1958; Spitzer 1962), as described above, there is evidence for a turbulent ICM which would require a non-viscous regime. Whatever the level of the effective viscosity, magneto-hydrodynamics (MHD) and plasma processes are

thought to be important in its determination (Kunz et al., 2015), although this is not yet fully clear.

### 1.5.3 Probes for ICM Transport Processes

Research into cold fronts could provide a method to constrain the transport processes of the ICM. Cold fronts are sharp contact discontinuities in the ICM where there are steep gradients in temperature and density across the front (see Section 1.6.4 for further details). As the temperature gradient at cold fronts is large, it has been implied that thermal conduction in the ICM is suppressed. This was found to be the case by Etori & Fabian (2000). One explanation for this, as shown by ZuHone et al. (2013) is that magnetic fields parallel to cold fronts can partially suppress thermal conduction.

Although sloshing cold fronts appear to be stable, subsonic velocity shears are known to exist across them, meaning that KHI's should be highly present along the front (e.g. ZuHone et al. 2010, Roediger et al. 2011). The observable signatures of KHI's at cold fronts are subtle therefore initially they were not recognised in observations. However, by combining observations of the Virgo Cluster and tailored hydrodynamical sloshing simulations of the cluster, Roediger et al. (2013a) identified KHIs at the sloshing cold fronts in the cluster and were able to describe in detail their appearance. KHIs have now been identified in several clusters, e.g. the Perseus Cluster (Ichinohe et al., 2019) and A3667 (Ichinohe et al., 2017). The presence of KHIs is particularly interesting as magnetic fields and viscosity should suppress the instability (Roediger et al., 2013b; ZuHone et al., 2011), Therefore the presence of KHIs can put limits on the strength of the magnetic field and viscosity. However, at present this is unclear and research maybe at a point where a sufficient amount of KHIs have been identified to say that they are not suppressed on any interesting scales.

To probe the level of viscosity, the morphology of stripped gas tail of galaxies falling into clusters can give information regarding its nature. The magnitude of the ICM viscosity shapes the flow around the galaxy, impacting on the appearance of its gaseous atmosphere and tail as it impacts the level of mixing that will occur with the ICM. For a low viscosity, the gas tail will mix efficiently well with the ICM and therefore a short visible X-ray tail would be expected as the stripped gas will quickly mix into the ICM and fade into the ambient density of the ICM. In contrast, for a viscous ICM, the amount of mixing will be significantly reduced, therefore the stripped galactic gas will survive for a longer, producing a substantially longer and cooler X-ray bright tail. With this notion, Kraft et al. (2017); Roediger et al. (2015a,b) investigated the infall of the early-type galaxy NGC 4552 (M89) into the Virgo cluster and determined that the ICM behaves as an inviscid fluid on macroscopic scales, finding that the ICM viscosity is sufficiently suppressed. Furthermore, the level of viscosity can be probed by studying KHI's, as Roediger et al. (2013a) find that a viscous ICM is able to suppress their formation. For example, Su et al. (2017b) based on the presence of eddies generated by KHIs, deduced an upper limit of 5% Spitzer for the viscosity of ICM using Chandra observations of the elliptical galaxy NGC 1404.

### 1.5.4 Enrichment of the ICM

Through the use of X-ray spectra, the ICM is revealed to be metal-enriched (Mitchell et al., 1976), with measurements finding a value of  $\sim 0.3$  solar in iron (Fukazawa et al., 1998), peaking to solar values or more around the very centres of clusters. This measurement clearly points towards the cluster gas being processed at some point along the way, as heavy elements cannot be produced directly in the ICM and therefore cannot be of primordial origin. At present, research poses a number of mechanisms that each play a role in the chemical enrichment of the ICM. Nucleosynthesis is one such method by which metal rich gas is injected into the ICM by supernovae (Mernier et al., 2016). AGN outbursts (Moll et al., 2007; Roediger et al., 2007), starbursts and galactic winds driven by supernovae in galactic stars and intracluster stars (Arnaud et al., 1992; De Young, 1978; Kapferer et al., 2007) have also been reported as a pathway to enrich the ICM. Dynamical removal, such as ram-pressure stripping of cluster galaxies (Domainko et al., 2006) and galaxy-galaxy interactions (Larson & Dinerstein, 1975) which strips metal rich gas and eventually mixes into the ICM also provide further methods for metal-enrichment. Significantly, these mechanisms naturally lead to the notion that cluster mergers also play a key role in the enrichment of the ICM and also the redistribution of metals throughout the cluster (Biffi et al., 2018; Cora, 2006; De Grandi & Molendi, 2001) as the process of dynamical removal can occur during the merger phase. The crucial point is that as cluster galaxies or subclusters lose their chemically enriched gas to the ICM, it therefore holds an indispensable amount of information regarding the chemical history of the cluster. This information can then be used to understand the dynamics of the cluster and also its merging history. Further, O’Sullivan et al. (2013) determined a close correlation exists between the metallicity distribution and the position of cold fronts in NGC 5044. This suggests that sloshing in clusters also has a strong impact on the distribution of metals in the ICM.

Balestra et al. (2007) conducted an analysis of 56 clusters within a redshift range  $0.3 < z < 1.3$  to trace the evolution of the iron content of the ICM. Their results found that for  $z \geq 0.5$  the mean iron content of the ICM is approximately constant with  $Z_{Fe} \approx 0.25Z_{\odot}$ . In contrast the iron content in the redshift range  $0.3 < z < 0.5$  is significantly higher with  $Z_{Fe} \approx 0.4Z_{\odot}$  and further deduced that the iron content at the present epoch is a factor of  $\sim 2$  larger than at  $z \simeq 1.2$ . In a similar vein, Liu et al. (2018) using Chandra archival data found that the spatial distribution of iron in the ICM increases by a factor of 3 from  $z = 1$  to  $z = 0.1$  and suggest that this could be the result of mixing with mechanical-mode feedback from the central cluster galaxy. In a study on the origin of the ICM, Cora et al. (2008) find that clusters have been significantly enriched by  $z \sim 1$ , supporting the above results. The outcome of these works coincide with the proposed mechanisms for enrichment, as these all require a significant amount of time to allow metal rich gas to be expelled and become mixed into the ICM, specifically in the context of cluster mergers, as these can take several Gyrs to complete. Thus providing an explanation as to why there is an observed higher metal content in the ICM at this present epoch than there is at higher redshifts.

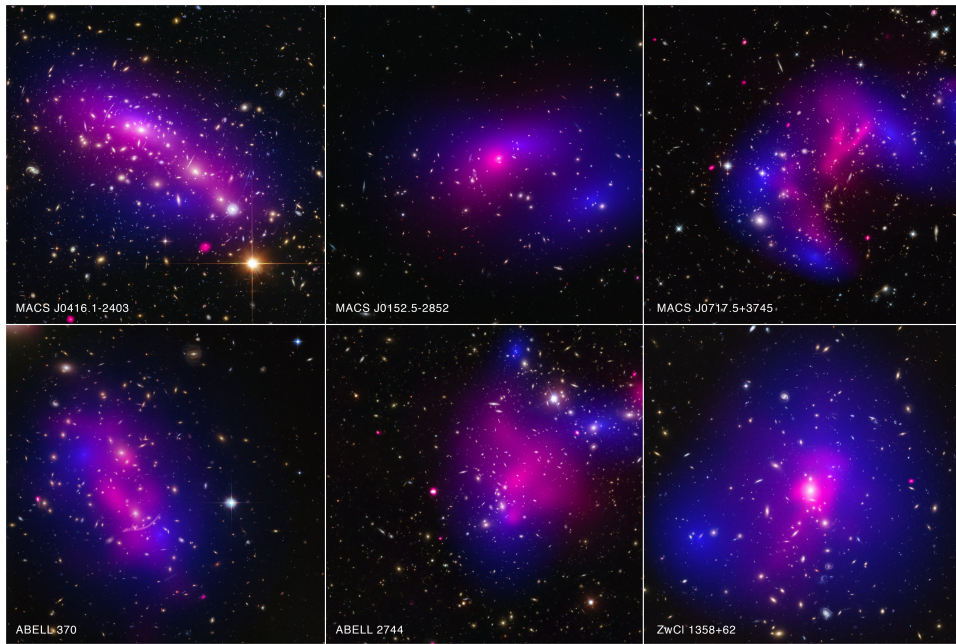


**Fig. 1.5:** A set of 6 composite X-ray and optical images of galaxy cluster mergers in action. The purple colours correspond to X-ray emission and the blue colour corresponds to the location of dark matter. Image credit for the X-ray image: NASA/CXC/Ecole Polytechnique Federale de Lausanne, Switzerland/D.Harvey & NASA/CXC/Durham Univ/R.Massey. For the optical image: NASA, ESA, D. Harvey (Ecole Polytechnique Federale de Lausanne, Switzerland) and R. Massey (Durham University, UK). Obtained from <http://chandra.harvard.edu/blog/node/548>

## 1.6 Mergers of Galaxy Clusters

### 1.6.1 Merger Basics

In the hierarchical cosmological model, the formation of galaxy clusters has occurred in the recent history of the universe, and X-ray telescopes and other observations clearly show that clusters are still growing through violent collisions and mergers (Buote, 2002) as merging timescales are close to, or on the order of the age of the universe (Binney & Merrifield, 1998). X-ray observations of the strongest mergers (i.e., major mergers), show that there are offsets between the peaks of X-ray surface brightness and dark matter density due to a merger. This is due to the dark matter being collisionless and therefore is only affected by gravity, whereas the gas, in addition to being affected by gravity, is also subjected to hydrodynamical effects, thus causing a displacement between the two components. Radio observations can also provide an indication for dynamical activity occurring in a cluster due to the presence of radio haloes and relics (Feretti et al., 2012) which result from increased turbulence and shocks arising during the merger. Many galaxy cluster mergers have been observed to date (e.g. Abell 520, Deshev et al. 2017; Abell 168, Hallman & Markevitch 2004; 1E 0657-56, Markevitch et al. 2002; MACS J0553.4-3342, Pandge et al. 2016). Figure 1.5 presents a set of six extreme cases of dissociative cluster mergers. The X-ray emission in pink shows the disrupted nature of the gas due to the merger and the dark matter in blue shows the offset with the gas.

A galaxy cluster merger can involve a merger between two clusters or could involve a main cluster and a smaller subcluster, group or galaxy. The mass ratio of the merger is

used to categorise them - i.e. a 1:1 merger would correspond to a major merger between two clusters of identical mass and a 1:10 merger would correspond to a minor merger between a cluster and a galaxy or a small group or subcluster. The impact parameter or closest approach can also be used to quantify a merger. For clarity in this work, the more massive merger partner is termed the primary, i.e., the cluster and the smaller merger partner is termed the secondary, i.e., an early-type galaxy or subcluster. A minor cluster merger has been defined as a mass ratio of  $< 1:3$  between the primary and secondary, thus a major merger corresponds to a mass ratio of  $> 1:3$  (Planelles & Quilis, 2009; Vitvitska et al., 2002). Using cosmological simulations, Vitvitska et al. (2002) showed that the infall velocity of the secondary in a merger is normally distributed, centred at  $0.71v_c$ , where  $v_c$  is the circular velocity of the primary. This infall velocity is typically  $\sim$  Mach 1. For minor mergers, Vitvitska et al. (2002) show that the tangential component of the infall velocity again is normally distributed and is centred on a value of  $0.71v_c$ .

### 1.6.2 Outline of Minor Merger Phases

A cluster minor merger can be characterised by distinctive merger phases. Here, the phases for an off-axis minor merger are described as these are the focus of this thesis. The first phase involves the infall of the secondary into the primary. Here, as mentioned above, the infall velocity of the secondary at the virial radius of the primary is  $\sim$  Mach 1. Thus, due to the supersonic motion, a bow shock will lead the secondary, shock heating the ICM gas in the primary. Further, the secondary is gas stripped due to its motion through the ICM (see Section 1.7 for further details), forming a long, cool, unmixed tail which traces the recent orbit path producing the typical head-tail structure of a ram pressure stripped galaxy (Roediger et al., 2015a). This work will provide additional knowledge to this merger phase (and the others described below) as a description of ongoing work into the effect that the gravitational potential of the secondary has on the surrounding ICM gas due to its motion during a merger is provided. This description will also detail how this effect impacts methods to estimate the infall velocity of secondaries. Figure 1.6 shows an example of a first infall for a minor merger with a mass ratio of 1:13, demonstrating the leading bow shock and gas tail of the secondary during this phase. For the primary there is little to no effect on it from the first infall.

Moving onto the next phase, after pericentre passage, gas sloshing is initiated in the core of the primary due to the motion of the secondary (see Section 1.6.4 below for more details) producing concentric cold fronts which spiral outwards (Ascasibar & Markevitch, 2006). This initiation of sloshing can be seen in Fig. 1.7 as the gas around the core of the primary takes on a spiral shape. As the secondary moves past pericentre toward apocentre, the ram pressure acting on its gas atmosphere reduces rapidly as the secondary slows down and turns around to begin its next infall into the primary. This process causes gas to overshoot the secondary in a slingshot effect (Hallman & Markevitch, 2004; Markevitch & Vikhlinin, 2007; ZuHone, 2011). Poole et al. (2006) described this overshooting gas in terms of plumes which then infall into the primary as filaments and Hallman & Markevitch

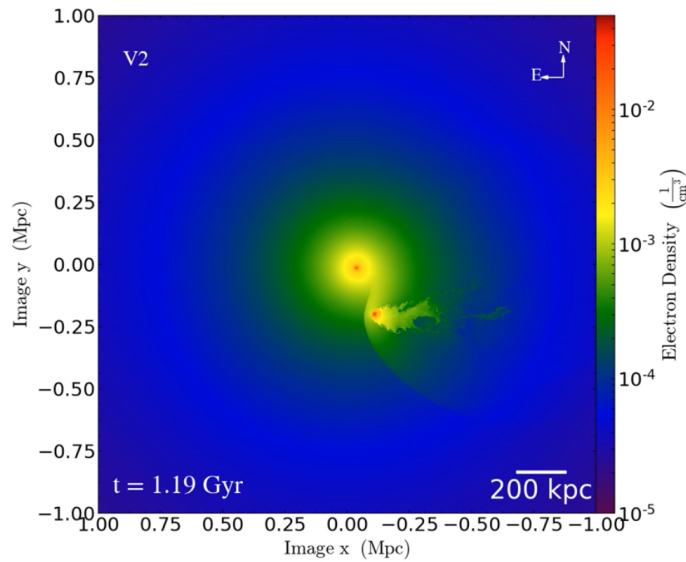


**Fig. 1.6:** A gas density snapshot demonstrating the first infall merger phase of a secondary merging with a primary with a mass ratio of 1:13. During this phase, the secondary is led by a bow shock due to its supersonic motion and has a long, cool, unmixed tail.

(2004); Markevitch & Vikhlinin (2007) describe this effect in the context of cold fronts. However, the characteristics of the gas tail of the secondary during this phase has not yet been reported on in the literature. This work will provide a detailed study of the characteristics of the gas tail during this merger phase and how it corresponds to features in the primary.

As the secondary moves away from apocentre, the next merger phase is established as the secondary undergoes its second infall into the primary. In this merger phase, the gas atmosphere of the secondary is truncated due to the continued gas stripping and its stripped gas tail is now well mixed with the ICM, this is demonstrated in Fig. 1.8. For the primary, the ongoing sloshing in the core has evolved further as the sloshing cold fronts continue to move outwards away from the core (e.g. see Fig. 11 in ZuHone 2011). If the secondary makes it through a second core passage, then the same merger evolution occurs as the phase from first pericentre passage to apocentre described above, however the sloshing initiated from the first core passage dominates over any additionally induced sloshing due to the most recent core passage. Again this work will provide a more complete picture of these merger phases by relating features of the secondary to the primary, such as the locations of shocks produced by the secondary and the location of sloshing cold fronts.

### 1.6.3 Energy Dissipation and Shocks in Mergers

Mergers of galaxy clusters represent the most energetic phenomena observed in the universe. This is due to their typical supersonic speeds, on the order of  $1000 \text{ km s}^{-1}$  (Sarazin, 2002). Thus, cluster mergers produce vast amounts of kinetic energy (on the order of  $10^{63} - 10^{64}$  ergs) in a cluster crossing timescale of  $\sim \text{Gyr}$  (Kravtsov & Borgani, 2012b). This energy is dissipated throughout the cluster primarily in the form of shocks. However, mergers also cause compression waves in the dark matter haloes of the merging systems

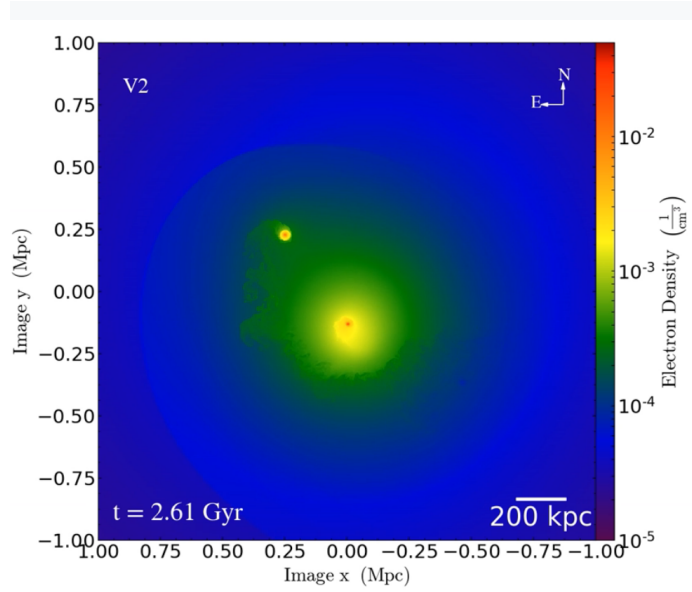


**Fig. 1.7:** A gas density snapshot of the post pericentre/apocentre merger phase. In this phase, gas sloshing in the core of the primary characterised by the spiral morphology of the gas is initiated due to the motion of the secondary through core passage.

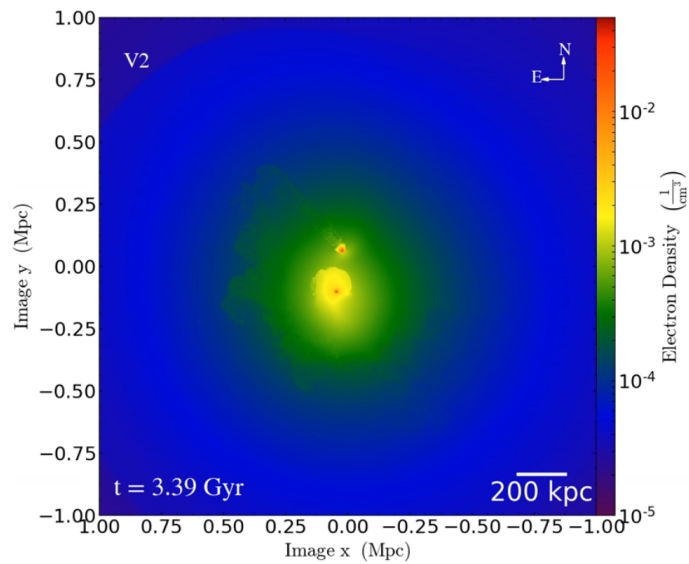


**Fig. 1.8:** A gas density snapshot of the second infall merger phase. The secondary has a truncated atmosphere with a tail which is mixed well with the ICM. Meanwhile sloshing continues to evolve in the primary core spiralling outwards.

which transfer gravitational potential energy from the merger to the final halo once the merger has completed.

As mentioned, the infall velocity of the secondary into the primary during a merger is supersonic, thus a bow shock is formed which leads the secondary. Shocks in clusters have typical mach numbers  $M \leq 3$  and are revealed in X-ray observations as sharp edges in the surface brightness (Markevitch & Vikhlinin, 2007). To date, shocks in clusters have been extensively studied (see: Botteon et al. 2018; Brunetti & Jones 2014; Ha et al. 2018; Schaal & Springel 2015) and are thought to be present in all cluster mergers (Vazza et al., 2011). Two of the best examples of a merger shock are found in the galaxy cluster 1E 0657-56, known as the Bullet Cluster (Markevitch et al., 2002) and Abell 665 (Dasadia et al., 2016). Merger shocks can dissipate their energy thermally by heating the ICM or through bulk motions of the ICM in the form of turbulence (Sarazin, 2002). Additionally, merger shocks can also dissipate their energy via the acceleration of relativistic particles (such as electrons in cosmic rays) or magnetic fields amplifying them in the process. The acceleration of electrons in cosmic rays by merger shocks produces synchrotron radiation in the form of diffuse radio emission, which in turn produces radio relics - these are essentially radio manifestations of the merger shocks. Therefore shocks are not only found in X-ray data, but also in radio observations too. Radio relics appear as arc-like structures in the outskirts of galaxy clusters, one clear example of this is found in the galaxy cluster Abell 115 (Hallman et al., 2018). Merger shocks however are difficult to detect as the geometry of the shock needs to be aligned favourably for an observer, because of this, there are few clear observational examples of merger shocks available in the literature. Nevertheless, when obtainable, merger shocks provide a vital tool to study the transport processes of the ICM along with the dynamics involved during a cluster merger and are thus a key focus of research in astrophysics.

#### 1.6.4 Gas Sloshing and Cold Fronts in Mergers

Mergers of galaxy clusters exhibit many features, and in particular, X-ray observations demonstrate sharp edges in surface brightness images. These edges correspond to contact discontinuities between regions of gas where there are steep temperature and density gradients and are known as cold fronts (Markevitch & Vikhlinin, 2007). At these cold fronts, the ICM gas is cooler on the denser side, with the pressure being continuous across the front (Markevitch et al., 2000).

In the case of a minor merger, cold fronts can be wrapped around the core of the primary in a spiral pattern, which is the result of gas sloshing in the primary's gravitational potential triggered by the primary core passage of the secondary (Ascasibar & Markevitch, 2006). Additionally, due the infall of the secondary into the primary, a cold front is formed at its upstream edge which is the contact discontinuity between the secondary atmosphere and the ICM. Sloshing cold fronts are particularly clear in cool core clusters due to their steep central entropy gradient. During an off-axis minor merger, the secondary rapidly accelerates the ICM gas and dark matter in the primary core, causing cool ICM gas to be

displaced and lifted upwards out of the primary's gravitational potential well. However, ram pressure acts to decelerate the ICM gas causing it to separate from the dark matter. As the ram pressure weakens, the ICM gas falls back to the dark matter core, but in the process overshoots it and causes it to slosh. In result, gas sloshing produces oscillations that ripple throughout the cluster propagating outwards and can survive for many Gyrs. The uplifted ICM gas acquires angular momentum which creates the observed spiral appearance of sloshing patterns in clusters, this is demonstrated in Figure 1.9. A number of sloshing fronts have been observed in galaxy clusters to date, e.g. the Perseus Cluster (Ichinohe et al., 2019; Walker et al., 2017), Abell 2502 (Blanton et al., 2011), Abell 496 (Ghizzardi et al., 2014), Abell 1644 (Johnson et al., 2010), Fornax Cluster (Su et al., 2017d) and Abell 2029 (Paterno-Mahler et al., 2013).

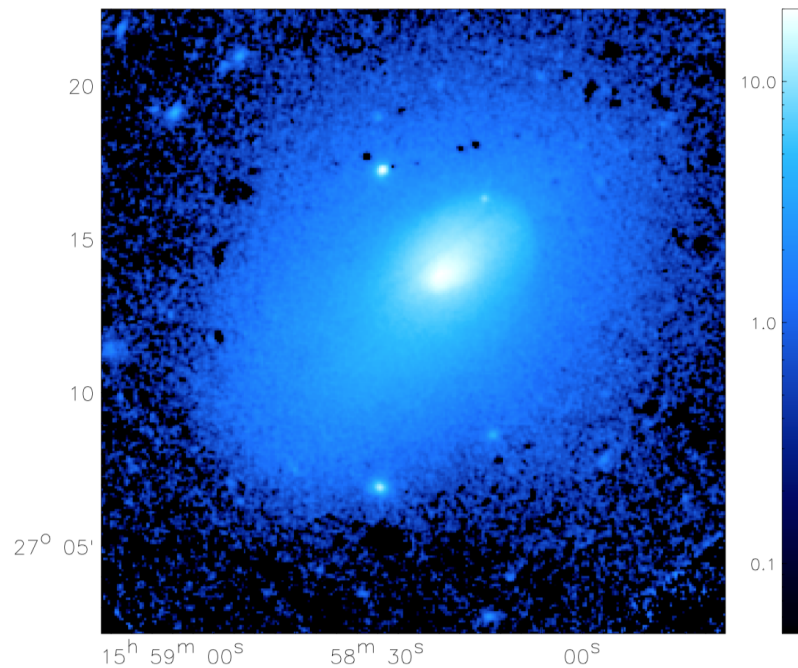


**Fig. 1.9:** Taken from Fig 1. in Rossetti et al. (2013). XMM-Newton observation of the core of the galaxy cluster Abell 2142 revealing the spiral patterns of sloshing cold fronts.

### 1.6.5 Simulations of Cluster Mergers

As galaxy clusters evolve on time scales close to the age of the universe, observations of clusters only provide a window into a particular phase of a merger. Thus, simulations can be used to investigate the evolution of the whole merger. In this regard, simulations can work in hand with observations to understand their formation and morphological properties, as well as providing a probe for cosmological parameters and high energy astrophysics. These simulations comprise of numerical models where the dark matter and cluster gas can be modelled with N-body and hydrodynamical methods. Ricker & Sarazin (2001); Roettiger et al. (1993, 1997); Schindler & Mueller (1993) paved the way for numerical simulations, establishing that they could successfully describe the gas dynamics of mergers. There are generally two methods in which to simulate cluster mergers, either using cosmological

initial conditions (e.g. Nagai & Kravtsov 2003; Mathis et al. 2005; Paul et al. 2011) or using idealised clusters (e.g. Poole et al. 2006; ZuHone 2011). Using cosmological initial conditions caters for mergers of numerous galaxies as they do naturally in the universe i.e. with a variety of mass ratios and impact parameters in the context of cosmological expansion. However, this complexity can hamper disentangling particular aspects of the merger physics. The other approach to take is using idealised clusters. Typically, this involves creating two spherical, self gravitating clusters in an isolated box which collide under their self gravity. These simulations allow for the highest resolution possible to probe the dynamics of mergers. The downside is they are run in a non cosmological environment which does not accurately reflect the true nature of cluster mergers. Idealised cluster simulations are useful for simulating specific cluster scenarios and comparing to observations of the clusters in question (e.g. Halbesma et al. 2019; Machado & Neto 2013; Randall et al. 2008b; Zuhone et al. 2009). My work on the Fornax Cluster in Chapter 3 follows this idea. Idealised merger simulations are also effective at performing parameter space explorations looking at mass ratios and impact parameters as was done by Poole et al. (2008); ZuHone (2011) or investigating specific features of mergers such as cold fronts Ascasibar & Markevitch (2006).

## 1.7 Gas Stripping of Cluster Galaxies, Groups and Sub-clusters

An important aspect of a minor merger is the evolution of the gas stripping of the secondary, i.e., the fate of the stripped gas atmosphere of the secondary. Therefore, this section provides a detailed description of this process. The motion of the secondary through the ICM of the primary produces a ram pressure which is exerted on its gaseous atmosphere causing the gas to be stripped. By considering the balance of ram pressure and the gravitational restoring force in application to disk galaxies in clusters, Gunn & Gott (1972) proposed that the disk should be easily stripped when the ram pressure exceeds the gravitational restoring force. The magnitude of this ram pressure is dependent on the density of the ICM,  $\rho_{\text{ICM}}$ , and the velocity of the secondary relative to the ICM,  $v_{\text{gal}}$ , given by the equation,

$$P_{\text{ram}} \approx \rho_{\text{ICM}} v_{\text{gal}}^2. \quad (1.2)$$

Based on the work of Mori & Burkert (2000), it can be argued that for spherical galaxies, ram pressure stripping removes shells from the atmosphere when the ram pressure of the ICM is greater than the thermal pressure, i.e.,  $P_{\text{ram}} > P_{\text{thermal}}$ . From Mori & Burkert (2000), this is described by,

$$\rho_{\text{ICM}} v_{\text{gal}}^2 > \frac{GM_{\text{gal}} \rho_{\text{gal}}}{3r_{\text{gal}}}. \quad (1.3)$$

where  $M_{\text{gal}}$ ,  $\rho_{\text{gal}}$ ,  $r_{\text{gal}}$  is the mass, density and radius of the galaxy respectively. By using a typical ICM density of  $\rho_{\text{ICM}} = 10^{-3} \text{cm}^{-3}$ , and typical values for an elliptical galaxy;

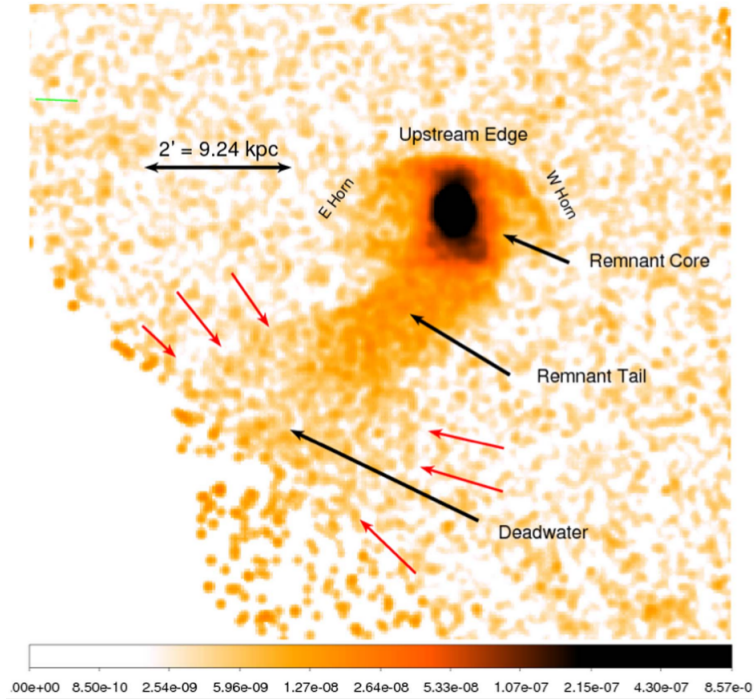


**Fig. 1.10:** Taken from Fig.1 in Kraft et al. (2017). Exposure-corrected, Chandra image of the ram pressure stripped tail of M89 taken in the 0.7 - 1.1 keV energy band.

$v_{\text{gal}} = 1000 \text{ km s}^{-1}$ ,  $M_{\text{gal}} = 10^{12} M_{\odot}$ ,  $\rho_{\text{gal}} = 10^{-2} \text{ cm}^{-3}$  and  $r_{\text{gal}} = 15 \text{ kpc}$ . Inserting these values into Eq. 1.3 shows indeed that the ram pressure is greater than the thermal pressure, therefore elliptical galaxies will be ram pressure stripped. In addition to ram pressure stripping, Nulsen (1982) showed that cluster galaxies can also be gas stripped by laminar viscous stripping and stripping due to turbulence, in many cases finding that this stripping is faster than the rate of ram pressure stripping.

Roediger et al. (2015a) provided a comprehensive study into the progressive gas stripping of the elliptical galaxy M89 in the Virgo Cluster, by taking into account the varying ram pressure during a cluster crossing. Roediger et al. (2015a) showed that the stripping of an early-type galaxy can be compared to that of the flow around a blunt body (see: Fig. 3. in Roediger et al. 2015a). Although this makes for a good representation, the ICM flow is non-steady and the galaxy is not a blunt object, therefore care must be taken when drawing conclusions based on the analogy. Roediger et al. (2015a) find that the ram pressure pushes back the upstream atmosphere of the galaxy and that the gas stripping takes place primarily along the sides via the KHI, producing a horn-like appearance to its gas atmosphere. However, the downstream atmosphere of the galaxy can survive longer than the upstream atmosphere as it is shielded from the ram pressure, thus the downstream atmosphere forms a remnant tail. The stripped gas is pushed downstream into the far wake where it then mixes with the ICM. The near wake contains a deadwater region in which the local flow velocity is directed back upstream, only in the far wake is the flow directed away from the galaxy. For high Reynold's numbers, the flow patterns in the wake correspond to turbulence.

The identification of ram pressure stripped early-type galaxies is aided by a number of characteristic observational signatures. The obvious signature of a ram pressure stripped galaxy is the existence of an X-ray bright tail due to the cool galactic gas. In addition, due to the ram pressure exerted on the galaxy atmosphere, the upstream atmosphere is deformed causing it to be truncated, producing a sharp upstream edge which indicates a contact discontinuity between the atmosphere of the galaxy and the ICM. Furthermore, a bowshock will likely exist leading the galaxy as they typically have supersonic speeds as they fall into a cluster. Ram pressure stripping has been observed to be at work on many early-type galaxies and subclusters (e.g. A2142, Eckert et al. 2014; NGC 1404, Machacek et al. 2005; NGC 4476, Lucero et al. 2005; M86, Randall et al. 2008a; M89, Machacek et al. 2006; Abell 2670, Sheen et al. 2017). When the strength of the ram pressure stripping is substantial enough, X-ray tails have been observed (Eckert et al., 2017; Machacek et al., 2006; Randall et al., 2008a), an example is shown in Fig. 1.10. The properties of the X-ray tails could depend on the properties of the ICM, in particular the viscosity and thermal conductivity as these determine in particular the mixing between the stripped galactic gas and the ambient gas of the ICM.

As mentioned in Section 1.5.2, building on the work by Roediger et al. (2015a), Kraft et al. (2017); Roediger et al. (2015b) both provided further analysis on the stripping of elliptical galaxies by investigating the impact of viscosity on the gas stripping of the elliptical galaxy M89 in the Virgo Cluster. Roediger et al. (2015b) concluded that if the ICM viscosity is similar to the Spitzer value, then the KHI is suppressed on small scales reducing the gas stripping. Further, the mixing in the wake is also suppressed leading to a cool X-ray bright wake which can survive for longer periods. Kraft et al. (2017) determined that the morphology of the tail of M89 suggests inviscid stripping scenario, finding that the viscosity of the Virgo ICM is significantly suppressed relative to the isotropic Spitzer value.

## 1.8 Outline of this Work

While major mergers of galaxy clusters have been studied extensively in simulations for their impact on many aspects of cluster evolution, e.g. Iapichino et al. (2017); Lidman et al. (2013); Liu et al. (2015, 2009); Martel et al. (2014); Mathis et al. (2005); Molnar (2016); Moster et al. (2011); Paul et al. (2011); Poole et al. (2007, 2008, 2006); Takizawa et al. (2010); Zhang et al. (2016); ZuHone (2011), there is little work in the literature in regards to a comprehensive study of cluster minor mergers, specifically the evolution of the morphological properties of the secondary throughout the merger and how it relates to the overall evolution and features of the primary. For example, Ascasibar & Markevitch (2006); Markevitch & Vikhlinin (2007); Owers et al. (2011a) detail minor mergers and their involvement in the formation of cold fronts, Acreman et al. (2003) present analysis for the ram pressuring stripping of galaxies falling into a cluster and McCarthy et al. (2007); Poole et al. (2007, 2008, 2006); Takizawa et al. (2010); ZuHone (2011); ZuHone et al. (2011) all

present parameter space explorations for cluster mergers, including minor mergers, but focus on the cluster morphology and the thermodynamic evolution of the cluster gas.

This thesis presents a detailed study of minor cluster mergers, and for the first time, combines the effects of the gas stripping of the secondary, and the sloshing and merger shocks in the primary during the same minor merger, providing a holistic view. This work specifically looks at secondaries which are early-type galaxies or subclusters. In this thesis, a new class of gas tail for secondaries at the apocentre of the merging orbit is presented. This new insight is then used to reclassify several gas tails in the literature. Additionally, this thesis provides analysis for the validation of the stagnation point pressure method to calculate the infall velocity of the secondary throughout a minor merger.

The thesis comprises of building a suite of N-body and hydrodynamic idealised minor cluster merger simulations to analyse and compare to multi-frequency observational data. For the first investigation of minor cluster mergers, Chapter 3 presents detailed analysis for a suite of simulations tailored to the minor merger involving the elliptical galaxy NGC 1404 and the Fornax Cluster. This system was chosen due to its relatively close proximity such that it has been imaged extensively and thus has a wealth of observational data to compare to. Also the system has relatively simple components and thus makes the process of tailoring the simulation much easier. This chapter has been published in *The Astrophysical Journal* as Sheardown et al. (2018).

For a wider look into cluster minor mergers, Chapter 4 analyses the suite of idealised cluster merger simulations by Poole et al. (2006); Sheardown et al. (2018); ZuHone (2011), as well as running some new simulations to show that there is a new class of gas tails, named slingshot tails. This chapter describes the formation of these slingshot tails, discusses their observable features and how to distinguish such tails from classic ram pressure stripped (RPS) tails. Other potential candidates for slingshot tails in the literature are also discussed. This chapter has been published in *The Astrophysical Journal* as Sheardown et al. (2019).

Chapter 5 describes further analysis of my simulations conducted in detail by my supervisor Dr. Elke Roediger and fellow post graduate student Thomas Fish on the stolen atmosphere effect. The theory behind the stolen atmosphere is described and is then applied to the simulations in Chapter 3 to estimate the infall velocity of NGC 1404 and to compare with other methods. In chapter 6, the results of this thesis are presented and avenues for future work are summarised. This includes a description of the holistic view of minor mergers, detailing the effects on both the primary and secondary at each merger phase. Future work described in this thesis includes how the tailored Fornax merger simulations can be used to probe the properties of the ICM and investigate physics at the outskirts of clusters, and furthermore, how the merger scenario determined for the Fornax merger can be used to understand the globular cluster content of NGC 1404 and the BCG galaxy in Fornax NGC 1399. This is currently a project being undertaken by MSc student Ben Marshall and my supervisor Dr Elke Roediger. Additionally, looking ahead to future X-ray telescopes coming online in the next decade, such as the ATHENA X-ray telescope, mock images of the ATHENA Wide Field X-ray imager (WFI) and the X-ray Integral Field Unit

(X-IFU) are made for the simulations in this work to investigate the level of physics which can be probed.

The important aspects of the simulation method are presented in Chapter 2, this includes how a model primary and secondary are initialised and how the code handles gas and dark matter throughout the simulation. Further, preliminary simulations are also presented to show how, in a series of modified steps, the N-body and hydrodynamical merger was made. This also demonstrates testing of the code used in the simulations.

# Chapter 2

## Simulation Method

### 2.1 Preface

The simulations presented in this work are idealised N-body and hydrodynamics simulations. This chapter describes the building of the simulations using the FLASH Code, focusing on how the code handles the dark matter and cluster gas throughout the simulation and how the clusters are initialised. A discussion between the two different ways to model flow in simulations - Eulerian and Lagrangian - is also presented. The final section briefly details preliminary simulations which show how in a series of modified steps, the idealised N-body and hydrodynamic merger was made, and additionally demonstrates testing of the FLASH Code.

### 2.2 Flow Descriptions

To be able to describe the motion of a fluid, properties such as the density, pressure, temperature and velocity need to be tracked as a function of time. When modelling hydrodynamics in numerical simulations, there are two main choices in which to describe the fluid motion. These are the grid based Eulerian method (Falkovich, 2011) and the particle based Lagrangian method, this is also referred to as smooth particle hydrodynamics (SPH) (Monaghan, 1992). Each method has its own advantages and disadvantages and is an important consideration when it comes to building a simulation to ensure the right method is prescribed for the aim of the simulation.

The Eulerian method uses the Euler equations of hydrodynamics (see below, Section 2.3.1) to provide a field description for fluid motion using a fixed, usually Cartesian, coordinate grid of spatial resolution elements. Thus, the flow properties are defined as functions of space and time. As well as a fixed grid, the grid may be adaptive such that higher levels of resolution can be placed in particular areas of interest, this is known as adaptive mesh refinement (AMR). By splitting the computational volume into fixed volume elements (or cells), the fluid motion is solved by computing the Euler equations to calculate the flux between the boundaries of adjacent cell walls. Thus, the conserved quantities in the Euler equations, the mass, momentum and energy are acquired by the sum of the

net flux through the adjacent cells which can then be used to calculate flow properties. The Eulerian method naturally gives the ability to obtain mean quantities of the flow i.e. velocity, pressure and temperature. For a stable solution to be guaranteed for this explicit scheme, the timestep needs to be limited. This is regulated by the Courant-Friedrichs-Lewy (CFL) condition, which is defined by the velocity (which for compressible flows is dependent on the sound speed), grid cell size and the timestep. The CFL condition ensures that information must not travel more than the length of one grid cell in the computational grid within a timestep, i.e., the distance information travels during a timestep must be less than the length of the grid cell. Therefore, when the CFL number is  $< 1$ , this condition is satisfied. If the CFL condition is not achieved, then it can lead to convergence problems when computing the Euler equations.

The Lagrangian or SPH method uses the Euler equations of hydrodynamics in the Lagrangian form. This method considers particles elements in a moving frame of reference, rather than spatial elements in a fixed frame as is done in the Eulerian method. As such, the resolution of the simulation will follow mass. These particles are 'tagged' so that the flow properties can be measured by tracking the motions of the particles in time. Thus, the SPH method does not require a grid and the fluid properties are calculated for each particle by averaging over its nearest neighbours such that each particle is smoothed over a finite volume of fixed mass. As a result, for each particle, detailed information is available to the user such as its position, temperature and velocity. The equations of motions used in SPH give exact solutions, thus SPH naturally provides the conservation of mass, momentum and energy (Springel & Hernquist, 2002), and therefore the advection of flow properties is inherent.

The Eulerian method is much more useful when the user requires the properties of flow in a particular volume, whereas the Lagrangian method is more suited for simulating the dynamics for individual particles in a fluid. For SPH, it is naturally easy to track the history of particles which is more difficult to achieve with the fixed spatial elements in Eulerian methods. As the SPH method does not use a fixed grid, it can adapt much easier to complex geometrical setups in comparison to the Eulerian method. However, the Eulerian method is able to offer higher resolutions than SPH methods for a given number of grid cells compared to an equal number of particles.

Numerical simulations are essential tools to study the physics of galaxy cluster mergers, however there have been notable differences in results depending on which method for the description of flow is used. In the case of SPH codes, the advection of flow properties is inherent, but this is not the case for AMR methods. Agertz et al. (2007) demonstrated that one of the main differences between Eulerian and SPH methods is their ability to handle fluid instabilities and mixing processes, finding that Eulerian methods are much more capable of handling them in contrast to basic SPH methods. Price (2008) showed that this is due to the treatment of contact discontinuities in SPH codes. There are also notable differences in the amount of entropy produced in both methods. In addition, this also causes differences in the two methods to model turbulence correctly (Agertz et al., 2007; Dolag et al., 2005; Mitchell et al., 2009; Wadsley et al., 2008), where particularly it

has been found that SPH codes have problems dealing with subsonic turbulence (Bauer & Springel, 2012). Despite this, Price & Federrath (2010) demonstrated that SPH and Eulerian do agree well in simulations dealing with supersonic flows. However, over the past decade, modern SPH codes have been extended to tackle the poor modelling of mixing (e.g., see Rosswog 2015 and Wadsley et al. 2017).

Over the last decade however, another simulation method has been developed which combines elements of grid and SPH codes by using a moving mesh called AREPO (Pakmor et al., 2016; Springel, 2010). This code uses a quasi-Lagrangian scheme for solving the Euler equations on an unstructured mesh that moves with the flow defined as the Voronoi tessellation of a finite set of points. This unstructured mesh allows the application of second-order Godunov methods to be used to evolve the fluid state in time in a similar vein as Eulerian codes. Due to the quasi-Lagrangian approach, this method reduces the advection problems associated with standard Eulerian methods and maintains useful aspects of grid codes such as the ability to refine or de-refine grid cells (see Springel 2010 for a full description of the method).

## 2.3 FLASH code and The yt Project

To simulate the mergers of clusters in this thesis, the grid based FLASH Code is chosen (webpage: <http://flash.uchicago.edu/site/>). Designed and developed at the Flash Center based at the University of Chicago, the FLASH Code is a publicly available, high performance, modular simulation code written in FORTRAN90 and C that is able to handle parallel multi-physical problems (Fryxell et al., 2000). The FLASH code has become a popular source for researchers in the fields of astrophysics, cosmology, high-energy physics and fluid dynamics, making it an ideal choice for this work. FLASH essentially consists of a set of units (each accompanied with their own subunits) divided into five categories; infrastructure (management of runtime parameters, administration of the simulation grid domain), physics (consists of physics solvers such as hydrodynamics), monitor (tracking of simulation progress), driver (controls simulation time and interaction between involved units), and simulation (defines the simulation and how it should be run i.e. initial conditions, grid parameters). A FLASH simulation is then built from a subset of each of these units, by specifying them in a configuration file. To work in parallel, FLASH employs the Message-Passing Interface (MPI) library to allow for communication between processors and uses HDF5 and PnetCDF libraries for parallel input and output of data. FLASH also comes with the ability to perform AMR to allow for specific areas of the grid to be resolved at high levels of resolution. This is particularly useful when simulating cluster mergers as areas of the grid that are of key interest, such as the cores of the clusters and galaxies can be held at high resolution.

To analyse the simulation output from FLASH, the yt Project application is used (webpage: <https://yt-project.org/>). The yt Project is an open source, Python based library tool, and offers users an excellent platform to perform quantitative data analysis and visualisation (Turk et al., 2011). Developed to handle astrophysical simulation data

embedded in grid based domains, it yields representation of the data in 2D or 3D, precisely what is required for the simulations in this work. Usefully yt harnesses the h5py python package to give an interface to HDF5 data files, giving us the opportunity to visualise the output from the FLASH simulations. Full details on the workings and opportunities available for data analysis with the yt Project can be found in Turk et al. (2011).

### 2.3.1 Hydrodynamics in FLASH

Creating a numerical simulation of a cluster merger requires three main physical units, hydrodynamics to treat the cluster gas, the particle unit to treat the dark matter, and the gravity unit to calculate gravitational forces. This subsection describes how the hydrodynamics solver in FLASH works, the following subsection will detail the particle unit and the gravity solver.

The hydrodynamics unit involves a list of calculations that needs to be done for each grid cell in each time step. Initially, each grid cell is given specific values for density, temperature, pressure, velocity, etc. Then, the evolution of these values is governed by the equations of hydrodynamics. Grid cells communicate with neighbouring cells to determine the changes to density etc due to fluxes through the cell walls during the current time step. The gas of the clusters in the simulations is treated as an ideal gas and is modelled as a compressible and inviscid fluid. Thus, the cluster gas can be modelled with the Euler equations of hydrodynamics which describes the evolution of the gas properties. These equations are:

$$\frac{\partial \rho}{\partial t} + \nabla \cdot (\rho v) = 0 \quad (2.1)$$

$$\frac{\partial \rho v}{\partial t} + \nabla \cdot (\rho v v + \nabla P) = \rho g \quad (2.2)$$

$$\frac{\partial \rho E}{\partial t} + \nabla \cdot [(\rho E + P)v] = \rho v g \quad (2.3)$$

where  $\rho$  is the gas density,  $P$  is the gas pressure,  $v$  is the 3D gas velocity vector,  $E$  is the total energy (the sum of internal and kinetic energy),  $g$  is the gravitational acceleration and  $t$  is the time. The Euler equations are conservation laws, Eq. 2.1 represents the conservation of mass Eq. 2.2 the conservation of momentum and Eq. 2.3 the conservation of energy. In addition to the Euler equations, to evolve the gas the hydrodynamics solver requires an equation of state (EOS) to relate between the thermodynamic quantities of the gas. The EOS used here is the gamma-law EOS which specifies the relationship between the pressure, density and internal energy:

$$P = (\gamma - 1)\rho\varepsilon \quad (2.4)$$

where  $\gamma = 5/3$  is the ratio of specific heats for an ideal monoatomic gas.

The hydrodynamics solver in FLASH is packaged into two different routines: directionally split and unsplit. Due to its high accuracy and resolution, and for the availability to couple the solver with a gravitational source term, the directionally split solver is chosen.

The directionally split solver uses the piecewise-parabolic method (PPM) of Colella & Woodward (1984) which is built from the direct Eulerian formulation of higher order Godunov (1959) PPM (for multidimensional simulations, second-order operator splitting developed by Strang 1968 is used). PPM is designed to simulate the flow regimes observed in astrophysics i.e. flows that are unsteady, involving shocks or contact discontinuities, such as the simulations in this work. Using the Euler equations, the flux at cell boundaries at each time step is computed which solves the numerical solution to the shock tube problem (Sod, 1978).

### 2.3.2 Dark Matter Particles and Gravity in FLASH

To accurately simulate the merging of galaxy clusters and incorporate the effects of dynamical friction and tidal stripping, dark matter must be accounted for and this can be done in FLASH by including particles to represent its behaviour. In FLASH, there is an option to use active particles which will contribute to the dynamics of the simulation. Active particles are dimensionless, defined by their mass, position and velocity and can move independent of the grid (this requires another layer of communication between processors as particles can move from grid block to grid block). Active particles are collisionless and are only affected by the force of gravity, mirroring the expected behaviour of dark matter. To compute the force of gravitational acceleration acting on the particles, FLASH invokes an N-body module using a particle-mesh method. The active particles are advanced in time using a variable-timestep leapfrog method which solves the differential particle equations formulated by Newton's Law's,

$$\frac{dx_i}{dt} = v_i \quad (2.5)$$

$$m_i \frac{dv_i}{dt} = F_i \quad (2.6)$$

where  $x_i$ ,  $v_i$ ,  $m_i$  are the position, velocity and mass of the particle respectively and  $F_i$  is the force acting on the particle.

To incorporate the contribution to the gravitational potential, the mass of the particle needs to be mapped to the grid to be stored as a dark matter density variable and the gravitational acceleration grid variable needs to be mapped to the particle accelerations. This mapping is achieved in FLASH using the Cloud-in-Cell method which uses a simple linear weighting by considering neighbouring points on the grid. Once the particles have been mapped, the overall force of gravity can be calculated. The gravity then couples to the hydrodynamics using the conservation of momentum and energy Euler equations. The force of gravity is defined by the gradient of the gravitational potential, which is related to the total density of the gas and dark matter by the Poisson equation,

$$\nabla^2 \phi = 4\pi G(\rho_g + \rho_{DM}) \quad (2.7)$$

where  $\rho_g$  is the gas density,  $\rho_{DM}$  is the particle or dark matter density and  $G$  is Newton's gravitational constant. By using the Poisson equation to determine the gravitational potential, this is then used to calculate the gravitational acceleration as  $g = -\nabla\phi$ , which is then used in the Euler equations to couple to the hydrodynamics. To solve the Poisson equation, the multigrid method in FLASH is used (Ricker, 2008). This computes the Newtonian gravitational field produced by the matter in the simulation and is based on the algorithm detailed in Huang, J., Greengard (2000). The simulations in this work use the multigrid method along with isolated boundary conditions such that  $\phi(\infty) \rightarrow 0$ .

## 2.4 Generating Model Clusters

To generate the model clusters and galaxies for the simulations in this work, John ZuHone kindly supplied his cluster generator code which uses the method as explained in ZuHone (2011) to produce model clusters and galaxies. This section briefly outlines the important elements of the code to produce the model clusters and galaxies. For each cluster (or galaxy), the gas (assumed to be an ideal gas) spherically symmetric and is set up in hydrostatic equilibrium - this is the key assumption when performing cluster merger simulations. The condition for hydrostatic equilibrium can be formulated by considering the Euler equation in Eq. 2.2, the conservation of momentum. By using the relation,

$$\frac{dv}{dt} = \frac{\partial v}{\partial t} + (v \cdot \nabla)v \quad (2.8)$$

which is the sum of the acceleration and inertia terms, and  $g = -\nabla\phi$ , Eq. 2.2 can be rewritten as,

$$\begin{aligned} \frac{dv}{dt} + \frac{1}{\rho} \nabla P &= -\nabla\phi \\ \frac{dv}{dt} &= -\frac{1}{\rho} \nabla P - \nabla\phi. \end{aligned} \quad (2.9)$$

Under hydrostatics, the pressure of the gas will counteract the gravitational force so there is no net acceleration giving the condition for hydrostatic equilibrium, i.e.,

$$\frac{dv}{dt} = 0 \quad (2.10)$$

By rewriting this equation as,

$$0 = -\frac{1}{\rho} \nabla P - \nabla\phi \quad (2.11)$$

and assuming the pressure support is purely thermal, the hydrostatic mass can be derived by using profiles of gas density and temperature. Thus, the hydrostatic mass can be written as,

$$M_{HE}(< r) = -\frac{kT(r)r}{\mu Gm_p} \left[ \frac{d \log \rho(r)}{d \log r} + \frac{d \log T(r)}{d \log r} \right] \quad (2.12)$$

where  $k$  is the Boltzmann constant,  $\mu$  is the mean molecular weight and  $m_p$  is the proton mass. For the cluster model generator, the only required inputs are profiles for the gas density and total density. Using these profiles, a hydrostatic equilibrium model is constructed which derives profiles for the pressure, temperature, gravitational potential, gas mass, total mass, dark matter density and dark matter mass. Thus, to tailor our model cluster and galaxies to their real life counterparts, a gas density profile which is derived from X-ray observations is used, and then a guess is made for the total density which is tuned to give a temperature profile which matches a temperature profile derived from observations (see Chapter 3, Sec. 3.5 for a more detailed description). Then, by using this hydrostatic model for the gas, and considering virial equilibrium, dark matter particles are generated with initial positions and velocities. For a detailed description of how this is achieved see ZuHone (2011).

Gas density profiles for clusters and galaxies can be modelled to fit their X-ray surface brightness profiles. The  $\beta$  profile developed by Cavaliere & Fusco-Femiano (1976, 1978) is found to provide a good representation of the observed surface brightness profiles of clusters and galaxies. The  $\beta$  profile is defined as,

$$\rho(r) = \rho_0 \left[ 1 + \left( \frac{r}{r_c} \right)^2 \right]^{-\frac{3\beta}{2}} \quad (2.13)$$

where  $r_c$  is the core radius. For groups of galaxies  $\beta$  is  $\sim 0.5$  (Mulchaey et al., 1996) and for clusters  $\beta \sim 0.64$  (Mohr et al., 1999). For cool core clusters, it is found that a double  $\beta$  profile provides a more accurate fit to the surface brightness (Jones & Forman, 1984):

$$\rho(r) = \rho_1 \left[ 1 + \left( \frac{r}{r_{c1}} \right)^2 \right]^{-\frac{3\beta_1}{2}} + \rho_2 \left[ 1 + \left( \frac{r}{r_{c2}} \right)^2 \right]^{-\frac{3\beta_2}{2}}. \quad (2.14)$$

The total density profile (i.e. gas plus dark matter) of the cluster or galaxy in the simulations is set to a Hernquist profile (Hernquist, 1990). This profile has the useful feature of finite mass as there is an asymptotic fall-off of the density of  $r^{-4}$  and so does not require truncation like the popular choice of a Navarro-Frenk-White (NFW) profile (Navarro et al., 1996) as this has a fall-off of  $r^{-3}$  leading to an infinite mass defect. The Hernquist profile is also convenient to model elliptical galaxies as it provides a good approximation to the de Vaucouleurs profile (de Vaucouleurs, 1953). The density of a spherical Hernquist model follows,

$$\rho(r) = \frac{M}{2\pi} \frac{a}{r} \left[ \frac{1}{r+a} \right]^3, \quad (2.15)$$

where  $M$  is the mass and  $a$  is a scale radius. In the Hernquist model, the gravitational potential is now defined as,

$$\phi(r) = -\frac{GM}{r+a} \quad (2.16)$$

For some work, a triple Hernquist potential is used to describe the total gravitational potential of a cluster. The benefit of this is that a triple Hernquist potential captures the potential of the cluster, the BCG and its stellar content.

The general setup of the binary merger is as follows. Using profiles which are generated from the cluster model generator (these contain profiles for density, pressure, temperature, etc.), a cluster and a galaxy are each setup in equilibrium. Grid cells in the simulation are filled depending on which cluster has the highest pressure. This is done by calculating the distance between the grid cell and the centres of the cluster and galaxy and comparing the corresponding pressure value for the cluster and galaxy at that radius. For example, if at a grid cell the cluster has a higher pressure than the galaxy, the cluster values for that corresponding pressure value are set. The galaxy is initially placed at the virial radius of the cluster and is given an initial velocity of  $\sim$  Mach 1 which is derived from cosmological conditions (Vitvitska et al., 2002), and can be split into radially and tangential components to control the impact parameter of the merger, this is explained in further detail in Chapter 3, Sec. 3.5.4. The size of the simulation domain is set to  $1.8 \text{ Mpc}^3$ , with boundary conditions set to outflow, i.e., anything that leaves the boundary does not re enter the simulation.

## 2.5 Simulation Resolution

A well built simulation requires careful consideration for the level of resolution that will be required for the aims of the user and particularly how the resolution will be implemented. As mentioned, FLASH is packaged with the ability to employ the adaptive mesh refinement (AMR) technique, which is implemented with PARAMESH (MacNeice et al., 2000) - a tool which manages the adaptive grid. AMR allows the user to concentrate increased levels of refinement, i.e. resolution, in areas of interest to the user and de-refine in areas which are not. The simulation domain is split into blocks which contain  $16^3$  physical grid cells. These blocks then consist of smaller blocks known as child blocks, this occurs in a hierarchical fashion using a tree data structure. Blocks at the root of the tree structure have the largest cells and under refinement, these blocks split into child blocks consisting of smaller grid cells which are said to be refined. Adjacent child blocks by rule are not allowed to differ by more than one level of refinement. In FLASH, the user defines a refinement variable which controls how the refinement should be done. For example, the refinement can be based on gas density at a particular level, such that if the gas density in a block exceeds this level then that block will be refined. This could be done with any grid variable such as the pressure, temperature velocity etc. In a similar vain, a refinement variable can also be defined so that the opposite occurs, i.e. in the case of selecting a refinement variable based on density, if a block has a density which is lower than the level set by the refinement variable, then the block is de-refined.

For the purposes of the simulations in this work, we wanted to capture the cores of the primary and secondary merger partners as well as the orbit of the secondary. This could be achieved by basing the refinement variable on the number of particles on a block. A particle threshold was set of 200 particles per block, this is to say that if there are more

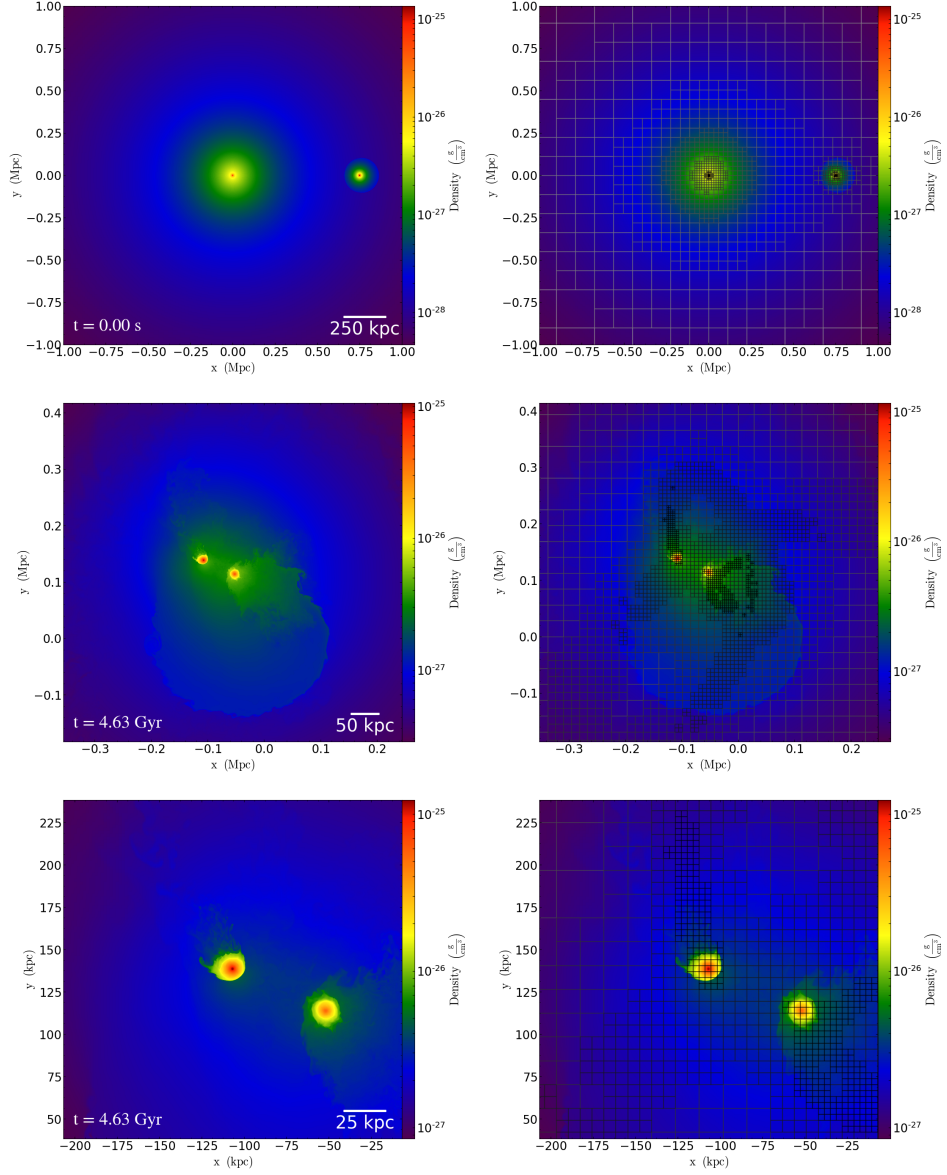


**Fig. 2.1:** Snapshots from a minor merger cluster simulation showing the refinement grid. The left images show the simulation snapshot without grids annotated whilst the images on the right show the same snapshot but with the refinement grid annotated. The colour codes the gas density in a slice in the merger plane. In the plots on the right, each black square marks the size of a ‘block’ of grid cells containing  $16^3$  grid cells. Top: the domain at the start of the simulation. Middle: A cluster wide view of the refinement grid at  $t = 4.63$  Gyr corresponding to the second infall of the secondary. Bottom: The same as the latter but zoomed in further. The snapshots show how well the refinement criteria based on the number particles captures the cores of the primary and secondary as well as the orbit path of the secondary.

than 200 particles on the block then refinement occurs. This criteria ensures that the cores of primary and secondary are refined at the highest level of refinement out to typically 50 kpc for the primary, and 12 kpc for the secondary. This criteria would also capture the orbit path of the secondary, as we do not select any derefinement criteria, therefore wherever the secondary had been that region would also remain refined, thus the trailing tail and wake of the secondary would always be captured. Figure 2.1 shows the refinement of the grid for a minor cluster merger simulation detailed in Chapter 3. The top row shows the simulation domain at the start of the simulation, clearly showing the increased refinement in the cores of the primary and secondary. The second and third rows show the simulation

at an epoch of 4.63 Gyr, as the secondary is falling into the cluster a second time. These images show how the refinement criteria tracks the orbit of the secondary which can be made out by following the highest level refined blocks. At this highest refinement level, the resolution of the simulation is 220 pc.

## 2.6 Preliminary Simulations

The purpose of this section is to briefly show the series of modified steps it took to make the N-body and hydrodynamical merger setup as described above. Additionally, this section is provided as a reference for future work and to demonstrate validation of the code. The building of the merger simulation began from scratch, and was built up from the default FLASH Mach 3 wind tunnel simulation with a step problem.

### 2.6.1 Wind Tunnel

This simulation places a 2D reflecting rectangular domain (a step) into a grid of 10 x 5 blocks. Here, the right hand x boundary is treated as an outflow, the left hand x boundary as the in-flowing wind (with the wind velocity parallel to the x axis) and the upper and lower y boundaries as reflecting. The plan was to first simulate a galaxy in the path of a flowing ICM wind, thus this simulation provided the basis for that as there is a domain with an in-flowing wind in which an obstacle is placed for the wind to interact with. Therefore, this simulation would logically be easy to adapt to produce an ICM wind interacting with a galaxy. The grid and domain setup can be seen in Fig. 2.2. For this simulation, the level

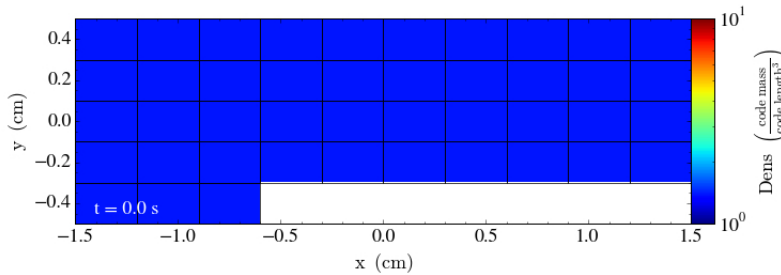


**Fig. 2.2:** Mach 3 wind tunnel with a step problem run with FLASH at  $t = 0.0$  s.

of refinement is set to 8 which corresponds to a grid resolution of  $\delta x = 1 \mu\text{m}$ , and uses the default simulation parameters set as follows; the rectangular domain sits between  $x = 0.6$  cm and  $x = 1.5$  cm, is 0.2 cm high and has a density,  $\rho$ , of  $1.4 \text{ gcm}^{-3}$ . The ambient background pressure,  $p_0$ , is set to  $1.0 \text{ dyn cm}^{-2}$ , with the inflowing wind velocity set to Mach 3 and the gas ratio of specific heats set to 1.4. As the outflow here is supersonic, there are no reflections at the right hand x boundary. However the top boundary is reflecting. The duration of the simulation run is set to 4.0 s, with plot intervals taken every 0.1 s.

Figure 2.3 clearly shows a flow that is unsteady with multiple shock reflections off the top boundary. The Mach 3 wind striking the step at  $t = 100.1$  ms produces a region of high density and pressure directly in front of the step, which corresponds to a formation of a

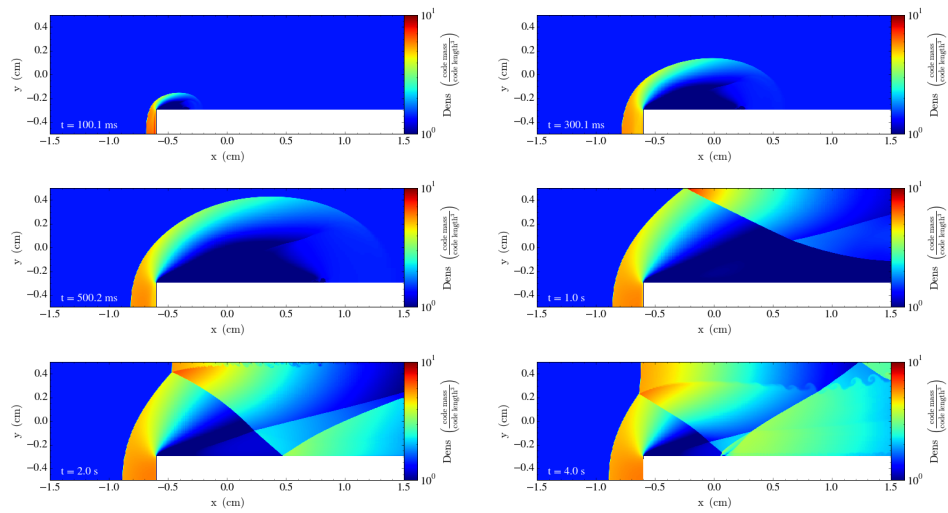


**Fig. 2.3:** Mach 3 wind tunnel with a step problem run with FLASH viewed at  $t = 100.1$  ms ,  $t = 300.1$  ms,  $t = 500.2$  ms,  $t = 1.0$  s,  $t = 2.0$  and  $t = 4.0$  s.

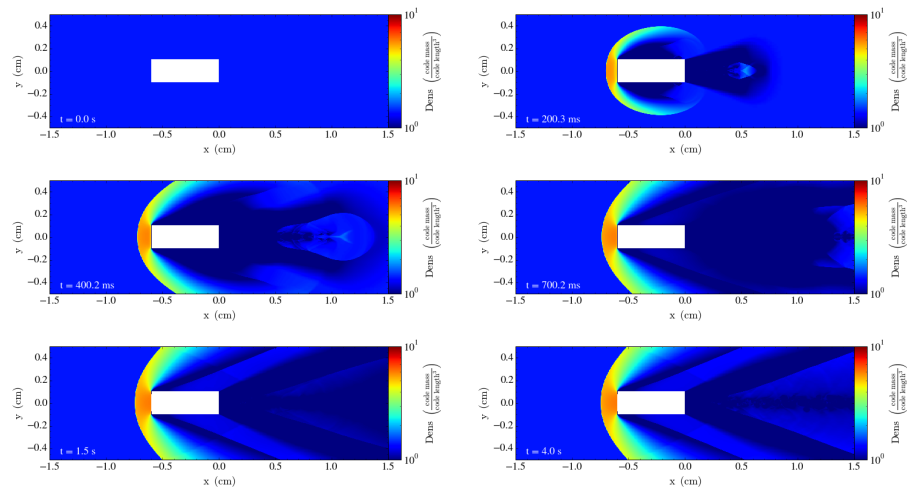


**Fig. 2.4:** Simulation run with the FLASH code of a Mach 3 wind flowing around a rigid rectangular domain at  $t = 0.0$  s,  $t = 200.3$  ms,  $t = 400.2$  ms,  $t = 700.2$  ms,  $t = 1.5$  s and  $t = 4.0$  s. The colours code the gas density. An image of a supersonic rifle bullet moving through air from van Dyke & White (1982) is also included to show the clearly similarities in the wave patterns, particularly the morphology of the shock waves.

shock. This shock then curves upwards extending downstream, growing larger as time progresses until it hits the upper boundary where it then reflects and moves towards the left. There is the formation of rarefaction fan which couples the steady gas on top of the step to the shock gas in front. A mach stem begins to form after  $t = 1.0$  s, as the angle between the incident shock and the reflected shock exceeds the maximum angle for normal reflection, which for  $\gamma = 1.4$  is  $40^\circ$ . At  $t = 2.0$  s, a KHI is visible due to parallel shear flow between the inflowing wind and the reflections. The KHI is observed to grow in size as the simulation time increases before it ends at  $t = 4.0$  s where we can clearly see the KHI.

Following the provided wind tunnel simulation, the next step was to simply place an obstacle in the flow of the wind so that the flow could pass either side. Therefore this simply involved re-positioning the 2D rectangular step to the centre of the grid, giving a rigid reflecting obstacle in the path of the wind flow. This setup is very similar to the flow past a sphere, just that the blunt body is a cuboid instead of a sphere as this is easy to create with the standard FLASH modules. This simulation would use the same parameter setup as previous but now the upper and lower boundaries will be outflowing instead of reflecting so that the formation of the wake behind the obstacle could be observed cleanly. The results of this simulation are shown in Fig. 2.4. The first feature to observe is the generation of a large bow shock at the onset of wind flow at  $t = 200.2$  ms, with a stagnation point located directly in front of the block. The bow shock extends either side of the block downstream, growing larger (much like the shock from the wind tunnel with a step problem, like we would expect). The onset of the mach 3 wind produces areas of lower density and pressure at the sides of the block and more significantly directly behind it. The wake is observed directly behind the block at  $t = 1.5$  s, extending the length of the x axis, becoming more defined after  $t = 4.0$  s. The simulation images show clear similarities to the supersonic rifle bullet shown in Fig. 2.4. There is a clear similarity in the bow shock leading the rectangular block and the bullet is apparent, as well as the wave patterns downstream in the wake.

## 2.6.2 Gas Cloud Stripping

The next logical progression was to insert a spherical cloud of gas into the path of the flow instead of a rigid block. The simulation domain is now increased, with a grid size of  $100 \text{ cm}^2$ . As with the previous simulations, the density and pressure of the ambient background are set to  $1.4 \text{ gcm}^{-3}$  and  $1.0 \text{ dyncm}^{-2}$  respectively. The spherical gas cloud is set with a radius of 10 cm and an internal density of  $15 \text{ gcm}^{-3}$  and a pressure of  $1.0 \text{ dyncm}^{-2}$ . The velocity of the inflowing wind is set to Mach 0.5, producing a subsonic wind flow. The resolution chosen is  $\delta x = 0.006 \text{ cm}$ , which corresponds to  $\sim 3,333$  grid cells per cloud diameter. This resolution allows for the formation of KHIs on scales much smaller than this. The simulation is run until the cloud is heavily deformed, but not fully disintegrated.

The results of the gas cloud stripping simulation are presented in Fig. 2.5. The initial striking of the wind produces a region of increased pressure and density to form upstream, and a decrease in density downstream, where there is a distinct boundary between the two

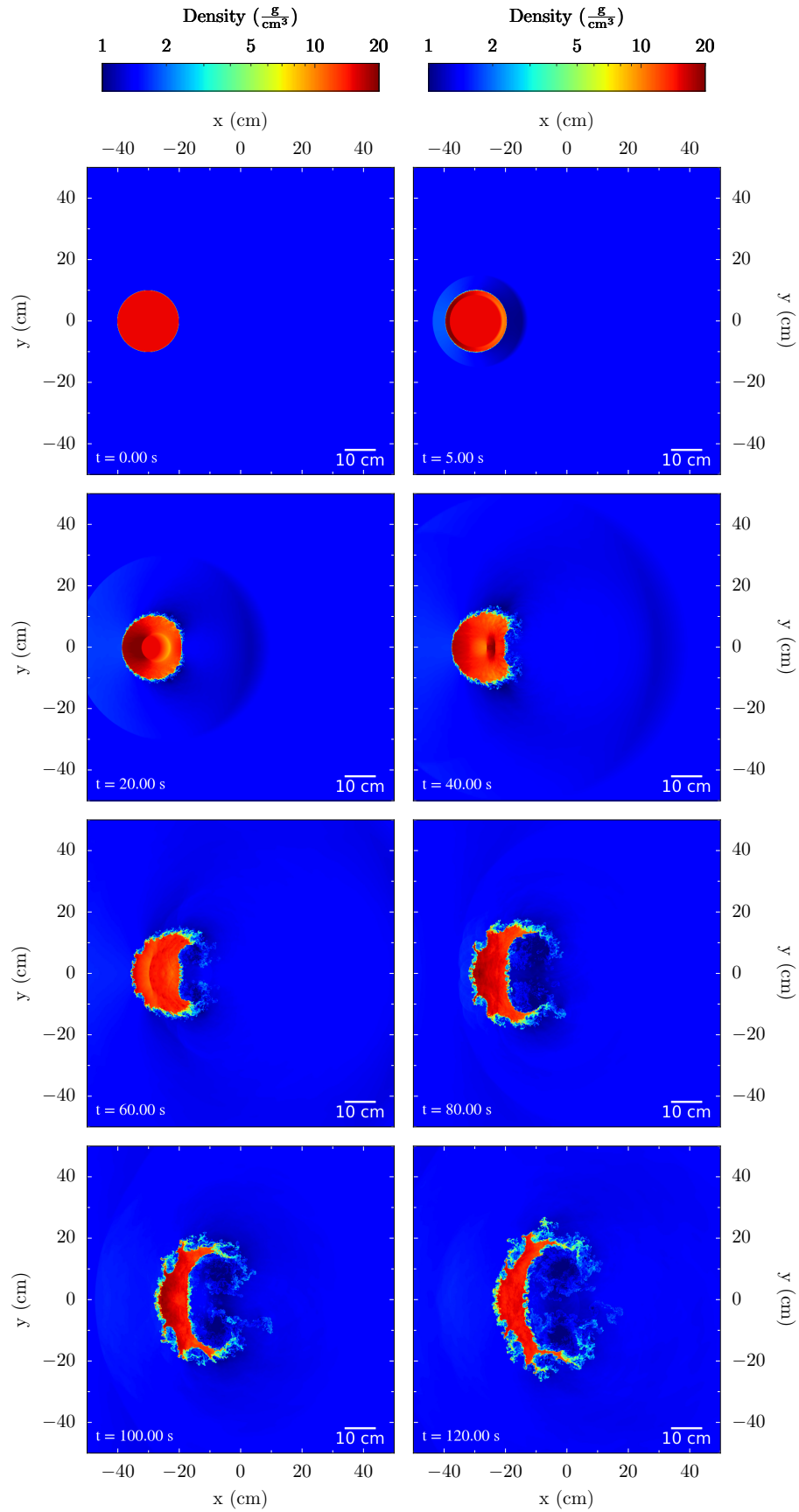


**Fig. 2.5:** Mach 0.5 subsonic simulation of the stripping of a gas cloud run with FLASH in a grid of  $16 \times 16$  blocks, with a grid size of  $100 \text{ cm}^2$ . The grid resolution is  $\delta x = 0.006 \text{ cm}$ , which corresponds to  $\sim 3,333$  grid cells per cloud diameter. Snapshots are taken at  $t = 0.0 \text{ s}$ ,  $t = 5.0 \text{ s}$ ,  $t = 20.0 \text{ s}$ ,  $t = 40.0 \text{ s}$ ,  $t = 60.0 \text{ s}$ ,  $t = 80.0 \text{ s}$ ,  $t = 100.0 \text{ s}$ ,  $t = 120.0 \text{ s}$ .

regions. As the simulation moves on, the lower density region splits into two streams, creating a faint horned appearance to the cloud, which feed into a low density region downstream i.e. the wake. From the onset of the wind flow, the density in the downstream atmosphere of the cloud decreases, with KHI's produced around the circumference of the cloud due to the velocity shear between the gas and the wind. This is also accompanied by the production of multiple eddies characterising a turbulent flow regime. Importantly, the KHI's are more prominent at the sides of the cloud, where they effectively peel off gas, transporting it downstream. Directly behind the cloud in the near wake, there is a region where the average flow velocity is directed upstream, this characterises the deadwater region. Moving far enough downstream into the far wake region, the average flow velocity reverses and begins to flow away from the gas cloud. The deadwater region, along with the transported gas from the KHI's, gives rise to the production of two large vortices observable from  $t = 60.0$  s, becoming clear at  $t = 100.0$  s. The near wake region is highly turbulent with multiple vortices and many eddies coexisting and dissipating the remaining gas. By this point, the gas cloud has clearly deformed from its spherical shape. Finally at the end of the simulation, at  $t = 120.0$  s, the gas cloud starts to fragment and disintegrate.

Following on from this, the inflow velocity is increased to Mach 1.5 to produce a supersonic flow so that a comparison can be made to the subsonic simulation. Figure 2.6 presents the results of this simulation. The most notable observation is that there is a formation of a bow shock in front of the gas cloud (as expected since the wind velocity has moved above mach 1). This bow shock, characterised by its high pressure, grows larger as the simulation moves on. Clearly in this regime, there is a more violent stripping scenario compared to the more gentle approach of the subsonic simulation. The striking of the wind pushes the upstream atmosphere back and quickly causes a band of rapidly decreasing density on the downstream atmosphere of the cloud. A turbulent boundary layer is formed in which KHI's remove gas from the sides of the cloud where the pressure is lowered, transporting it downstream. Again as with the subsonic case, multiple shocks are occurring inside the gas cloud although here they are much more extreme. The upstream atmosphere becomes significantly stripped and fragments with many tiny vortices and eddies saturating the upstream region. When comparing to other cloud stripping simulations which use different simulation codes (e.g. see Agertz et al. (2007)), our FLASH simulations of the subsonic and supersonic stripping cases have demonstrated the same stripping evolution and stripping features as these other simulations.

The ability to resolve simulations to a high degree is crucial when trying to accurately describe the physics of the problem. One question in particular is how much does the simulation need to be refined so that it correctly captures the physical features. The higher the level of refinement, the higher the cost of computing time and memory, and thus it is a crucial factor to consider when planning a simulation run. For instance, certain physical processes, particularly instabilities such as the KHI can be hidden by low refinement levels and hence require a higher level. Figure 2.7 presents snapshots of the subsonic gas cloud stripping simulation at the levels of refinement of 1, 3, 5 and 7 to compare how this effects the stripping physics, particularly the presence of the KHI. The snapshots show that there

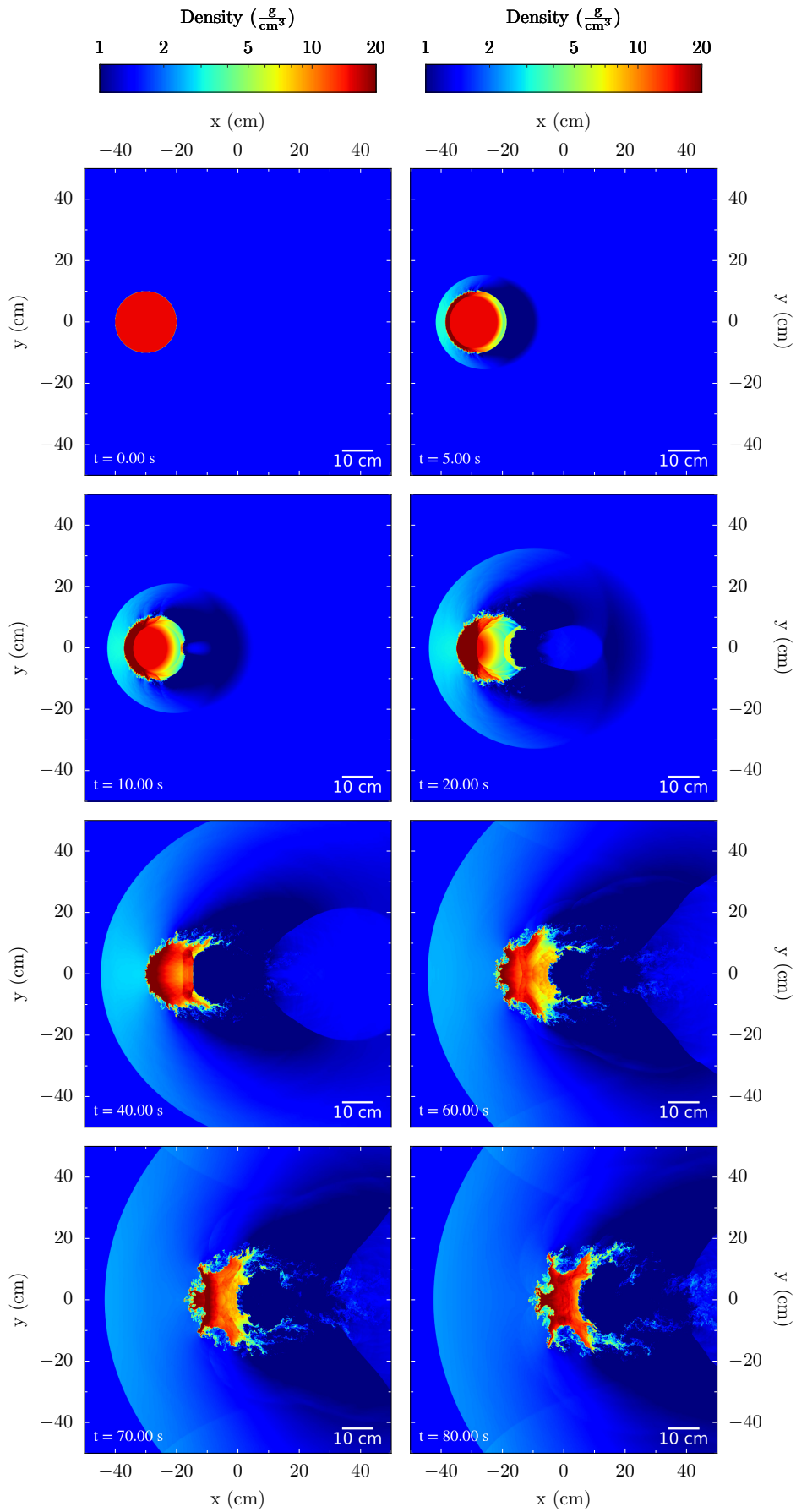


**Fig. 2.6:** Same as Fig. 2.5, but the in-flowing wind is now Mach 1.5 producing a supersonic flow. Plots are taken at  $t = 0.0$  s,  $t = 5.0$  s,  $t = 10.0$  s,  $t = 20.0$  s,  $t = 40.0$  s,  $t = 60.0$  s,  $t = 70.0$  s,  $t = 80.0$  s.

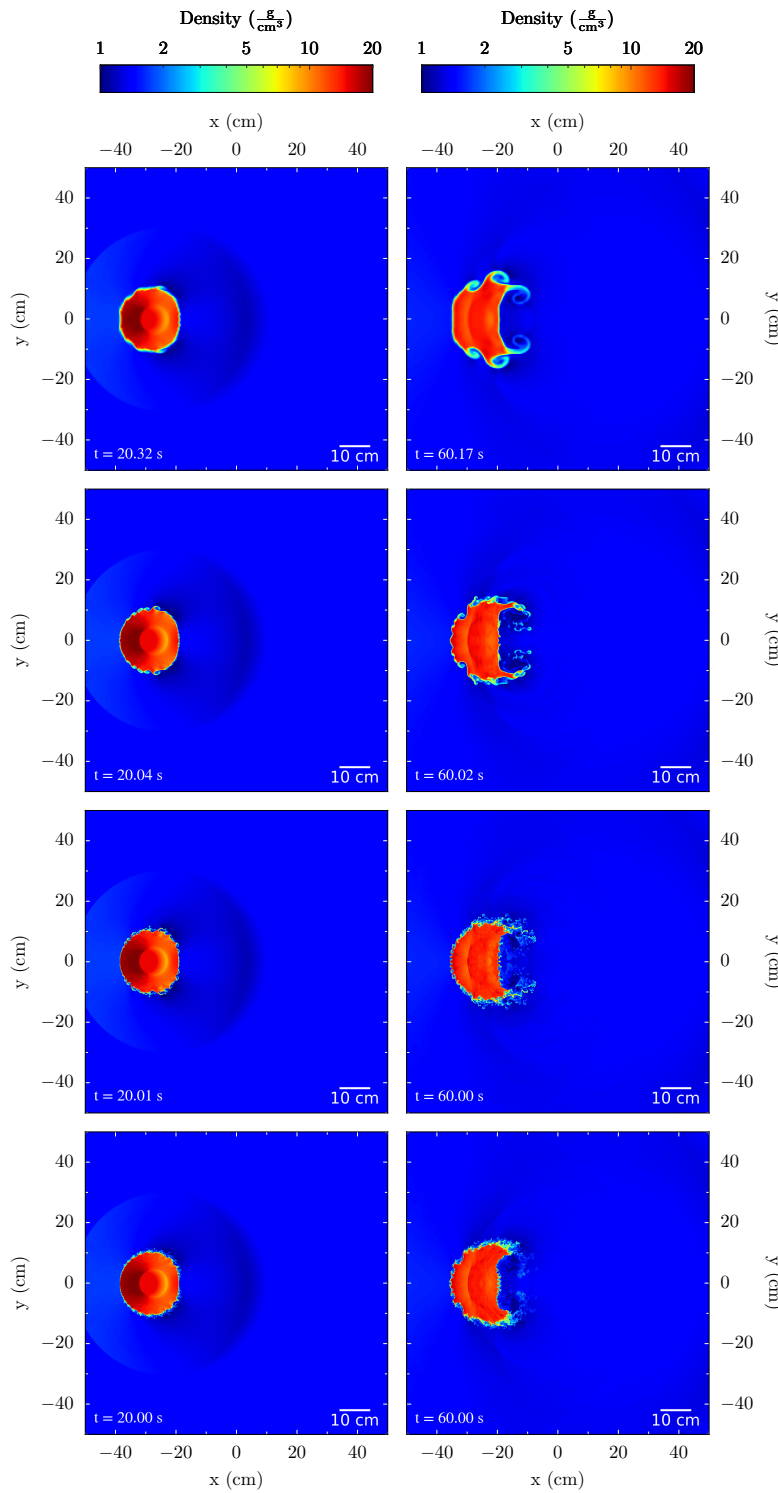


**Fig. 2.7:** Comparison of levels of refinement for a Mach 0.5 cloud-wind stripping simulation with FLASH (see also Fig. 2.6). Snapshots are taken at  $t = 20.0$  s and  $t = 60.0$  s for each level of refinement. The first row represents a refinement level 1 which corresponds to a resolution of 51 grid cells per cloud diameter. The second row represents a refinement level 3 which corresponds to a resolution of 204 grid cells per cloud diameter. The third row represents a refinement level 5 which corresponds to a resolution of 952 grid cells per cloud diameter and the fourth row represents a refinement level 7 which corresponds to a resolution of 3,333 grid cells per cloud diameter.

is a dramatic difference in size of KHIs between each level of refinement, as the increasing of refinement leads to smaller KHIs. However, the overall picture of the cloud stripping is captured even at the lowest resolution employed here (a resolution of 51 grid cells per cloud diameter), including the main stripping feature of the double vortex behind the cloud.

### 2.6.3 Galaxy Stripping

The next step after simulating the stripping of a gas cloud was to turn the gas cloud into a galaxy. This involved increasing the scales used in the simulation, e.g., changing cm to kpc to reflect astrophysical quantities. The galaxy is modelled to be an elliptical galaxy with a spherical distribution of gas. No particles, i.e. dark matter, are included in this simulation therefore it is purely hydrodynamical. To simulate this scenario, gravity needed to be added to the previous gas cloud simulation, and this was introduced using the Hernquist model for a static gravitational potential. From this model, a simple density profile for hydrostatic equilibrium can be formulated,

$$\rho_{\text{gal}}(r) = \rho_{\text{con}} \cdot \rho_{\text{amb}} \exp\left[\frac{-\phi(r)m_p}{kT}\right] \quad (2.17)$$

where  $\phi = \frac{GM}{r+a}$  is the Hernquist potential,  $\rho_{\text{con}}$  is a contrast factor and  $\rho_{\text{amb}}$  is the density of the ambient ICM gas. The pressure of the galaxy is then described by,

$$P_{\text{gal}}(r) = \frac{\rho_{\text{gal}}(r)}{m_p} kT. \quad (2.18)$$

The mass of the galaxy is  $10^{12}M_{\odot}$ , the radius is 10 kpc, the scale length  $a = 10$  kpc, the ICM density  $10^{-27} \text{ gcm}^{-3}$ , the ICM pressure  $3.0 \times 10^{-12} \text{ dycm}^{-2}$ , the density contrast  $\rho_{\text{con}} = 10$  and the ICM wind velocity is set to  $850 \text{ kms}^{-1}$ . The refinement level is set to 5 which corresponds to a resolution of 150 pc, or  $\sim 133$  grid cells per galaxy diameter. Figure 2.8 presents the results of this simulation. As expected, the flow past the galaxy resembles the flow around a blunt object as described in Chapter 1 and as demonstrated by Roediger et al. (2015a). It is also similar to the cloud stripping presented before, however here the static gravitational potential of the galaxy prevents the total destruction of the cloud. The onset of the flow produces a bow shock in front of the galaxy, signifying supersonic motion. The upstream atmosphere is pushed back becoming deformed due to the pressure of the ICM wind. KHI's are produced along the sides of the galaxy due to the shear between the galaxy atmosphere and the ICM which strips away the atmosphere downstream producing a horned appearance similarly to Fig. 2 in Roediger et al. (2015a). The stripped gas enters the wake of the galaxy downstream and mixes with the ICM, gradually fading into the ambient density. The downstream atmosphere of the galaxy is shielded from the upstream and can survive the gas stripping forming a remnant tail.

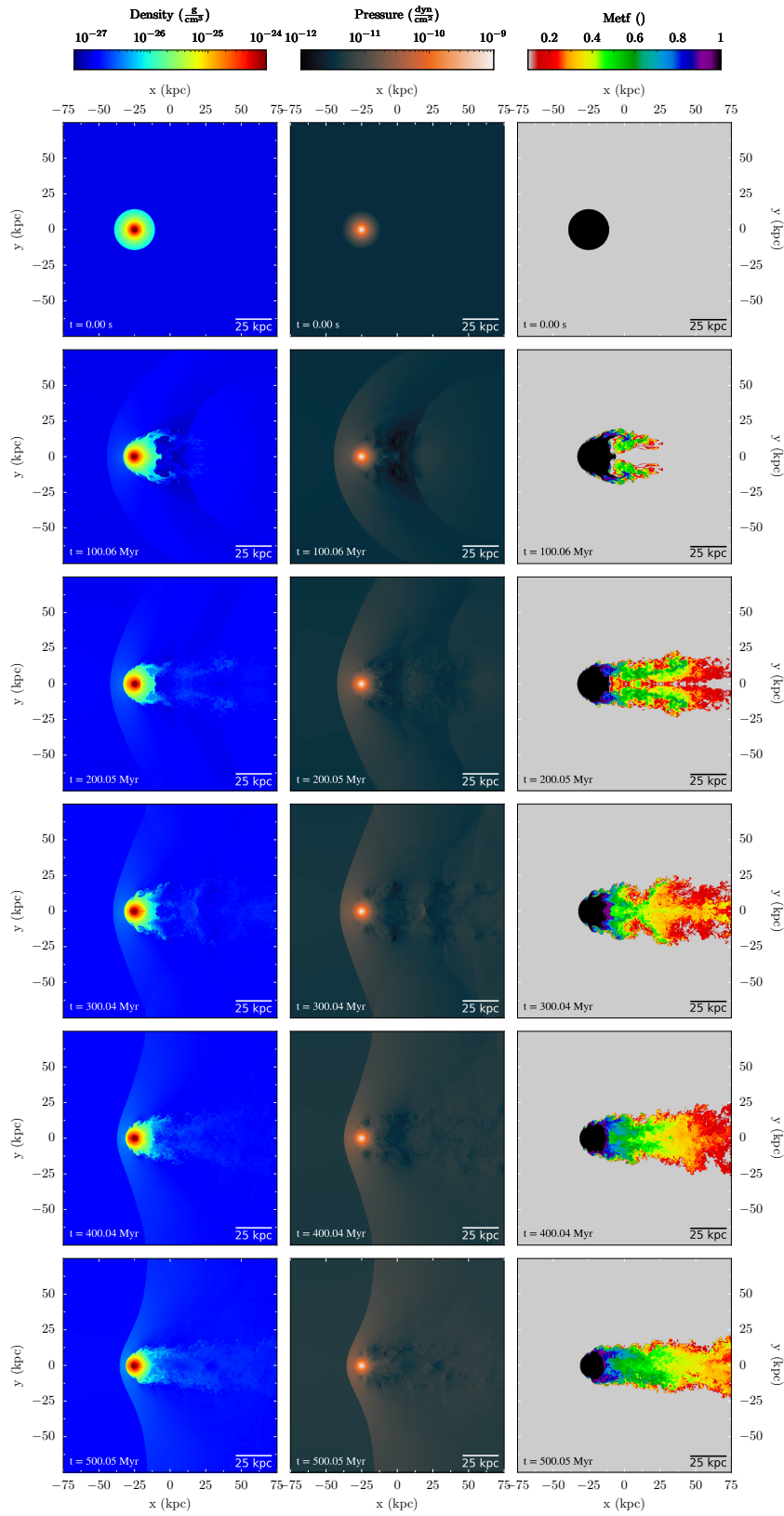


**Fig. 2.8:** Simulated images of the gas stripping of a galaxy. The ICM wind is set to a velocity of  $850 \text{ km s}^{-1}$  and flows in from the left hand boundary.

### 2.6.4 Rigid Potential Merger Simulations

The next step to take after simulating the gas stripping of a galaxy was to insert a cluster and make a minor merger simulation. The model cluster and galaxy here follow a similar setup as the galaxy stripping simulation, where a Hernquist model for a static gravitational potential is used to describe the potential of the cluster and galaxy. The galaxy follows a particle test orbit and the effects of dynamical friction and tidal stripping are neglected. This simulation is made with the intention for providing a rough approximation to the minor merger between the Fornax Cluster and NGC 1404. For this simulation, the cluster and galaxy are characterised by their mass, density and temperature profiles as follows. The mass distribution for a Hernquist model in a static gravitational potential is given by,

$$\rho(r) = \frac{M_o}{2\pi a^3} \frac{1}{\frac{r}{a}(1 + \frac{r}{a})^3} \quad (2.19)$$

where  $M$  and  $a$  are the mass and scalelength of the cluster. The density and temperature profiles for the cluster and galaxy are derived from hydrostatic equilibrium under a Hernquist potential using the numerical model by Ascasibar & Markevitch (2006) (hereby referred to as Ascasibar model). In the Ascasibar model, the temperature profile is described by,

$$T(r) = \frac{T_o}{1 + \frac{r}{a}} \frac{c + \frac{r}{a_c}}{1 + \frac{r}{a_c}} \quad (2.20)$$

where  $c$  is a free parameter that characterises the depth of temperature drop in the cluster/galaxy centre ( $0 < c < 1$ ) and  $a_c$  is the radius of this temperature drop. From this, the gas density profile is derived by considering hydrostatic equilibrium,

$$\rho_{gas}(r) = \rho_o \left(1 + \frac{r}{a_c}\right) \left(1 + \frac{r}{c}\right)^\alpha \left(1 + \frac{r}{a}\right)^\beta \quad (2.21)$$

where,

$$\alpha \equiv -1 - n \frac{c-1}{c - \frac{a}{a_c}} \quad (2.22)$$

$$\beta \equiv 1 - n \frac{1 - \frac{a}{a_c}}{c - \frac{a}{a_c}}. \quad (2.23)$$

where,  $n$  is a parameter that represents the baryon fraction. Table 2.1 summarises the parameters used for the Hernquist mass and Ascasibar profiles to approximate a Fornax like cluster and an NGC 1404 like galaxy used for the rigid gravitational merger. The galaxy is placed at the outskirts of the cluster at a radius of 800 kpc and is given an initial tangential velocity of  $150 \text{ km s}^{-1}$  to ensure that the merger is not head on as this is ruled out by observations. At the highest refinement level, the resolution is  $\delta x = 360 \text{ pc}$ .

Figure 2.9 presents snapshots from the rigid gravitational merger. The galaxy shows the same features as the galaxy stripping simulation presented previously as it falls into the cluster. A bow shock is formed in front of the galaxy as it reaches supersonic speeds as it falls into the cluster, and a gas tail is produced as it encounters the head-wind of the

	Cluster	Galaxy
Central Density $\rho_o$ ( $gcm^{-3}$ )	$0.8 \times 10^{-26}$	$3.0 \times 10^{-25}$
Mass $M_{\odot}$	$1.0 \times 10^{14}$	$1.5 \times 10^{13}$
$a$ (kpc)	400.0	75.0
$a_c$ (kpc)	40.0	10.0
$n$	5.0	5.0
$c$	0.5	0.09

**Table 2.1:** Parameters for the mass, temperature and gas profiles for the cluster and galaxy for the rigid gravitational potential merger. These parameters were chosen to provide a close match to the Fornax Cluster and NGC 1404.

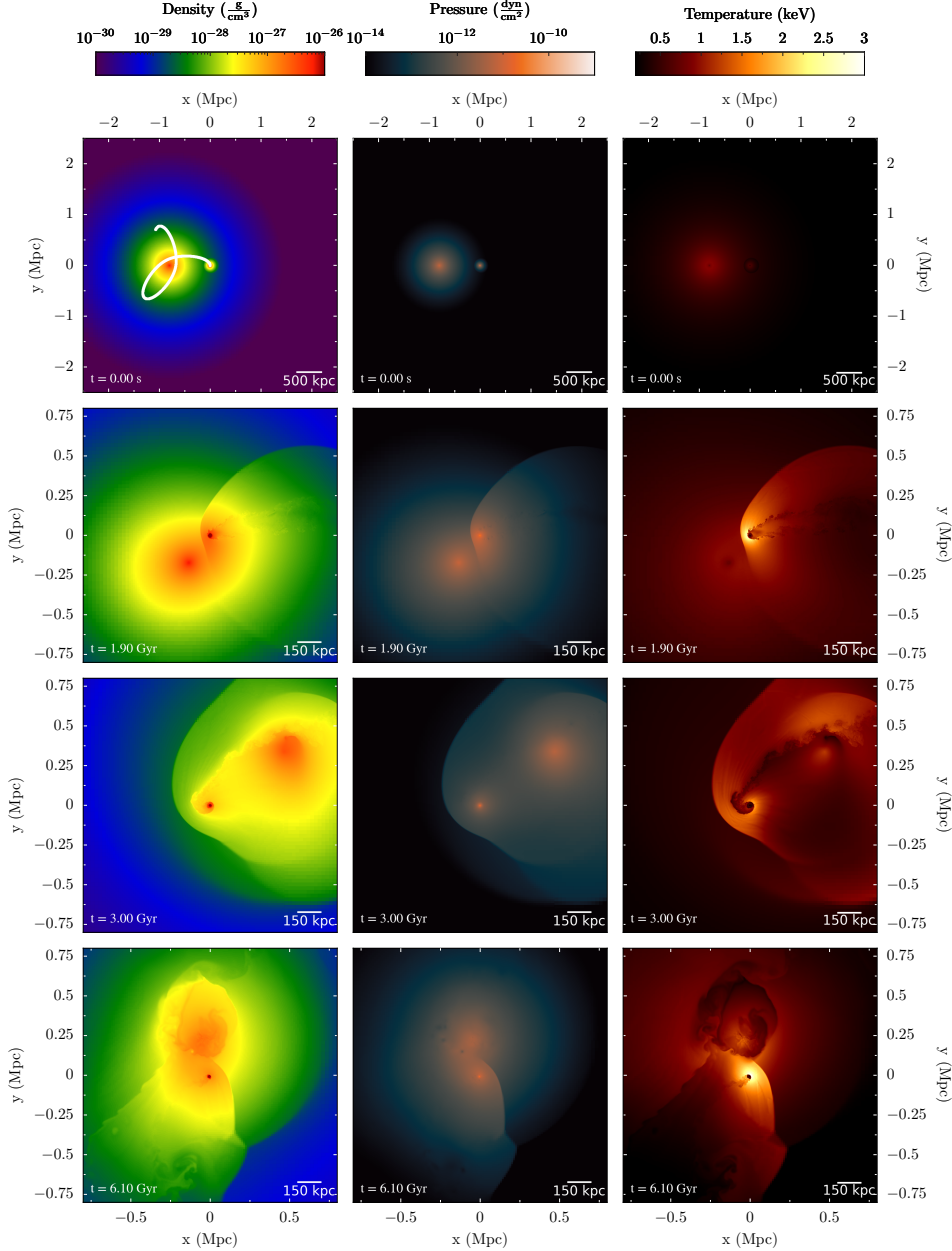


**Fig. 2.9:** Snapshots from a rigid potential merger between a cluster and a galaxy. Snapshots are centred on the galaxy. The first column colour codes gas density, the second column pressure and the third column temperature. The first row show snapshots are at  $t = 0$ , and are in a larger frame of view to show the whole cluster and galaxy. The  $t = 0$  gas density snapshot has the galaxy orbit overlaid to show the orbit path during the merger. The second row shows the first infall into the cluster at  $t = 1.9$  Gyrs. The third shows the galaxy at apocentre at  $t = 3.0$  Gyrs and the fourth row shows the galaxy on its second infall into the cluster at  $t = 6.1$  Gyrs.

clusters ICM. This simulation was run until it provided a visual match to observed images of NGC 1404, this corresponded to the second infall at  $t = 6.1$  Gyr (the bottom row of Fig. 2.9). When comparing the infall velocity of the galaxy at this timestep, the velocity in the simulation is found to be much higher. One reason why this increased velocity occurs could be due to the fact that dynamical friction is not taken into account. Dynamical friction will cause a loss in momentum and kinetic energy for the simulated galaxy as it moves through the cluster gravitational potential, this in turn will reduce the velocity of the galaxy as it falls into the cluster. Furthermore, as dynamical friction is not included, the galaxy reaches a much larger apocentre distance and spends much more time in orbit around apocentre, leading to a long merger time. As we show in the following chapters, the merger time is significantly reduced when dynamical friction is incorporated into the simulation.

Therefore the final step to take to create an N-body and hydrodynamical merger is to replace the rigid gravitational potential of the cluster and galaxy with real life dark matter halos. This process and the results of this are described in the following chapters.



## **Chapter 3**

# **The Recent Growth History of the Fornax Cluster Derived from Simultaneous Sloshing and Gas Stripping: Simulating the Infall of NGC 1404**

### **3.1 Prologue**

This chapter has been published in The Astrophysical Journal as Sheardown et al. (2018).

### **3.2 Abstract**

We derive the recent growth history of the Fornax Cluster, in particular the recent infall of the giant elliptical galaxy NGC 1404. We show, using a simple cluster minor merger simulation tailored to Fornax and NGC 1404, that a second or more likely third encounter between the two reproduces all main merger features observed in both objects; we firmly exclude a first infall scenario. Our simulations reveal a consistent picture: NGC 1404 passed by NGC 1399 about 1.1 - 1.3 Gyrs ago from the NE to the SW and is now almost at the point of its next encounter from the S. This scenario explains the sloshing patterns observed in Fornax - a prominent northern cold front and an inner southern cold front. This scenario also explains the truncated atmosphere, the gas stripping radius of NGC 1404, and its faint gas tail. Independent of the exact history, we can make a number of predictions. A detached bow shock south of NGC 1404 should exist which is a remnant of the galaxy's previous infall at a distance from NGC 1404 between 450 - 750 kpc with an estimated Mach number between 1.3 and 1.5. The wake of NGC 1404 also lies S of the galaxy with enhanced turbulence and a slight enhancement in metallicity compared to the undisturbed regions of the cluster. SW of NGC 1404, there is likely evidence of old

turbulence originating from the previous infall. No scenario predicts enhanced turbulence outside of the cold front north west of the cluster centre.

### 3.3 Introduction

Embedded in the large scale structure, galaxy clusters are the largest gravitationally bound systems in the universe containing hundreds or more galaxies. Under the framework of the hierarchical model, clusters are still growing through sequential mergers and accretion of smaller systems - from subclusters to galaxy groups to the infall of galaxies. Studying the dynamics of cluster mergers is particularly suited to the X-ray regime, as gas rich mergers leave a clear trace of the merger history due to the thermal bremsstrahlung emission of the intra-cluster medium (ICM). Mergers have a significant impact on the thermal state of the cluster by inducing bulk motions, driving shocks in the ICM, and generating regions of turbulence which then dissipate and heat the surrounding gas (Roediger et al., 2009, Bykov et al., 2015). Excellent examples of such merger shocks can be seen in the galaxy cluster 1E 0657-56 commonly known as the Bullet Cluster (Markevitch et al., 2002) and in Abell 520 (Markevitch et al., 2004). Further merger shocks have also been observed in Abell 85 (Ichinohe et al., 2015), Abell 2146 (Russell et al., 2010), and Abell 665 (Dasadia et al., 2016).

Using mass ratios, mergers can roughly be distinguished into two main regimes - major mergers and minor mergers. The former occur between approximately equal mass systems such as two clusters (a 1:1 mass ratio), whereas minor mergers involve a low and a high mass system, where the infall of an early-type galaxy into a cluster can be regarded as a very minor merger. In what follows below, for clarity we will refer to the lower mass merger partner as "the galaxy", however all explanations are valid for subclusters as well.

Consider the scenario of a small subcluster merging with a larger main cluster. Two processes occur simultaneously: the sloshing of the main (larger) cluster and gas stripping of the infalling galaxy or subcluster. Gas sloshing in the main cluster occurs as the subcluster moves through the pericentre, offsetting the ICM and dark matter in the main cluster core which then begins to move towards the subcluster as it is pulled gravitationally towards it. During this phase, ram pressure can act to decelerate the ICM gas separating it from the dark matter as the dark matter is still free to move towards the subcluster. As the subcluster completes its passage, the offset ICM gas falls back towards the main cluster core generating cold fronts that propagate outwards (Ascasibar & Markevitch, 2006, ZuHone & Markevitch, 2009, Figures 12 and 14 in Bykov et al., 2015). The outward propagation of the cold fronts depends mainly on the cluster potential and ICM profiles. Therefore the recent merger history of a given cluster can be reconstructed from the observed cold fronts. The sloshing cold fronts are sharp contact discontinuities in the ICM density and temperature (but not pressure) that can be seen through X-ray observations. Although cold fronts appear to be stable, velocity shears are likely present giving rise to Kelvin-Helmholtz instabilities (KHI) (Roediger et al., 2013a). However, the strength of the

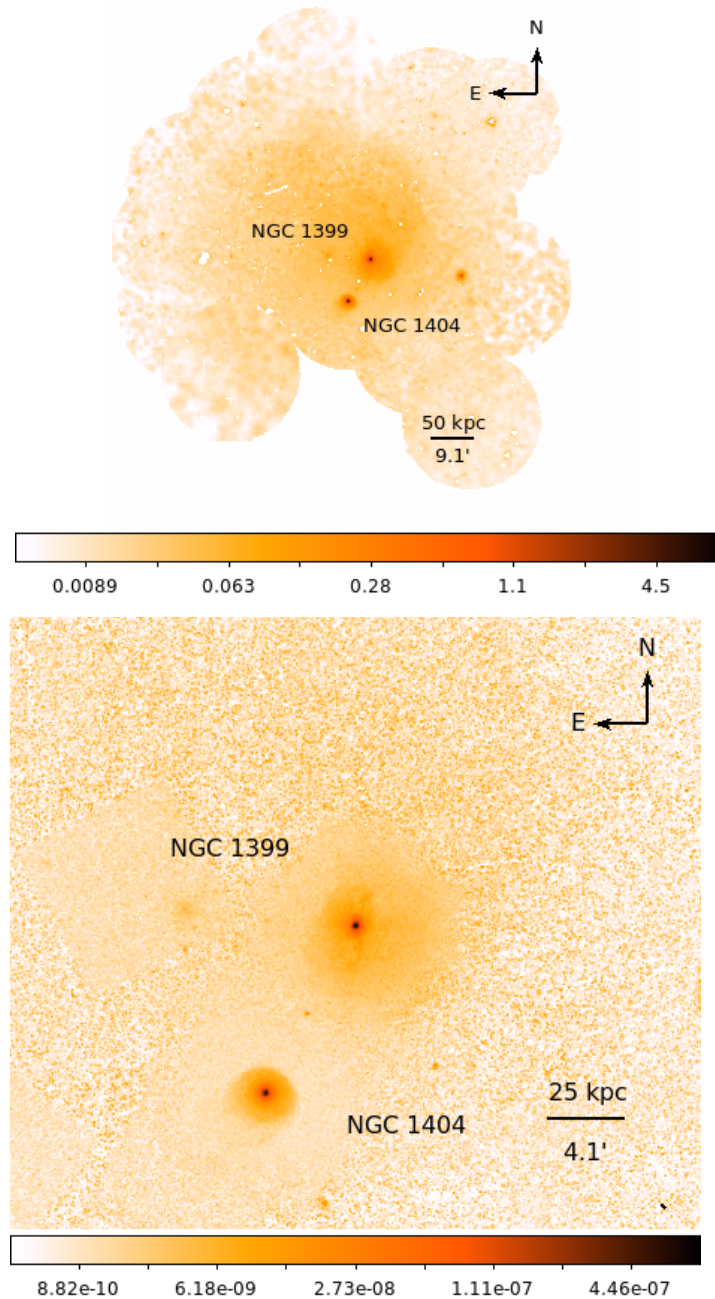


**Fig. 3.1:** Top: XMM image of Fornax in the energy band of 0.5 - 2.0 keV taken from Su et al. (2017d) in units of photons/s/cm<sup>2</sup>/deg<sup>2</sup>. A prominent cold front is evident to the north of the cluster centre as well as a smaller cold front to the south due to sloshing in the cluster gas. Bottom: Taken from Su et al. (2017a), exposure-corrected with blank-sky background subtracted Chandra mosaic image of Fornax in the energy band of 0.5 - 2.0 keV and in the unit of photon cm<sup>-2</sup>s<sup>-1</sup>. Chandra gives a clear view of the truncated atmosphere of NGC 1404 as well as its faint gas tail indicative of a galaxy being gas stripped due to infall.

ICM viscosity and magnetic field can act to potentially suppress the instability (Vikhlinin et al., 2001b, ZuHone, 2011).

The second process is the gas stripping of the infalling galaxy. As the galaxy moves through the ICM, it is progressively stripped due to a ram pressure which causes a drag force on the galaxy which in turn strips away its gaseous atmosphere (Gunn & Gott, 1972, Larson et al., 1980, Roediger & Brüggen, 2008, Roediger et al., 2015a, De Grandi et al., 2016). Additionally, the galaxy can be stripped via Kelvin-Helmholtz instabilities which arise due to velocity shears between the ICM gas and the galactic atmosphere. As the ram pressure is  $P_{\text{ram}} = \rho_{\text{ICM}} v_{\text{gal}}^2$ , the strength of the gas stripping is dependent on the galaxies orbit through the cluster, in particular the pericentre distance to the cluster centre. This determines the density of the ICM that the galaxy will experience and the orbital velocity of the galaxy. When the ram pressure is great enough, the stripped gas appears as an X-ray tail as observed in several elliptical galaxies; NGC 4552 (Machacek et al., 2006), NGC 4406 (Randall et al., 2008a), NGC 4472 (Kraft et al., 2011), NGC 1400 (Su et al., 2014), CGCG254-021 in Zwicky 8338 (Schellenberger & Reiprich, 2015). Thus, an infalling galaxy can be characterised by a leading upstream edge which hosts a truncated atmosphere along with a downstream tail of stripped galactic gas. In the tail, the stripped gas should mix with the ambient ICM, unless mixing is suppressed by e.g. viscosity or magnetic fields. The exact state of the tail gas can thus be potentially used to determine the transport properties of the ICM (Roediger et al., 2015b, Su et al., 2017d).

Using our tailored hydro+Nbody simulations, we present a case study of a merger between an infalling galaxy and a cluster, that of the elliptical galaxy NGC 1404 and the Fornax Cluster. The motivation in choosing to model this system is due to its relatively simple components which are not complicated by galaxy-galaxy interactions or AGN outbursts, coupled with its relatively close proximity which offers extensive observational data in the X-ray and optical regimes. In this regard, NGC 1404 offers a unique probe to study transport processes along with cluster wide physics due to its pre-truncated atmosphere. Thus, the uncertainty regarding its initial gas contents and spatial configuration is unimportant. Our aim is to simulate a simple cluster minor merger between NGC 1404 and Fornax by using appropriate gravitational potentials and gas contents which agree with observationally derived profiles. Comparing the resulting sloshing and stripping features to the real observations, we determine the recent merger history of Fornax. In Section 3.4, we describe the target galaxy and cluster, detailing key features of both systems. In Section 3.5, we outline the initial conditions used for generating our model, designed based on observational constraints. Section 3.6 presents the result of the simulation while section 3.7 discusses implications for the history and physics of the Fornax cluster. In section 3.8, we summarise our findings.

### 3.4 Setting the Scene: NGC 1404 and the Fornax Cluster

The Fornax Cluster is a nearby, low mass, cool core galaxy cluster located in the southern hemisphere at a distance of 19 Mpc ( $1' = 5.49$  kpc) and a redshift of  $z = 0.00475$  (Paolillo

et al., 2002). Due to its close proximity, Fornax has been extensively imaged in a number of wavelengths by a range of telescopes and instruments, in particular in X-rays by ROSAT, Chandra and XMM-Newton, with the latter two having the ability to resolve structures in Fornax down to 100 pc. Schematically speaking, the main body of Fornax is dominated by the brightest cluster galaxy NGC 1399, a large almost spherical elliptical galaxy (E1), with another sub system situated  $> 1$  Mpc south west of NGC 1399 centred around Fornax A. The Fornax core, centred around NGC 1399, is encapsulated by the ICM with a temperature of  $\sim 1.5$  keV (Rangarajan et al., 1995, Jones et al., 1997, Paolillo et al., 2002, Machacek et al., 2005, Su et al., 2017a). In terms of size, using a scaling relation based on the ICM temperature, Su et al. (2017a) estimated the virial mass of Fornax to be  $r_{vir} \approx 750$  kpc and Drinkwater et al. (2001) calculated a dynamical mass of  $7 \pm 2 \times 10^{13} M_{\odot}$  within a projected radius of 1.4 Mpc. Using joint Chandra and XMM observations of Fornax, Su et al. (2017d) revealed evidence of asymmetry and merger induced gas sloshing occurring in the cluster core, in particular identifying four sloshing cold fronts as was suggested by Su et al. (2017a). From joint Suzaku and XMM observations, Murakami et al. (2011) also found evidence of asymmetry by analysing temperature and metallicity distributions in Fornax. They found that the region  $13'$  (71 kpc) north of the cluster centre has a low ICM temperature and high Fe abundance in comparison to the region  $\sim 17' - 27'$  (93 kpc - 148 kpc) south of the cluster centre, pertaining to recent dynamical evolution.

NGC 1404 is an elliptical galaxy and the second brightest galaxy in Fornax, located south east to the central galaxy, NGC 1399, at a projected radius of  $\sim 60$  kpc. The galaxy's atmosphere harbours a sharp upstream leading edge 8 kpc from its centre forming a cold front towards NGC 1399 and an  $\sim 8$  kpc long gaseous tail to the south east (Jones et al., 1997, Machacek et al., 2005, Su et al., 2017a). Using stagnation point analysis, Machacek et al. (2005) determined the galaxy to be in the same plane of the sky as the cluster centre and provided an estimate for the Mach number of NGC 1404 to be 0.83-1.03 with a relative velocity to the ICM being 531-657  $\text{km s}^{-1}$ , whilst Scharf et al. (2005) estimate a Mach number of  $1.3 \pm 0.3$  and a velocity of  $660 \pm 260 \text{ km s}^{-1}$ . Using a 670 ks Chandra observation, Su et al. (2017a) led an extensive study based on stagnation point pressure analysis to determine that the galaxy is infalling at an inclination angle of  $33^{\circ}$  with a Mach number of 1.32. Inside the leading edge of the galaxy, they calculate an electron density of  $n_e = 6.1 \times 10^{-3} \text{ cm}^{-3}$  with a gas temperature of  $0.6 \pm 0.02$  keV. Further, they calculate that the tail of NGC 1404 is 16 kpc wide and 8 kpc in length in projection with a gas temperature in the region of 0.9-1.0 keV. They suggest that since the temperature in the gas tail is consistently hotter than the remnant core of the galaxy (0.6 keV) and cooler than the ambient ICM gas (1.5 keV), that thermal conduction is heating the stripped gas and/or turbulent mixing of the ICM gas is happening downstream in the tail.

Another indication for an ongoing merger between NGC 1404 and Fornax is the globular cluster content of both systems. In particular, Forbes et al. (1998) and Bekki et al. (2003) both find that NGC 1399 has rich globular cluster content (high specific frequency) whilst NGC 1404 has poor globular cluster content (low specific frequency) compared to the average for elliptical galaxies, suggesting that NGC 1399 may have stripped NGC

1404 of some its globular clusters as it undergoes a merger. Under this argument it would imply that NGC 1404 has already fallen through the cluster once already.

## 3.5 Simulation Setup

### 3.5.1 Initial Conditions

To tailor our simulations to NGC 1404 and Fornax, we aimed to match their gravitational potentials and gas atmospheres to observations. This information is available through observations of stellar light, stellar velocity dispersion, ICM temperature, pressure, and density distribution from X-rays. We aim to match the observational data at the end of the simulation run, this required some test runs to find initial conditions such that the evolved cluster, after the merger, matches the data. Our models for NGC 1404 and Fornax are set up to be spherically symmetric, self gravitating and in hydrostatic equilibrium following the set up procedure as described in ZuHone (2011). Each simulation has a different merger time and geometry (explained in Section 3.5.4). Therefore, to get a perfect match for each would require a slightly different initial model for each simulation. This wouldn't only be impractical, but would also prevent an easy comparison between the different simulations. Thus, the initial model we have chosen is a suitable compromise for making our simulations representative of NGC 1404 and Fornax, while being practical at the same time. Furthermore, we experimented with a range of initial models similar to the one presented here, and the main conclusion is independent of the exact choice.

#### Fornax

To tailor our simulation to Fornax, we use Chandra and XMM-Newton data to model the Fornax ICM gas density in the form of a double  $\beta$  profile. Chandra data covers the inner 25 kpc of Fornax while the XMM data reaches out to 200 kpc; we extrapolate the observational results out to larger radii. Figure 3.2 compares the Fornax ICM density and temperature profiles taken from Chandra and XMM with our model profiles for the V0 and V2 simulations. The parameters for the double beta model are presented in Table 3.1. The match and deviations between observations and model are explained below.

We model the total gravitational potential of Fornax with a double Hernquist potential (eq. 1):

$$\rho(r) = \frac{M_{\text{dm}}}{2\pi a_{\text{dm}}^3} \frac{1}{\frac{r}{a_{\text{dm}}} (1 + \frac{r}{a_{\text{dm}}})^3} + \frac{M_*}{2\pi a_*^3} \frac{1}{\frac{r}{a_*} (1 + \frac{r}{a_*})^3} \quad (3.1)$$

$$M(< r) = M_{\text{dm}} \frac{r^2}{(r + a_{\text{dm}})^2} + M_* \frac{r^2}{(r + a_{i*})^2}$$

where  $M_{\text{dm}}$  and  $a_{\text{dm}}$  are the mass and scale length for the outer component of Fornax, and  $M_*$  and  $a_*$  are the mass and scale length for the inner component respectively. This model is chosen for the useful property of a finite total mass and thus does not require

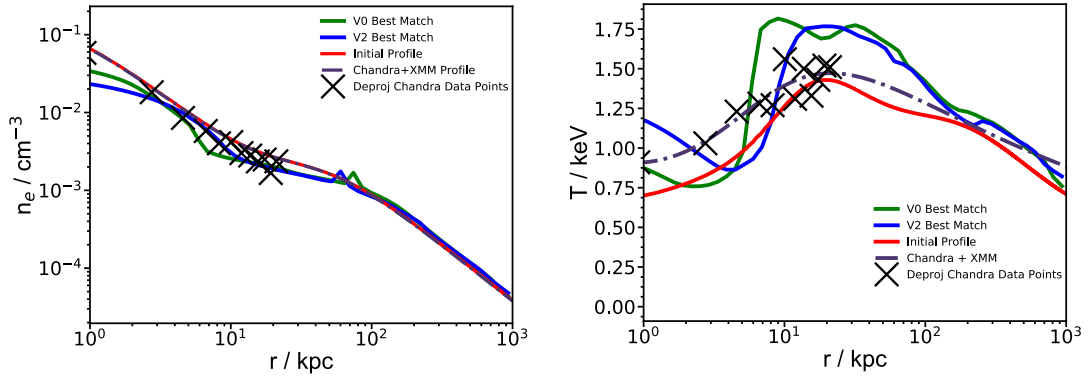


**Fig. 3.2:** Comparison of simulated and observed ICM profiles for the Fornax cluster from the V0 and V2 simulations. Observed profiles are spherically averaged. Profiles from the simulation are taken at the final merger state which provides a visual match to observation and are spherically averaged. Left: Electron density profiles. Right: Temperature profiles. The overall ICM distribution in the observed and simulated Fornax cluster agree well, considering our simple model. The decrease in density at the very centre of Fornax in our profiles is partly due to gas stripping and partly due to resolution.

truncation like an NFW profile. Further, using two components allows us to better capture the inner and outer potentials of Fornax. Although we do not distinguish between luminous and dark matter, we can think of one potential (the outer component) as the dark matter content of Fornax described by mass  $M_{\text{dm}}$  and scale length  $a_{\text{dm}}$ , and the inner component as the dominant central galaxy in Fornax, NGC 1399 described by mass  $M_*$  and scale length  $a_*$ . We note that this total potential includes the ICM as well. The particle density in the simulation is set as the difference between the total density and the ICM density. For the "dark matter" component of the Hernquist potential, we have a constraint for the total mass of Fornax from Drinkwater et al. (2001) of  $7 \pm 2 \times 10^{13} M_{\odot}$  based on the method of Diaferio (1999). Furthermore,  $M_{\text{dm}}$  and  $a_{\text{dm}}$  affect the overall ICM temperature profile, which is constrained by the X-ray data. Thus we select a dark matter mass of  $6 \times 10^{13} M_{\odot}$  with a scale length of 250 kpc for the parameters  $M_{\text{dm}}$  and  $a_{\text{dm}}$ . For the inner potential we are guided by the stellar light. We convert the K-band luminosity profile of NGC 1399 to a cumulative mass profile using a stellar mass-to-light ratio in the K-band of  $1.3 \frac{M_{\odot}}{L_{\odot}}$  (taken from Silva & Bothun, 1998). However, the central potential component also impacts the central ICM temperature profile. A very steep central potential that closely matches the stellar light data leads to unrealistically high central ICM temperatures. Therefore, we find that a stellar mass of  $M_* = 3.2 \times 10^{11} M_{\odot}$  with scale length  $a_* = 3.8$  kpc provides the best compromise. Figure 3.3 compares the cumulative mass profiles for our model to the observed stellar mass. Table 3.1 summarises the parameters used in the double Hernquist model for Fornax. Figure 3.2 shows that our choices for the Fornax model lead to a good overall agreement with the ICM profiles to the observations at the end of the V0 and V2 simulations. For our simulated profiles, gas density is lost in the very centre which is partly due to gas stripping and resolution. This gas loss would be different if cooling and heating were accurately modelled in our simulation. This is also the same for NGC 1404. Significantly however, our results do not rely on the central gas cores.

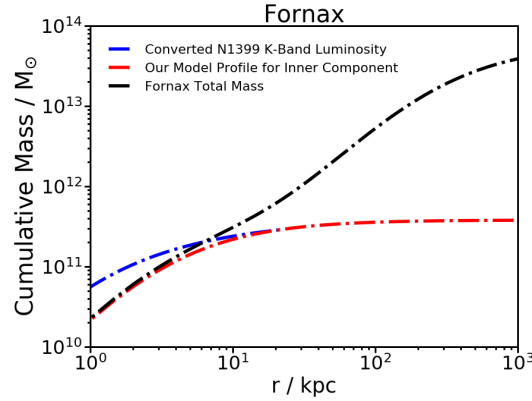


**Fig. 3.3:** Cumulative mass profile for our model Fornax cluster compared to cumulative stellar mass of NGC 1399, converted from K-Band luminosity. The total mass of the model cluster consists of an inner and outer Hernquist potential, where roughly the inner potential represents the NGC 1399 stellar component. As a compromise between the stellar light data and the observed ICM temperature profile, we chose an inner component somewhat less compact than observed because otherwise the hydrostatic initial setup of the cluster results in an unrealistically high central ICM temperature.

**Table 3.1:** Fornax Cluster Model Parameters

Double Hernquist	
$M_{\text{dm}} / 10^{13} M_{\odot}$	6.0
$a_{\text{dm}} / \text{kpc}$	250.0
$M_{*} / 10^{11} M_{\odot}$	3.2
$a_{*} / \text{kpc}$	3.8
Double $\beta$ Model	
$A_1 / \text{cm}^{-3}$	0.151
$r_1 / \text{kpc}$	0.623
$\beta_1$	0.44
$A_2 / \text{cm}^{-3}$	0.0024
$r_2 / \text{kpc}$	55.0
$\beta_2$	0.48

**Table 3.2:** NGC 1404 Model Parameters

Double Hernquist	
$M_{\text{dm}} / 10^{13} M_{\odot}$	0.45
$a_{\text{dm}} / \text{kpc}$	45.0
$M_{*} / 10^{11} M_{\odot}$	2.2
$a_{*} / \text{kpc}$	1.5
Single $\beta$ Model	
$A_1 / \text{cm}^{-3}$	0.151
$r_1 / \text{kpc}$	0.623
$\beta$	0.5

### NGC 1404

As with Fornax, we tailor the simulation to NGC 1404 using Chandra data to model its gas density as a single  $\beta$  model. Figure 3.4 compares the NGC 1404 gas density and temperature profiles taken from Chandra with our initial and evolved model profiles for the V0 and V2 simulations. We initially set the gas density twice as large as the Chandra single  $\beta$  model as from testing we find that during the early Fornax core passages, the NGC 1404 gas density decreases by about a factor of two due to gas stripping and we need to match to observations at the evolved stage. In the course of the merger, the central gas density of NGC 1404 decreases somewhat. This is partly a real effect due to gas loss via gas stripping combined with gas redistribution via sloshing in NGC 1404, but the inner kpc is affected by resolution as well. We aimed to keep a good match to the observed gas profile outside  $\sim 4$  kpc. Furthermore, our model choice of potentials, gas content, and galaxy orbit which are driven by the overall properties of Fornax and NGC 1404, lead to an upstream stripping radius of  $\sim 6$  kpc, remarkably close to the observed 8 kpc, given our simple model.

Again, like for Fornax, we use a double Hernquist potential to model the overall potential of NGC 1404. To constrain the inner components of NGC 1404 we are guided by the K-band luminosity data (see Figure 3.5) and fit  $M_{*}$  and  $a_{*}$  appropriately with values of  $M_{*} = 2.2 \times 10^{11} M_{\odot}$  and  $a_{*} = 1.5$  kpc respectively. Here we also find the compromise between matching the stellar data and keeping a reasonable gas temperature profile. For the outer potential component, we follow the model of M89 used in Roediger et al. (2015a) as M89 is comparable to NGC 1404 in regards to the gas temperature and stellar luminosity. Therefore we select values of  $M_{\text{dm}} = 0.45 \times 10^{13} M_{\odot}$  and  $a_{\text{dm}} = 45.0$  kpc. Table 3.2 summarises the parameters for the double Hernquist model and the single beta model parameters for NGC 1404.

### 3.5.2 Metallicity Profiles

In our simulation, we include a mass scalar which holds metallicity information for both NGC 1404 and Fornax. This mass scalar is carried throughout the simulation as a dye and does not interact with the problem dynamics. In turn, this allows us to track the redistribution of metals throughout the cluster during the merger. For Fornax, the Chandra

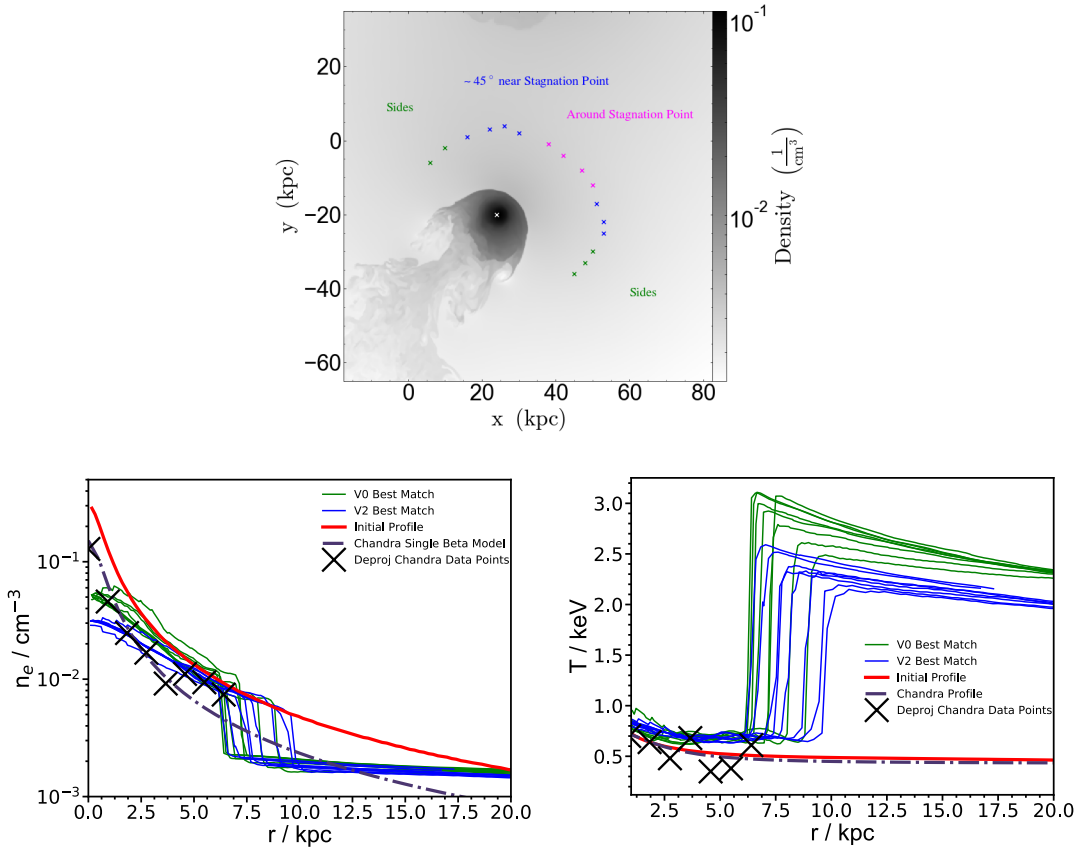


**Fig. 3.4:** Comparison of simulated and observed gas atmosphere profiles for NGC 1404 from the V0 and V2 simulations. The observed profiles for electron density (bottom left) and temperature (bottom right) are azimuthally averaged. For the simulated galaxy, profiles are taken along rays from the galaxy centre to the locations indicated in the top panel (the example shown is for the V0 simulation). The simulated profiles are taken at the stage of the merger which provide a visual match to observation. The sharp drop in density marks the radius of the galaxy, where the density then becomes the Fornax ICM. The simulations reproduce the observed upstream stripping radius and agree well with the observed profiles around this point considering our simple model. The decrease in density at the very centre of NGC 1404 in our profiles is partly due to gas stripping and internal sloshing, and partly due to resolution (the decrease in density gets a little lower after each pericentre passage - this is why we set the initial profiles twice as high as the observational profile). The temperature profiles reveal an increased ICM temperature around the stripped NGC 1404 atmosphere. This is due to the stolen atmosphere effect as explained further in Section 3.6.4.

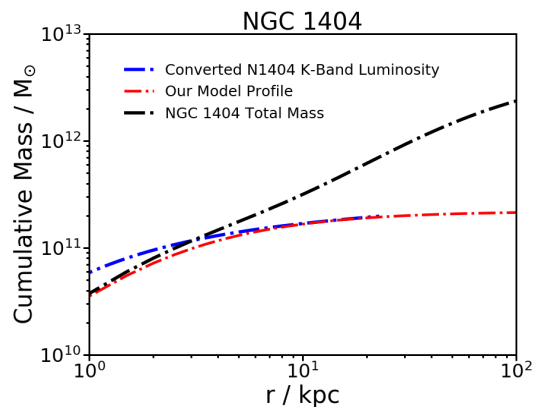


**Fig. 3.5:** Cumulative mass profile for our model NGC 1404 compared to cumulative stellar mass of NGC 1404, converted from K-Band luminosity. The total mass of the model galaxy consists of an inner and outer Hernquist potential, where roughly the inner potential represents the NGC 1404 stellar component. As a compromise between the stellar light data and the observed NGC 1404 temperature profile, We chose an inner component somewhat less compact than observed because otherwise the hydrostatic initial setup of the cluster results in an unrealistically high central NGC 1404 temperature.

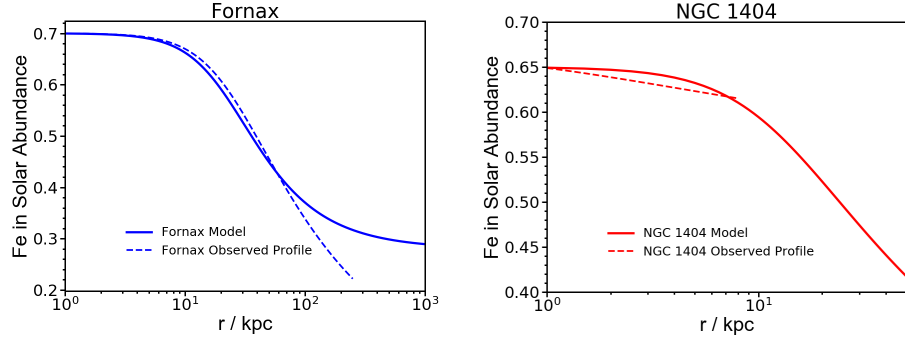


**Fig. 3.6:** Left: Initial metallicity profiles in Fe solar abundance for Fornax. Chandra and XMM data are valid out to 250 kpc for Fornax, thus we extrapolate the observed data to approach a metallicity of 0.3 solar as observed in other clusters (Simionescu et al., 2011). Right: Initial metallicity profiles in Fe solar abundance for NGC 1404. Chandra data is only valid for the inner 8 kpc of the galaxy, so again we extrapolate so that it approaches 0.3 solar at large radii. Observed profiles are represented by the dashed lines and our model profile by the thick line.

and XMM data are valid out to 250 kpc; from this point we extrapolate the observed data to approach a metallicity of 0.3 solar as observed in other clusters (Simionescu et al., 2011). Likewise for NGC 1404, the data are only valid for the inner 8 kpc, so we adapt again so that it approaches 0.3 solar at large radii. The abundance profiles we use are:

$$\text{Fe}_{\text{Fornax}} = 0.42 \left( 1 + \left( \frac{r}{22 \text{ kpc}} \right) \right)^{-0.5} + 0.28 \quad (3.2)$$

$$\text{Fe}_{\text{N1404}} = 0.45 \left( 1 + \left( \frac{r}{12 \text{ kpc}} \right) \right)^{-0.25} + 0.2 \quad (3.3)$$

Figure 3.6 compares the model and observed profiles.

### 3.5.3 FLASH - The Simulation Code

Our simulations use the FLASH Code - a high performance modular code developed to handle multi-physical problems (Fryxell et al., 2000). We utilise its 3D hydrodynamic + Nbody capabilities to simulate the interaction between the gaseous and collisionless (dark matter and stars - both self gravitating) components, respectively. Including the self gravity of the collisionless particles, and the gas, as well as the gravity between both components, allows us to accurately characterize tidal forces and dynamical friction during the merger. This has a significant impact on the orbit of the galaxy and hence plays a pivotal role in the merger timescales.

For simulation V0, we use a particle resolution of 4 million particles for Fornax and 400,000 particles for NGC 1404. Whereas for V1 and V2, we use a particle resolution of 1 million particles for Fornax and 100,000 particles for NGC 1404. FLASH Code has the capability to use adaptive mesh refinement defined by specific refinement criteria. Our simulation refines a grid block if it has more than 200 particles. This simple choice allows us to capture the tail of the galaxy as well as the centres of both the galaxy and the cluster at a maximum resolution, since these regions contain the largest particle numbers. At the

highest refinement level the resolution is 0.22 kpc. The Fornax centre and the NGC 1404 are refined to this level typically out to 50 kpc and 12 kpc respectively. This refinement criteria certifies that the majority of the wake of NGC 1404 is also refined to this highest level. We found that not refining enough i.e. having a lower resolution, produced ripples in the potential centres which expanded outwards from the centres of the cluster and galaxy. This also caused the very centres of galaxy and cluster to lose gas. Both effects decrease with higher resolution and are negligible in our simulations.

### 3.5.4 Simulation Design

We select a simulation box size of  $1.5 \text{ Mpc}^3$ . This is chosen to be sufficient to capture the potential of the Fornax gas past the virial radius,  $\sim 750 \text{ kpc}$ , and so the infall path is not subjected to boundary effects. The simulation boundaries are set to outflow (shocks can leave the simulation domain) but we do not anticipate any impact on the simulation as the main physics occurs far enough away from the boundaries. Our simulations neglect both radiative cooling and heating by active galactic nuclei (AGN), i.e., we assume that over time, both processes balance out as implied by observations (Bîrzan et al., 2008). The addition of cooling, and the balancing AGN activity, would affect mostly the gas properties in the central kpc's of NGC 1399, and the very central kpc's of NGC 1404, where the cooling time is shortest. None of our results rely on the central gas cores.

#### Orbit

We match the velocity of NGC 1404 from observational constraints by Machacek et al. (2005), Scharf et al. (2005) and Su et al. (2017a). This must be reflected in our simulation. Further, we match the radius of our model galaxy to the radius from the centre of NGC 1404 to the upstream cold front measured in Machacek et al. (2005) and Su et al. (2017a) of  $\sim 8 \text{ kpc}$ .

At the beginning of the simulation, Fornax sits at the centre of the simulation box with NGC 1404 placed at roughly the virial radius of the cluster,  $\sim 750 \text{ kpc}$ . We test several orbits for NGC 1404 through Fornax (Table 3.3). In simulation V0, we give NGC 1404 only an initial tangential velocity to control the impact parameter of the merger. A head on merger would strip all gas from NGC 1404 which is ruled out by observations. An initial tangential velocity of  $150 \text{ km s}^{-1}$  in the -y-direction leads to a gas stripping radius comparable to the observed one. However, such an almost zero-velocity infall from the virial radius is not what is typically seen in cosmological simulations. Vitvitska et al. (2002) show that during the initial phase of a merger, the merging subcluster already has an infall velocity of  $\sim 1.1v_c$  when it reaches the virial radius, where  $v_c$  is the circular velocity of the main cluster defined in the Hernquist model by  $v_c = \frac{\sqrt{GM(r)r}}{r+a}$ , where  $a$  is the scale length of the main cluster. Their work also finds that, for a major merger, the tangential component of the infall velocity is typically around  $0.45v_c$  whereas for a minor merger this typical value becomes  $0.71v_c$ . We therefore run two further simulations of a faster infall, V1 and V2 described in Table 3.3. Using a virial radius of 750 kpc, a scale length of

**Table 3.3:** Simulation Runs

Sim Name	Initial Separation (kpc)	$v_{\parallel}$ ( $\text{km s}^{-1}$ )	$v_{\perp}$ ( $\text{km s}^{-1}$ )
V0	650 (x = -430, y = 480)	0	+150
V1	750 (x = 750, y = 0)	-333	$0.45v_c = -149$
V2	750 (x = 750, y = 0)	-279	$0.71v_c = -236$

250 kpc and a virial mass of  $3.4 \times 10^{13} M_{\odot}$  (calculated using the Hernquist mass formula given in eq.1) gives a circular velocity of  $v_c = 332 \text{ km s}^{-1}$  and therefore an infall velocity of  $v_{in} = 365 \text{ km s}^{-1}$ . Simulations V1 and V2 have the same  $v_{in}$ , but different tangential and radial velocities,  $v_{\perp}$  and  $v_{\parallel}$  respectively (see Table 3.3), sampling the range given by Vitvitska et al. (2002).

It turns out that in simulations V1 and V2 the galaxy reaches about the virial radius on its first apocentre passage, i.e. it falls back into the Fornax cluster almost from rest after that point. This means that our simulation V0 is comparable to the second and third infall in V1 and V2. We therefore orient our simulations such that their final infall occurs in a comparable direction; i.e. in simulation V0, NGC 1404 approaches from the top left (NE). In V1 and V2, NGC 1404 approaches from the +x-direction, from the right (W), with a tangential velocity component in the -y-direction.

## 3.6 Results

### 3.6.1 Overall Merger History

The overall merger history for all three simulations is presented in Figures 3.7 and 3.8 using snapshots of electron density and temperature slices, respectively, in the orbital plane. We first describe simulation V0. Here, NGC 1404 approaches from the NE and reaches the centre point on its first infall into Fornax at an epoch of 1.52 Gyr. At this stage, the galaxy has a long extended gas tail  $\sim 100$  kpc in length, moving supersonically, as evidenced by the strong bow shock in front of the galaxy. Moving past pericentre, the galaxy is slowed by gravity and dynamical friction as it approaches apocentre producing a slingshot like tail. apocentre is attained at 2.19 Gyr, revealing highly irregular flow patterns around the galaxy leaving behind a wake of turbulent gas. Moving past apocentre, the galaxy begins to infall into Fornax a second time reaching a match to observation at an epoch of 2.79 Gyr, 1.27 Gyr after its last pericentre passage. At this second infall stage, the sharp upstream edge, truncated atmosphere and stripping radius of the galaxy are comparable to the observation. The passage of NGC 1404 near the Fornax centre triggers sloshing in the central Fornax ICM which leads to a cold front north of the Fornax centre as observed.

The simulations V1 and V2 portray an almost identical picture for the recent merger history, but they include one earlier Fornax core passage. NGC 1404 originally approaches from the W and reaches its first pericentre south of Fornax at 1.18 Gyr and 1.35 Gyr for V1 and V2 respectively before moving out to the apocentre in the NE. Again, NGC 1404

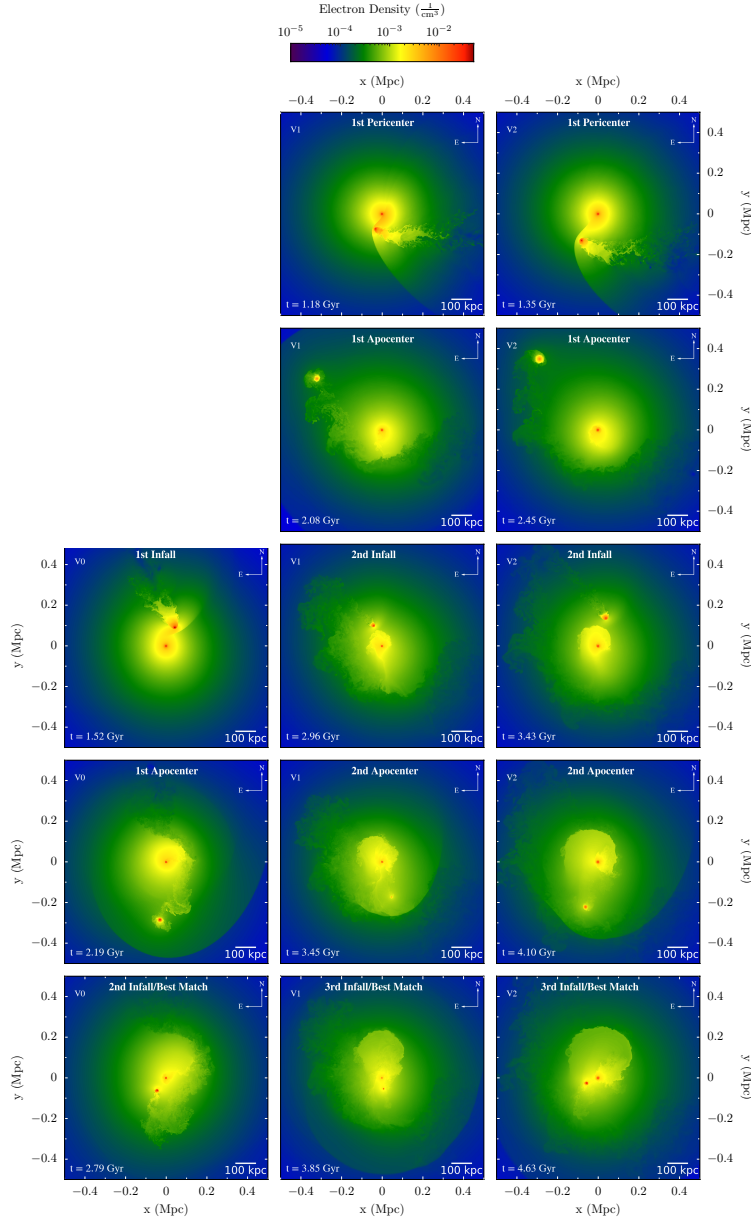


**Fig. 3.7:** Electron density snapshots in the orbital plane for the overall evolution of the infall of NGC 1404 into Fornax. Each column represents a different simulation run. From left to right; V0, V1, V2. In rows, we align the snapshots by evolutionary stage rather than exact time. Row 1 shows the first infall of NGC 1404 into Fornax for V1 and V2 revealing the bow shock and a long gas tail of NGC 1404. Row 2 shows the galaxy now at apocentre for V1 and V2 revealing irregular flow patterns. Row 3 shows the second infall of V1 and V2 along with the first infall of V0. Here, for V1 and V2, the galaxy hosts a short gas tail but is still moving supersonically evidenced by the bow shock. For V0, this first infall is comparable to the second infall of V1 and V2 as the galaxy begins its infall with almost zero velocity. Row 4 shows the 1st apocentre of V0 and 2nd apocentre of V1 and V2. The detached bow shock at this stage is clearly evident, propagating outwards south of the galaxy. Row 5 represents the best match for each simulation. At this stage the cold front to the north of the cluster centre, along with the sharp upstream edge, truncated atmosphere, stripping radius and faint tail of NGC 1404 are comparable to the observation. For the electronic version of the paper, we include an electron density animation of the three simulations alongside each other in separate panels in the same fashion as this figure. The animation covers the full run time for each simulation. At the start, simulations V1 and V2 begin to run. V0 begins to run once V1 and V2 reach their first apocentre. This is because the first infall of V0, which has an almost zero initial velocity, is comparable to the second infall of V1 and V2.

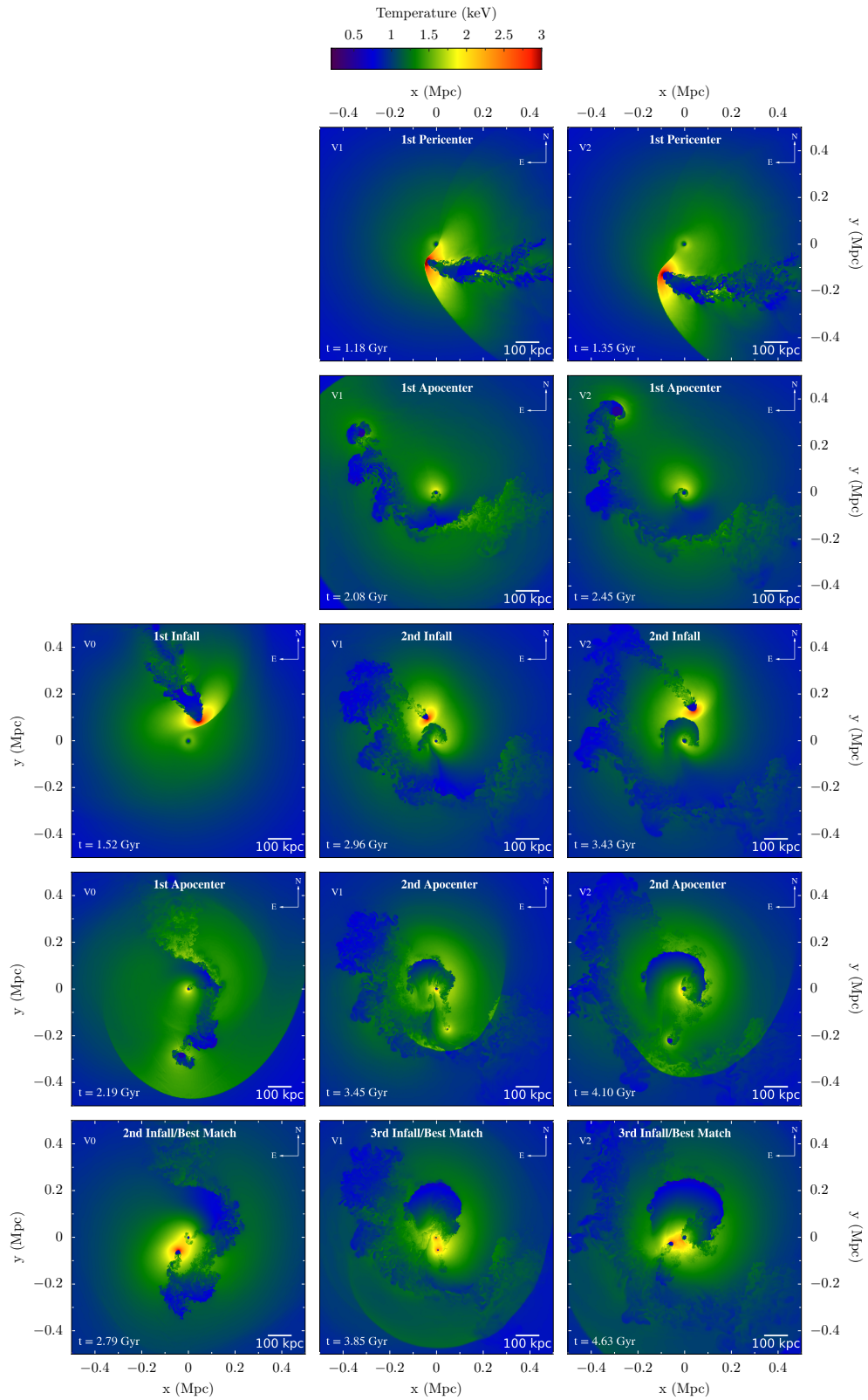


**Fig. 3.8:** Same as the previous figure but temperature slices in the orbital plane for the overall evolution of the infall of NGC 1404 into Fornax. Slushing fronts and NGC 1404's turbulent wake are seen more easily in the temperature slices.

still has a prominent gas tail on first infall, despite the higher infall velocity and it is not until approaching the first apocentre that NGC 1404 is fully truncated.

This first encounter induces typical sloshing motion in Fornax, producing a prominent front which sweeps around the centre (Rows 2 and 3 in Figures 3.7 and 3.8). The prominent sloshing front in the V2 simulation reveals the appearance of KHI rolls along its interface. The KHIs are clearest in V2 because here the shear flow along the cold front is cleanest and strongest. The second infall occurs from the NE along the NW of the Fornax core at 2.96 Gyr for V1 and 3.43 Gyr for V2. This stage corresponds to the first infall in V0 except for the gas contents of NGC 1404. Critically during the second infall, even though the galaxy resembles a sharp upstream edge and truncated atmosphere, it is still moving supersonically, as evidenced by a bow shock, and it is not until the third infall that this bow shock disappears.

The third infall occurs from the S/SE. At this stage, the galaxy still harbours a sharp upstream edge and truncated atmosphere. Most significantly at this stage, if we orient the images to match the observed infall direction of NGC 1404 from the SSE, the direction and position of the sloshing fronts appear to coincide with observational images of Fornax. When comparing the two test simulations with V0, the story looks relatively similar when comparing the evolution past the second apocentre. It could be considered that actually the V0 simulation also represents a third infall in the sense that this simulation begins at the second apocentre of the test simulations. This would concur as V0 starts with an almost zero infall velocity which would correspond to the galaxy reaching apocentre and falling back in again.

### 3.6.2 Second + Third Infall

As shown in Figures 3.7 and 3.9, in regards to the V0 simulation, the second infall at an epoch of 2.79 Gyr provides the best match to observation for this simulation. Here as already mentioned, the simulation reproduces the sharp upstream edge and truncated atmosphere with a galaxy radius between 7 - 11 kpc compared to the observationally measured radius of 8 kpc (Machacek et al., 2005, Su et al., 2017a). By using our simple method of prescribing appropriate gravitational potentials, gas contents and using a sensible orbit through Fornax, we are able to attain the correct radius (see also Figure 3.4). At this stage, the velocity of NGC 1404 relative to NGC 1399 (the Fornax centre) is  $871 \text{ km s}^{-1}$ .

After the merger, the temperature profile for NGC 1404 comes out a little high (see Figure 3.4) as we set up our initial model to match the observed temperature profile. At the initial stage, NGC 1404 is in the outskirts of the Fornax cluster, where the ambient ICM pressure is low. In the final timestep, it is near the Fornax centre, where the higher ambient ICM pressure somewhat compresses the NGC 1404 atmosphere, leading to a slight temperature increase. In addition, the temperature profiles show that inside the atmosphere of the galaxy there are small "bumps" in temperature - these are sloshing cold fronts inside the galaxy.

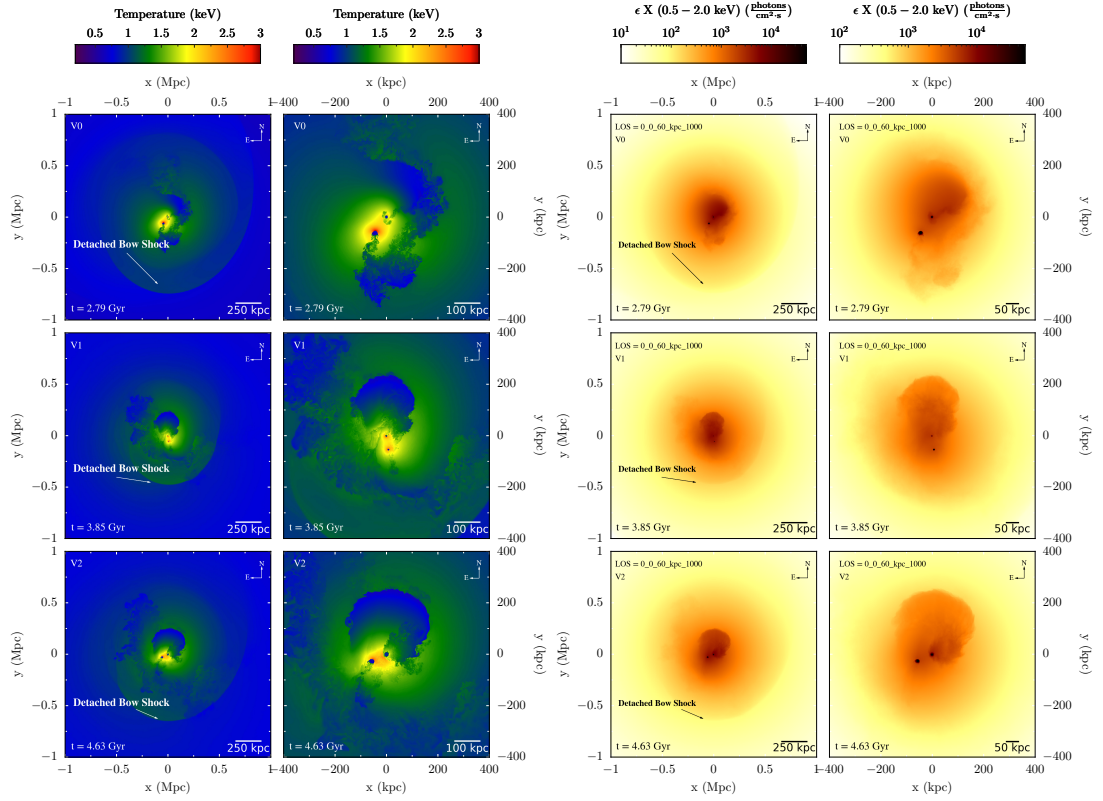


**Fig. 3.9:** Comparison of the best match stage for all 3 simulations, in temperature slices in the orbital plane (columns 1 and 2) and mock X-ray images (columns 3 and 4). Columns 1 and 3 show the cluster-wide view, whereas columns 2 and 4 show a zoomed in image of the cluster centre. For the cluster wide images, we indicate the position of the detached bow shock south of NGC 1404 which is a remnant of the previous infall of NGC 1404. In the temperature slices, the path of destruction caused by the merger of NGC 1404 is revealed in the cluster gas, and we can see where the galaxy did not at least stir turbulence (other galaxy's may have). In the zoomed in temperature slices, the stolen atmosphere effect is evident surrounding the halo of the galaxy where the temperature is increased higher than the original ICM temperature. The X-ray photon emissivity projections are calculated in the 0.5 - 2.0 keV energy band along the axis perpendicular to the orbital plane. The X-ray images show a prominent cold front to the north of the cluster centre matching the XMM image of the cluster (see Figure 3.1) along with the truncated atmosphere and faint gas tail of NGC 1404.

If we would want to match the second infall of simulations V1 and V2 to the observations, we would need to invert the merger geometry about the y axis. However, despite the fact that in all cases the galaxy has a sharp upstream edge, a truncated atmosphere with a comparable radius, the galaxy is still moving too fast as seen by the bow shock. Also at this stage, the sloshing in Fornax does not quite match the observed XMM image of the cluster in terms of the prominent front north of the cluster centre as seen in Figure 3.12. The most prominent cold front would be to the south instead. Though in each simulation the cold region does exist to the north of the cluster centre, it is more like a cold fan rather than a cold front which would give the sharp discontinuity across the edge like the XMM image.

It is not until the third infall stage that the tail of the galaxy in the V1 and V2 simulations has almost disappeared and is now comparable to the second infall/best match of V0. A significant factor in producing this short length of tail is that our simulations are inviscid, therefore any inclusion of viscosity would likely make it difficult to replicate this feature. One point of note is that in the V0 simulation, the galaxy has a more visible short gaseous tail whereas it is much fainter in V1 and V2. This is partly due to the longer amount of time the galaxy has travelled through Fornax, ensuring the NGC 1404 outer atmosphere is fully stripped. In the rapidly varying Fornax ICM, NGC 1404 can drag part of its outer atmosphere in a tail beyond its first apocentre.

At the best match stage, during the third infall of the V1 and V2 simulations, NGC 1404 has a velocity relative to NGC 1399 of  $603 \text{ km s}^{-1}$  and  $656 \text{ km s}^{-1}$  respectively. The most noticeable difference between V1 and V2 is that NGC 1404 has lost a lot more gas in V1. This is due to the second passage of Fornax smashing right through the middle of a cold front resulting in the galaxy being heavily stripped, whereas in V2, the galaxy only clips the edge of the front due to its wider orbit. This would be evidence that the first passage through Fornax had a large impact parameter, as was suggested by Machacek et al. (2005).

The overall merger history that emerges is this:

- 1.8 - 2.8 Gyr ago, NGC 1404 was at virial radius from the Fornax centre to the E, NE or N, and started falling into Fornax with an almost only tangential velocity. Starting from the E would require a stronger tangential velocity than starting from the N.
- This was either a particularly slow first infall, or the second infall.
- 1.1 - 1.3 Gyr ago, NGC 1404 passed close to the Fornax centre in the NW reached its most recent apocentre 0.4 - 0.6 Gyr ago at 180-230 kpc S-SSE from the Fornax core and is now close to the next pericentre passage. At this stage the simulations reproduce a heavily stripped NGC 1404 with a gaseous tail and the overall sloshing geometry of Fornax.

As is the case in all the simulations, in terms of the best match, that being the second infall of V0 and the third infall of V1 and V2, the position of the galaxy does not come out right. To fix this would require quite some fine tuning of setting an appropriate initial

velocity of the galaxy and hence its orbit through Fornax so that the galaxy would align with observed images. Crucially however, even with our small set of simulations with varied velocities and orbits, we see that the major features of NGC 1404 as well as the sloshing in Fornax are reproduced in each simulation, indicating their robustness. Therefore we believe that correcting for the position NGC 1404 would not significantly change the overall merger history.

### 3.6.3 Evolution of Fornax

#### V0

Moving our focus to the evolution of Fornax through each simulation we will first examine the V0 simulation. During the first infall of NGC 1404, the centre of Fornax is drawn upwards towards the galaxy due to their gravitational interaction. As the Fornax potential is rather compact, we find that using a pericentre distance that is too small results in the Fornax centre either being disrupted or losing far too much gas so it is not comparable to the observed profiles. Again, this would then suggest that the first encounter between NGC 1404 and Fornax was not a close one. After the first infall, as the galaxy moves out to the apocentre of the orbit, the centre of Fornax turns around and moves back towards NGC 1404. During this stage the Fornax centre is itself ram pressured stripped as it moves through the ICM resulting in the gas tail trailing to the north of the cluster centre, this can be clearly seen in Figures 3.7 and 3.8 (left column) at the  $t = 2.19$  Gyr snapshot. This stripping of the Fornax centre leads to a somewhat too low central ICM density compared to the observations (Figure 3.2). Including cooling may resolve the gas core. Moving into the second infall, in V0, a large cold fan of gas becomes prominent north of the cluster centre with a large cold wake behind NGC 1404 in the south, this can be seen in further detail in Figure 3.9. The temperature profiles for Fornax in Figure 3.2 reflect the cool wake of NGC 1404 and the northern cold front or fan.

#### V1 + V2

The two simulations V1 and V2 follow a similar scenario. The first encounter induces sloshing in the cluster core which has time to evolve and sweep around by the time the second encounter occurs. We can see the path of turbulence caused by the first infall of NGC 1404 across the southern region of Fornax. By the time of the third infall, the sloshing front has more time to develop, increasing in size, producing a prominent cold front north of the cluster centre, along with a smaller cold front to the south as shown in Figure 3.9 (bottom panel). At the third infall stage, highlighted by the velocity map out of the merger plane shown in Figure 3.11, we can see the wake of destruction caused throughout the cluster due to its interactions with NGC 1404, and we can clearly see regions where NGC 1404 caused turbulence and regions where no turbulence is predicted (as a result of NGC 1404).

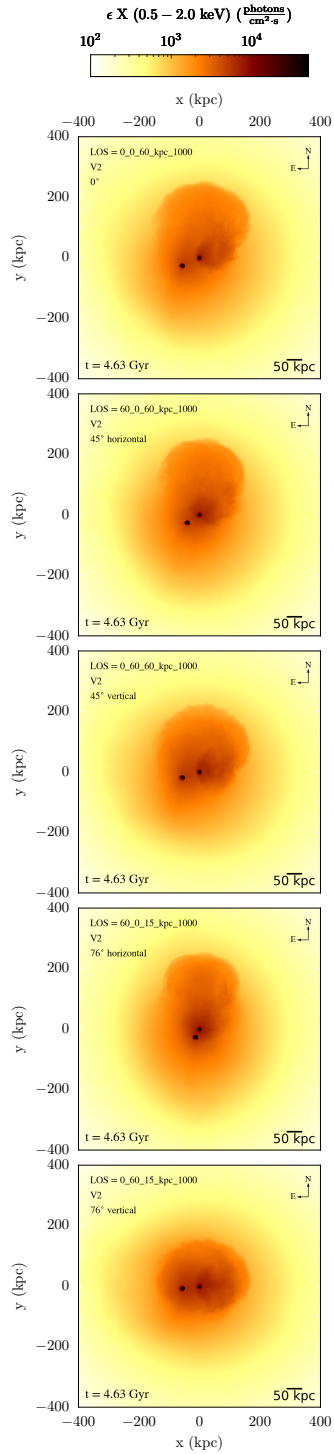


**Fig. 3.10:** X-ray photon emissivity projections for the V2 simulation calculated in the 0.5 - 2.0 keV energy band. The top image is a projection perpendicular to the orbital plane. The following images are a selection of LOS rotated vertically or horizontally to the orbital plane by  $46^\circ$  and  $76^\circ$ . Each image is annotated with its corresponding rotation and angle. Regardless of the choice of LOS, there is no obvious difference in the brightness or shape of NGC 1404 and the centre of Fornax.

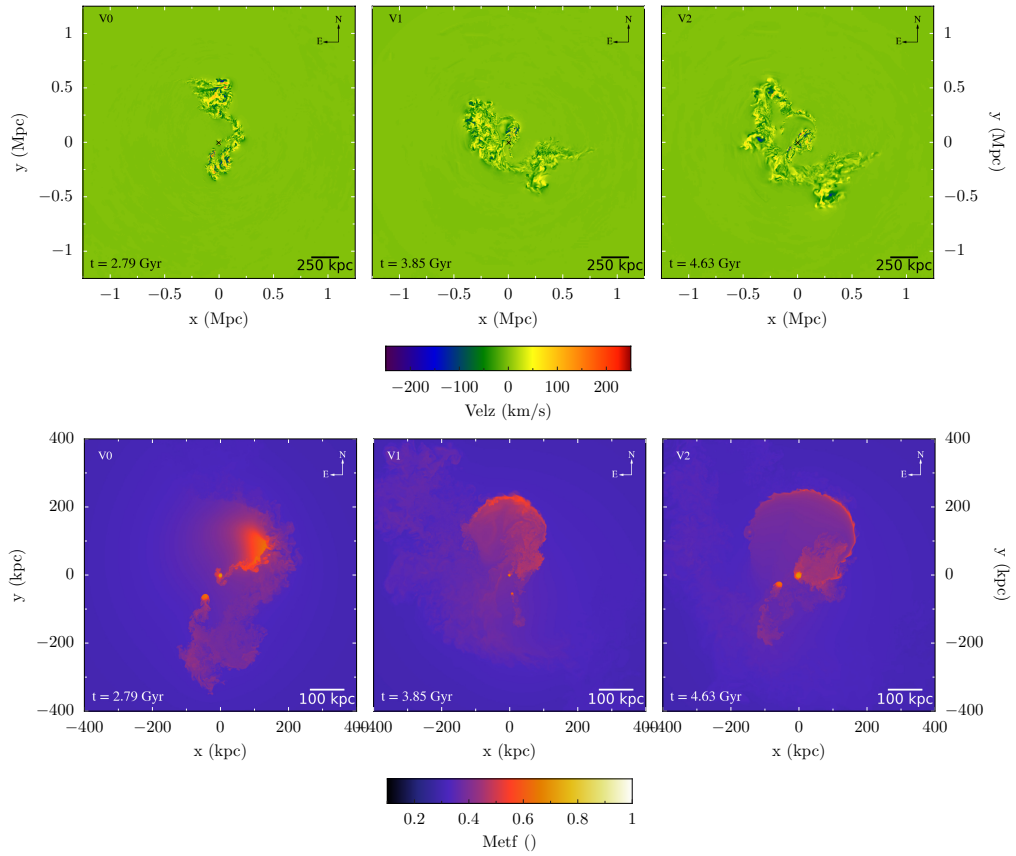


**Fig. 3.11:** Top: Velocity slices out of the orbital plane for each simulation revealing likely regions of turbulence caused by the infall of NGC 1404. Each column represents a simulation, from left to right: V0, V1, V2. Bottom: Same as top, but Metal fraction slices in the orbital plane in units of Fe solar abundance. The merger with NGC 1404 strips metal rich gas from the cluster centre (NGC 1399) displacing it northwards producing an increased abundance in this region as was noted by Murakami et al. (2011).

In all of the simulations, the best match case predicts a cold region of gas at temperatures around 0.9-1.0 keV to exist  $\sim 75$ -150 kpc north of the cluster centre, as a result of sloshing. This cold region coincides with observations made by Murakami et al. (2011) who detected gas of 0.9-1.0 keV in a similar region north of the cluster centre. Therefore we can attribute this cold region to be the result of sloshing caused by the infall of NGC 1404. In addition, when looking at the metallicity distribution in Fornax at the second and third infall stage, shown in Figure 3.11, we see that there is an increased Fe abundance of  $\sim 0.6$  Fe (solar)  $\sim 75$ -150 kpc north of the cluster centre. This metal rich gas once belonged to NGC 1399 but was displaced by sloshing. Murakami et al. (2011) detected an increased abundance of 0.53 - 0.71 Fe (solar)  $\sim 75$  kpc north of the cluster centre, which puts it roughly in the same region as our simulation. Again, we could attribute this region of increased abundance to the recent encounter with NGC 1404.

To make a direct visual comparison, Figure 3.12 presents an XMM image of Fornax alongside a mock X-ray image for the best match in the V2 simulation in the same units. We choose this particular simulation to make the comparison rather than V0 or V1 due to its sloshing features providing the best match, including both the northern and southern cold fronts. This time step is the best compromise between matching the cold front radii and the NGC 1404 position to the observation. At a slightly earlier time, the sloshing spiral would be smaller, and match the observation, while NGC 1404 would then be even a bit farther from its desired position. Fine-tuning its original infall velocity could reconcile this but brings no new insights. Given the simplicity of the model the achieved and consistent match between all the simulations and the observation is remarkable.

To see how sensitive the features of the simulation are to projection effects, we took the mock X-ray image of the V2 simulation and made images using various lines of sight (LOS). The results of this are presented in Figure 3.10. The x-y image plane as shown corresponds to the orbital plane and we vary the projection along the z axis, either perpendicular to the image plane or rotated about the horizontal or vertical axis. The overall sloshing features are independent of the LOS for a range of LOS rotated horizontally or vertically by  $45^\circ$  and  $76^\circ$ . The most notable difference is that the more you rotate the view, the less visible are the KHI's along the prominent cold front to the north. Regardless of the LOS, NGC 1404 and the centre of Fornax show no real change in brightness or shape.

### 3.6.4 Predictions

So far we have discussed the comparison of the simulations to the known features in the observation. Here we predict some features that have not yet been observed, but should exist if the proposed merger scenario is correct.

#### Detached Bow Shock Prediction

Evident in all of the simulations is the robust feature of a detached bow shock south of NGC 1404 as indicated in Figure 3.7. This shock is a remnant from the galaxy's previous encounter with Fornax. As the galaxy moved through pericentre, this shock led the galaxy.

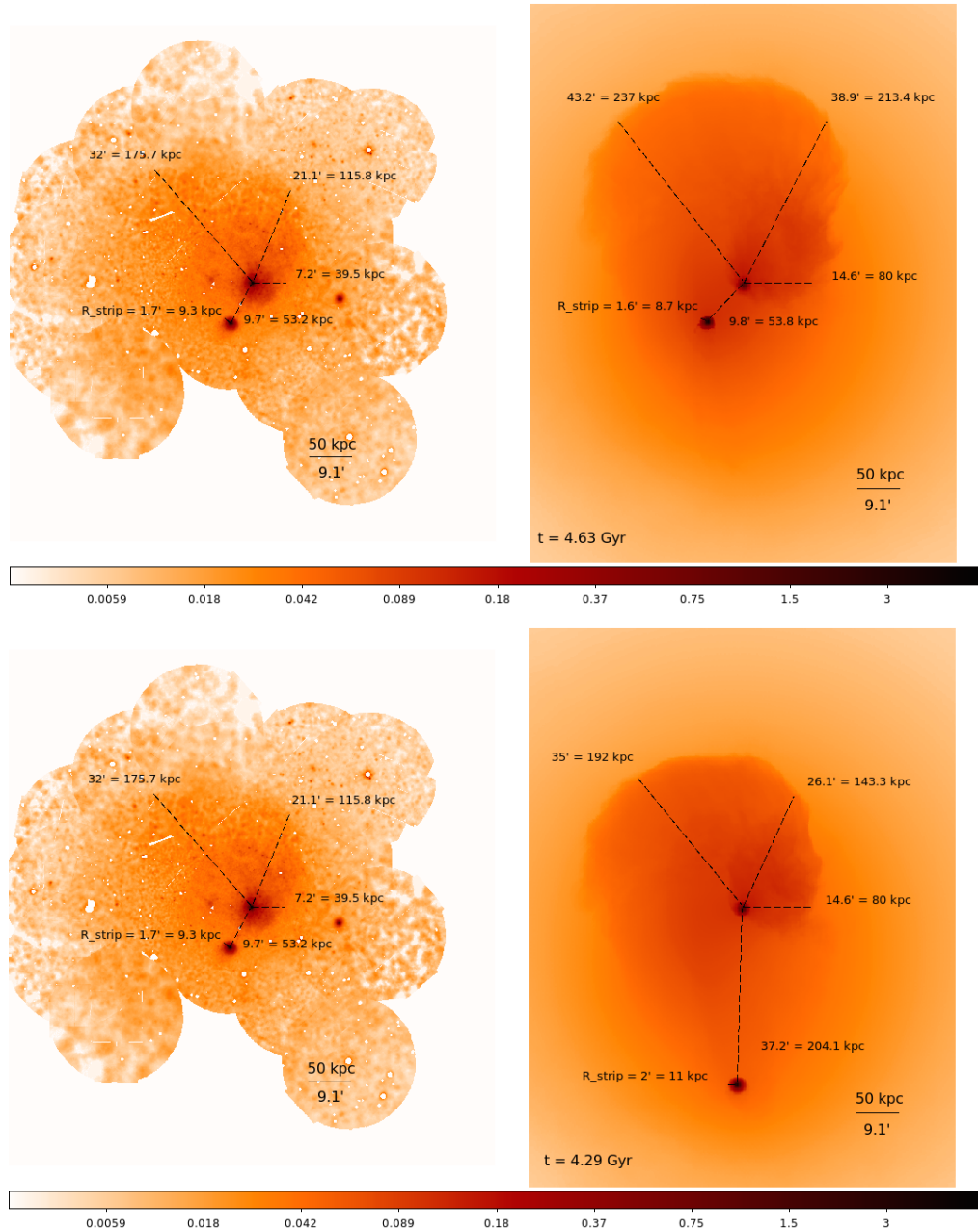


**Fig. 3.12:** Comparing simulation to observation. Top: An XMM image of Fornax in the 0.5 - 2.0 keV energy band alongside a mock X-ray image of the V2 simulation. This simulation timestep is chosen to provide the best match in projected distance between NGC 1404 and the Fornax centre. Our simulation reproduces the prominent cold front to the north of the cluster along with a comparable stripping radius for NGC 1404. However, at this moment, the sloshing is slightly too advanced, i.e., the CF radii are somewhat too large. Given the simplicity of the simulation model, this quantitative agreement is good. Bottom: Same as top, but an earlier simulation time to provide a better distance match to the northern sloshing front. This shows that a faster infall velocity is probably required to enable NGC 1404 to reach the best match point so that the distances to the sloshing fronts are a closer match to observation. Images are in units of photons/s/cm<sup>2</sup>/deg<sup>2</sup>. 1' = 5.49 kpc.

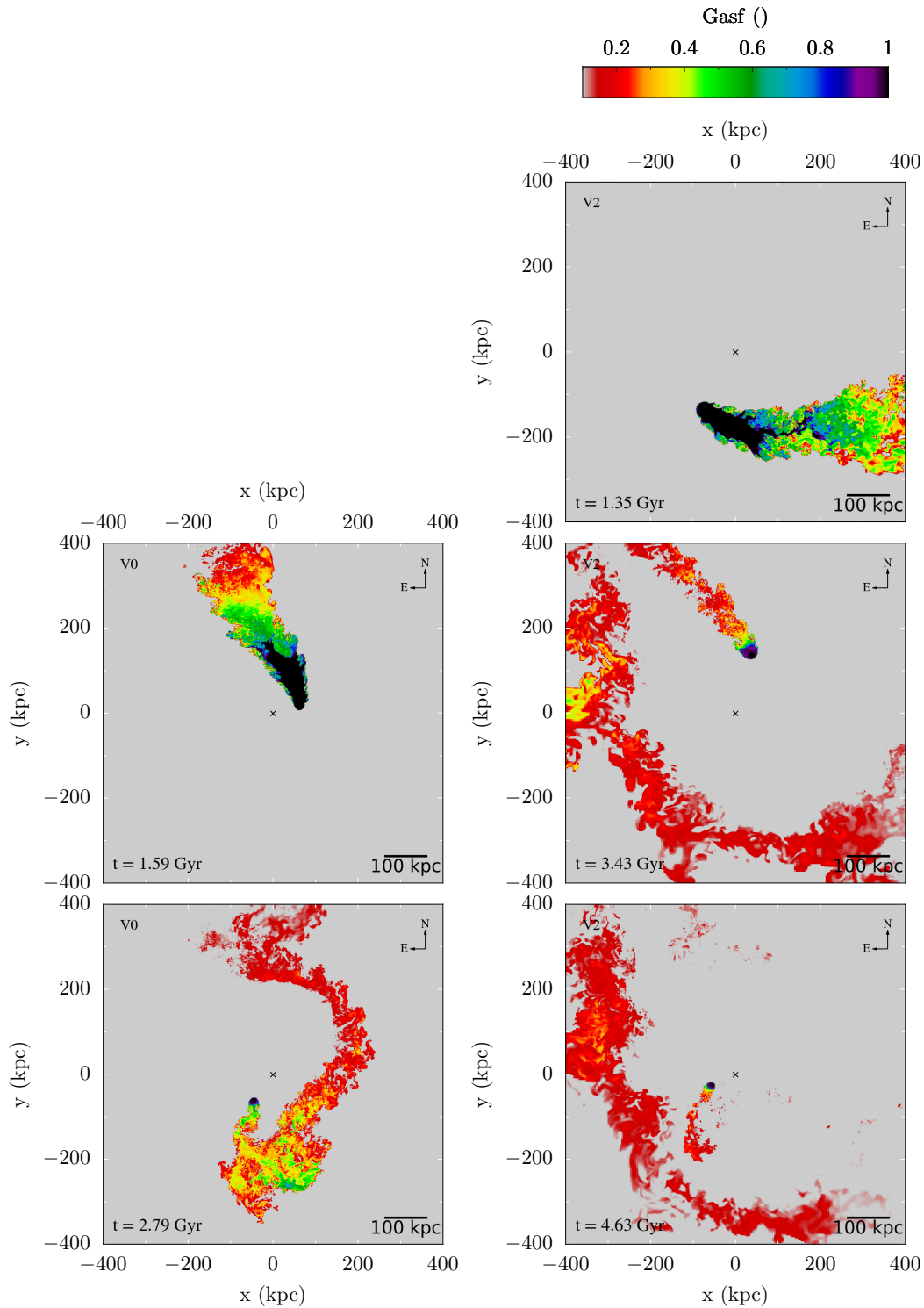


**Fig. 3.13:** Left: Comparison between the galactic gas fraction slices in the orbital plane for the first and second infall for the V0 simulation. Right: Same as right but also the third infall for the V2 simulation. On the first infall into the cluster, the first 100 kpc of the tail is the unmixed remnant tail, just the pushed-back atmosphere of NGC 1404 (compare Figure 4 in Roediger et al., 2015a). It is not until the second or third infall that the atmosphere of NGC 1404 is truly stripped. The cluster centre is marked by "x". gasf = 1.0 means 100% galactic gas.

But, as the galaxy moves out of the cluster reaching the southern apocentre and then begins to fall back towards the centre for the next infall, this shock becomes "detached" and continues to propagate outwards, while the galaxy turns back towards the Fornax centre. This is a significant characteristic of the merger history and could be seen in other merging clusters such as NGC 4839 in the Coma cluster (Neumann et al., 2003). The distance of this detached bow shock in Fornax from the galaxy varies in each of the simulations between 450 - 750 kpc, depending on the angular momentum of NGC 1404. However, in each case the strength of the shock remains approximately the same. We estimate the shock Mach number between 1.3 and 1.5. At this strength, we note that this feature could potentially be observed and would therefore support our scenario of a second or third infall for NGC 1404. Also the fact that the distance of the shock appears to be dependent on the angular momentum gives us an ability to disentangle the history from observation.

### **Wake Region + Turbulence**

This single merger between NGC 1404 and Fornax leaves a trail of destruction throughout the cluster and importantly we can identify regions where NGC 1404 did not stir any turbulence (other galaxies may have). It is important to note that a caveat in our setup is that our simulations begin as an idealized system without initial turbulence in the cluster gas, which is not the most realistic setup to use, but is adequate for the aims of this paper. From Figures 3.8 and 3.11 we can identify that none of the simulations predict enhanced turbulence outside the northern cold front, towards the north and north west. There is robust apocentre turbulence south of the galaxy in all cases which is embedded in a cooler region. Further the most recent wake of NGC 1404 is in the same location where we have an enhanced turbulent region along with a slight enhancement in metallicity. If we believe the slow first infall case is unlikely, then there should be old turbulence driven by an earlier infall of NGC 1404 to the south west of the cluster centre, this is clearly evident in the V1 and V2 simulations. An overriding thought here is that this simulation offers an opportunity to study turbulence in clusters as we have predicted regions where we believe it should or should not have been stirred substantially.

### **Stolen Atmosphere**

A particularly interesting result from our simulations is the observed hot ICM "halo" surrounding the galaxy at the second and third infall stage as shown in Figure 3.9 (right column). It is clear that the surrounding ICM is heated up to temperatures much higher than the original ICM temperature at this cluster-centric radius and this effect is slightly stronger on the second infall compared to the third infall. The hot halo seen here is essentially a "stolen atmosphere" i.e. Fornax ICM drawn into the NGC 1404 potential by gravity. The heating occurs as the cluster gas is compressed by the potential of the galaxy as it traverses the ICM. This enhancement is most noticeable on the second infall as the acceleration due to the potential of the galaxy is much greater due to its smaller gas radius, resulting in the accretion of more Fornax gas. From an observational standpoint, this stolen atmosphere

effect has been seen in the dark subcluster of A520 which is undergoing a cluster merger (H. S. Wang et al., 2016). Furthermore, the ICM compression in the "stolen atmosphere" could lead to an over-estimate of the galaxy velocity from the standard stagnation point method. An example of this effect could possibly be seen with NGC 4472 which is falling into the Virgo cluster, as Kraft et al. (2011) calculate very high velocities for the galaxy. We will study this effect in detail in Fish et al. (in prep).

## 3.7 Discussion

### 3.7.1 Merging History

Attempting to decipher a Gyr-long merging history from a single snapshot in time may seem like an adventurous undertaking, however by simply applying the governing physics - gravity and hydrodynamics, combined with the available constraints on the cluster and galaxy gas distribution as well as the gravitational potentials, leads to a consistent recent merger history of Fornax and infall history of NGC 1404. The merger scenario proposed above explains both the stripping state of NGC 1404 and the overall sloshing features of Fornax. Our tailored merger simulations match the features of Fornax and NGC 1404 qualitatively and also almost quantitatively. We derive slightly different merger ages from the position of NGC 1404 and the positions of the sloshing cold fronts. However, this simply reflects the uncertainty in the exact infall velocity as well as the outer potential of Fornax.

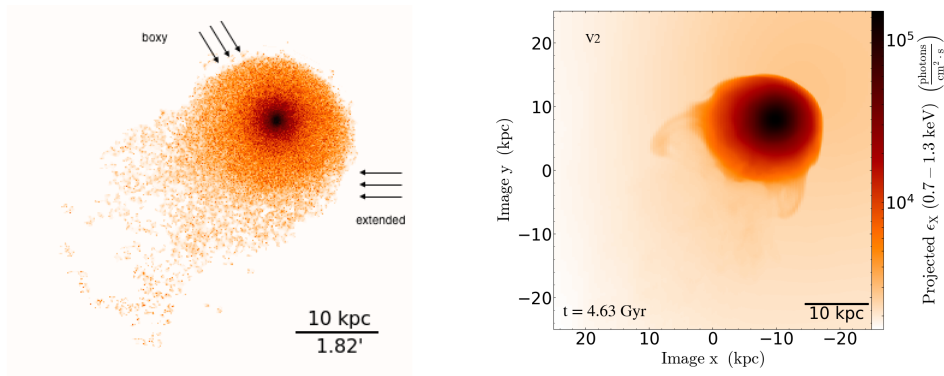


**Fig. 3.14:** Comparing the simulation to observation. Left: Chandra image of NGC 1404 in the 0.7 - 1.3 keV energy band taken from Su et al. (2017b). Right: X-ray photon emissivity projection in the same energy band for the best match of the V2 simulation. The simulation reproduces a comparable stripping radius for NGC 1404 as well as the faint gaseous tail.

We can rule out that NGC 1404 is still on its very first infall, unless, for an unknown reason, it already had a strongly truncated gas atmosphere prior to infall. Any extended atmosphere, as typical for isolated ellipticals, could not be stripped on first infall, but would trail the galaxy as a bright, long, cool tail, easily detectable. Further, NGC 1404 would be supersonic and a bow shock would be evident in data from Chandra and this is not the case. Figure 3.13 illustrates that this first infall tail is indeed unmixed galactic gas.

This result is consistent with the simulations of Roediger et al. (2015a) for M89 in Virgo, which also showed that the near tail of M89 can be readily explained as a remnant tail.

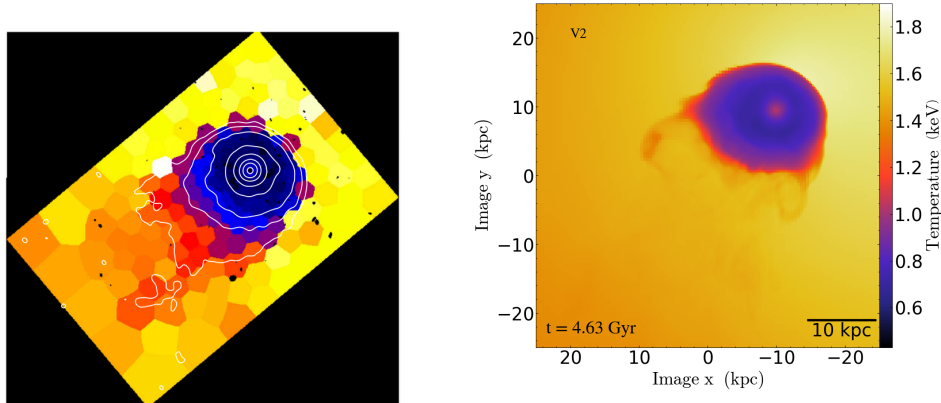


**Fig. 3.15:** Comparing the simulation to observation. Left: Chandra derived temperature map of NGC 1404 taken from Su et al. (2017b). Right: Projected temperature map weighted by X-ray emissivity for the best match of the V2 simulation. The simulation reproduces the cooler inner atmosphere of NGC 1404. A short, cool gas tail is also just about evident in the simulation. Both have units of keV and the same colour scale.

### 3.7.2 Enrichment Processes

Our simulations show that the interstellar medium from a single galaxy is distributed widely through the host cluster (Figure 3.11). Biffi et al. (2018) conducted a study into tracing back the spatial origin of metals in the outskirts of simulated galaxy clusters. They found that in situ enrichment of the ICM in the outskirts is not a major contribution in the metallicity content of present day clusters, but that merging substructures play a more influential role in the enrichment. As demonstrated in our simulations, the NGC 1404 merger with NGC 1399, redistributes metal-rich gas that was originally in the centres of NGC 1399 and NGC 1404. Gas from NGC 1404 is distributed along its tail, although stripping of the outer, metal-poor atmosphere does not lead to enrichment of the Fornax ICM. Metal-rich gas from NGC 1399 is redistributed to  $\sim 200$  kpc by sloshing. Thus, the entire merger history of a cluster is imprinted in the distribution of temperature and metallicity. If the notion that merging substructures play a more influential role in the enrichment of clusters is true, then the ability to access this information with XARM and the Athena XIFU in the years to come could transform our understanding of the formation of clusters.

### 3.7.3 Importance of Dynamical Friction

Originally we experimented with pure hydrodynamic simulations using rigid gravitational potentials. With this method, the cluster and galaxy are not self gravitating, but instead are modelled by the sum of their individual rigid gravitational potentials that evolve on a mutual orbit. Initially, this orbit was a test particle through the more massive cluster i.e. dynamical friction was absent. This method is technically easier to deal with and

reduces the computational load, but has the drawback of lacking the important effects of tidal forces and dynamical friction. Qualitatively, the simulation characteristics remain largely the same between the two physical models in the sense that we see the same gas stripping physics which produce the same features of instabilities and wakes.

However, the lack of dynamical friction acting on the galaxy allows the galaxy to travel further out of the cluster after the first pericentre passage and consequently it lingers for too long around the apocentre, thus resulting in a greatly increased merger timescale. This also has an impact on the strength of the ram pressure the galaxy feels as this is dependent on the square of the velocity, and therefore impacts how much gas is stripped from the galaxy. Comparing the two methods and using the same simulation design as in V0, we found that including dynamical friction reduces the orbiting radius and the merging time scale by 60% and 55%, respectively.

### 3.7.4 NGC 1404 as a Test Case for ICM Plasma Physics

Both merger history and ICM plasma physics could affect ICM properties (tail, wake, cold fronts etc). Our work demonstrates that before using observations to probe ICM plasma physics, we need to understand the merger history. It is worth emphasizing that we have reproduced the short tail, boxy front, and the temperature gradient in the tail. Our simulations are inviscid (assuming numerical viscosity is small). Therefore, the Fornax ICM must have a low viscosity. As we have determined the dynamics of the Fornax ICM, we can confidently use this cluster as a test case for ICM properties such as its effective viscosity and thermal conductivity. Viscosity or aligned magnetic fields could prevent mixing of cold and warmer ICM gas in two locations: along the sloshing cold fronts around the Fornax centre and in the wake of NGC 1404. The near wake would be the best target as it is easiest to observe. Suppressing mixing in the wake should lead to a brighter, cooler tail for NGC 1404 even if its atmosphere is already pre-truncated due to the previous cluster passages. We will investigate this question in a forthcoming paper.

### 3.7.5 Globular Cluster Debate

An interesting point to note is that the second/third infall could offer an explanation to the globular cluster content debate of NGC 1404 and NGC 1399. It has been suggested through measurements of their specific frequency that NGC 1404 has lost some of its globular clusters to NGC 1399 (Forbes et al., 1998, Bekki et al., 2003) due to a possible interaction via tidal stripping. Our proposed scenario requires that NGC 1404 passed by NGC 1399 at least once, where the loss of globular clusters could have happened. Especially if the third infall scenario is the correct case, this gives two opportunities for NGC 1404 and NGC 1399 to interact and exchange globular clusters. It should be noted here that our simulations differ greatly from that in Bekki et al. (2003) in terms of the galaxy orbit. In their simulation, the orbit radius does not extend past 60 kpc compared to reaching between 280-450 kpc in our simulations. Our simulation is more advanced than Bekki et al. (2003) and we have direct access to tidal forces. If the particles are traceable and can

be considered as representative of GCs, we can quantify the tidal stripping process and compare to the observed and kinematical properties of the GCs (future work).

### 3.8 Summary

We used simple hydro+Nbody tailored simulations to model the infall of NGC 1404 into the Fornax Cluster in an attempt to analyse its recent evolutionary history. Our simulations varied the infall velocity between almost zero at  $\sim$  virial radius to an initial approach velocity of Mach 1 at the virial radius. Furthermore, we varied the impact parameter of the merger, independent of these choices, and our results reveal a consistent picture over the last 1.1 - 1.3 Gyrs. Our results are as follows:

- We can firmly exclude that NGC 1404 is on its first infall into the cluster. It is either on a second or (more likely) third infall due to the position of the sloshing fronts in Fornax.
- NGC 1404 came from the E or NE and passed by NGC 1399 about 1.1 - 1.3 Gyrs ago and is now at the point of its next encounter.
- This merging history can explain the sloshing patterns observed in Fornax and the truncated atmosphere and stripping radius of NGC 1404. Furthermore, this scenario also reproduces the observed temperature and abundance asymmetries observed by Murakami et al. (2011).

In our simulations, the exact position of NGC 1404 is not matched and requires fine tuning. The features produced in our simulations are robust that making a more accurate match to the galaxy's position would not change the overall merger scenario sufficiently. Independent of the exact history of the merger, several features remain robust and therefore we can make the following predictions:

- A detached bow shock at a distance between 450-750 kpc south of NGC 1404, a remnant of the galaxy's previous infall, should exist with an estimated Mach number between 1.3 and 1.5.
- The most recent wake of NGC 1404 lies S of the galaxy with enhanced turbulence and a slight enhancement in metallicity.
- If we believe a slow first infall is unlikely, then there should be old turbulence from a previous infall to the SW of NGC 1404.
- None of our simulations predicts enhanced turbulence outside of the cold front N, NW of the cluster centre. That is to say, NGC 1404 did not stir turbulence in this region.

### **3.9 Acknowledgments**

The software used in this work was in part developed by the DOE NNSA-ASC OASCR Flash centre at the University of Chicago Fryxell et al., 2000.

ER acknowledges the support of STFC, through the University of Hull's Consolidated Grant ST/R000840/1 and access to viper, the University of Hull High Performance Computing Facility.

## **Chapter 4**

# **A New Class of X-Ray Tails of Early-Type Galaxies and Subclusters in Galaxy Clusters - Slingshot Tails vs Ram Pressure Stripped Tails**

### **4.1 Prologue**

This chapter has been published in The Astrophysical Journal as Sheardown et al. (2019). However the subsections 4.9.6 and 4.9.7 have been added to this thesis. My work on the NGC 4839 Group in Coma in subsection 4.9.3 raised conversations with Natalia Lyskova, who was working on a paper about the group at the time to which I provided some discussion about the merging history and features observed in the cluster. This led me to be a co-author on her paper Lyskova et al. (2019). In a similar vein, I used my findings on the M49 group in Virgo detailed in subsection 4.9.4 to provide input on the merging history of the group for Su et al. (2019) of which I am a co-author on.

### **4.2 Abstract**

We show that there is a new class of gas tails - slingshot tails - which form as a subhalo (i.e. a subcluster or early-type cluster galaxy) moves away from the cluster centre towards the apocentre of its orbit. These tails can point perpendicular or even opposite to the subhalo direction of motion, not tracing the recent orbital path. Thus, the observed tail direction can be misleading, and we caution against naive conclusions regarding the subhalo's direction of motion based on the tail direction. A head-tail morphology of a galaxy's or subcluster's gaseous atmosphere is usually attributed to ram pressure stripping and the widely applied conclusion is that gas stripped tail traces the most recent orbit. However, during the slingshot tail stage, the subhalo is not being ram pressure stripped (RPS) and the tail is shaped by tidal forces more than just the ram pressure. Thus, applying a classic RPS scenario to a slingshot tail leads not only to an incorrect conclusion regarding the

direction of motion, but also to incorrect conclusions in regard to the subhalo velocity, expected locations of shear flows, instabilities and mixing. We describe the genesis and morphology of slingshot tails using data from binary cluster merger simulations, discuss their observable features and how to distinguish them from classic RPS tails. We identify three examples from the literature that are not RPS tails but slingshot tails and discuss other potential candidates.

### 4.3 Introduction

Galaxy clusters grow through the sequential merging and accretion of galaxies, groups and subclusters (Kravtsov & Borgani 2012a). As one of the latter begins the merging process, it must traverse the intra-cluster medium (ICM) of its host cluster. This motion through the ICM acts as a head wind on a galaxy or subcluster, producing a ram pressure which progressively strips its gaseous atmosphere (Gunn & Gott 1972, Nulsen 1982). This stripped gaseous atmosphere appears as an X-ray bright tail downstream, producing a head-tail structure and has been used to account for many observed objects e.g. in the Virgo cluster (M86: Forman et al. 1979; Randall et al. 2008a, M49: Irwin & Sarazin 1996; Kraft et al. 2011, M89: Machacek et al. 2006; M60: Randall et al. 2004, Wood et al. 2017), NGC 4839 in Coma (Neumann et al. 2003, Lyskova et al. submitted), and NGC 1404 in Fornax (Jones et al. 1997, Machacek et al. 2005; Su et al. 2017b). In recent years, new X-ray tails have been discovered in several clusters at larger cluster-centric radii, e.g., in Hydra A (De Grandi et al. 2016), Abell 2142 (Eckert et al. 2017), and Abell 85 (Ichinohe et al. 2015).

The gas stripping of a subcluster or early-type galaxy in the ICM of a larger, more massive cluster (the primary cluster) is very much the same process. Many simulations have confirmed that ram pressure stripping of the secondary potential is a viable process (Gisler 1976; Takeda et al. 1984; Stevens et al. 1999; Toniazzo & Schindler 2001; Acreman et al. 2003; McCarthy et al. 2008, among others), and produces the expected downstream gas tail. However, gas stripping of the secondary's atmosphere is not an instantaneous process. Using a large mass ratio of  $\sim 30 : 1$  for the primary and secondary, Roediger et al. (2015a) showed that in a gradually strengthening ICM head wind, the secondary can retain a large part of its downstream atmosphere as a 'remnant tail' of unstripped gas (see Figure 3 in Roediger et al. 2015a for a schematic). The retained remnant tail can be larger for smaller mass ratios because the flow relaxation time and primary cluster crossing time become more equal. Thus, the secondary can retain a significant fraction of its atmosphere as it moves through the centre of the primary cluster (see our images in Figure 4.2, rows 1 and 2, and images of simulated mergers in, e.g., Poole et al. 2006; ZuHone 2011).

Remnant tails that survived pericentre passage evolve into slingshot gas tails as the secondary moves outward from the primary's centre and nears the apocentre. The idea of a slingshot gas effect has been described in previous works in the context of cold fronts (Hallman & Markevitch 2004, Markevitch & Vikhlinin 2007) and gas sloshing in cluster cores (Ascasibar & Markevitch 2006). Poole et al. (2006) also provided an insight

into the slingshot effect and described these tails as plumes at apocentre passage, and the subsequent infall of the plume into the primary as infalling filaments. These works describe the dynamics of a slingshot tail, but focus on the formation of cold fronts and plumes rather than the characteristics of the gaseous tail. In this paper, we describe two different forms of slingshot tails, highlighting the need for caution in drawing conclusions regarding both the subhalo's direction of motion based on the tail direction, and the flow patterns surrounding slingshot tails. To this end, we analyze slingshot tails in binary cluster merger simulations, focusing on distinguishing slingshot tails from classic ram pressure stripped tails.

In Section 4.4, we outline the setup of the idealized binary cluster merger simulations we analyze in this work. In Section 4.5 we describe the differences between a ram pressure stripped tail and a slingshot tail. Using the simulations we describe the genesis of slingshot tails and the two different forms in Section 4.6. In Section 4.7 we describe the evolution of the flow patterns surrounding the subhalo during its journey from pericentre to apocentre, detailing how this interplays with the formation of a slingshot tail. In Section 4.8 we discuss how to distinguish between ram pressure stripped tails and slingshot tails, highlighting the key observable signatures of slingshot tails. Finally, applying these insights, we identify a few known X-ray tails as slingshot tails and mark some as possible slingshot tails in Section 4.9. In what follows, for clarity, we term the more massive merger partner (e.g. a cluster), the primary and the less massive merger partner (e.g. subcluster or early-type galaxy), the secondary.

## 4.4 Simulations

For our analysis of slingshot tails, we visually inspected the suites of idealized binary cluster merger simulations by Poole et al. (2006), ZuHone (2011) and Sheardown et al. (2018) as well as setting up some of our own simulations for this paper based on the method detailed in Sheardown et al. (2018). In short, all of these simulations model idealized binary cluster mergers, i.e., they set up two clusters, each in its own hydrostatic equilibrium, assign initial relative velocities to both clusters and let them collide and merge due to their mutual gravity. All simulations use the N-body method to describe the behaviour of the clusters' dark matter. This ensures dynamical friction is modelled correctly and the clusters eventually merge. It also ensures correct treatment of tidal forces. The cluster atmospheres, i.e., the ICM, is treated hydrodynamically, either by smooth particle hydrodynamics (SPH) as used in Poole et al. (2006) or by a grid method as used in Sheardown et al. (2018); ZuHone (2011). All simulations vary the mass ratio and orbital characteristics of the merging clusters. For readers interested in more technical details we summarise those below.

Poole et al. (2006) present an analysis of a suite of idealized binary mergers using smoothed particle hydrodynamics (SPH) run with GASOLINE (Wadsley et al., 2003). Their simulations include the effects of radiative cooling, star formation and feedback from supernovae but neglect feedback from active galactic nuclei (AGN). The simulated

clusters are idealized X-ray clusters initialised to resemble relaxed cool core clusters. The gas and dark matter properties of the clusters follow the prescription by Babul et al. (2002) and McCarthy et al. (2004). They analyse three different cluster merger setups with mass ratios of 1:1, 1:3 and 1:10. Within each of these three setups, they run a further three sub setups which vary the initial kinematics of the secondary subhalo in concordance with the lower half of the Vitvitska et al. (2002) distribution. Vitvitska et al. (2002) showed that the average infall velocity for mergers at the virial radius is distributed normally with an average infall velocity of  $v_{in}=1.1v_c$ , where  $V_c$  is the circular velocity of the secondary at the virial radius of the primary cluster. Specifically, for their three sub setups Poole et al. (2006) used values of  $v_t/V_c = 0, 0.15$  and  $0.4$ , where  $v_t$  and  $V_c$  are the transverse and circular velocity of the secondary respectively. For the primary cluster in their simulations, the mass is set to  $10^{15}M_{\odot}$ .

The simulations by ZuHone (2011) present an idealised suite of high resolution adiabatic binary cluster mergers run using FLASH, a grid based, modular hydrodynamics and N-body astrophysical code (Fryxell et al. 2000). The main difference between grid based and SPH codes as used by Poole et al. (2006) is their ability to resolve and handle fluid instabilities and mixing processes. While grid codes are able to do this, basic SPH methods provide poor results (Agertz et al., 2007). Furthermore, the two methods also differ in their ability to model turbulence, see Agertz et al. (2007); Dolag et al. (2005). The mixing that will occur in the ICM due to mergers is significantly influenced by turbulence and the presence of magnetic fields. In this regard, ZuHone (2011) choose the simplest model for the ICM - an unmagnetized and inviscid gas. The N-body component of the code uses particles which simulate the behaviour of dark matter, i.e. collisionless, self gravitating particles. Including this along with the gravity associated to the gas and the gravity between both elements provides an accurate representation of tidal forces and dynamical friction during the mergers. This importantly influences the orbit of the merging subhaloes and thus the merger timescales. With FLASH, ZuHone (2011) employs the use of adaptive mesh refinement (AMR). AMR allows the user to prioritise areas of particular interest for high resolution whilst not having to use the same resolution for the whole grid. In these simulations, the authors were interested in capturing ICM shocks and cold fronts along with the inner cores of the clusters, thus high resolution is placed in these regions. Their choice of cluster initial conditions is based on cosmological simulations and observations, with the clusters initialised to be consistent with observed relaxed clusters and cluster scaling relations. More specifically, choosing clusters that lie along the  $M_{500}-T_X$  relation of Vikhlinin et al. (2009a). In a similar fashion to Poole et al. (2006), the author presents a set of three different cluster merger setups with mass ratios of 1:1, 1:3 and 1:10. Again like Poole et al. (2006), the three merger setups each have three sub setups which are initialised with different impact parameters, but this time such that the relative tangential velocities are consistent with the Vitvitska et al. (2002) distribution. The mass of the primary cluster in this suite of simulations is set to  $6 \times 10^{14} M_{\odot}$ .

Sheardown et al. (2018) work presents three tailored simulations of the infall of the elliptical galaxy NGC 1404 into the Fornax Cluster. As with ZuHone (2011), their

simulations were run using FLASH, using a similar simulation design. Their simulations did not include the effects of radiative cooling or heating by AGN. The inclusion of both these features would only affect the properties of the gas in the very central regions of the cluster and the galaxy, and as the authors report, their results did not rely on the central gas cores. Each simulation differed by the initial kinematics of NGC 1404, i.e., the secondary. One simulation starts with NGC 1404 having an almost zero infall velocity, with just a small tangential component to ensure that the merger is not a head on collision (as this was ruled out by observation). For the other two simulations the initial velocity is set to  $v_{in}=1.1v_c$ , the average infall velocity at the virial radius in accordance with Vitvitska et al. (2002). They then differ by the initial tangential velocity component which is set in agreement with Vitvitska et al. (2002). The mass of the Fornax Cluster is set at  $6 \times 10^{13} M_{\odot}$  and for NGC 1404,  $0.45 \times 10^{13} M_{\odot}$ , making it  $\sim 1:10$  merger.

The 1:3 merger shown in Figures 4.2, 4.3 and 4.5 we ran for the purposes of this paper. The primary and secondary are modelled such that they follow the setup procedure in ZuHone (2011) but use a Hernquist profile for the total mass distribution. The simulation design follows Sheardown et al. (2018). The mass of the primary is set to  $6 \times 10^{14} M_{\odot}$  (this is to match the mass used for the primary in the setup of ZuHone 2011) and the initial velocity of the secondary follows the Vitvitska et al. (2002) condition,  $v_{in}=1.1v_c$  using a tangential velocity of  $v_{\perp}=0.71v_c$ . The 1:1 merger shown in Figure 4.7 we ran to provide a visual match to the observed image of NGC 7618 and UGC 12491. This is the same simulation as described in Sheardown et al. (2018), using the setup for the cluster which has a mass of  $6 \times 10^{13} M_{\odot}$  and using an initial tangential velocity component of  $v_{\perp}=0.71v_c$ .

## 4.5 Ram Pressure Stripped Tail vs Slingshot Tail

To begin with, it is important that we affirm the difference between a ram pressure stripped tail and a slingshot tail. A ram pressure tail is formed due to the motion of the secondary against the ICM of the primary, where the ram pressure is equal to  $P_{ram} \approx \rho_{ICM} v_{sec}^2$ , where  $v_{sec}$  is the velocity of the secondary with respect to the ICM of the primary. During the infall phase, the increasing ram pressure progressively strips the gaseous atmosphere of the secondary into a downstream tail which points directly opposite to the direction of motion, producing an orderly head-tail structure, as demonstrated in e.g. Acreman et al. (2003) and Roediger et al. (2015a). The part of the gas tail closest to the secondary is a remnant tail, i.e., the still unstripped, bound downstream atmosphere of the secondary that is shielded from the upstream ICM wind, as shown in Figure 4.2, row 1. In the frame of the secondary, the flow of the primary's ICM around the secondary closely follows the classic flow around a blunt body, including an upstream stagnation point, strong shear flow along the sides of the secondary and a downstream deadwater region as the start of a long wake.

The dynamics change when the secondary has passed the pericentre and moves toward the next apocentre of its orbit. Now the ram pressure on the secondary's atmosphere rapidly decreases due to its decreasing velocity and the decrease in ICM density. As the

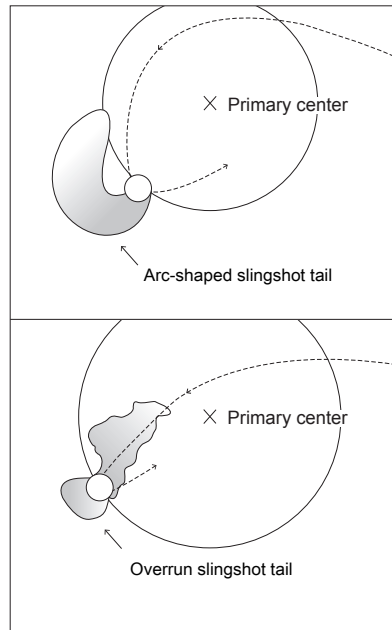


**Fig. 4.1:** A cartoon image showing a clear distinction between the two slingshot tail forms. The primary centre is marked with a cross and the small white circle represents the secondary at apocentre. The dashed line represents the approximate orbit of the secondary. In the arc-shape slingshot form, a prominent arc-shaped tail is produced when the secondary reaches apocentre. For the overrun slingshot form, the tail slingshots directly over the secondary producing an irregular shaped atmosphere followed by a conical shape tail behind it.

secondary slows and eventually turns around, the still bound gas from the ram pressure tail falls back toward the secondary's centre due to the secondary's gravity and overshoots it in a slingshot effect, resulting in a slingshot tail that can point sideways or even opposite to the direction of motion of the secondary, contrasting with the orderly head-tail structure of a ram pressure stripped tail. Additionally, during the formation of the slingshot tail, the ICM flow around the secondary does not follow the flow around a blunt body any more but becomes highly irregular, as detailed further in Section 4.7. Along with this gas dynamics effect, tidal decompression of the secondary after pericentre passage plays a role too in the shaping of the tail, similar to the long tidal tails created in pure N-body mergers. Adiabatic expansion makes the tail cooler too as it is sling-shotted into the lower pressure ICM environment. In short, around the apocentre of the orbit, the secondary is not being ram pressure stripped and the tail has been shaped by tidal forces more than just the ram pressure. Therefore a tail observed in the slingshot state should not be identified as a gas stripping tail as this scenario does not accurately describe the physics of the situation. The application of the classic ram pressure stripping scenario to a slingshot tail will lead to incorrect conclusions in regard to the subhalo velocity, expected locations of shear flows, instabilities and mixing (detailed in Section 4.7). For example, as the slingshot tail can point sideways or ahead of the subhalo, it does not trace the recent orbit path like an orderly ram pressure stripped tail would, and is therefore misleading when drawing naive conclusions regarding the direction of the subhalo based on the tail direction.

As mentioned, Hallman & Markevitch (2004) described a ram pressure slingshot mechanism to explain the cold front which appears ahead of the northern subcluster in the merging cluster A168. This idea has further been used to describe merger features in Abell 2744 also (Merten et al. 2011; Owers et al. 2011b). The formation of these cold fronts found ahead of the subcluster were predicted in hydrodynamical simulations by Mathis et al. (2005) and by Ascasibar & Markevitch (2006) in the context of gas sloshing. These slingshot cold fronts are the contact discontinuity between the slingshot tail and the primary's ICM.

## 4.6 Slingshot Tails

We find that as long as the secondary can retain some remnant tail through pericentre passage, it develops a slingshot tail. We further find that slingshot tails can be split into two main distinct forms, each giving characteristically different morphologies dependent on the impact parameter and mass ratio of the merger. We term these forms *arc-shaped slingshot tails* and *overrun slingshot tails*. For both forms, we find that the slingshot tail stage typically lasts between 0.5 - 1.0 Gyr, thus slingshot tails may be fairly common since the secondary spends much more time around apocentre than during pericentre passage, where they are moving faster. Figure 4.1 presents a cartoon image of both cases to provide a clear visual distinction between the two. We note that there are some cases which do not fall cleanly into one of these forms and are somewhere in between, in this paper we only focus on the two extreme cases of the *overrun* or *arc-shaped* form. We find that lower mass ratio mergers tend to result more in the overrun form, however as seen in Figure 11 in ZuHone (2011), a 1:10 mass ratio with large impact parameter results in an arc-shaped slingshot tail, so this is not always the case. In addition to the impact parameter and mass ratio, bulk motions of the ICM in the primary cluster, triggered by the merger also, play a significant role in the evolution of the secondary's slingshot tail. Deriving the exact conditions for one or the other slingshot forms requires a separate, more systematic study. In the following we describe the generation of the two main slingshot forms and discuss their underlying physics. We remind the reader that we are now concerned with the merger phase where the secondary moves from pericentre toward apocentre and starts its next infall.

### 4.6.1 Arc-Shaped Tails

When the impact parameter of the merger is large, the remnant tail of the secondary, that was once pointing downstream (toward the direction of pericentre), is carried out sideways, by angular momentum conservation, to the side of the secondary furthest from the primary cluster centre as it approaches apocentre. This results in a prominent arc-shaped tail that can point sideways to the secondary as shown in Figure 4.2, columns 3 and 4, and in Figures, 5, 8 and 11, snapshot 2.0 Gyr in ZuHone (2011). The archetypal arc-shaped slingshot tails tend to consist largely of still unmixed, cool gas that always belonged to the

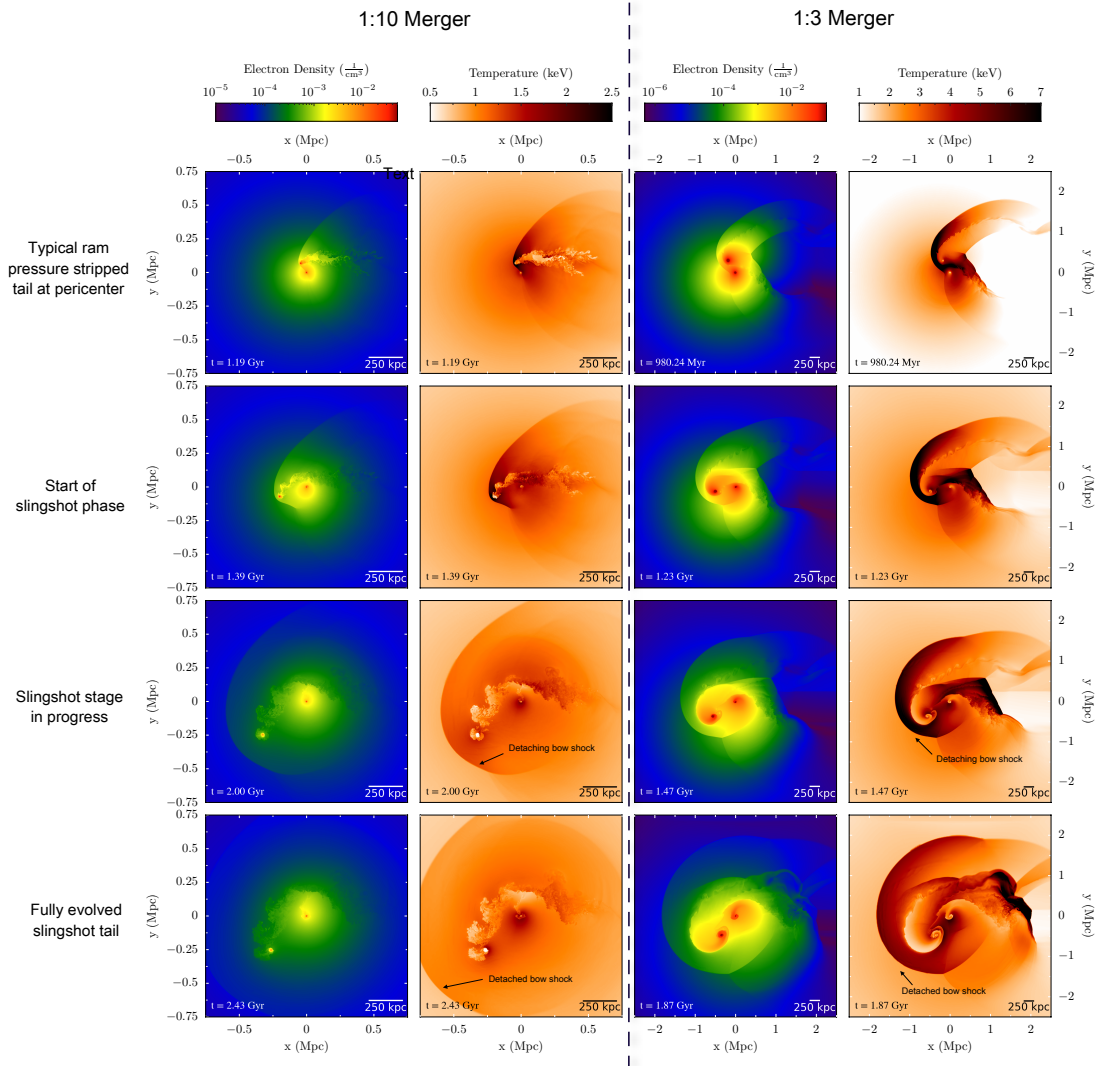


**Fig. 4.2:** Evolution of two different cluster mergers. The first and second column show electron density and temperature slices for a  $\sim 1:10$  merger with a small impact parameter from the VI simulation in Sheardown et al. (2018). The third and fourth column likewise show electron density and temperature slices but for a 1:3 merger using a large impact parameter. The first row shows the secondary at pericentre with a typical ram pressure tail. Note that in the 1:3 merger, the secondary still contains a large amount of unstripped gas. The second row shows the start of the slingshot tail being produced as the secondary slows toward apocentre. In the third row, for the 1:10 merger, the first phase of the overrun slingshot form is established, with the secondary harboring an irregular shaped atmosphere as the remnant tail overruns directly the remnant atmosphere. For the 1:3 merger, the arc-shaped tail becomes a prominent feature. In the fourth row, for the 1:10 merger, the second phase is reached as the remnant tail continues to overrun the remnant atmosphere and fans out along the direction of apocentre away from the secondary. For the 1:3 merger, the arc-shaped tail reaches its full prominence as the secondary turns around and begins to infall again. In the fourth row, we also mark the bow shock that detaches from the slowing down secondary. The detached bow shock will continue moving away from the primary’s centre.

secondary. Due to the absence of internal shear, these tails also tend not to be turbulent. Shear and the resulting Kelvin-Helmholtz instabilities (KHI) appear mainly along the far end or the outer wing of the arc-shaped slingshot (see also Section 4.7). The size of the arc-shape tail is very much dependent on the impact parameter and initial gas contents, as this generally dictates the amount of gas the secondary can carry through pericentre passage. Naturally, the larger the impact parameter, the larger the tail, as the stripping due to ram pressure will not be as strong, hence more gas can be retained. Therefore, the size of the arc-shape tail can potentially be used to infer the impact parameter for the merger. We also find that the arc-shaped slingshot tails can 'swing' all the way around from one side of the secondary as it approaches apocentre, to the other side as it moves through apocentre to the beginning of the next infall. Furthermore, when the masses of the merging systems are similar, we see that the primary develops a slingshot tail that is similar in size to the secondary's, appearing symmetric. In Figure 4.3, column 3, we present a variety of X-ray projections for the arc-shaped slingshot tail form. Most features of the tail do not change depending on the viewing angle. The tail remains homogeneous in brightness and has a sharp edge away from the merger companion. These edges have been called slingshot cold fronts previously. When we see the plane of the merger almost edge-on, the arc-shape slingshot tail may not point sideways, in this scenario the homogeneous brightness and sharp edge of the tail can be used to distinguish from a ram pressure stripped tail.

#### 4.6.2 Overrun Tails

In contrast to arc-shaped slingshot tails, when the impact parameter is small, the remnant tail slingshots directly along the outgoing orbit and, as the secondary reaches apocentre, it is overrun by its own slingshot tail. We term this *overrun slingshot tail*. Its evolution can be split into two distinct phases. As the secondary decelerates due to the gravitational pull of the primary cluster and dynamical friction, the lower orbital angular momentum causes the gaseous tail to overshoot directly over the potential centre of the secondary. This creates the first phase where the secondary appears to harbor a second gas atmosphere which encompasses the secondary's true remnant atmosphere, resulting in an overall 'fuzzy' irregular shape as shown in Figure 4.2, column 1 row 3 and in Figure 4.3, column 1. This secondary atmosphere is turbulent (assuming no other processes suppress turbulence) as the remnant tail continues to overrun the secondary. This feature can also be seen in the simulations of Acreman et al. (2003), specifically in their Figure 2d. In the second phase, the actual slingshot tail appears as a conical shaped tail which progressively fans out along the direction pointing away from the primary cluster centre, as shown in Figure 4.2, column 1 row 4 and Figure 4.3, column 2. The overrun slingshot tail is likely always turbulent as there are more locations with shear flows. In result, the overrun tail is well mixed with the ambient ICM, and appears homogeneous in both density and surface brightness where both lie in between that of the ambient ICM and the remnant core of the secondary. We also find that the fanned out tail in the second phase is cut off on the far side away from the cluster centre, in a similar manner to the arc-shaped slingshot tails. This cut off

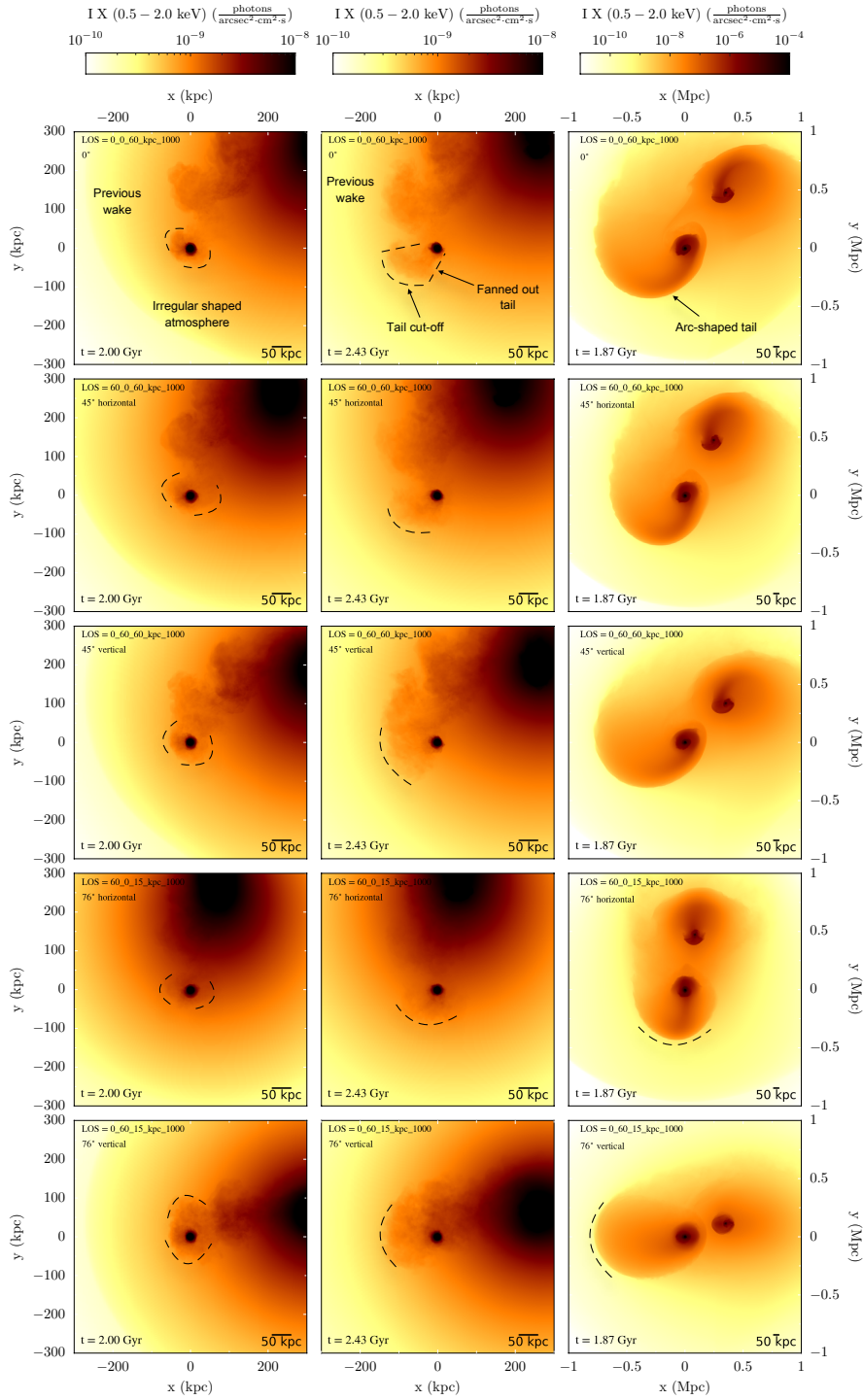


**Fig. 4.3:** X-ray photon intensity field projections calculated in the 0.5–2.0 keV energy band for the different slingshot tail forms as shown in Figure 4.2. The first column shows the overrun slingshot tail in the first phase, where the secondary harbors an irregular shaped atmosphere. The second column shows the overrun slingshot tail in the second phase, where the secondary possesses a fanned out tail. The third column shows the arc-shaped slingshot tail. The top row is a projection perpendicular to the orbital plane. The following images are a selection of LOS rotated vertically or horizontally to the orbital plane by 45° and 76°. Each image is annotated with its corresponding rotation and angle. Crucially, we see that regardless of projection angle, the features of both slingshot forms remain intact. For the arc-shaped form, the tail remains prominent but for certain angles it may not appear as arc-like. To distinguish this case from a ram pressure tail would be the homogeneous brightness of the tail along with its distinct downstream edge.

point marks the maximum radius the tail slingshots to. For this form, the next infall of the secondary occurs almost along the path of its previous wake due to the lower orbital angular momentum. In Figure 4.3, columns 1 and 2, we show X-ray projections for a variety of viewing angles for both phases of the overrun slingshot tail. Regardless of the viewing angle, the characteristic features of the overrun form remain clear.

## 4.7 Flow Patterns of Slingshot Tails

Ram pressure tails or slingshot tails recently attracted interest as locations to study turbulence or its suppression in the ICM (Eckert et al., 2017; Roediger et al., 2015b). To do so, it is important to understand the principal flow conditions in and around such tails. Furthermore, the regular flow patterns around the secondary are a prerequisite to the meaningful application of the stagnation point method to determine the secondary's velocity (Su et al., 2017a; Vikhlinin et al., 2001a). In what follows, we show that this method is not applicable to secondaries that produce slingshot tails due to their complex flow patterns which differ from the classic ram pressure scenario.

The genesis of a slingshot tail can be split into two periods as discussed above and shown in Figures 4.4 and 4.5. True for both slingshot tail forms, right after pericentre passage, the secondary continues to drag a significant amount of its downstream atmosphere along as a remnant tail. As the secondary slows and changes direction approaching apocentre, the remnant tail is carried by its momentum and its attraction to the secondary potential as it falls back toward the remnant atmosphere of the secondary. At this point, there is significant flow within the remnant tail transverse to the secondary's direction of motion, with similar flow patterns regardless of the form of slingshot tail.

The flow patterns in the second period are complex and potentially misleading. The secondary either develops into an *arc-shaped slingshot tail*, (Figure 4.5b), or develops into an *overrun slingshot tail*, (Figure 4.4b), as the tail begins to fall back and wash over the secondary. For the latter, the remnant tail washes over the secondary causing a 'false' head-tail shape to form (i.e. a head-tail that does not represent the motion through the ICM); this is the process which generates the conical tail of the *overrun slingshot tail*. Additionally in this process, the overrunning tail causes some stripping of the remnant atmosphere of the secondary, adding to the 'false' head-tail shape. An example of this is shown in Figure 4.4b, where the sharpest edge in the X-ray plot may naively suggest a roughly north-easterly direction of motion, although the secondary moves to the south. Additionally, this process disrupts the internal structure of the secondary, as its atmosphere sloshes around its potential. Also note the complex flow patterns in the surrounding ICM which do not resemble a flow around a blunt body.

As mentioned, the beginning of the flow for both slingshot cases is similar, but there are some key differences. One such difference can be seen when comparing rows 2 and 3 in Figures 4.4 and 4.5. In the *arc-shaped* form, the secondary's tail holds significantly more of its own gas through pericentre passage, with an area of laminar flow following the secondary within the tail. This laminar flow appears to translate to the smooth arc-shaped

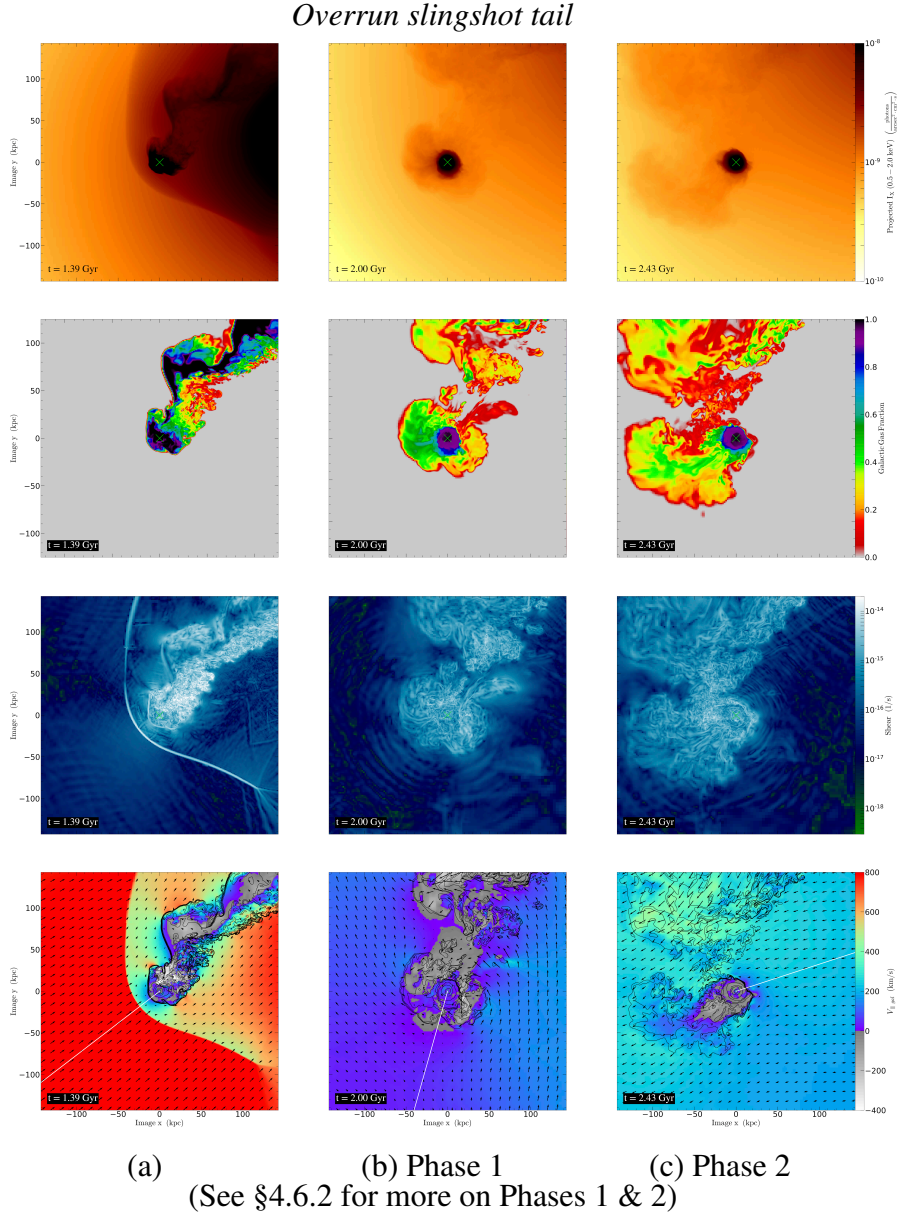


**Fig. 4.4:** The aim of this figure is to show the flow patterns in and around secondaries with *overrun slingshot tails*. The images are made from the V1 simulation in Sheardown et al. (2018), the same as the two left-hand columns of Figure 4.2. Each column shows an X-ray photon intensity projection in the orbital plane; a gas fraction slice of the secondary, showing the extent that the tail has been stripped and mixed with the ICM; a slice of the shear rate, showing the locations of strong shear flows; and finally a colourmap of the flow field, overlaid with velocity vectors. For the latter, the colourmap codes the velocity component  $V_{\parallel gal}$  parallel to the secondary's direction of motion, in the rest frame of the secondary. The white line from the secondary centre shows the direction of motion of the secondary with respect to the grid and the contours show the gas density of the secondary's atmosphere as it is stripped. The rainbow part of the colourmap shows gas flow toward the secondary's downstream direction, while the gray scale part shows the flow toward the upstream direction.

The images in Column (a) show the unstable flow beginning to develop. (b) shows the secondary near apocentre as the *overrun slingshot tail* is in the first phase with an irregular shaped atmosphere. (c) shows the flow shortly before it becomes classed by this paper as a stable infall again, where now we have phase two of the *overrun slingshot tail* as a conical tail develops behind the secondary. Both (a) and (c) can both be considered fringe cases in terms of the flow stability. This figure demonstrates that during the creation of a slingshot tail, the secondary undergoes a significant asymmetrical flow relative to its direction of motion - even in the case of (c), which may be considered steady based on X-ray observations.

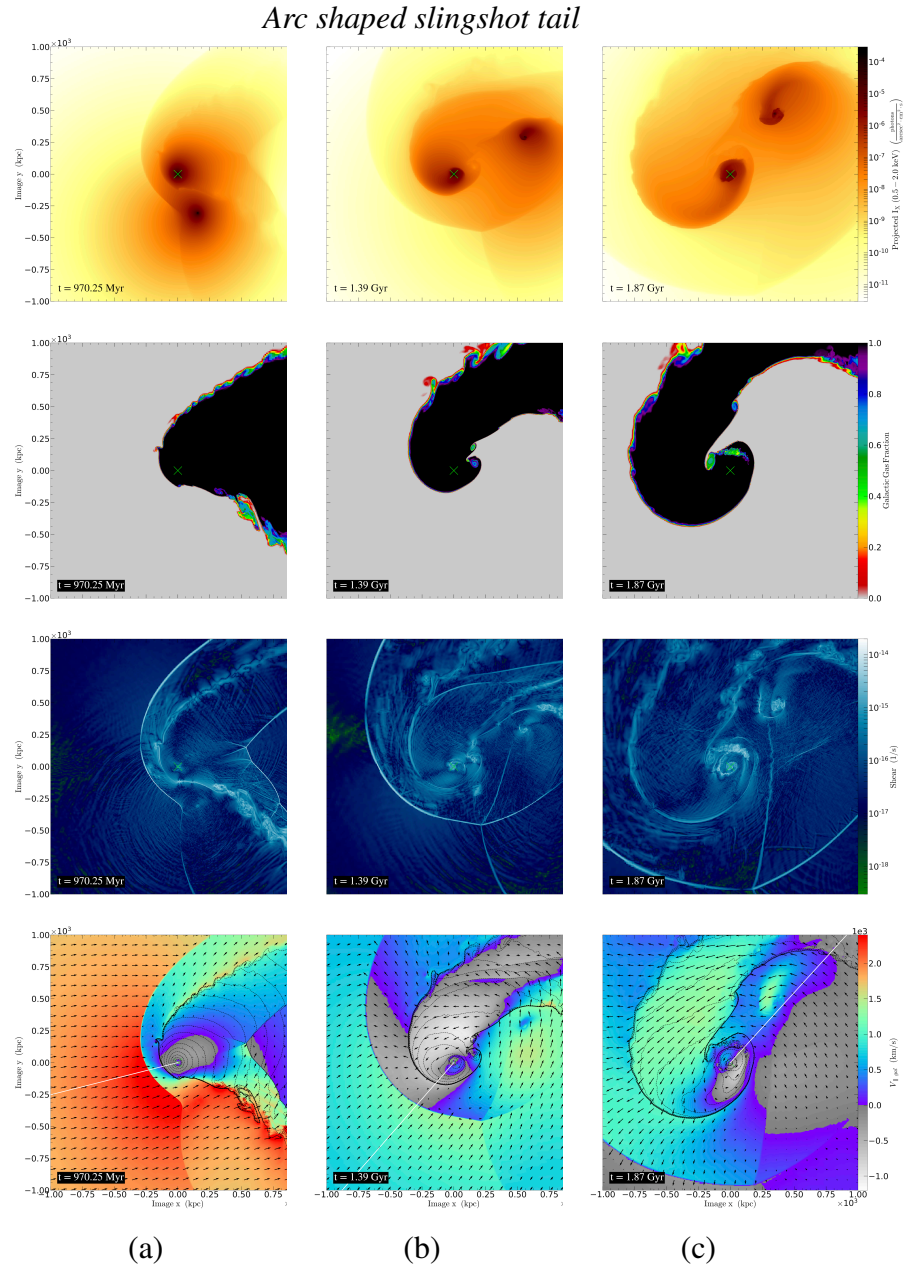


**Fig. 4.5:** This figure presents the *arc-shaped slingshot tail* version of Figure 4.4. These images are taken from the 3:1 merger simulation shown in the two right-hand columns of Figure 4.2.

The images in Column (a) show the unstable flow beginning to develop, with a particularly asymmetric flow beyond the shock due to the location of the primary. (b) shows the secondary near apocentre, midway through the development of the slingshot tail; the secondary's tail starts to create an arc, as the outer edge of the tail is pushed out beyond the secondary. (c) shows the flow shortly before it becomes classed by this paper as a stable infall again.

edge in Figure 4.5b,c. Conversely, the *overrun* form shows a much more turbulent/broken tail (see Figure 4.2, rows 1 and 2 for a wider view of the simulation), perhaps better described as a wake at later stages, as the secondary gas is now well mixed with ICM. This is made obvious when comparing the shear rate in both slingshot forms. For the *arc-shaped* form, we see that there is significantly less shear in comparison to the *overrun* form as the tail gas co-moves with the ICM and the turbulent regions of the tail at the outer edge are mostly shed as the secondary reaches apocentre. We note that an *arc-shaped slingshot tail* can be more turbulent if the secondary does not manage to retain such a large amount of its own atmosphere past its pericentre passage, for example Figure 4.6.

As the secondary moves away from apocentre, starting its next infall into the primary, the flow patterns return to a quasi-steady flow state of the ram pressure stripping scenario (Figures 4.4c and 4.5c), similar to the blunt body case. Figure 4.4c shows the *overrun tail* during the second phase as the flow begins to return to the ram pressure stripping scenario. The flow here is fairly stable, but retains some asymmetry from the internal disruption/sloshing of the secondary and the bulk motions of the ICM; this image is chosen to illustrate the difficulty in judging whether the flow is steady.

It is worth noting that the stagnation point method (Su et al., 2017a; Vikhlinin et al., 2001a) to determine a secondary's velocity from stagnation point pressure relies on the analogy of a (quasi-)stable flow past a blunt body. The merger stage prior and near pericentre passage would qualify for this, with columns (a) in Figures 4.4 and 4.5 showing borderline cases. However, around apocentre the flow patterns in the ICM around the secondary are quite different and the stagnation point method is not applicable. Only when the regular flow patterns have been re-established during the next infall can the stagnation point method be applied again. Fish et al. (in preparation) discuss this point and further limitations of the stagnation point method.

## 4.8 Observable Features of Slingshot Tails

In this section we highlight the key observable signatures of slingshot tails, explaining how to use them to distinguish between a slingshot and ram pressure stripped tail. We remind the reader that we are concerned with the slingshot tail stage which occurs around apocentre of the orbit, i.e., we are only dealing with gas tails of secondaries that are at a large distance from the primary's cluster centre, a prerequisite for identifying a slingshot tail. It is secondaries located at large distances from the primary's centre that need careful consideration.

The main signature to distinguish between a ram pressure stripped tail and a slingshot tail is the tail orientation and morphology. As mentioned, a classic ram pressure stripped tail has an orderly head-tail structure, where the tail generally fades continuously away from the remnant atmosphere into the wake of mixed gas (see Roediger et al. 2015a). However, slingshot tails can point sideways or ahead relative to the direction of motion and do not fade continuously away, but rather have a sharp cut off, highlighted by the dashed line in Figure 4.3 showing a clear edge between the tail and the ambient ICM. If

a gas tail of a secondary which is located at a large distance from the primary's centre points transversely to the radius between the secondary and the cluster centre, instead of radially away, a slingshot tail should be suspected. Subclusters rarely move on circular orbits with large radii which would be required to produce a ram pressure tangential to the cluster centre. Such transverse tails arise naturally in the slingshot phase. Both slingshot tail forms typically have a density, temperature and brightness which is in between that of the ambient ICM and the remnant atmosphere of the secondary.

Another observational signature of slingshot tails is that in both slingshot tail forms, the secondary's atmosphere can show the presence of shells due to internal sloshing and re-accretion of gas. These shells are not apparent in a simple, ram pressure stripped secondary. Additionally, in the slingshot tail phase it can be difficult to identify a clear upstream edge (as described in Section 4.7). This is especially applicable to the overrun slingshot tail as described in Section 4.6.2, the turbulent nature of the tail creates a phase where the secondary appears to have an irregular shaped atmosphere.

If present, the position of a bow shock can also help to distinguish between a ram pressure stripped or slingshot tail. In the ram pressure tail case, a bow shock leads just ahead of the secondary as it moves through the ICM of the primary cluster, shock heating the gas. For a slingshot gas tail, this is not the case. As the secondary slows toward apocentre, the previously leading bow shock continues to propagate outwards as the secondary turns around, hence the shock appears behind the secondary on the tail side, not leading it, and can be found at large distances behind the secondary (the shock can be located up to 1 Mpc behind the secondary). Such a detached bow shock is visually marked in Figure 4.2 and in the simulations of Sheardown et al. (2018).

If the secondary has a slingshot tail, the primary's cluster centre should show signs of the earlier core passage of the secondary. For large mass ratios, this could be the onset of sloshing and for low mass ratios, the primary could form a slingshot tail of its own. After the first passage, the cluster core will show elongation in the direction toward the secondary. If the pericentre passage was close enough, this may have even destroyed the central core. If the secondary has completed a second passage of the cluster centre, the sloshing in the core will have evolved further, producing a prominent cold front on the opposite side of the cluster to the secondary. Further, the wake of the secondary could appear as a characteristic brightness edge in the primary, marking roughly the secondary's orbit (see Sheardown et al. (2018)). However, a caveat to using the dynamical state of the cluster to help identify a slingshot tail is that it would only work with a simple cluster setup, i.e. an ideal case of a binary merger or few possible merger candidates. For a system which has many merger partners it would be too difficult to attribute features of the cluster core to one single candidate.

## 4.9 Classifying Some Known X-ray Tails

In this section, we argue that some examples of gas tails reported in previous papers are likely slingshot tails instead of classic ram pressure stripped tails. We note that at this

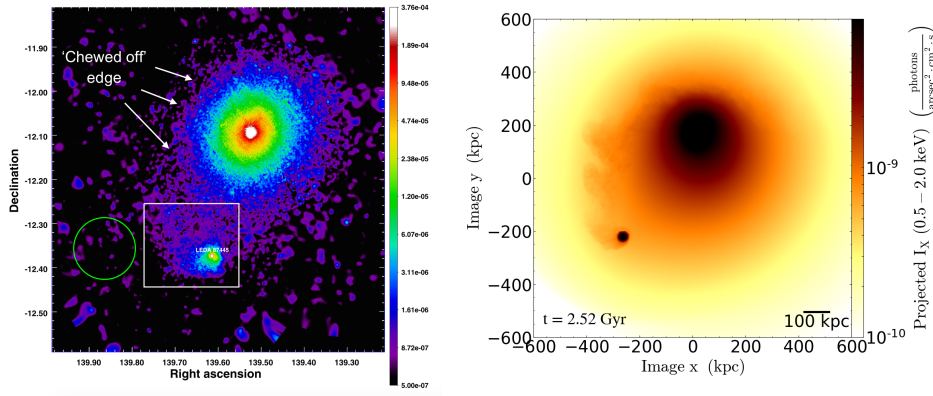


**Fig. 4.6:** Left: Image taken from De Grandi et al. (2016). An adaptively-smoothed, vignetting-corrected XMM/EPIC mosaic image of the Hydra A Cluster in the 0.7-1.2 keV band. Right: X-ray photon intensity projection made from the V2 simulation in Sheardown et al. (2018). This simulation image is chosen to provide a visual match to the observational features of the tail in LEDA 87445 as the secondary reaches apocentre. The cluster in the simulation also shows elongation of the primary towards the secondary, much like the image of the Hydra A Cluster.

stage, our arguments and comparisons are purely qualitative. A full confirmation of our suggestions may require tailored simulations to reproduce the observations quantitatively.

#### 4.9.1 LEDA 87745 in Hydra A

Located 1.1 Mpc south of the Hydra A Cluster centre, LEDA 87445 is the dominant member of a galaxy group with a gas tail about 760 kpc long (De Grandi et al. 2016) that demonstrates several features which resemble a slingshot tail in action. Firstly, the galaxy group is at a large distance from the cluster centre, and from Figure 4.6, we see the tail direction is transverse to the radius joining LEDA 87445 to the cluster centre. If this tail direction is taken to indicate the direction of motion, the transverse orbit would be hard to explain. Further evidence for a slingshot tail is the dynamical state of the cluster. An offset central AGN shock (Nulsen et al. 2005 and Simionescu et al. 2009) toward the north of the cluster indicates large scale bulk motions and an east-west asymmetry is apparent showing a 'chewed off' edge in the east as indicated in Figure 4.6. The observed asymmetry implies LEDA 87745 passed by the cluster centre from the north-east with a large impact parameter which created the 'chewed off' edge, and as the galaxy group moved out to the apocentre, it produced the observed slingshot tail. In Figure 4.6, we provide a visual simulation match to LEDA 87745 using the V2 simulation in Sheardown et al. (2018). The secondary in this simulation has a turbulent arc-shaped tail because due to its low mass, it could not retain a very large remnant tail past pericentre passage. As mentioned in Section 4.6.1, this could be an example of an intermediate case which lies inbetween the arc-shape and overrun slingshot forms. If the slingshot tail scenario is correct for this case, there should be a detached bow shock located south LEDA 87445 (in the direction away from the cluster centre) at a distance of  $> 750$  kpc.

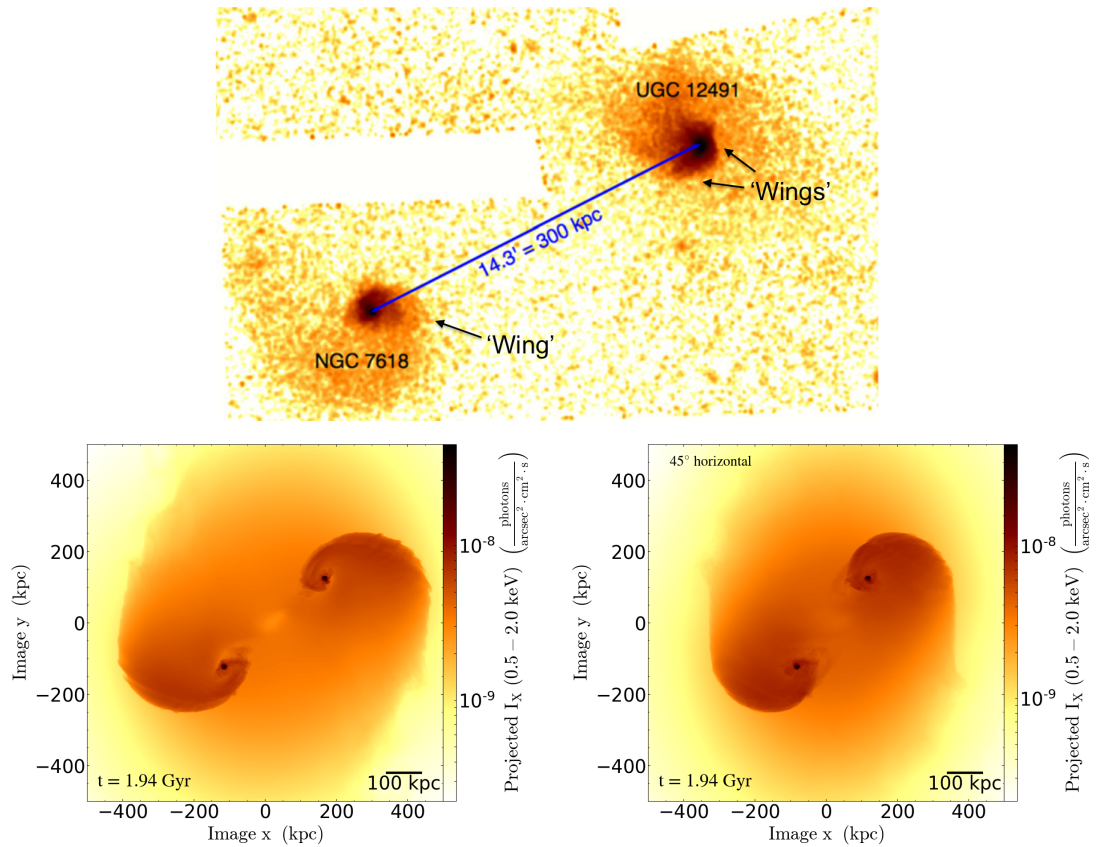


**Fig. 4.7:** Top: Image taken from Roediger et al. (2012). A co-added, background-subtracted, and exposure-corrected 30 ks Chandra/ACIS-S image of the NGC 7618 and UGC 12491 galaxy groups in the 0.5-2.0 keV band, smoothed with a 4 arcsec Gaussian kernel. Bottom left: A simulated X-ray photon intensity projection for a 1:1 merger with a pericentre distance of 265 kpc between two clusters with a mass of  $6 \times 10^{13} M_\odot$  as setup in Sheardown et al. (2018). Bottom right: Likewise but the simulation image is rotated by  $45^\circ$ . The simulation images shows the two clusters at the first apocentre stage of their merger and reveals prominent arc-shaped slingshot tails in both, providing a visual match to the observed image. Rotating the merger plane by an angle of  $45^\circ$  accounts for the more highly wound arc-shaped tails observed here. Given that the merger partners are at apocentre, no relative velocity between the two is expected, as observed in NGC7618 and UGC12491.

### 4.9.2 NGC 7618 and UGC 12491

Shown in Figure 4.7, NGC 7618 and UGC 12491 are at the centres of merging galaxy groups of approximately equal mass. Using Chandra observations, Roediger et al. (2012) found that the pair both displayed arc-like sloshing cold fronts and  $\sim 100$  kpc long spiral tails. The authors also suggest that since the cores of both groups are not destroyed, that the encounter between them was not a close one. From our analysis, we find that arc-shaped slingshot tails are produced only when the impact parameter is large, as is likely the case here. With these ideas in mind, we ran a 1:1 merger simulation with a large impact parameter (a pericentre distance of 265 kpc) using the cluster setup as in Sheardown et al. (2018). This cluster setup was chosen simply for its roughly similar mass to NGC 7618 and UGC 12491.

An X-ray projected image from the simulation is shown in Figure 4.7 and we can see that it provides an excellent match to the observed features as it clearly replicates the arc-shaped tails and position of the groups. Therefore, we propose that these are not simple sloshing cold fronts, but rather arc-shaped slingshot tails and both groups are at apocentre of their merging orbit. Based on their original idea of sloshing cold fronts, Roediger et al. (2012) therefore suggested that there should be Kelvin-Helmholtz instabilities (KHI) along the spiral tails of both groups. However, as shown in our simulation, with the arc-shaped slingshot tail form, there are only a few regions with strong shear, and KHIs form only slowly near the far end of the arced tails. Therefore, using a different pointing of Chandra to look further down the spiral tail could perhaps reveal the presence of KHI in this system. As shear flows along the apparent cold fronts or slingshot tails may appear in different locations, it is important to distinguish between both scenarios for studying the presence of KHI or their suppression by ICM microphysics, such as viscosity or draped magnetic fields.

### 4.9.3 NGC 4839 Group in Coma

In the outskirts of the Coma Cluster lies the galaxy group NGC 4839, approximately 1 Mpc in projection south-west from the cluster centre (Neumann et al. 2003, Lyskova et al. 2019). As shown in the left image of Figure 4.8, the group is merging with the cluster as X-ray images reveal a truncated atmosphere along with a  $\sim 600$  kpc elongated tail of cool gas which is homogeneous in brightness and temperature and fanned out in the direction away from the group (Sasaki et al., 2016).

Thus we have several features for this case which resemble an overrun slingshot tail instead of a ram pressure stripped tail which was previously thought. Furthermore, the far edge of this fanned out tail marks the maximum radius the tail has slingshotted to. The truncated atmosphere would suggest the group has fallen through the cluster once already. Additionally, a radio relic was discovered near the virial radius of the Coma cluster, 2 Mpc in projection from the cluster centre, far beyond NGC 4839, but in the same south-west direction as the group (Akamatsu et al., 2013). This radio relic could potentially be the detached bow shock of the galaxy group. Therefore, we propose that the group passed

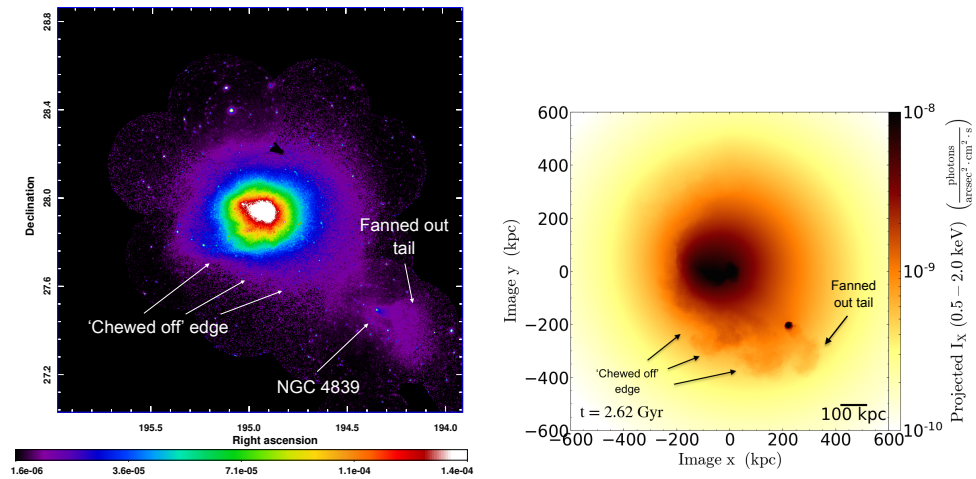


**Fig. 4.8:** Left: Image taken from Lyskova et al. (2019). An XMM-Newton image of the Coma Cluster and the NGC 4839 group in the 0.5-2.5 keV energy. Right: X-ray photon intensity projection from the V1 simulation in Sheardown et al. (2018). The simulated image shows the overrun slingshot tail in action and we see that the tail geometry matches the observed tail of NGC 4839. Physical scales are different as this simulation is not tailored to the Coma Cluster. See Lyskova et al. (2019) for the tailored simulation of Coma and the NGC 4839 group.

by the cluster centre from the east with a small impact parameter, went into the overrun slingshot tail form and is now on its next infall. In Figure 4.8, we show a simulated X-ray projection from the V1 simulation in Sheardown et al. (2018) in this slingshot stage to provide a visual match to NGC 4839. The idea that the tail of NGC 4839 is not due to ram pressure, but due to the group falling through the cluster once has also been confirmed independently by Lyskova et al. (2019).

#### 4.9.4 NGC 4472/M49 and NGC 4649/M60 in Virgo

For these two early-type galaxies it is unclear whether or not they do indeed have slingshot tails, here we only offer a possible suggestion that a slingshot tail scenario can be applied. Shown in the left image of Figure 4.9, M49 lies  $\sim 1$  Mpc south of the Virgo Cluster centre and has a  $\geq 60$  kpc long tail pointing somewhat transversely to the radius between M49 and the cluster centre, which has been attributed to ram pressure stripping (Kraft et al. 2011). In the right image of Figure 4.9, M60 is located  $\sim 1$  Mpc to the east of M87, the cluster centre, and shows a truncated atmosphere and no gas tail. The evidence for a slingshot scenario is that M49 and M60 are located at large distances from the Virgo cluster centre and have clearly truncated atmospheres which would be unusual for a first infall. M49 appears to have a tail which points transversely to the radius between it and the cluster centre which could be an arc-shaped slingshot tail, although the tail does not appear to be a prominent arc as we have shown for this form, so this seems unlikely. Perhaps this could be a turbulent arc-shaped case as with LEDA 87745, i.e. M49 was strongly stripped on its first passage. This could be the stage where the overshooting tail is currently almost directly over the remnant atmosphere which gives the group its irregular and fuzzy shape. M60 arguably has a fuzzy atmosphere, like the first phase of the overrun slingshot tail. For both cases, it could be that they are at a less favourable viewing angle, or on their third

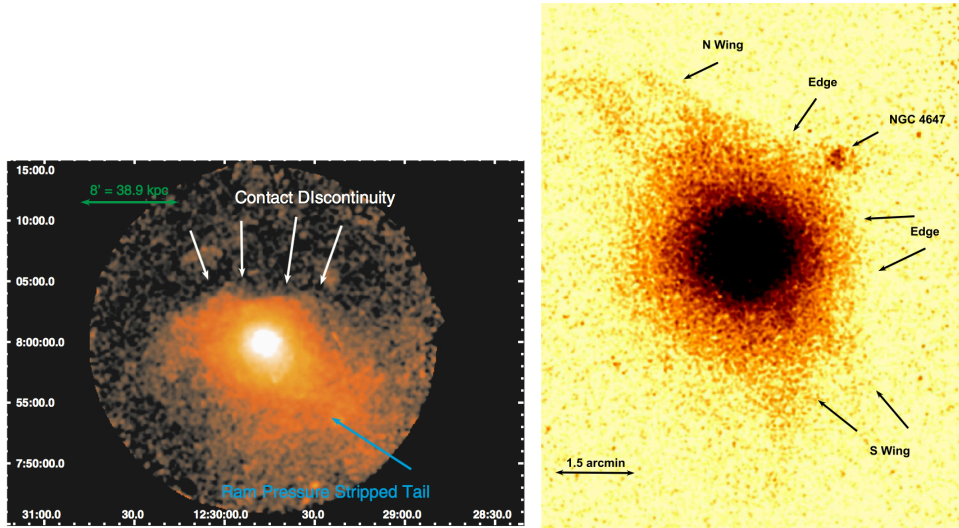


**Fig. 4.9:** Left: Image taken from Kraft et al. (2011). An exposure corrected, Gaussian smoothed XMM-Newton image of M49 in the 0.5-2.0 keV band with point sources removed. Right: Image taken from Wood et al. (2017). An Exposure-corrected, background-subtracted, coadded Chandra X-ray image of M60 in the soft band (0.5-2.0 keV).

infall into the cluster, as this would give a truncated atmosphere with little or no gas tail, but given the distance to the cluster centre this would be unlikely.

#### 4.9.5 Abell 85

A dynamically evolving, cool core cluster, Abell 85 boasts an array of merger features, substructures and filaments. The rich cluster is located at a redshift of  $z = 0.0554$ , with mass,  $M_{500} = 5.77 \pm 1.12 \times 10^{14} M_{\odot}$  (Andrade-Santos et al., 2012) and plays hosts to the BCG, MCG-02-02-086. Combining optical and X-ray spectroscopy, Yu et al. (2016) identify five merging substructures within 600 kpc of the cluster core, of which two to the north east and north west appear to have been recently accreted. As seen in Figure 4.10, two prominent merging subclusters are visible in the X-ray image of Abell 85, located to the south and south-west of the cluster centre. Nearby to the two subclusters, Schenck et al. (2014) also detect asymmetric temperature substructures which could indicate merger shocks that were produced by the two subclusters. Analysing Chandra, XMM-Newton and Suzaku observations of the cluster, Ichinohe et al. (2015) find ongoing sloshing in the cluster core which spirals out to 600 kpc that was likely triggered by merger events which occurred several Gyr's ago. The authors find that the subcluster to the south is  $\sim 600$  kpc in projection from the cluster centre, moving close to the plane of the sky and has a clear X-ray tail pointing to the south-east, perpendicular to the cluster centre. They further determine that the outer gas of the subcluster has already been stripped away and now it is the low-entropy core that is being stripped. The stripped gas forms a gas tail which is  $> 200$  kpc in length which appears to be fanned out in the downstream direction and has an abrupt drop in surface brightness at the end of the tail. Ichinohe et al. (2015) analysis of the tail determined that the tail has been bent and pushed eastwards due to the velocity field of the ongoing sloshing in the cluster. Thus, taking all of these features

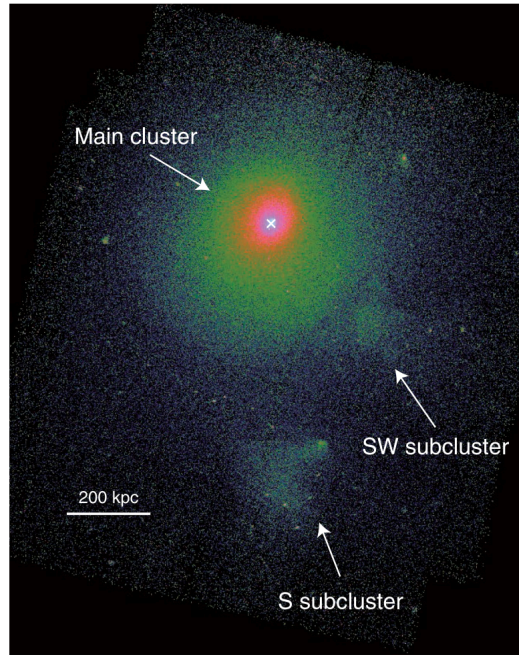


**Fig. 4.10:** Image taken from Ichinohe et al. (2015). A Gaussian-smoothed, exposure and vignetting-corrected, background-subtracted Chandra image of Abell 85 in the 0.6-7.5 keV energy band.

into account, it indicates a possible slingshot tail in action. The first indication is that the subcluster has been stripped of its outer gas already, suggesting it has already passed through the cluster once. This idea could be supported by the cluster's elongation towards the south, in the direction of the subcluster. Second, the tail has a fanned out shape that has an abrupt drop in surface brightness at the end of the tail, which would correspond to an overrun slingshot tail. Although the orientation of the tail perpendicular to the cluster core would not coincide with this overrun slingshot scenario as we would expect the overrun tail to be found south of the subcluster in correlation to its northward motion. However, as mentioned, Ichinohe et al. (2015) indicate that sloshing has bent and pushed the tail eastwards into its observed position to the east/south-east of the subcluster, therefore the tail could well have been located south of the subcluster, fitting the overrun slingshot tail scenario. If this were the case, the subcluster will have begun its merger with the cluster from the north, passing by the cluster centre on its eastern side, before reaching its current southern position. This scenario could well be similar to that of the NGC 4839 group in Coma.

#### 4.9.6 Abell 1644

At a redshift of  $z = 0.047$ , Abell 1644 is a binary cluster, consisting of a main cluster in the south and a smaller subcluster to the north. The main cluster to the south has a mass of  $M_{500} = 3.1 \pm 0.4 \times 10^{14} M_{\odot}$  and a core temperature of  $5.10 \pm 0.14$  keV, whilst the smaller northern subcluster has a mass of  $M_{500} = 2.6 \pm 0.4 \times 10^{14} M_{\odot}$  and a core temperature of  $T = 4.62^{+0.24}_{-0.16}$  keV (Johnson et al., 2010). The main cluster and the smaller subcluster are separated by a distance of  $\sim 700$  kpc and are weakly connected via the ICM which has a temperature of 4-6 keV (Reiprich et al., 2004). Both Reiprich et al. (2004) and

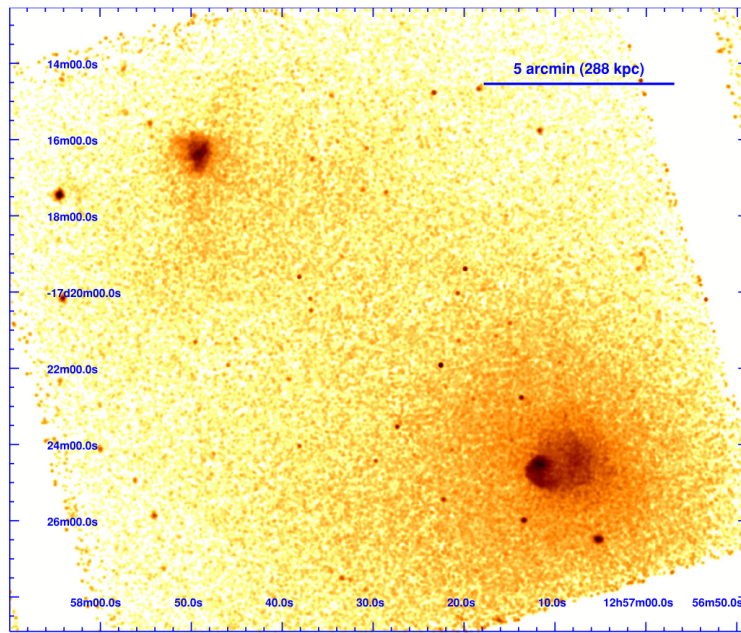


**Fig. 4.11:** A combined 70 ks Chandra ACIS-I image of Abell 1644 taken in the 0.5 - 2.5 keV energy band from Johnson et al. (2010). The X-ray emission clearly shows two merging subclusters in the cluster, one to the north and one to the south. The main cluster to the south is slushing revealed by the spiral pattern of the X-ray emission, whilst the northern subcluster is at the apocentre of the merging orbit where it will likely have a slingshot tail.

Johnson et al. (2010) find significant evidence for an off axis merger between the two bodies, as the gas around the main cluster core is disturbed and reveals a spiral slushing pattern and the smaller subcluster to the north has a truncated atmosphere with what could be a very faint tail pointing somewhat to the east, i.e., transversely to the line joining the cores of both bodies (the tail is made more clear in the temperature map of Abell 1644 in Fig 13. in Reiprich et al. (2004)). Thus there are several features in Abell 1644 which would correspond to a slingshot tail. Firstly the northern subcluster is at a large distance from the main cluster centre and is moving tangentially with a faint tail which points transversely to the line joining the centre of the subcluster and the cluster. The geometry of the spiral slushing pattern of the main cluster also corresponds to a likely slingshot tail for the northern subcluster as it is on the opposite side to the subcluster, coinciding with the observational signatures outlined in the previous section. Johnson et al. (2010) find that the truncated atmosphere of the northern subcluster indicates its westerly motion. However, the truncation of the northern cluster's atmosphere is not as clear as for NGC 1404 (see Fig. 3.1), which would be consistent with the chaotic ambient flow patterns at apocentre passage. As mentioned by both Reiprich et al. (2004) and Johnson et al. (2010), the northern subcluster will have passed by the main cluster on its eastern side moving northwards to its current position at apocentre where it has produced a likely slingshot tail. Evidence can be seen in the X-ray contour image of the main cluster which shows elongation on the eastern side which would correspond to the passing of the smaller subcluster in this region.

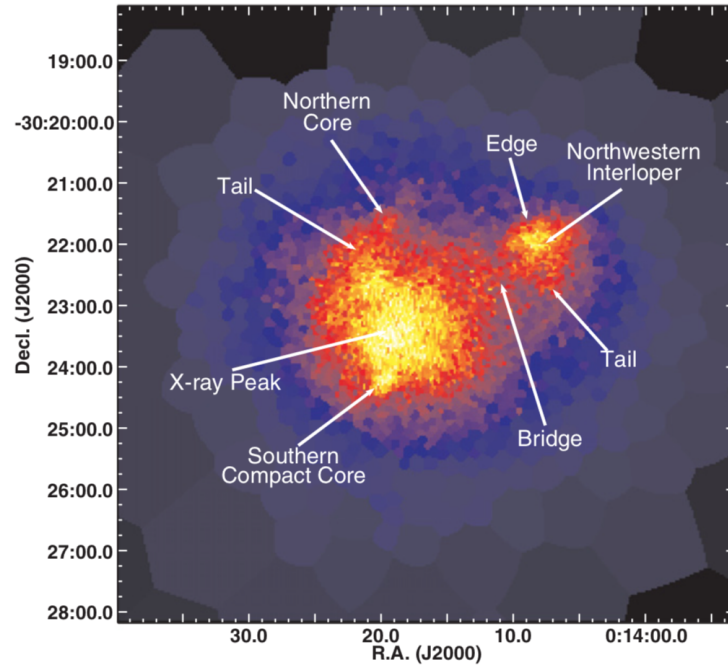


**Fig. 4.12:** Taken from Owers et al. (2011b). Background-subtracted and exposure-corrected Chandra image of the Abell 2744 cluster. Abell 2744 is a complex merging scenario between two subclusters in the central region of the cluster and another subcluster to the NW. The subcluster to the NW appears to be in a post-merger state as evidence suggests it has falling into the central region of Abell 2744 from the south-east before moving out to the NW in its current position likely around the apocentre point. This evidence along with an apparent tail which points transversely to line which joins the centres of the NW subcluster to the central region suggests a likely slingshot tail scenario.

#### 4.9.7 Abell 2744

Abell 2744 is an extremely X-ray luminous cluster at a redshift of  $z = 0.3$  with a mass of  $M_{200} \sim 2 \times 10^{15} M_{\odot}$  (Medezinski et al., 2016) which appears to be undergoing a complex merger involving three subclusters. Giovannini et al. (1999) detected a luminous radio halo which encompasses the central 1.8 Mpc of the cluster and a large radio relic located at a distance of  $\sim 2$  Mpc north-east from the centre of the cluster (see also Govoni et al. 2001; Eckert et al. 2016), which are indicative of shock fronts produced as a result of an ongoing merger. Figure 4.12 shows a Chandra image of the cluster, located in the centre is the main body of the cluster which consists of two large subclusters. Kempner & David (2004) find that a major merger is occurring in this central region with an estimated mass ratio of 1:3 (Boschin et al., 2006). Similarly, Owers et al. (2011b) find that the subclusters in the central region have undergone a significant major merger along a rough north-south axis with a small impact parameter, similar to that of the Bullet Cluster (Markevitch et al., 2002). Kempner & David (2004); Merten et al. (2011); Owers et al. (2011b) find that the subcluster to the north-west is undergoing a minor merger with the main cluster centre. This subcluster in the north-west exhibits a cold front pointing to the north/north-east and has an estimated mass of  $1.1 \times 10^{14} M_{\odot}$  (Merten et al., 2011). Owers et al. (2011b) suggested that the north-west subcluster is in a post merger phase. They surmise that the evidence would correspond to the subcluster passing the main cluster centre from the south-east moving toward its current position in the north-west. The subcluster has

extended X-ray emission to the south i.e. in the direction of the suggested recent orbit path, which has a curvature, this would suggest that the merger had a large impact parameter. Both Owers et al. (2011b) and Merten et al. (2011) find that for the north-west subcluster there is an offset between the dark matter peak and the gas, to which Owers et al. (2011b) put forward the idea of a slingshot mechanism to explain this feature. Thus because of these features, this subcluster could well be in the slingshot tail phase. The main cluster does not provide any significant clues to identify the slingshot tail due to it undergoing a major merger itself. Kempner & David (2004) however found that there maybe a possible bow shock located 90 kpc ahead of the cold front of the subcluster, i.e. leading the subcluster and estimated an infall velocity of  $M \sim 1.2$ . In the slingshot scenario the bow shock does not lead the subcluster but propagates behind it as it continues to move along the same direction as the subcluster turns around at apocentre. Thus, this subcluster may have recently turned around at apocentre but has now already begun its next infall, i.e. moving out of the slingshot phase.

## 4.10 Conclusion

In this paper we have visually inspected a suite of idealized binary cluster merger simulations to show that as well as ram pressure stripped tails, there is a second class of gas tails, named slingshot tails. These tails are formed as a secondary subhalo moves *away* from the primary cluster centre, toward the apocentre of its orbit, producing tails which can at times point perpendicular or opposite to the subhalo's current direction of motion. Importantly, whilst in the slingshot tail stage, the secondary is not being subjected to ram pressure stripping and the morphology of the tail is influenced more by tidal forces than ram pressure. In consequence a tail observed in the slingshot tail stage should not be identified as a gas stripping tail as this does not give an accurate description of the ongoing physics. We find that slingshot tails differ from ram pressure tails in the following way.

- Ram pressure stripped tails have an orderly head-tail morphology in contrast to slingshot tails which are generally oriented radially but can well point transverse to the radius between the secondary and the primary cluster centre while the secondary is at a large distance from the primary cluster centre.
- The brightness of slingshot tails has a distinct end, unlike ram pressure stripped tails which continuously fade away.
- For a ram pressure stripped tail, a bow shock will lead the secondary, whereas, for a slingshot tail, the shock that once led the secondary continues to propagate outward as the secondary turns around and heads back toward the cluster, therefore the shock appears behind the secondary on the tail side and can be found at large distances.
- The remnant atmosphere of secondaries with slingshot tails can show evidence of shells in the remaining gas core due to internal sloshing and re-accretion of gas.

From our analysis, we find that slingshot tails can be split into two characteristically different forms:

- **Arc-Shaped:** This form occurs when the impact parameter is large and produces a prominent arc-shaped tail which can temporarily point perpendicular to the secondary's motion (as shown in Figure 3, the top image of column (b) in the arc-shaped tail section).
- **Overrun:** This form occurs when the impact parameter is small and can be separated into two distinct phases. The first phase produces an irregular shaped secondary atmosphere, as the slingshot tail overruns the remnant core of the secondary and partially settles into its potential. The second phase is reached as the remnant tail continues to overrun the core of the secondary, becoming conical in shape, fanning outward along the orbit direction, away from the secondary. The edge of the fanned out tail marks the cut off radius which the secondary has overshoot to.

Furthermore, we find that in the slingshot tail stage, flow patterns around the subhalo are highly irregular. Thus, interpreting an observed slingshot tail using a simple ram pressure stripped tail scenario leads to incorrect conclusions regarding subhalo velocity or expected locations of shear flows, instabilities or mixing. Future work will involve a deeper investigation to derive the exact conditions as to why one or the other slingshot form occurs, or any other intermediate regime for that matter. Understanding slingshot tails can provide an insight into the gas physics at the cluster outskirts and also help disentangle the merger history of galaxy clusters. Therefore, with the new X-ray instruments coming online in the next decade such as XARM and Athena XIFU, further work will involve making images of slingshot tails using mock instruments such as these to probe the level of understanding into these areas that can be achieved.

## 4.11 Acknowledgments

We thank the anonymous referee for helpful comments to improve the clarity of the paper.

The software used in this work was in part developed by the DOE NNSA-ASC OASCR Flash centre at the University of Chicago, Fryxell et al., 2000.

E.R. acknowledges the support of STFC, through the University of Hull's Consolidated Grant ST/R000840/1 and access to viper, the University of Hull High Performance Computing Facility.

N.L. acknowledges partial support by grant No. 18-12-00520 from the Russian Scientific Foundation.

A.S. thanks Hazel Morrish for providing the cartoon image in Figure 1 to distinguish the main slingshot tail forms.

# Chapter 5

## Stolen Atmosphere Theory - Assessing Stagnation Point Methods and the Stolen Atmosphere Effect in Tailored Simulations of a Minor Cluster Merger

### 5.1 Prologue

The focus of this chapter is based on the theoretical understanding of the stolen atmosphere effect. This effect was mentioned in passing without this name in Roediger et al. (2015a), and was first reported on using this name in Sheardown et al. (2018) (section 3.6.4 of this thesis). My Fornax Cluster simulations are used for a deeper analysis of the effect, led by my supervisor, Dr. Elke Roediger and former BSc and now MSc student Thomas Fish at the University of Hull. The result of our analysis is in the form of two paper drafts which will go on to be submitted for publication. One paper led by Dr. Elke Roediger, focuses on the theory behind the stolen atmosphere effect (Roediger et al. in preparation), whilst the other paper, lead by Thomas Fish, assesses stagnation point methods and the stolen atmosphere effect on the tailored simulations of the Fornax Cluster merger (Fish et al. in preparation). Though I am not the lead author on either of the two drafts, I am a key co-author, as my simulations are used for the detailed analysis, and I was directly involved in the interpretation of the results. I also provided help and supervision to Thomas during his work. Therefore, this chapter describes our work on the stolen atmosphere effect, written in my own words, and discusses how it relates to the context of my thesis. The mathematical derivations and equations written below in this chapter are taken from their respective work.

### 5.2 Introduction

When a blunt body moves through an ambient gas, a stagnation point is established at its upstream edge. At the stagnation point, the flow velocity is zero, but the gas pressure is

enhanced compared to the free-stream pressure by an amount called the ram pressure. The ram pressure is a function of the body's velocity, thus, from measuring the ram pressure, the body's velocity can be determined.

This strategy is used widely to determine the velocity of a subcluster or galaxy travelling through the intra-cluster medium (ICM) of its host cluster (e.g., Su et al. 2017a; Vikhlinin et al. 2001a). However, this standard method neglects the fact that the subcluster's gravitational potential attracts and compresses the host cluster's ICM surrounding it. The subcluster's gravitational attraction on the ambient ICM leads to the subcluster being surrounded by a secondary atmosphere of 'stolen' or 'borrowed' host cluster ICM, even if the subcluster does not move through the ICM. This stolen atmosphere is somewhat enhanced pressure, density and temperature compared to the original host cluster ICM. Thus, the ICM pressure at the stagnation point arises not only from the ram pressure, i.e., the subcluster's motion, but also from the stolen atmosphere. If this contribution to the pressure enhancement from the stolen atmosphere is neglected, and the pressure enhancement at the stagnation point is attributed solely to the ram pressure, the subcluster's velocity will be overestimated.

In this chapter, we describe a simple analytical model for the stolen atmosphere effect. We show that the effect is relevant even for elliptical galaxies moving through clusters, and outline a procedure to correct the standard stagnation point analysis for this effect. We also describe results from a full hydro+Nbody simulation of a binary minor cluster merger (my Fornax merger simulations in Chapter 3) and demonstrate the success and limits of different stagnation point methods in a dynamic, more realistic context.

Early-type galaxies or subclusters which are falling into their host cluster during a minor merger display characteristic observational signatures which have been analogised to that of the quasi-steady flow around a blunt body, where the galaxy's remnant atmosphere takes the place of the blunt body. Due to the flow past the remnant atmosphere, a stagnation point is established at the upstream edge, where the local flow velocity is zero and the ICM gas pressure becomes enhanced by the ram pressure compared to the free stream region (the free-stream region is the region where the flow is relaxed and stable). Therefore, the ram pressure essentially characterises the difference between the stagnation point pressure and the free-stream pressure. As the ram pressure is dependent on the velocity of the galaxy, by measuring the ram pressure exerted on the remnant atmosphere, the velocity of the galaxy can be calculated. To date, many velocity measurements of galaxies and subclusters have been made using the stagnation point method (e.g. De Grandi et al. 2016; Machacek et al. 2005; Springel & Farrar 2007; Su et al. 2017a; Vikhlinin et al. 2001a). The ability to calculate the infall velocity of a given galaxy or subcluster into a cluster is important for understanding the growth and merger history of clusters, as well as probing cosmological constraints. In particular, the properties of the ICM can be probed by understanding the infall velocity, as this shapes the flow conditions and impacts the production of KHIs which can be used as probes for the transport coefficients of the ICM.

Current stagnation point methods do not consider the impact of the gravitational potential of the galaxy or subcluster on the ambient flow of the ICM, i.e. the effect of the

stolen atmosphere. This is the effect of the galaxy's or subcluster's gravitational potential attracting and compressing the surrounding host cluster ICM, producing a secondary atmosphere which has enhanced temperature, pressure and density in comparison to the original ICM. The stolen atmosphere effect provides enhancement to the stagnation point pressure, therefore if the enhancement of the stagnation point pressure is prescribed entirely to the motion of the galaxy, then the velocity of the galaxy becomes overestimated. Below, current descriptions of stagnation point methods are presented, followed by the new stagnation point method taking into account the effect of a gravitational potential. For the full analysis and theory behind the stolen atmosphere effect and stagnation point methods, see the respective papers Roediger et al. (in preparation) and Fish et al. (in preparation).

### 5.3 Current Stagnation Point Methods

The simplest stagnation point method considers the flow in the rest frame of the galaxy, assuming that the ICM is incompressible and homogeneous, and neglects the effect of gravity. The stagnation point pressure is formulated from the Bernoulli principle, this is the notion that along each streamline in the flow, the quantity

$$P + \frac{1}{2}\rho v^2 \quad (5.1)$$

is conserved, where  $P$  is the gas pressure,  $\rho$  is the gas density and  $v$  is the flow velocity. As this quantity holds for all streamlines, then by considering the streamline that connects the stagnation point to the free-stream region, the stagnation pressure can be calculated. Thus, for this particular streamline we can write,

$$P_{\text{stag}} + \frac{1}{2}\rho_{\text{stag}}v_{\text{stag}}^2 = P_{\text{free}} + \frac{1}{2}\rho_{\text{free}}v_{\text{free}}^2 \quad (5.2)$$

where 'stag' and 'free' denote the stagnation point and free-stream quantities. As the velocity is zero at the stagnation point, i.e.  $v_{\text{stag}} = 0$ , this equation becomes,

$$P_{\text{stag}} = P_{\text{free}} + P_{\text{ram}} \quad \text{where} \quad P_{\text{ram}} = \frac{1}{2}\rho_{\text{free}}v_{\text{free}}^2. \quad (5.3)$$

$P_{\text{ram}}$  is the ram pressure and quantifies the enhancement of the stagnation point pressure over the free-stream pressure. By using the relation for the speed of sound of an ideal gas  $c = \sqrt{\frac{\gamma kT}{m_p}}$  and the ideal gas law  $P = \frac{\rho}{m_p}kT$ , where  $\gamma$  is the ratio of specific heats,  $k$  is the Boltzmann constant,  $T$  is the gas temperature and  $m_p$  is the particle mass, equation 5.3 can be written in terms of the Mach number,  $M$ ,

$$\frac{P_{\text{stag}}}{P_{\text{free}}} = 1 + \frac{\gamma}{2}M^2. \quad (5.4)$$

However, this simplistic incompressible model does not accurately reflect the compressible nature of the ICM. In this regard, Vikhlinin et al. (2001a) extended the model

to include the compressibility of the ICM based on the equations in Landau & Lifshitz (1959), catering for transonic and supersonic flows. However, this model still neglected the force of gravity. In the Vikhlinin et al. (2001a) extended model, the ratio of the free-stream pressure to the stagnation point pressure is defined as a function of the cloud velocity, i.e. the velocity of the galaxy or subcluster. For subsonic and supersonic flows (i.e.  $M \leq 1$  and  $M > 1$  respectively), the ratio of  $\frac{P_{\text{stag}}}{P_{\text{free}}}$  is,

$$\frac{P_{\text{stag}}}{P_{\text{free}}} = \left[ 1 + \frac{(\gamma - 1)M_{\text{free}}^2}{2} \right]^{\frac{\gamma}{\gamma - 1}} \quad \text{for } M_{\text{free}} \leq 1 \quad (5.5)$$

$$\frac{P_{\text{stag}}}{P_{\text{free}}} = \left[ \frac{\gamma - 1}{2} \right]^{\frac{\gamma + 1}{\gamma - 1}} M_{\text{free}}^2 \left[ \gamma - \frac{\gamma - 1}{2M_{\text{free}}^2} \right]^{\frac{\gamma}{\gamma - 1}} \quad \text{for } M_{\text{free}} > 1 \quad (5.6)$$

where  $M_{\text{free}} = v/c_s$  is the Mach number for the free-stream region. Fish et al. (in preparation) shows that the incompressible and compressible models differ significantly once the Mach number of the flow becomes transonic or greater, as the compression ratio  $P_{\text{stag}}/P_{\text{free}}$  becomes much larger for the compressible model. To determine the velocity of a galaxy moving through the ICM,  $P_{\text{stag}}$  and  $P_{\text{free}}$  need to be measured and this can be done by calculating the Mach number  $M$ . Then, with  $\rho_{\text{free}}$  known,  $v_{\text{free}} = v_{\text{galaxy}}$  can be calculated.

Further expanding on the above models, Su et al. (2017a) using the Bernoulli equations and the idea of a compressible flow around a sphere, formulated a 3D pressure distribution across a spherical front. This was then applied to observations of the elliptical galaxy NGC 1404 in the Fornax Cluster. The motivation in doing this is because the two previous methods only consider the stagnation point - this requires favourable geometry (parallel to the plane of the sky) for the infalling galaxy or subcluster which is not usually the case, and also due to projection effects, the stagnation point is typically too difficult to detect. Su et al. (2017a) model assumes spherical symmetry across the upstream edge of the galaxy, accounting for the angle between the merger plane and the plane of the sky, and the angle around the upstream edge. They use this method to determine the inclination angle and velocity of the galaxy by measuring the pressure along the upstream edge instead of measuring  $P_{\text{stag}}$  in a single location.

## 5.4 Stagnation Point Method Including The Stolen Atmosphere Effect

### 5.4.1 Incompressible Model

In this section, two models for the stagnation point method which include the effects of gravity are described. The first model is a simple model which includes gravity but still treats the ICM flow as incompressible so that model can be formulated from the incompressible Bernoulli equation. The model considers the incompressible flow around a

subcluster moving at constant velocity through a homogeneous ICM and is considered in the rest frame of the subcluster. The subcluster has its own atmosphere and gravitational potential, where its atmosphere is considered to be a solid sphere. Following the same formulation as the previous methods, but now including a gravitational potential term,  $\Phi$ , to characterise the gravitational potential of the subcluster, the Bernoulli principle would now state that along a streamline the quantity,

$$P + \frac{1}{2}\rho v^2 + \rho\Phi \quad (5.7)$$

is now conserved. The potential  $\phi$  varies with distance from the subcluster, therefore if the potential is spherical, we can write  $\phi = \phi(r)$ . Again, applying this conservation to the streamline connecting the stagnation point to the free-stream region,

$$P_{\text{stag}} + \frac{1}{2}\rho_{\text{stag}}v_{\text{stag}}^2 + \rho_{\text{stag}}\Phi(r)_{\text{stag}} = P_{\text{free}} + \frac{1}{2}\rho_{\text{free}}v_{\text{free}}^2 + \rho_{\text{free}}\Phi(r)_{\text{free}} \quad (5.8)$$

Again, as  $v_{\text{stag}} = 0$ ; and under the assumption that the free-stream region is far enough away from the gravitational potential, such that  $\Phi_{\text{free}} = 0$ , then this equation can be written as,

$$P_{\text{stag}} + \rho_{\text{stag}}\Phi_{\text{stag}} = P_{\text{free}} + P_{\text{ram}} \quad (5.9)$$

$$P_{\text{stag}} = P_{\text{free}} + P_{\text{ram}} + P_{\text{grav}} \quad (5.10)$$

$$\text{where } P_{\text{free}} = \frac{\rho_{\text{free}}}{m_p} k_b T_{\text{free}} \quad \text{and} \quad (5.11)$$

$$P_{\text{ram}} = P_{\text{free}} \frac{1}{2}\rho_{\text{free}}v_{\text{free}}^2 \quad \text{and} \quad P_{\text{grav}} = -\rho_{\text{stag}}\Phi_{\text{stag}} = -\rho\phi(r_{\text{strip}}).$$

We define the contribution of gravity to the pressure enhancement as  $P_{\text{grav}}$ . This is the contribution from the stolen atmosphere. Due to the ram pressure stripping, the gas atmosphere of the galaxy is stripped to a certain radius called the stripping radius,  $r_{\text{strip}}$ , this is also the distance of the stagnation point from the subcluster or galaxy centre. Thus gravitational pressure,  $P_{\text{grav}}$ , is dependent on the stripping radius. From this formulation, the stagnation pressure becomes enhanced by not only subclusters motion but also by its own gravitational potential.

By comparing the ratio of  $P_{\text{grav}}$  to  $P_{\text{ram}}$  and using typical subcluster parameters, the significance of the gravitational pressure can be determined. For algebraic simplicity, we use a Hernquist potential to describe the subcluster potential i.e.  $\phi = \frac{GM}{a+r_{\text{strip}}}$ , where;  $M$  is the subcluster mass on the order of  $10^{13}M_{\odot}$ ,  $a$  is a scalelength and  $r_{\text{strip}}$  is the stripping radius, both on the order of 100 kpc. For a subcluster moving through the ICM of its host cluster, velocities are typically on the order of  $1000\text{kms}^{-1}$ . Therefore comparing  $P_{\text{grav}}$  and  $P_{\text{ram}}$ ,

$$\frac{P_{\text{grav}}}{P_{\text{ram}}} = \frac{-\rho\phi_{\text{stag}}}{P_{\text{free}} \frac{1}{2}\rho_{\text{free}}v_{\text{free}}^2} = \frac{\phi_{\text{stag}}}{\frac{1}{2}v_{\text{free}}^2} \quad (5.12)$$

$$\frac{P_{\text{grav}}}{P_{\text{ram}}} = \frac{GM}{\frac{1}{2}v_{\text{free}}^2} (a + r_{\text{strip}}) \quad (5.13)$$

$$\frac{P_{\text{grav}}}{P_{\text{ram}}} = 0.86 \frac{M}{10^{13}M_{\odot}} \left( \frac{a + r_{\text{strip}}}{100\text{kpc}} \right)^{-1} \times \left( \frac{v_{\text{free}}}{1000\text{kms}^{-1}} \right)^{-2}. \quad (5.14)$$

The end result demonstrates that the gravitational pressure is a significant factor in enhancing the stagnation point pressure in comparison to just the ram pressure. Due to the dependence of the term  $M/(a + r_{\text{strip}})$  on the gravitational pressure, the mass of the subcluster is not a critical factor. For example, if the subcluster had a smaller mass, say closer to the mass of an elliptical galaxy, then the scalelength and stripping radius on this scale would become sufficiently reduced so that a similar effect would be observed, i.e., the gravitational pressure due to either a subcluster or an elliptical galaxy is a significant component in the enhancement of the stagnation point pressure.

If the enhancement of the stagnation point pressure is prescribed solely to the motion of the subcluster, a false velocity can be estimated by considering just the enhancement by the motion. This is calculated by,

$$v_{\text{false}} = v_{\text{free}} \sqrt{1 + \frac{\phi_{\text{strip}}}{\frac{1}{2}v_{\text{free}}^2}}. \quad (5.15)$$

When using the same typical subcluster parameters as above, plugging these into the equation for the false velocity reveals that attributing the stagnation point pressure solely to motion of the subcluster leads to a 35% overestimation of the subcluster velocity.

## 5.4.2 Compressible Model

We now determine the pressure enhancement due to the stolen atmosphere effect including compressibility of the ICM. For simplicity, this calculation assumes a stationary subcluster embedded in a homogeneous ICM, i.e., we treat the contributions from  $P_{\text{grav}}$  and  $P_{\text{ram}}$  as fully independent at this point. A more sophisticated treatment in future work may treat both effects simultaneously, but we find this independent treatment successful in comparing to simulations. Thus, for now, our model for the full stagnation point pressure is,

$$P_{\text{stag}} = P_{\text{free}} + P_{\text{ram}} + P_{\text{grav}} \quad \text{or}$$

$$\frac{P_{\text{stag}}}{P_{\text{free}}} = 1 + \frac{P_{\text{ram}}}{P_{\text{free}}} + \frac{P_{\text{grav}}}{P_{\text{free}}}$$

$$\frac{P_{\text{stag}}}{P_{\text{free}}} = \frac{P_{\text{stag,nograv}}}{P_{\text{free}}} + \frac{P_{\text{grav}}}{P_{\text{free}}}. \quad (5.16)$$

The term  $\frac{P_{\text{stag,nograv}}}{P_{\text{free}}}$  follows Eqs. 5.4 and 5.5 (and from Vikhlinin et al. 2001a) and describes the stagnation pressure enhancement due to the motion only. We now calculate  $\frac{P_{\text{grav}}}{P_{\text{free}}}$  (see Eq. 5.26 below) the contribution from the subclusters gravity, i.e, the stolen atmosphere effect. For this model, the motion of the subcluster is neglected to simplify the case.

To calculate  $P_{\text{grav}}$ , the contribution due to the stolen atmosphere, the model considers a subcluster with a spherical gravitational potential,  $\phi(r)$ , that is placed into a homogeneous ICM. It is assumed that the ICM settles adiabatically into hydrostatic equilibrium, this is written mathematically as,

$$\frac{dP}{dr} = -\rho g(r) = \rho \frac{d\phi}{dr}. \quad (5.17)$$

The ICM is considered to be an ideal gas, which can be described by the equation of state,

$$P = nkT = \frac{\rho}{m_p} kT \quad (5.18)$$

where  $m_p = 0.6$  amu is the mean particle mass. The process of the ICM gas settling down into hydrostatic equilibrium is adiabatic and therefore the entropy of the ICM stays constant, thus,

$$S = \frac{kT}{n^{2/3}} = S_{\text{free}} \quad (5.19)$$

$$n = \frac{\rho}{m_p} = \left( \frac{kT}{S_{\text{free}}} \right)^{3/2}. \quad (5.20)$$

The pressure can be related to the entropy and temperature by combining equations 5.18 and 5.20. This gives,

$$P = \left( \frac{1}{S_{\text{free}}} \right)^{3/2} (kT)^{5/2}. \quad (5.21)$$

Now using this equation and Eq. 5.20, functions for the pressure and density can be subbed into Eq. 5.17, which when simplified becomes,

$$\frac{d(kT)}{dr} = -\frac{2}{5} m_p \frac{d\phi}{dr}. \quad (5.22)$$

Thus, integrating this equation from the radius  $r$  to infinity, and using  $kT(\infty) = kT_{\text{free}}$ , gives the temperature profile for the stolen atmosphere,

$$kT(r) = kT_{\text{free}} \left( 1 - \frac{2 m_p \phi(r)}{5 kT_{\text{free}}} \right). \quad (5.23)$$

Density and pressure profiles can then be determined by using this equation and Eqs. 5.20 and 5.21,

$$n(r) = n_{\text{free}} \left( 1 - \frac{2 m_p \phi(r)}{5 kT_{\text{free}}} \right)^{3/2} \quad (5.24)$$

$$P(r) = P_{\text{free}} \left( 1 - \frac{2 m_p \phi(r)}{5 kT_{\text{free}}} \right)^{5/2}. \quad (5.25)$$

Thus, the term  $\frac{P_{\text{grav}}}{P_{\text{free}}}$  needed in Eq. 5.16 is this expression evaluated at the stripping radius,

$$\frac{P_{\text{grav}}}{P_{\text{free}}} = \frac{P_{\text{grav}}(r_{\text{strip}})}{P_{\text{free}}} = \left( 1 - \frac{2 m_p \phi(r_{\text{strip}})}{5 kT_{\text{free}}} \right)^{5/2}. \quad (5.26)$$

The result of these profiles shows that the term,  $\frac{m_p \phi(r)}{kT_{\text{free}}}$ , which is the ratio of the gravitational potential energy for a particle in the ICM in the potential of the subcluster and its thermal energy, controls the increase of the temperature, density and pressure of the stolen atmosphere. Roediger et al. (in preparation) show that this ratio is typically around 1, meaning that the stolen atmosphere effect can cause an increase in the ICM temperature, density and pressure of tens of percent compared to the free-stream ICM levels. The ICM gas will accumulate adiabatically onto the subcluster potential, and the derived profiles show that the temperature, density and pressure of this stolen atmosphere increases towards the centre of the subcluster. Roediger et al. (in preparation) show that when comparing the incompressible and compressible stolen atmosphere pressure profiles, they converge for low compressions, but are significantly different at high compressions toward the subcluster centre as would be expected. This result means that if an estimate for the stagnation point pressure is made using the incompressible model for the stolen atmosphere pressure, and this estimate shows the stolen atmosphere pressure has a significant contribution, then an estimate using the compressible method would become even more significant. The model for the stolen atmosphere effect is particularly sensitive to the size of the gravitational potential, and therefore requires an accurate calculation of the galaxy or subcluster mass which is known to have considerable uncertainty (Takizawa et al., 2010). Therefore, when estimating the infall velocity using the stagnation point method including gravity, the significant source of uncertainty is the gravitational potential.

## 5.5 Comparing Stagnation Point Models in a Minor Merger Simulation

The stagnation point methods described above allow for a measurement of the galaxy or subcluster velocity to be made. However, none of these methods take into account the variation of the galaxy velocity that is expected during cluster passage. Furthermore, a minor merger itself can cause bulk motions in the ICM which can consequently bias the determined galaxy velocity. By applying the methods explained above to the tailored minor merger simulations of the Fornax Cluster, specifically using them to estimate the infall velocity of NGC 1404, their accuracy in measuring the infall velocity can be analysed. This is achieved by estimating the velocity of the galaxy at each timestep using each stagnation point method, and then comparing these results to the velocity of the galaxy which can be calculated directly from the simulation. We will compare the following three versions of the stagnation point method:

- the incompressible treatment, neglecting the stolen atmosphere effect, i.e., the relation in Eq. 5.3
- the compressible treatment following Vikhlinin et al. (2001a), but neglecting the stolen atmosphere, i.e., Eqs. 5.5 and 5.6

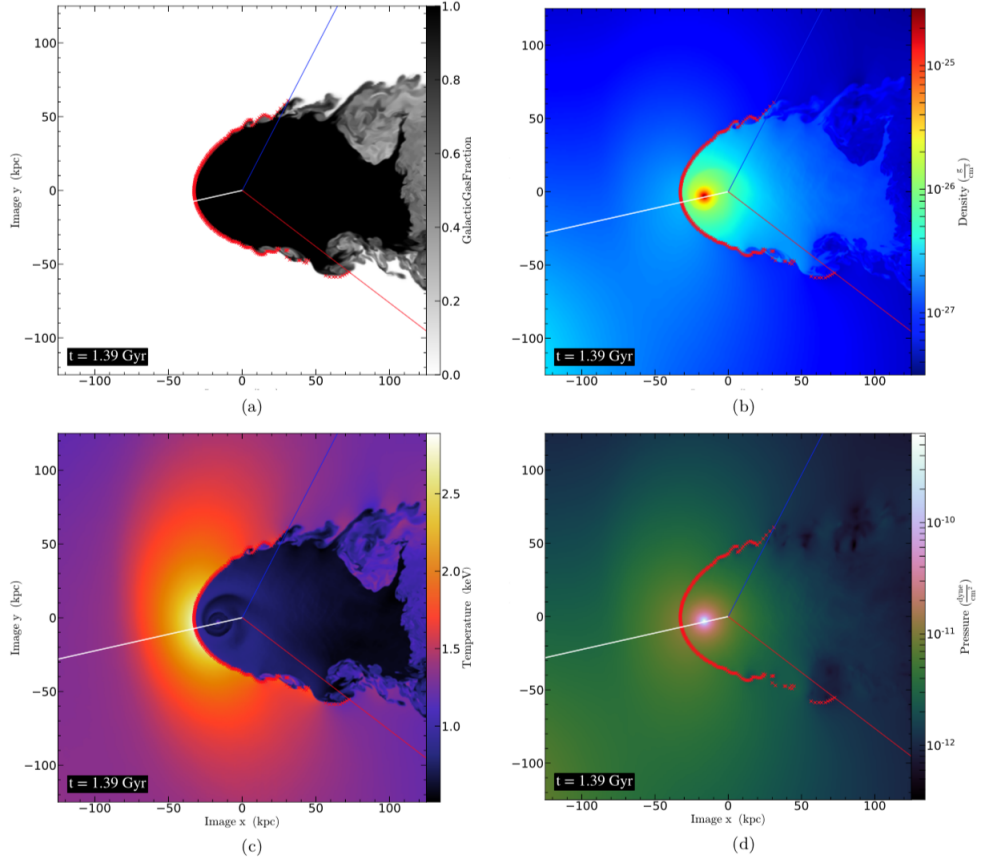


**Fig. 5.1:** Figure taken from Fish et al. (in preparation). Slices through NGC 1404 in the plane of the merger at an epoch of 1.39 Gyr in the V0 simulation described in Chapter 3. Top Left: A galactic gas fraction slice showing the level of mixing between the galaxy gas and the ICM, a value of 1.0 corresponds to 100% galaxy gas. Top Right: Gas density slice. Bottom Left: Gas temperature slice. Bottom Right: Gas pressure slice. In each image, the white line corresponds to the direction of the galaxy velocity which intersects the centroid and the stagnation point. The red and blue lines show the bounds of the galaxy edge finding algorithm, while the red data points correspond to the location where the data is taken along the boundary of the galaxy atmosphere.

- the compressible treatment including the stolen atmosphere effect, i.e., using Eq. 5.16

To be able to do this, the variables which are required by the stagnation point method need to be defined in a consistent way to ensure an accurate comparison between the methods. These variables include the velocity of the galaxy as taken from the simulation, the upstream edge of the galaxy, the location of the stagnation point and the free-stream variables. Firstly, the velocity of the galaxy which will be calculated directly from the simulation needs to be defined. The centres of NGC 1404 and the Fornax Cluster are set by the centre of their dark matter haloes, this is where the velocity is calculated. There is a choice between using either the relative velocity between NGC 1404 and Fornax, or the velocity of NGC 1404 with respect to the grid, i.e. the initial rest frame of the Fornax ICM. We consider both versions. The upstream edge of the galaxy is defined by following the direction of the velocity vector from the centre of the galaxy to the point where the galaxy's atmosphere significantly drops - this is defined by the galactic gas fraction (see Fig. 5.1). The location of the stagnation point is defined by using the maximum of a

polynomial fit to the pressure profile along the upstream edge. This is because during the merger, the pressure distribution around the upstream edge of the galaxy becomes asymmetric as there is a large gradient in ICM pressure in the Fornax core. The values of the free-stream variables are calculated in the merger plane by azimuthally averaging around the cluster centre. The free-stream values are taken at the azimuthal radius which joins the cluster centre to upstream edge of NGC 1404. To ensure the average correlates to the free-stream, values which lie in disturbed regions in the cluster (due to the orbital path of the galaxy) and close to NGC 1404 are excluded from the averaging as these do not reflect the free-stream. This method is similar to the observers approach to determining the free-stream values. For the full description of the analysis procedures see Fish et al. (in preparation).

### 5.5.1 Results

The stagnation point methods that are analysed are the following; the incompressible method with no gravity (Eq. 5.3), the compressible method with no gravity (Eqs. 5.5 and 5.6) and the compressible method with gravity (i.e. including the stolen atmosphere effect, Eq. 5.16). These methods have been applied to each timestep in the minor merger simulations of the Fornax Cluster as described in Chapter 3 to estimate the velocity of NGC 1404. Figure 5.2 presents the evolution of the velocity estimation throughout the merger for the V2 simulation. In this simulation, NGC 1404 starts with an initial  $\sim$  Mach 1 velocity and has a large impact parameter (a pericentre distance of 152 kpc). Only the results for the V2 simulation are shown here as the result is essentially the same for V0 and V1 simulations, and the V2 simulation is used as this represented the best match to the observational data for NGC 1404 and Fornax Cluster. The top plot in Fig. 5.2 shows the separation distance between the centres of NGC 1404 and the Fornax Cluster to give a representation of the evolution of the merger. NGC 1404 initially starts at a separation distance of 750 kpc. The middle plot in Fig. 5.2 shows the evolution of the stagnation point pressure throughout the merger based on the method including the stolen atmosphere (Eq. 5.16), as well as its components, i.e., the free-stream pressure, the ram pressure and the gravitational pressure. The bottom plot shows the velocity of NGC 1404 throughout the merger as estimated by each method along with the comparison velocity of NGC 1404 calculated with respect to the grid and the velocity of NGC 1404 with respect to the Fornax Cluster centre.

The evolution of the merger, with regards to the pressure evolution and the velocity estimation can be split into separate periods. The first period at the start of the simulation is influenced by the initial conditions and requires time ( $\sim$  0.5 Gyrs) to settle into a steady flow state. Significantly in this period, the stolen atmosphere is being established as NGC 1404 begins its infall into the cluster. This can be seen by looking at the blue line which represents  $P_{\text{stag}}$  as calculated directly from the simulation in Fig. 5.2.  $P_{\text{stag}}$  begins lower, but gradually increases to the value of the  $P_{\text{stag}}$  model which is calculated by the sum of its individual components;  $P_{\text{free}}$ ,  $P_{\text{ram}}$  and  $P_{\text{grav}}$ .

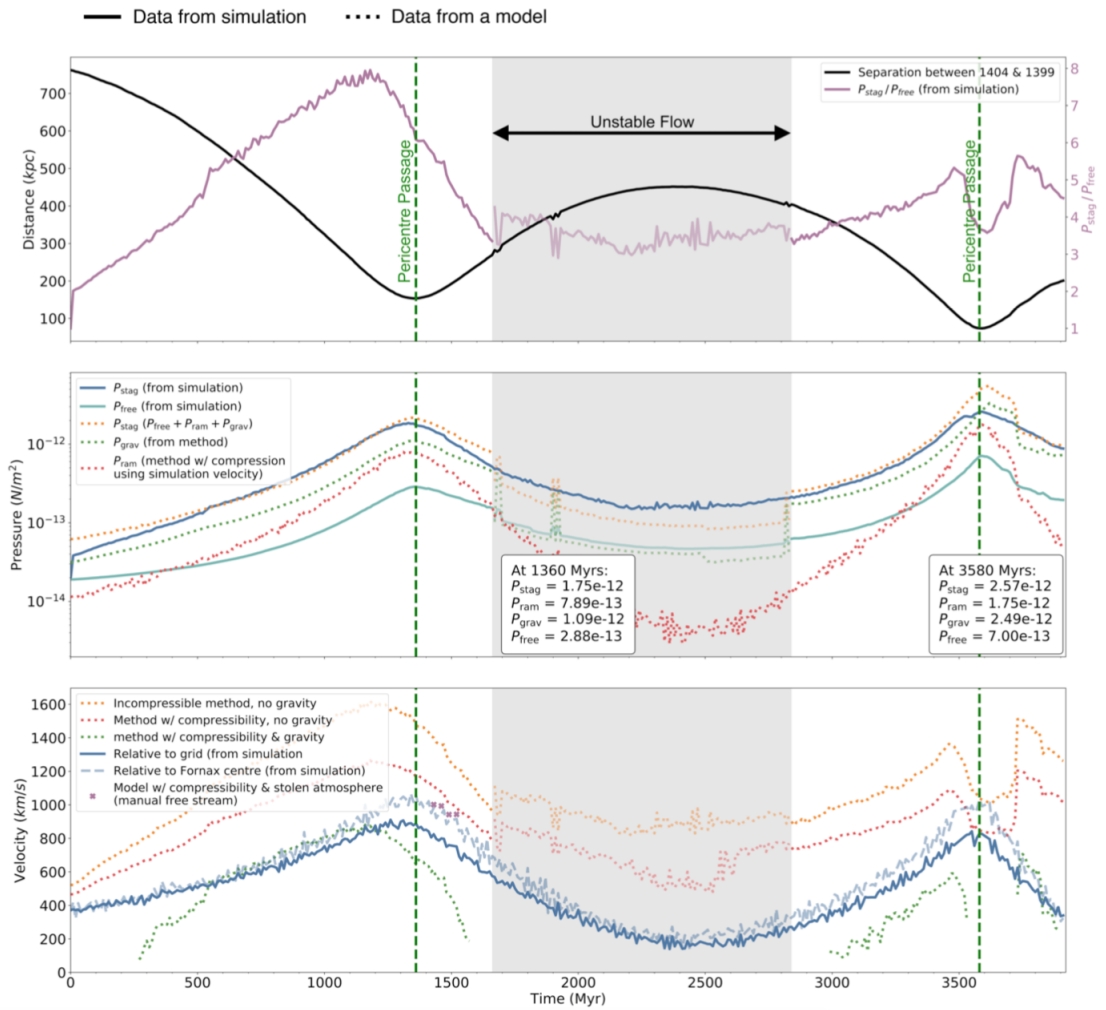


**Fig. 5.2:** Figure taken from Fish et al. (in preparation). These plots correspond to the V2 simulation of the infall of NGC 1404 in the Fornax Cluster as described in Chapter 3.

Top: The separation distance between the centre of NGC 1404 and the Fornax Cluster centre throughout the merger. The ratio of  $P_{stag}/P_{free}$  (as calculated directly from the simulation) is also annotated to show how it varies throughout the merger.

Middle: A comparison between the stagnation point pressure,  $P_{stag}$ , as calculated by the simulation (blue line), and the stagnation point pressure as calculated by the model (Eq. 5.16) which includes the stolen atmosphere effect (orange dotted line) along with its components;  $P_{free}$ ,  $P_{ram}$  and  $P_{grav}$  according to Eq. 5.26.

Bottom: A comparison of the infall velocity estimates of NGC 1404 by the different stagnation point models, as well as the velocity as calculated by the simulation with respect to the grid. During the period of unstable flow, the centroid could not be fit consistently for the stagnation point method with gravity, thus there are no values for the velocity estimate. Shortly after pericentre, there are additional velocity values over-plotted for the stagnation point method including gravity which used manually chosen free-stream locations as there were systematic issues in how these locations are defined.

Once the simulation has evolved past 0.5 Gyrs, the next period is established as the flow settles and becomes stable. This flow state continues until the galaxy nears pericentre passage. This period is the flow around a blunt body as the galaxy is being ram pressure stripped. Here, the ICM gas the galaxy is moving through is mostly undisturbed, which makes the defining of the free-stream variables a straight forward task. In this period, our full model predicts the stagnation pressure well, and the velocity derived from  $P_{\text{stag}}$ , accounting for  $P_{\text{grav}}$  agrees well with the velocity calculated directly by the simulation. However, the methods which do not include gravity significantly overestimate the infall velocity by about 60% in the compressible model and more in the incompressible model. As we predicted analytically, neglecting the gravitational pressure systematically overestimates the infall velocity of the galaxy. This is also made evident by the fact that the gravitational pressure is always higher than the ram pressure, as can be seen in Fig. 5.2.

As the galaxy nears pericentre and moves through it, the stagnation point method breaks down for two reasons. Near to the core of the cluster, there are steep gradients in the ICM variables, i.e., the temperature, pressure and density. Also, the galaxy becomes accelerated due to the gravitational attraction to the core which causes rapid changes to the state of the flow. As a result, it becomes an incredibly difficult task to define the free-stream variables. This is crucial when calculating  $P_{\text{grav}}$  as this depends strongly on the definition of  $T_{\text{free}}$ , thus minor changes to this value gives significant differences to the result. This becomes even more so for second pericentre passage, as now, as well as these features, there is significant sloshing ongoing in the cluster core which also acts to disrupt the flow, causing more problems in defining the free-stream variables.

Moving away from pericentre, the flow around the galaxy becomes unstable meaning that the stagnation point method cannot be applied - this period is highlighted by the grey box in Fig. 5.2. As described in Chapter 4, during the period where the galaxy moves away from pericentre toward apocentre, the ICM flow patterns around it become highly irregular as the galaxy decelerates rapidly and turns around at apocentre. Here, it even becomes difficult to define an upstream edge. Even more so, due to the chaotic nature of the ICM flow, the free-stream variables which the stagnation point method requires are far too difficult to define. Once the galaxy moves away from apocentre and begins its next infall into the cluster, a steady flow is established once again, with the galaxy once again being subjected to ram pressure stripping. However, bulk motions in the ICM now create a bias in the galaxy's estimated velocity, as any stagnation point method only measures the relative velocity between the ICM and the galaxy. When significant ICM bulk flows are present, this velocity differs from the galaxy's velocity w.r.t. the cluster centre.

## 5.6 Discussion and Conclusion

The stolen atmosphere effect is a phenomenon which naturally arises during the infall of a galaxy or subcluster into a cluster. The gravitational potential of the galaxy or subcluster compresses the gas in and around the infalling halo, causing a noticeable enhancement in temperature, density and pressure compared to the ambient ICM. Crucially, the infall

velocity of a galaxy or subcluster is typically calculated by using the stagnation point method. However, current stagnation point methods do not take into account the effect of the galaxy's or subclusters gravitational potential and therefore the enhancement in stagnation pressure because of it. We have presented a new stagnation point method which extends on the previous methods by taking into account the effects of gravity, i.e., the stolen atmosphere effect and applied this to the tailored Fornax minor merger simulations described in Chapter 3. We have shown that;

- both analytically and in a minor merger simulation, the enhancement of  $P_{\text{stag}}$  over  $P_{\text{free}}$  is due to both the ram pressure (i.e., the motion of the galaxy) and the galaxy's gravitational attraction and compression of the ambient ICM.
- $P_{\text{ram}}$  and  $P_{\text{grav}}$  can easily be equally as strong, thus attributing the enhancement of  $P_{\text{stag}}$  solely to the motion of the galaxy leads to overestimating the infall velocity by tens of percent. In other words, neglecting the gravitational pressure due to the galaxy's potential systematically overestimates the infall velocity.
- any estimate of the infall velocity during the approach to apocentre and around apocentre passage is almost impossible. This is not a surprise in hindsight, given the chaotic ICM flow in this phase as described in Chapter 4, Sec. 4.7.
- even during the second infall of a truly minor merger (mass ratio  $\sim 1:13$  for the Fornax minor merger), ICM bulk motions considerably bias the infall velocity measurement.

As we have shown, the stagnation point method can only be reasonably applied up until the point just before pericentre passage. Around pericentre, there are steep gradients in the ICM temperature, pressure and density which causes uncertainty when defining the sensitive free-stream variables required by stagnation point methods. After pericentre passage, as the galaxy or subcluster moves to apocentre, the flow becomes unstable (as shown in Chapter 4, Sec. 4.7), and is defined by chaotic motions up until the next infall. In this period, the free-stream variables cannot be fit as it is difficult to define the upstream edge of the galaxy, as the edge becomes disrupted due to the flow. Thus, the stagnation point method cannot be applied during this phase as they require a steady flow to calculate the free-stream variables. Only when the galaxy or subcluster moves away from apocentre, and is well underway on its next infall, do the flow patterns return to a stable state and the stagnation point methods can be applied again. However, it is not easy to define when this transition from not being able to use the stagnation point method to being able to use it occurs, i.e. when the ICM flow changes from non-steady to steady. One possibility is to use the smoothness of the upstream edge, say once a certain level of smoothness is attained, can the stagnation point method be realistically applied. Also the tail morphology of the galaxy can likely be used to define between the two periods of flow. As shown in Chapter 4, a slingshot tail is formed during the period of unstable flow, where the tail is characterised by a sharp edge between the tail gas and the ambient ICM, this is in

contrast to a ram pressure stripped tail which fades away continuously. Therefore the transition from the slingshot tail to a ram pressure stripped tail signifies the transition from unstable to stable flow. However, even at this point, there are still significant uncertainties in defining free-stream values, which makes it difficult to precisely measure the infall velocity, though the stagnation point method which includes the stolen atmosphere effect offers a considerable improvement in the estimation of the infall velocity.

The stolen atmosphere effect maybe be observable directly due to its temperature and density enhancement which surrounds the upstream edge of a galaxy or subcluster, as shown in Eqs. 5.23 and 5.24 and Fig. 5.1. In observations however, this may be interpreted as a region of shock heated gas due to a bow shock instead of a stolen atmosphere and is therefore potentially misleading. Thus, care should be taken when considering whether the temperature and density enhancement is due to a bow shock or is actually this stolen atmosphere effect.

# Chapter 6

## Concluding Remarks and Future Work

### 6.1 The New, Holistic View of a Minor Merger

The goal of this thesis was to provide the first holistic study of binary cluster minor mergers by taking into account the effects on both merger partners simultaneously. In result, we are now able to develop a more complete picture for the different phases of a minor binary merger. In the following, we describe how a minor binary merger proceeds, detailing the effects on both the secondary and the primary from the first infall up until reaching second apocentre. Table 6.1 provides a summary of the merger phases and corresponding effects on the primary and secondary.

#### 6.1.1 Initial Conditions

A minor binary merger is generally defined as merger with a mass ratio lower than 1:3 between the primary, i.e., a cluster, and the secondary, i.e., a galaxy or subcluster (Planelles & Quilis, 2009; Vitvitska et al., 2002). From analysis of cosmological simulations, Vitvitska et al. (2002) showed that the infall velocity of the secondary at the virial radius of the primary is normally distributed, centred around  $\sim 1.1v_c$ , where  $v_c$  is the circular velocity of the primary. Furthermore, Vitvitska et al. (2002) showed that for a minor binary merger, the tangential component of the infall velocity for the secondary is typically  $0.71v_c$ . Idealised minor binary merger simulations therefore sample a range of infall velocities based on the distributions from Vitvitska et al. (2002), as was done in Poole et al. (2006), ZuHone (2011) and in our simulations.

#### 6.1.2 First Infall

On the first infall into the primary, the secondary is subjected to ram pressure due to the ICM head-wind producing a long, cool, unmixed tail which traces its orbit path. This process has been comprehensively described by Roediger et al. (2015a) and confirmed in our simulations, e.g. Fig. 3.7 and Fig: 4.2. Here, the gas atmosphere of the secondary is pushed back downstream, and is stripped of gas along its sides. The downstream atmosphere of the galaxy is shielded from the ICM headwind and thus forms the remnant gas tail.

Depending on the mass ratio, i.e., mass ratios closer to 1:3, the atmosphere of the secondary may simply appear deformed rather than producing a long tail as seen in Fig. 10 and 11 in ZuHone (2011). The first infall is typically supersonic (Vitvitska et al., 2002) thus a bow shock forms in front of the secondary. Additionally as shown in Fig. 5.2, the stolen atmosphere starts being established, enhancing the temperature around the upstream atmosphere of the secondary. As for the primary, there is no major effect during the first infall, apart from slight asymmetry due to the movement of the bow shock from the infalling secondary through the ICM.

### 6.1.3 First Pericentre to First Apocentre

As the secondary moves through pericentre and approaches apocentre, the gas atmosphere of the secondary is often still not fully stripped. In this phase, as described in Chapter 4, the secondary will develop a slingshot tail. As the secondary slows down due to dynamical friction, the ram pressure acting on the secondary atmosphere rapidly decreases causing the gas tail to be slingshotted toward the secondary producing a slingshot tail. Depending on the impact parameter of the binary merger, the slingshot tail will either be one of two extreme cases; an arc-shaped slingshot tail or an overrun slingshot tail (however it is noted that there is likely an intermediate regime containing elements of the two cases). For the arc-shaped case, this slingshot tail arises when the impact parameter of the merger is large and produces a prominent arc-shaped tail which can point perpendicular to the secondary's direction of motion as the tail slingshots to one side. For the overrun case, this slingshot tail form occurs when the impact parameter is small and causes the tail to slingshot directly over the secondary. It first produces a phase in which the secondary has an irregular shaped atmosphere as the slingshotting tail is directly over the secondary. Then as the tail continues to overshoot, it fans outward along the orbit direction away from the secondary. As the secondary turns around at apocentre, the bow shock which was once leading the secondary continues to propagate outward along the orbit direction producing a detached bow shock. Thus, a shock can be located behind the secondary. Crucially during this merger phase, the secondary is not being ram pressure stripped, thus the morphology of the tail is influenced by tidal forces more than ram pressure. Furthermore the flow patterns in the slingshot tail phase are highly irregular and do not reflect the steady flow which is assumed in the classic ram pressure stripped tail case. Therefore, a slingshot tail should not be characterised as a classic ram pressure stripping tail as it does not accurately describe the physical processes occurring during the slingshot tail phase.

As for the primary during this phase, sloshing is initiated in the core due to the passage of the secondary. This process of sloshing has been described in detail by Ascasibar & Markevitch (2006); Markevitch & Vikhlinin (2007); Roediger et al. (2011); ZuHone et al. (2013). Additionally, the core will show elongation in the direction toward the secondary and for close pericentre passages, the core may even be destroyed. The detached bow shock of the secondary will continue to propagate outward out into the outskirts of the cluster's ICM. Significantly, the wake of the secondary may appear as a characteristic

brightness edge in the primary, thus revealing the orbit path of the merger, as seen in our simulations in Fig. 3.9.

#### 6.1.4 Second Infall

On the second infall into the primary, the gas atmosphere of the secondary is now significantly stripped, with a truncated atmosphere and a well mixed remnant tail as can be seen in our simulations in Fig. 3.7 and Fig. 3.11. The secondary will continue to be stripped mostly via the KHI. In this phase the ambient ICM flow patterns surrounding the secondary return to a stable flow, however it is now exposed to ICM bulk motions originating from the first infall. Again the stolen atmosphere effect remains present during the second infall enhancing the temperature around the upstream halo.

The sloshing triggered from the first infall continues to evolve in the primary, as the sloshing cold fronts move further outwards. For second infall cases, this sloshing cold front will appear on the same side of the cluster as the secondary, as can be seen in our simulations in Fig. 3.8. The ICM bulk motions initiated from the first passage of the secondary are still active in the primary, and depending on the velocity of the secondary, a bow shock will be present leading it. Again the wake of the secondary may appear as a characteristic brightness edge revealing the previous orbit path.

#### 6.1.5 Second Pericentre to Second Apocentre

At this stage in the binary merger, the secondary is significantly stripped and may have even lost all of its gas depending on how close the previous core passages were. However, if the secondary is able to hold on to its remnant tail during the second core passage, it will again form a slingshot tail as it approaches second apocentre. As for the primary, the sloshing in the core originating from the first infall dominates the merger picture. The sloshing has now evolved further producing prominent cold fronts. The most prominent cold front is located on the opposite side of the primary to the secondary as can be seen in our simulations in Fig 3.8. As with the previous apocentre passage, the detached bow shock of the secondary (produced from this most recent core passage) propagates outward into the outskirts of the primary's ICM. Again, in the ICM, the wake of the previous core passage and even the first core passage, may be present as characteristic brightness edges revealing the path of destruction caused by the minor merger of the secondary.

#### 6.1.6 Implications

With this new, more complete picture of minor binary mergers, we have shown that by following the evolution of the gas tail of the secondary and the primary as a whole, we can distinguish between key phases of a minor merger, demonstrating that the features of the gas tail of the secondary can be related to the features of the cluster. We have reclassified several gas tails in the literature as slingshot tails (see Section 4.9). This is important because in this slingshot phase, the ambient ICM flow is distinctly different from

**Table 6.1:** Summary of the Minor Binary Merger Phases. SA - stolen atmosphere, DBS - detached bow shock.

Merger Phase	Features of Secondary	Features of Primary
First infall	Long, cool, unmixed tail along orbit path.	Slight asymmetry.
First pericentre to first apocentre	Not fully stripped. Slingshot tail forms. ICM flow chaotic. SA present.	Core starts sloshing. DBS in ICM. Turbulent wake of secondary.
Second infall	Truncated atmosphere. Faint short tail. ICM flow stable. SA present.	Sloshing continues. Cold front moves outward located on same side as secondary. ICM bulk motions active.
Second pericentre to second apocentre	Truncated atmosphere. Significantly stripped. Slingshot tail forms if remnant tail still present. ICM flow chaotic. SA present.	Sloshing continues. Prominent cold front on opposite side to secondary. DBS in ICM.

the ram pressure scenario during the infall stages, and therefore caution is needed for any interpretations that rely on the ram pressure scenario, such as the measurement of velocity using the stagnation point method or the identification of locations of clear shear flows for measurements of gas mixing.

We have pointed out potential difficulties of applying classic stagnation point methods to measure the infall velocity of a secondary. We find that these methods are not applicable at all around the apocentre of the binary merger due to chaotic ICM flow patterns which surround the secondary. We have demonstrated that the gravitational potential of the secondary compresses the surrounding ICM gas causing an enhancement of temperature, pressure and density compared to the ambient ICM, producing a stolen atmosphere effect. We have shown that this stolen atmosphere may be visible although it can potentially be mis-identified as a bow shock due to its similar enhancement of the gas properties. This stolen atmosphere effect can provide a significant contribution to the stagnation point pressure, and thus, we find that using a stagnation point method which ignores the gravitational potential of the secondary, systematically overestimates the infall velocity by tens of percent.

We have applied this holistic view to the specific case of the Fornax Cluster and have successfully been able to simultaneously match the features of the cluster to that of the infall of NGC 1404. Independent of the choice of initial velocity and impact parameter, the simulations were able to constrain the merger history of the cluster over the last few Gyrs. The simulations were able to replicate all the main merger features in both NGC 1404 and Fornax, this included the truncated atmosphere and remarkably short gas tail of NGC 1404, and the location of the sloshing cold fronts in the cluster core. Results showed that a

first infall scenario can be firmly excluded, and that a second or more likely third infall was the more likely scenario due to the match with the sloshing fronts observed in Fornax. The simulations also provided several predictions including the location of a detached bow shock and the wake of NGC 1404, as well as the locations of enhanced turbulence and metallicity as a result of the minor merger. Importantly, this work has demonstrated how the features of the galaxy during a minor merger can be related to the overall features of a cluster and vice versa. Furthermore, this work has also demonstrated the effectiveness of being able to tailor a simulation to a real system to understand its recent growth history.

## 6.2 Future Work

The results of this thesis, and the simulations themselves, provide a wealth of opportunities for future avenues of work to be pursued, the ongoing stolen atmosphere work in Chapter 5 is an example of this. In what follows, examples of future work are outlined.

### 6.2.1 The Globular Cluster Content of NGC 1404 and NGC 1399

The Fornax merger scenario in Chapter 5 is derived almost solely from X-ray data, i.e., the features of the ICM and NGC 1404. However, the merger should affect other parts of the cluster and member galaxies which would produce features which are not available in the X-ray regime. An interesting point raised in the Fornax merger scenario is that the encounter between NGC 1404 and the BCG galaxy in Fornax, NGC 1399, could potentially explain the observed globular cluster contents in both galaxies. Globular clusters (GCs) are densely packed, spheroidal collections of stars (on the order of  $10^4$  to  $10^5$  stars), with typical masses of  $\sim 10^5 M_{\odot}$  (Fall & Zhang, 2001) bound together by gravity and are thought to exist in all galaxies (Hudson et al., 2014). GCs contain little to no gas, implying they are no longer star forming, and thus consist of an old population of stars with low metallicities - the oldest populations of GCs have an average age of  $\sim 12.8$  Gyr (Marín-Franch et al., 2009). The stars in GCs are considered to be a single stellar population as they are thought to have all formed at the same time from the same nebula. Significantly, GCs can act as good passive tracers of the gravitational forces (Brodie & Strader, 2006), thus GCs are important tools for astrophysicists and cosmologists as they can be used as probes for understanding, e.g., the age of the universe (e.g. Krauss & Chaboyer 2003), stellar evolution (e.g. Dotter et al. 2007), the dark matter distribution in early-type galaxies (e.g. Pota et al. 2015; Zhu et al. 2016) as well as their formation (e.g. Chaboyer et al. 1995; Li & Gnedin 2014). GCs are typically located in the outer halo of galaxies, thus they are prone to being stripped away by tidal forces during encounters with other galaxies or clusters. Several clusters have been found to have a population of GCs in the ICM around the core of the cluster, e.g. Coma Cluster (Peng et al., 2011), Fornax Cluster (D’Abrusco et al., 2016), Abell 1689 (Alamo-Martínez et al., 2013) and Abell 1185 (West et al., 2011). These GCs may have originated in cluster galaxies previously, but were stripped away due to merging with the cluster. Using numerical simulations of mergers in a Virgo-like cluster,

Ramos et al. (2015) investigated the evolution of GC populations. Ramos et al. (2015) showed that the stripping of GCs from cluster galaxies is a continuous and viable process that increases with the number of passages with the cluster core. In the case of Fornax, Iodice et al. (2017) find that there are many sources of intra-cluster light (ICL) around the Fornax core which is made up of stars and GCs as a result of dynamic activity in the cluster. Forbes et al. (1998) measured the specific frequency  $S_N$  (a parameter which describes the total number of GCs in terms of galaxy luminosity) of NCG 1399 and NGC 1404 to find that NGC 1399 had a  $S_N = 11.5$  and NGC 1404  $S_N = 2.0$ . As the average  $S_N$  for a cluster elliptical galaxy is 5.0, Forbes et al. (1998) showed that NGC 1399 has a much higher  $S_N$  than average and NGC 1404 a lower  $S_N$  than average. Additionally, Bassino et al. (2006) discovered a GC bridge between NGC 1399 and NGC 1404 suggesting a possible interaction between the two systems. Potentially, the merger scenario from Chapter 3 can offer an explanation to the observed GC content in NGC 1404 and NGC 1399. The second or third infall scenario would offer a significant opportunity for GCs to be stripped from NGC 1404 during its encounters with the central BCG galaxy NGC 1399 which could then accumulate onto NGC 1399. This would give the low  $S_N$  for NGC 1404 and the high  $S_N$  for NGC 1399. This would coincide with the result from Ramos et al. (2015) that the GC stripping process is a continuous process that increases with the number of core passages. Along the same line of thought, Bekki et al. (2003) used numerical simulations to explain the GC content of NGC 1404 and NGC 1399 in Fornax. They found that the observed  $S_N$  value of NGC 1404 can only be replicated if NGC 1404 is tidally stripped on a highly eccentric orbit. However, in Bekki et al. (2003), both galaxies orbit each other rather closely, following rather idealised orbits, whereas our merger scenario is derived from the overall cluster ICM distribution. Therefore, by adapting the simulations in this work to analyse the GC content of NGC 1404 and NGC 1399, a deeper analysis of the scenario can be achieved. This is currently a project being undertaken by MSc student Ben Marshall and my supervisor Dr Elke Roediger. Firstly, a set of dark matter particles that can represent GCs in the simulations need to be selected. These particles or GCs can then be marked and tracked throughout the simulation to observe their evolution. This could be done for a range of initial merger conditions to see how this affects the tidal stripping and eventual fate of the GCs. This analysis would be able to quantify the tidal stripping process (including stripping timescales) and compare to the kinematical properties of the GCs and could then possibly confirm if the GC content in both NGC 1399 and NGC 1404 can be attributed to the merger of NGC 1404 and Fornax. This would also represent a test of the proposed merger scenario with a completely independent dataset, and could therefore provide substantial evidence to the proposed merger scenario. Furthermore, the dynamics of the representative GCs could potentially be calculated to determine their properties, this can then be used by observers to understand observed GCs. For example, stripped GCs from galaxies should be more dynamically active than GCs which were not stripped, thus observers can attempt to disentangle their history.

### 6.2.2 Probing the Viscosity of the ICM

The simulations of the the Fornax merger in Chapter 3 were able to accurately reproduce the observed merger features in both Fornax and NGC 1404 and thus offer a useful laboratory for probing the properties of the ICM. In this regard, a logical expansion to these simulations is to include the effect of viscosity. As indicated by the results of the simulations, in particular the characteristics of the gas tail of NGC 1404, the Fornax ICM must be of low viscosity to replicate the well-mixed, stripped tail of the galaxy. Thus the stripped tail can be used to constrain the ICM viscosity. A low viscosity of the Fornax ICM was also predicted by Su et al. (2017b). A high level of viscosity would prevent mixing in the gas tail and wake of the galaxy so that cool galactic gas remains intact, likely in the form of strands as was shown in Roediger et al. (2015b). Furthermore, viscosity will inhibit the production of KHI along cold fronts, thus their presence can indicate the level of viscosity in the ICM. Thus, by performing a parameter exploration for the level of viscosity in the Fornax simulations, results can then be compared to observations of the cluster to constrain the ICM viscosity. We could also make predictions for the effect of viscosity for observations with the Chandra X-ray telescope and then make a measurement of the viscosity.

### 6.2.3 Deeper Analysis on Slingshot Tails

A logical extension to the work in this thesis would be to provide a deeper analysis into slingshot tails, in particular as to exactly why either the arc-shape or overrun form occurs, or any other intermediate regime. Further, it would be interesting to see how viscosity plays a role in the formation of slingshot tails too, such that a parameter exploration for viscosity could be implemented to see how this impacts on their formation. Additionally, Chapter 4 identified possible candidates of X-ray tails in the literature which are likely slingshot tails, to confirm this statement, tailored simulations of each could be produced.

### 6.2.4 Observational Aids for Minor Merger Interpretation

Future telescope missions such as the Large Synoptic Survey Telescope (LSST) and eRosita will provide extensive maps of the night sky in the optical and X-ray regimes respectively. To help with these future observations, we could set up a series of minor merger mock X-ray images using our simulations to document the evolution of the merger. This could then be used as a diagnostic to aid identification and interpretation of minor mergers - this would be in a similar vein as the Galaxy Cluster Merger Catalog produced by ZuHone & Kowalik (2016). In this regard, the mock images could help disentangle features of an already known merger or even help to determine a previously unknown minor merger. However, this would require more simulations of minor mergers which sample a range of cluster shapes (i.e. gravitational potentials and gas atmospheres) and infall histories. This would test how important the inclusion of the BCG potential into the initial cluster setup (as was done in the Fornax simulations) is to the overall merger history.

## 6.2.5 Predicting Future High-Resolution X-ray Observations

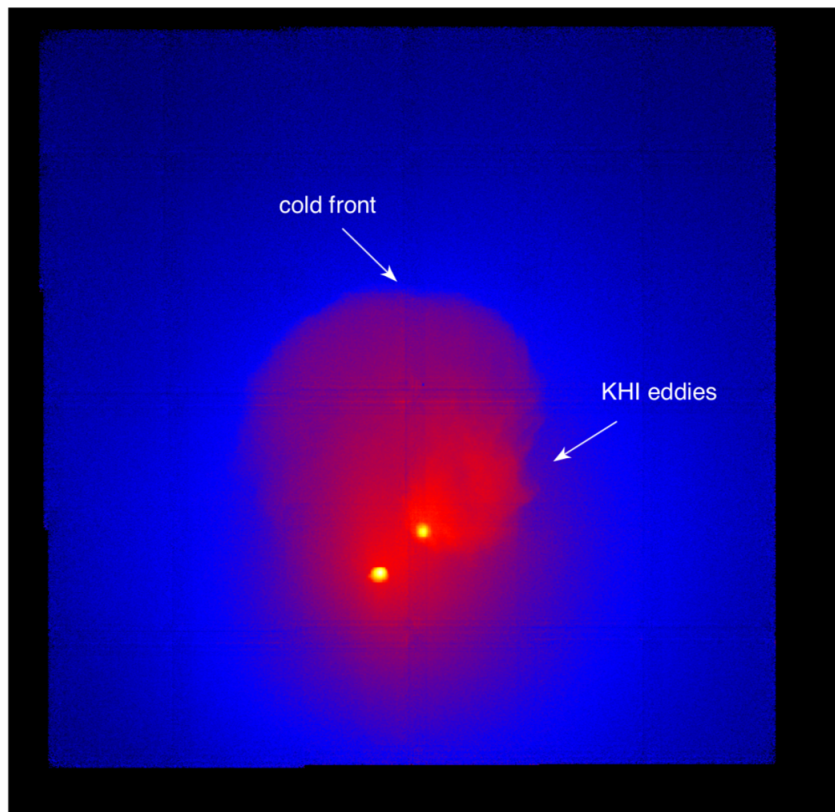


**Fig. 6.1:** A Simulated Athena WFI 3x3 30ks mosaic observations of the Fornax Cluster made using SOXS from the V2 simulation in Sheardown et al. (2018) at the best observed timestep in the 0.5-2.0 keV energy band. The increased resolution of WFI allows for the finer substructures along the sloshing cold fronts to be observed out to large radii. Image made by Yuanyuan Su from my simulation data.

The simulations of the Fornax merger in this work provide an opportunity to predict future high-resolution X-ray observations of clusters. To this end, the simulations have been used as a part of a proposed Astro2020 Science white paper titled 'A Unification of the Micro and Macro Physics in the Intracluster Medium of Nearby Clusters' led by Yuanyuan Su of which I am a co-author. This white paper outlines how the next generation of X-ray telescopes coming online in the next decade, such as XARM, Athena and Lynx, will be able to study gas dynamics in clusters and put quantitative constraints on the transport coefficients of the ICM. The Athena X-ray Telescope consists of two instruments; the Wide Field X-ray imager (WFI) which has an energy range of 0.2 - 15 keV and an 40' x 40' field of view (Meidinger et al., 2017) allowing for the ICM to be imaged out to large radii for the first time, and the X-ray Integral Field Unit (X-IFU) which offers high spectral and spatial resolution microcalorimeter of 2.5 eV over a 5'x5' field of view (Barret et al., 2018).

To gain an insight into the level of detail Athena can achieve, Fig. 6.1 presents a mock WFI 3x3 30ks mosaic for the V2 Fornax merger simulation at the best matching timestep made using SOXS 2.2.0 (a python based, X-ray observation simulator). This figure demonstrates how successful the WFI is at capturing the finer structures in the core of Fornax, particularly the structures along the sloshing cold fronts as KHIs and eddies

can be observed. As the Fornax merger simulations predicted the location of NGC 1404's previous wake and a detached bow shock south of the galaxy, both of which are beyond the reach of existing observations, future X-ray missions could be used to locate these regions, which if found, would cement the growth history of the cluster and demonstrate even more so the effectiveness of tailored simulations. For the first time, the WFI will allow for a deep study into the physics at the outskirts of galaxy clusters. The gas dynamics of the ICM in these regions, i.e., around the virial radius of the cluster, can be studied in detail which will provide further insight into the formation processes of clusters and large scale structure in general (Walker et al., 2019). For example, using the simulations of the Fornax merger, the simulated data can be compared to observations of the Fornax cluster outskirts to study the gas dynamics in these regions. Slingshot tails can also play a role here too, as the slingshot phase occurs at the apocentre of the merging orbit, which can be close to the virial radius. The slingshot phase has demonstrated that there are irregular flow patterns surrounding the galaxy or subcluster and hence offer an interesting tool to study the gas dynamics in this regime. The identified examples of slingshot tails in the literature discussed in Chapter 4 offer a potential basis to do this. Furthermore, the X-IFU instrument could potentially measure the kinematics of the ICM (see next paragraph) in and around the secondary during the slingshot phase and confirm whether the flow is turbulent as is predicted by the simulations.

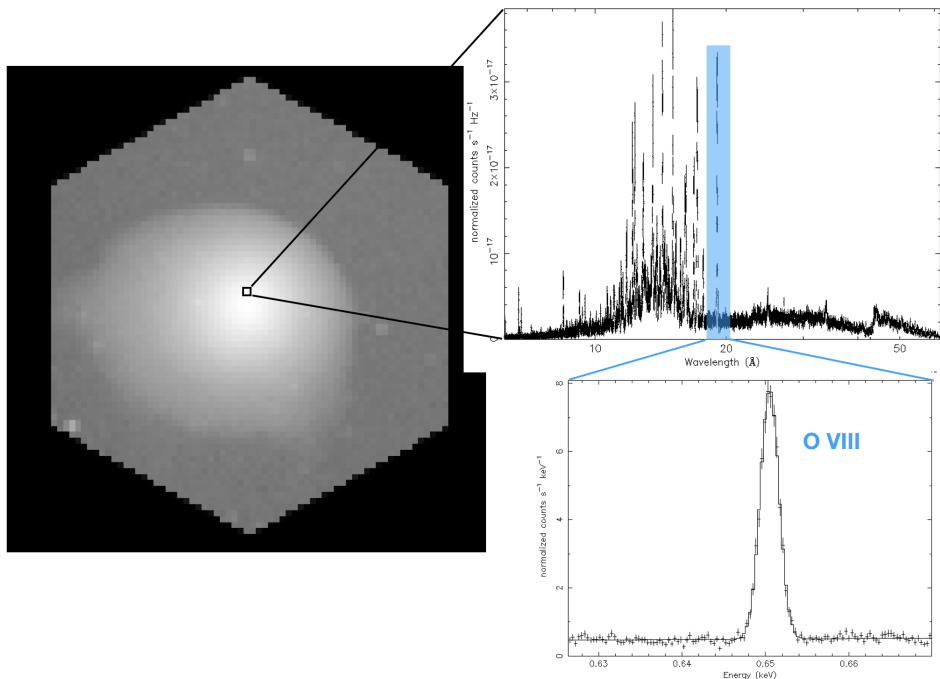


**Fig. 6.2:** A mock 100 ks Athena X-IFU observation made using SOXS of NGC 1404 from the V2 simulation in Sheardown et al. (2018) in the 0.5–2.0 keV energy band. The spectrum of the galaxy reveals the isolated and bright O VIII line which can be used to constrain its gas dynamics. Made by Yuanyuan Su from my simulation data.

The calorimeter on the X-IFU instrument will allow for line of sight gas motions in the ICM to be studied to an unprecedented level of detail due to its high spatial and spectral resolution. Line of sight gas motions can be measured by observations of the gas velocity via centroid-shift (Ota et al., 2007; Ueda et al., 2019), and velocity dispersion

via broadening of emission lines based on the Doppler effect (Roncarelli et al., 2018). At present, these measurements are observationally challenging due to the current energy resolution of X-ray telescopes, however the X-IFU will provide a significant improvement on this (Roncarelli et al., 2018). For low mass clusters and galaxies, such as Fornax and NGC 1404, the O VIII line at 0.654 keV is bright and isolated in their spectrum. Thus, the centroid and broadening of this emission line can be used to measure the velocity of the gas, and hence can be used to probe for turbulence. Figure 6.2 presents a mock 200 ks X-IFU observation of NGC 1404 from the V2 simulation made with SOXS demonstrating the bright isolated peak of the O VIII line. The simulations in Chapter 3 predicted likely regions of turbulence caused by NGC 1404 merging with Fornax. Therefore, these simulations provide a map of where potentially turbulent gas regions exist. For example, observations by the X-IFU could be concentrated on these regions to confirm for the presence of turbulence, which would then provide an opportunity to study the ICM under turbulent conditions. Furthermore, our simulations showed that the entire merger history was imprinted in the temperature and metallicity distributions of the cluster. The metallicity distribution will be available with the X-IFU as metal abundances which will be able to be mapped out to large radii. Biffi et al. (2018) stated that merging substructures are the key factor in the metallicity content in the ICM of present day clusters rather than in situ enrichment. Thus, the X-IFU and other future high-resolution X-ray telescope observations could significantly probe the formation processes of clusters.

### 6.2.6 Summary of Future Work

The simulations in this work have successfully demonstrated that, provided the dynamics of a merger are captured correctly, then many observed features of minor mergers can be explained by considering the simultaneous evolution of the primary and secondary merger partner. From an observational standpoint, we are in the position to measure a wealth of subtle features that give insights into additional cluster physics, e.g., ICM microphysics, turbulence and relativistic particle acceleration. However, we have shown that the cluster's dynamical conditions matter enormously, and that correct conclusions about the additional cluster physics can only be drawn with the correct interpretation of the dynamics, which can be determined through simulations. Thus, over the coming decade with the new, advanced telescopes coming online, utilising simulations such as those in this work combined with the wealth of observational data that will be collected will transform our understanding of galaxy clusters.

# References

- Abbott, B., Abbott, R., Abbott, T., Abernathy, M., Acernese, F., Ackley, K., Adams, C., Adams, T., Addesso, P., Adhikari, R., Adya, V., Affeldt, C., Agathos, M., Agatsuma, K., Aggarwal, N., Aguiar, O., Aiello, L., Ain, A., Ajith, P., Allen, B., Allocca, A., Altin, P., Anderson, S., Anderson, W., Arai, K., Arain, M., Araya, M., Arceneaux, C., Areeda, J., Arnaud, N., Arun, K., Ascenzi, S., Ashton, G., Ast, M., Aston, S., Astone, P., Aufmuth, P., Aulbert, C., Babak, S., Bacon, P., Bader, M., Baker, P., Baldaccini, F., Ballardini, G., Ballmer, S., Barayoga, J., Barclay, S., Barish, B., Barker, D., Barone, F., Barr, B., Barsotti, L., Barsuglia, M., Barta, D., Bartlett, J., Barton, M., Bartos, I., Bassiri, R., Basti, A., Batch, J., Baune, C., Bavigadda, V., Bazzan, M., Behnke, B., Bejger, M., Belczynski, C., Bell, A., Bell, C., Berger, B., Bergman, J., Bergmann, G., Berry, C., Bersanetti, D., Bertolini, A., Betzwieser, J., Bhagwat, S., Bhandare, R., Bilenko, I., Billingsley, G., Birch, J., Birney, R., Birnholtz, O., Biscans, S., Bisht, A., Bitossi, M., Biwer, C., Bizouard, M., Blackburn, J., Blair, C., Blair, D., Blair, R., Bloemen, S., Bock, O., Bodiya, T., Boer, M., Bogaert, G., Bogan, C., Bohe, A., Bojtos, P., Bond, C., Bondu, F., Bonnand, R., Boom, B., Bork, R., Boschi, V., Bose, S., Bouffanais, Y., Bozzi, A., Bradaschia, C., Brady, P., Braginsky, V., Branchesi, M., Brau, J., Briant, T., Brillet, A., Brinkmann, M., Brisson, V., Brockill, P., Brooks, A., Brown, D., Brown, D., Brown, N., Buchanan, C., Buikema, A., Bulik, T., Bulten, H., Buonanno, A., Buskulic, D., Buy, C., Byer, R., Cabero, M., Cadonati, L., Cagnoli, G., Cahillane, C., Bustillo, J. C., Callister, T., Calloni, E., Camp, J., Cannon, K., Cao, J., Capano, C., Capocasa, E., Carbognani, F., Caride, S., Diaz, J. C., Casentini, C., Caudill, S., Cavaglià, M., Cavalier, F., Cavalieri, R., Cella, G., Cepeda, C., Baiardi, L. C., Cerretani, G., Cesarini, E., Chakraborty, R., Chalermongsak, T., Chamberlin, S., Chan, M., Chao, S., Charlton, P., Chassande-Mottin, E., Chen, H., Chen, Y., Cheng, C., Chincarini, A., Chiummo, A., Cho, H., Cho, M., Chow, J., Christensen, N., Chu, Q., Chua, S., Chung, S., Ciani, G., Clara, F., Clark, J., Cleva, F., Coccia, E., Cohadon, P.-F., Colla, A., Collette, C., Cominsky, L., Constancio, M., Conte, A., Conti, L., Cook, D., Corbitt, T., Cornish, N., Corsi, A., Cortese, S., Costa, C., Coughlin, M., Coughlin, S., Coulon, J.-P., Countryman, S., Couvares, P., Cowan, E., Coward, D., Cowart, M., Coyne, D., Coyne, R., Craig, K., Creighton, J., Creighton, T., Cripe, J., Crowder, S., Cruise, A., Cumming, A., Cunningham, L., Cuoco, E., Canton, T. D., Danilishin, S., D'Antonio, S., Danzmann, K., Darman, N., Da Silva Costa, C., Dattilo, V., Dave, I., Daveloza, H., Davier, M., Davies, G., Daw, E., Day, R., De, S., DeBra, D., Debreczeni, G., Degallaix, J., De Laurentis, M., Deléglise, S., Del Pozzo, W., Denker, T., Dent, T., Dereli, H., Dergachev, V., DeRosa, R., De Rosa, R., DeSalvo, R., Dhurandhar, S., Díaz, M., Di Fiore, L., Di Giovanni, M., Di Lieto, A., Di Pace, S., Di Palma, I., Di Virgilio, A., Dojcinoski, G., Dolique, V., Donovan, F., Dooley, K., Doravari, S., Douglas, R., Downes, T., Drago, M., Drever, R., Driggers, J., Du, Z., Ducrot, M., Dwyer, S., Edo, T., Edwards, M., Effler, A., Eggenstein, H.-B., Ehrens, P., Eichholz, J., Eikenberry, S., Engels, W., Essick, R., Etzel, T., Evans, M., Evans, T., Everett, R., Factourovich, M., Fafone, V., Fair, H., Fairhurst, S., Fan, X., Fang, Q., Farinon, S., Farr, B., Farr, W., Favata, M., Fays, M., Fehrmann, H., Fejer, M., Feldbaum, D., Ferrante, I., Ferreira, E., Ferrini, F., Fidecaro, F., Finn, L., Fiori, I., Fiorucci, D., Fisher, R., Flaminio, R., Fletcher, M., Fong, H., Fournier, J.-D., Franco, S., Frasca, S., Frasconi, F., Frede, M., Frei, Z., Freise, A., Frey, R., Frey, V., Fricke, T., Fritschel, P., Frolov, V., Fulda, P., Fyffe, M., Gabbard, H., Gair, J., Gammaitoni, L., Gaonkar, S., Garufi, F., Gatto, A., Gaur, G., Gehrels, N., Gemme, G., Gendre, B., Genin, E., Gennai, A., George, J., Gergely, L., Germain, V., Ghosh, A., Ghosh, A., Ghosh, S., Giaime, J., Giardina, K., Giazotto, A., Gill, K., Glaefke, A., Gleason, J., Goetz, E., Goetz, R., Gondan, L., González, G., Castro, J. G., Gopakumar, A., Gordon, N., Gorodetsky, M., Gossan, S., Gosselin, M., Gouaty, R., Graef, C., Graff, P., Granata, M., Grant, A., Gras, S., Gray, C., Greco, G., Green, A., Greenhalgh, R., Groot, P., Grote, H., Grunewald, S., Guidi, G., Guo, X., Gupta, A., Gupta, M., Gushwa, K., Gustafson, E., Gustafson, R., Hacker, J., Hall, B., Hall, E., Hammond, G., Haney, M., Hanke, M., Hanks, J., Hanna, C., Hannam, M., Hanson, J., Hardwick, T., Harms, J., Harry, G., Harry, I., Hart, M., Hartman, M., Haster, C.-J., Haughian, K., Healy, J., Heefner, J., Heidmann, A., Heintze, M., Heinzl, G., Heitmann, H., Hello, P., Hemming, G., Hendry, M., Heng, I., Hennig, J., Heptonstall, A., Heurs, M., Hild, S., Hoak, D., Hodge, K., Hofman, D., Hollitt, S., Holt, K., Holz, D., Hopkins, P., Hosken, D., Hough, J., Houston, E., Howell, E., Hu, Y., Huang, S., Huerta, E., Huet, D., Hughey, B., Husa, S., Huttner, S., Huynh-Dinh, T., Idrisy, A., Indik, N., Ingram, D., Inta, R., Isa, H., Isac, J.-M., Isi, M., Islas, G., Isogai, T., Iyer, B., Izumi, K., Jacobson, M., Jacqmin, T., Jang, H., Jani, K., Jaranowski, P., Jawahar, S., Jiménez-Forteza, F., Johnson, W., Johnson-McDaniel, N., Jones, D., Jones, R., Jonker, R., Ju, L., Haris, K., Kalaghatgi, C., Kalogera, V., Kandhasamy, S., Kang, G., Kanner, J., Karki, S., Kasprzack, M., Katsavounidis, E., Katzman, W., Kaufer, S., Kaur, T., Kawabe, K., Kawazoe, F., Kéfélian, F., Kehl, M., Keitel, D., Kelley, D., Kells, W., Kennedy, R., Keppel, D., Key, J., Khalaidovski, A., Khalili, F., Khan, I., Khan, S., Khan, Z., Khazanov, E.,

- Kijbunchoo, N., Kim, C., Kim, J., Kim, K., Kim, N.-G., Kim, N., Kim, Y.-M., King, E., King, P., Kinzel, D., Kissel, J., Kleybolte, L., Klimenko, S., Koehlenbeck, S., Kokeyama, K., Koley, S., Kondrashov, V., Kontos, A., Koranda, S., Korobko, M., Korth, W., Kowalska, I., Kozak, D., Kringel, V., Krishnan, B., Królak, A., Krueger, C., Kuehn, G., Kumar, P., Kumar, R., Kuo, L., Kutynia, A., Kwee, P., Lackey, B., Landry, M., Lange, J., Lantz, B., Lasky, P., Lazzarini, A., Lazzaro, C., Leaci, P., Leavey, S., Lebigot, E., Lee, C., Lee, H., Lee, H., Lee, K., Lenon, A., Leonardi, M., Leong, J., Leroy, N., Letendre, N., Levin, Y., Levine, B., Li, T., Libson, A., Littenberg, T., Lockerbie, N., Logue, J., Lombardi, A., London, L., Lord, J., Lorenzini, M., Lorette, V., Lormand, M., Losurdo, G., Lough, J., Lousto, C., Lovelace, G., Lück, H., Lundgren, A., Luo, J., Lynch, R., Ma, Y., MacDonald, T., Machenschalk, B., MacInnis, M., Macleod, D., Magaña-Sandoval, F., Magee, R., Mageswaran, M., Majorana, E., Maksimovic, I., Malvezzi, V., Man, N., Mandel, I., Mandic, V., Mangano, V., Mansell, G., Manske, M., Mantovani, M., Marchesoni, F., Marion, F., Márka, S., Márka, Z., Markosyan, A., Maros, E., Martelli, F., Martellini, L., Martin, I., Martin, R., Martynov, D., Marx, J., Mason, K., Masserot, A., Massinger, T., Masso-Reid, M., Matichard, F., Matone, L., Mavalvala, N., Mazumder, N., Mazzolo, G., McCarthy, R., McClelland, D., McCormick, S., McGuire, S., McIntyre, G., McIver, J., McManus, D., McWilliams, S., Meacher, D., Meadors, G., Meidam, J., Melatos, A., Mendell, G., Mendoza-Gandara, D., Mercer, R., Merilh, E., Merzougui, M., Meshkov, S., Messenger, C., Messick, C., Meyers, P., Mezzani, F., Miao, H., Michel, C., Middleton, H., Mikhailov, E., Milano, L., Miller, J., Millhouse, M., Minenkov, Y., Ming, J., Mirshekari, S., Mishra, C., Mitra, S., Mitrofanov, V., Mitselmakher, G., Mittleman, R., Moggi, A., Mohan, M., Mohapatra, S., Montani, M., Moore, B., Moore, C., Moraru, D., Moreno, G., Morriss, S., Mossavi, K., Mours, B., Mow-Lowry, C., Mueller, C., Mueller, G., Muir, A., Mukherjee, A., Mukherjee, D., Mukherjee, S., Mukund, N., Mullavey, A., Munch, J., Murphy, D., Murray, P., Mytidis, A., Nardecchia, I., Naticchioni, L., Nayak, R., Nacula, V., Nedkova, K., Nelemans, G., Neri, M., Neunzert, A., Newton, G., Nguyen, T., Nielsen, A., Nissanke, S., Nitz, A., Nocera, F., Nolting, D., Normandin, M., Nuttall, L., Oberling, J., Ochsner, E., O'Dell, J., Oelker, E., Ogín, G., Oh, J., Oh, S., Ohme, F., Oliver, M., Oppermann, P., Oram, R. J., O'Reilly, B., O'Shaughnessy, R., Ott, C., Ottaway, D., Ottens, R., Overmier, H., Owen, B., Pai, A., Pai, S., Palamos, J., Palashov, O., Palomba, C., Pal-Singh, A., Pan, H., Pan, Y., Pankow, C., Pannarale, F., Pant, B., Paoletti, F., Paoli, A., Papa, M., Paris, H., Parker, W., Pascucci, D., Pasqualetti, A., Passaquieti, R., Passuello, D., Patricelli, B., Patrick, Z., Pearlstone, B., Pedraza, M., Pedurand, R., Pekowsky, L., Pele, A., Penn, S., Perreca, A., Pfeiffer, H., Phelps, M., Piccinni, O., Pichot, M., Pickenpack, M., Piergiovanni, F., Pierro, V., Pillant, G., Pinard, L., Pinto, I., Pitkin, M., Poeld, J., Poggiani, R., Popolizio, P., Post, A., Powell, J., Prasad, J., Predoi, V., Premachandra, S., Prestegard, T., Price, L., Prijatelj, M., Principe, M., Privitera, S., Prix, R., Prodi, G., Prokhorov, L., Puncken, O., Punturo, M., Puppo, P., Pürerer, M., Qi, H., Qin, J., Quetschke, V., Quintero, E., Quitzow-James, R., Raab, F., Rabeling, D., Radkins, H., Raffai, P., Raja, S., Rakhmanov, M., Ramet, C., Rapagnani, P., Raymond, V., Razzano, M., Re, V., Reed, J., Reed, C., Regimbau, T., Rei, L., Reid, S., Reitze, D., Rew, H., Reyes, S., Ricci, F., Riles, K., Robertson, N., Robie, R., Robinet, F., Rocchi, A., Rolland, L., Rollins, J., Roma, V., Romano, J., Romano, R., Romanov, G., Romie, J., Rosińska, D., Rowan, S., Rüdiger, A., Ruggi, P., Ryan, K., Sachdev, S., Sadecki, T., Sadeghian, L., Salconi, L., Saleem, M., Salemi, F., Samajdar, A., Sammut, L., Sampson, L., Sanchez, E., Sandberg, V., Sandeen, B., Sanders, G., Sanders, J., Sassolas, B., Sathyaprakash, B., Saulson, P., Sauter, O., Savage, R., Sawadsky, A., Schale, P., Schilling, R., Schmidt, J., Schmidt, P., Schnabel, R., Schofield, R., Schönbeck, A., Schreiber, E., Schuette, D., Schutz, B., Scott, J., Scott, S., Sellers, D., Sengupta, A., Sentenac, D., Sequino, V., Sergeev, A., Serna, G., Setyawati, Y., Seigny, A., Shaddock, D., Shaffer, T., Shah, S., Shahriar, M., Shaltev, M., Shao, Z., Shapiro, B., Shawhan, P., Sheperd, A., Shoemaker, D., Shoemaker, D., Siellez, K., Siemens, X., Sigg, D., Silva, A., Simakov, D., Singer, A., Singer, L., Singh, A., Singh, R., Singhal, A., Sintès, A., Slagmolen, B., Smith, J., Smith, M., Smith, N., Smith, R., Son, E., Sorazu, B., Sorrentino, F., Souradeep, T., Srivastava, A., Staley, A., Steinke, M., Steinlechner, J., Steinlechner, S., Steinmeyer, D., Stephens, B., Stevenson, S., Stone, R., Strain, K., Straniero, N., Stratta, G., Strauss, N., Strigin, S., Sturani, R., Stuver, A., Summerscales, T., Sun, L., Sutton, P., Swinkels, B., Szczepańczyk, M., Tacca, M., Talukder, D., Tanner, D., Tápai, M., Tarabrin, S., Taracchini, A., Taylor, R., Theeg, T., Thirugnanasambandam, M., Thomas, E., Thomas, M., Thomas, P., Thorne, K., Thorne, K., Thrane, E., Tiwari, S., Tiwari, V., Tokmakov, K., Tomlinson, C., Tonelli, M., Torres, C., Torrie, C., Töyrä, D., Travasso, F., Traylor, G., Trifirò, D., Tringali, M., Trozzo, L., Tse, M., Turconi, M., Tuyenbayev, D., Ugolini, D., Unnikrishnan, C., Urban, A., Usman, S., Vahlbruch, H., Vajente, G., Valdes, G., Vallisneri, M., van Bakel, N., van Beuzekom, M., van den Brand, J., Van Den Broeck, C., Vander-Hyde, D., van der Schaaf, L., van Heijningen, J., van Veggel, A., Vardaro, M., Vass, S., Vasúth, M., Vaulin, R., Vecchio, A., Vedovato, G., Veitch, J., Veitch, P., Venkateswara, K., Verkindt, D., Vetrano, F., Viceré, A., Vinciguerra, S., Vine, D., Vinet, J.-Y., Vitale, S., Vo, T., Vocca, H., Vorvick, C., Voss, D., Voudsen, W., Vyatchanin, S., Wade, A., Wade, L., Wade, M., Waldman, S., Walker, M., Wallace, L., Walsh, S., Wang, G., Wang, H., Wang, M., Wang, X., Wang, Y., Ward, H., Ward, R., Warner, J., Was, M., Weaver, B., Wei, L.-W., Weinert, M., Weinstein, A., Weiss, R., Welborn, T., Wen, L., Weßels, P., Westphal, T., Wette, K., Whelan, J., Whitcomb, S., White, D., Whiting, B., Wiesner, K., Wilkinson, C., Willems, P., Williams, L., Williams, R., Williamson, A., Willis, J., Willke, B., Wimmer, M., Winkelmann, L., Winkler, W., Wipf, C., Wiseman, A., Wittel, H., Woan, G., Worden, J., Wright, J., Wu, G., Yablon, J., Yakushin, I., Yam, W., Yamamoto, H., Yancey, C., Yap, M., Yu, H., Yvert, M., Zadrożny, A., Zangrando, L., Zanolin, M., Zendri, J.-P., Zevin, M., Zhang, F., Zhang, L., Zhang, M., Zhang, Y., Zhao, C., Zhou, M., Zhou, Z., Zhu, X., Zucker, M., Zuraw, S., & Zweigig, J. 2016, *Physical Review Letters*, 116, 061102

- Abell, G. O. 1958, *The Astrophysical Journal Supplement Series*, 3, 211
- Acreman, D. M., Stevens, I. R., Ponman, T. J., & Sakelliou, I. 2003, *Monthly Notices of the Royal Astronomical Society*, 341, 1333
- Agertz, O., Moore, B., Stadel, J., Potter, D., Miniati, F., Read, J., Mayer, L., Gawryszczak, A., Kravtsov, A., Nordlund, Å., Pearce, F., Quilis, V., Rudd, D., Springel, V., Stone, J., Tasker, E., Teyssier, R., Wadsley, J., & Walder, R. 2007, *Monthly Notices of the Royal Astronomical Society*, 380, 963
- Akamatsu, H., Inoue, S., Sato, T., Matsusita, K., Ishisaki, Y., & Sarazin, C. L. 2013, *Publications of the Astronomical Society of Japan*, 65, 89
- Alamo-Martínez, K. A., Blakeslee, J. P., Jee, M. J., Côté, P., Ferrarese, L., González-Lópezlira, R. A., Jordán, A., Meurer, G. R., Peng, E. W., & West, M. J. 2013, *The Astrophysical Journal*, 775, 20
- Allen, S. W., Evrard, A. E., & Mantz, A. B. 2011, *Annual Review of Astronomy and Astrophysics*, 49, 409
- Alpher, R. A. & Herman, R. 1948, *Nature*, 162, 774
- Andrade-Santos, F., Lima Neto, G. B., & Laganá, T. F. 2012, *The Astrophysical Journal*, 746, 139
- Arnaud, M., Rothenflug, R., Boulade, O., Vigroux, L., & Vangioni-Flam, E. 1992, *Astronomy and Astrophysics V.254*, 254, 49
- Ascasibar, Y. & Markevitch, M. 2006, *The Astrophysical Journal*, 650, 102
- Baade, W. & Minkowski, R. 1954, *The Astrophysical Journal*, 119, 206
- Babul, A., Balogh, M. L., Lewis, G. F., & Poole, G. B. 2002, *Monthly Notices of the Royal Astronomical Society*, 330, 329
- Balestra, I., Tozzi, P., Ettori, S., Rosati, P., Borgani, S., Norman, V. M. C., & Viola, M. 2007, *Astronomy & Astrophysics*, 462, 429
- Balogh, M. L., Navarro, J. F., & Morris, S. L. 2000, *The Astrophysical Journal*, 540, 113
- Barrena, R., Boschin, W., Girardi, M., & Spolaor, M. 2007, *Astronomy & Astrophysics*, 469, 861
- Barret, D., den Herder, J.-W., Lam Trong, T., Piro, L., Cappi, M., Houvelin, J., Kelley, R., Mass-Hesse, M., Mitsuda, K., Paltani, S., Rauw, G., Rozanska, A., Wilms, J., Bandler, S., Barbera, M., Barcons, X., Bozzo, E., Ceballos, M., Charles, I., Costantini, E., Decourchelle, A., den Hartog, R., Duband, L., Duval, J.-M., Fiore, F., Gatti, F., Goldwurm, A., Jackson, B., Jonker, P., Kilbourne, C., Macculi, C., Mendez, M., Molendi, S., Orleanski, P., Pajot, F., Pointecouteau, E., Porter, F., Pratt, G., Prele, D., Ravera, L., Sato, K., Schaye, J., Shinozaki, K., Thibert, T., Valenziano, L., Valette, V., Vink, J., Webb, N., Wise, M., Yamasaki, N., Douchin, F., Mesnager, J.-M., Pontet, B., Pradines, A., Branduardi-Raymont, G., Bulbul, E., Dadina, M., Ettori, S., Finoguenov, A., Fukazawa, Y., Janiuk, A., Kaastra, J., Mazzotta, P., Miller, J., Miniutti, G., Naze, Y., Nicastro, F., Scioritino, S., Simonescu, A., Torrejon, J.-M., Frezouls, B., Geoffray, H., Peille, P., Aicardi, C., André, J., Daniel, C., Clénet, A., Etcheverry, C., Gloaguen, E., Hervet, G., Jolly, A., Ledot, A., Paillet, I., Schmitter, R., Vella, B., Damery, J.-C., Boyce, K., Dipirro, M., Lotti, S., Schwander, D., Smith, S., Van Leeuwen, B., van Weers, H., Clerc, N., Cobo, B., Dauser, T., Kirsch, C., Cucchetti, E., Eckart, M., Ferrando, P., & Natalucci, L. 2018, in *Space Telescopes and Instrumentation 2018: Ultraviolet to Gamma Ray*, ed. J.-W. A. den Herder, K. Nakazawa, & S. Nikzad, Vol. 10699 (SPIE), 51
- Bassino, L. P., Faifer, F. R., Forte, J. C., Dirsch, B., Richtler, T., Geisler, D., & Schubert, Y. 2006, *Astronomy & Astrophysics*, 451, 789
- Bauer, A. & Springel, V. 2012, *Monthly Notices of the Royal Astronomical Society*, 423, 2558
- Bekki, K., Forbes, D. A., Beasley, M. A., & Couch, W. J. 2003, *Monthly Notices of the Royal Astronomical Society*, 344, 1334
- Bialas, D., Lisker, T., Olczak, C., Spuzem, R., & Kotulla, R. 2015, *Astronomy & Astrophysics*, 576, A103
- Biffi, V., Planelles, S., Borgani, S., Rasia, E., Murante, G., Fabjan, D., & Gaspari, M. 2018, *Monthly Notices of the Royal Astronomical Society*, 476, 2689
- Binney, J. & Merrifield, M. 1998, *Galactic Astronomy (Princeton Series in Astrophysics)*
- Bîrzan, L., McNamara, B. R., Nulsen, P. E. J., Carilli, C. L., & Wise, M. W. 2008, *The Astrophysical Journal*, 686, 859

- Blanton, E. L., Randall, S. W., Clarke, T. E., Sarazin, C. L., McNamara, B. R., Douglass, E. M., & McDonald, M. 2011, *The Astrophysical Journal*, 737, 99
- Böhringer, H. & Werner, N. 2010, *The Astronomy and Astrophysics Review*, 18, 127
- Bonafede, A., Feretti, L., Giovannini, G., Govoni, F., Murgia, M., Taylor, G. B., Ebeling, H., Allen, S., Gentile, G., & Pihlström, Y. 2009, *Astronomy & Astrophysics*, 503, 707
- Bonafede, A., Feretti, L., Murgia, M., Govoni, F., Giovannini, G., Dallacasa, D., Dolag, K., & Taylor, G. B. 2010, *Astronomy and Astrophysics*, 513, A30
- Bond, J. R., Cole, S., Efstathiou, G., & Kaiser, N. 1991, *The Astrophysical Journal*, 379, 440
- Boschin, W., Girardi, M., Spolaor, M., & Barrena, R. 2006, *Astronomy & Astrophysics*, 449, 461
- Boselli, A., Cuillandre, J. C., Fossati, M., Boissier, S., Bomans, D., Consolandi, G., Anselmi, G., Cortese, L., Côté, P., Durrell, P., Ferrarese, L., Fumagalli, M., Gavazzi, G., Gwyn, S., Hensler, G., Sun, M., & Toloba, E. 2016, *Astronomy & Astrophysics*, 587, A68
- Botteon, A., Gastaldello, F., & Brunetti, G. 2018, *Monthly Notices of the Royal Astronomical Society*, 476, 5591
- Braginskii, S. 1958, *JETP*, 33, 459
- Braginskii, S. I. 1965, *Reviews of Plasma Physics*, 1, 205
- Brodie, J. P. & Strader, J. 2006, *Annual Review of Astronomy and Astrophysics*, 44, 193
- Brunetti, G. & Jones, T. W. 2014, *International Journal of Modern Physics D*, 23, 1430007
- Brunetti, G. & Lazarian, A. 2011, *Monthly Notices of the Royal Astronomical Society*, 412, no
- Buote, D. A. 2002, in *Merging Processes in Galaxy Clusters* (Dordrecht: Springer Netherlands), 79–107
- Burns, J. O., Hallman, E. J., Gantner, B., Motl, P. M., & Norman, M. L. 2008, *The Astrophysical Journal*, 675, 1125
- Bykov, A. M., Churazov, E. M., Ferrari, C., Forman, W. R., Kaastra, J. S., Klein, U., Markevitch, M., & de Plaa, J. 2015, *Space Science Reviews*, 188, 141
- Byram, E. T., Chubb, T. A., & Friedman, H. 1966, *Science*, 152, 66
- Byrd, G. & Valtonen, M. 1990, *The Astrophysical Journal*, 350, 89
- Carlstrom, J. E., Holder, G. P., & Reese, E. D. 2002, *Annual Review of Astronomy and Astrophysics*, 40, 643
- Cavaliere, A. & Fusco-Femiano, R. 1976, *Astronomy and Astrophysics*, 49, 137
- . 1978, *Astronomy and Astrophysics*, 70, 677
- Chaboyer, B., Demarque, P., & Sarajedini, A. 1995, *Astrophysical Journal* v.459, p.558, 459, 558
- Chandrasekhar, S. 1961, *Hydrodynamic and hydromagnetic stability*
- Chen, H., Jones, C., Andrade-Santos, F., ZuHone, J. A., & Li, Z. 2017, *The Astrophysical Journal*, 838, 38
- Churazov, E., Bruggen, M., Kaiser, C. R., Böhringer, H., & Forman, W. 2001, *The Astrophysical Journal*, 554, 261
- Churazov, E., Vikhlinin, A., Zhuravleva, I., Schekochihin, A., Parrish, I., Sunyaev, R., Forman, W., Böhringer, H., & Randall, S. 2012, *Monthly Notices of the Royal Astronomical Society*, 421, 1123
- Cohn, J. & White, M. 2005, *Astroparticle Physics*, 24, 316
- Colella, P. & Woodward, P. R. 1984, *Journal of Computational Physics*, 54, 174

- Collaboration, H., Aharonian, F., Akamatsu, H., Akimoto, F., Allen, S. W., Anabuki, N., Angelini, L., Arnaud, K., Audard, M., Awaki, H., Axelsson, M., Bamba, A., Bautz, M., Blandford, R., Brennerman, L., Brown, G. V., Bulbul, E., Cackett, E., Chernyakova, M., Chiao, M., Coppi, P., Costantini, E., de Plaa, J., den Herder, J.-W., Done, C., Dotani, T., Ebisawa, K., Eckart, M., Enoto, T., Ezoe, Y., Fabian, A. C., Ferrigno, C., Foster, A., Fujimoto, R., Fukazawa, Y., Furuzawa, A., Galeazzi, M., Gallo, L., Gandhi, P., Giustini, M., Goldwurm, A., Gu, L., Guainazzi, M., Haba, Y., Hagino, K., Hamaguchi, K., Harrus, I., Hatsukade, I., Hayashi, K., Hayashi, T., Hayashida, K., Hiraga, J., Hornschemeier, A., Hoshino, A., Hughes, J., Iizuka, R., Inoue, H., Inoue, Y., Ishibashi, K., Ishida, M., Ishikawa, K., Ishisaki, Y., Itoh, M., Iyomoto, N., Kaastra, J., Kallman, T., Kamae, T., Kara, E., Kataoka, J., Katsuda, S., Katsuta, J., Kawaharada, M., Kawai, N., Kelley, R., Khangulyan, D., Kilbourne, C., King, A., Kitaguchi, T., Kitamoto, S., Kitayama, T., Kohmura, T., Kokubun, M., Koyama, S., Koyama, K., Kretschmar, P., Krimm, H., Kubota, A., Kunieda, H., Laurent, P., Lebrun, F., Lee, S.-H., Leutenegger, M., Limousin, O., Loewenstein, M., Long, K. S., Lumb, D., Madejski, G., Maeda, Y., Maier, D., Makishima, K., Markevitch, M., Matsumoto, H., Matsushita, K., McCammon, D., McNamara, B., Mehdipour, M., Miller, E., Miller, J., Mineshige, S., Mitsuda, K., Mitsuishi, I., Miyazawa, T., Mizuno, T., Mori, H., Mori, K., Moseley, H., Mukai, K., Murakami, H., Murakami, T., Mushotzky, R., Nagino, R., Nakagawa, T., Nakajima, H., Nakamori, T., Nakano, T., Nakashima, S., Nakazawa, K., Nobukawa, M., Noda, H., Nomachi, M., O'Dell, S., Odaka, H., Ohashi, T., Ohno, M., Okajima, T., Ota, N., Ozaki, M., Paerels, F., Paltani, S., Parmar, A., Petre, R., Pinto, C., Pohl, M., Porter, F. S., Pottschmidt, K., Ramsey, B., Reynolds, C., Russell, H., Safi-Harb, S., Saito, S., Sakai, K., Sameshima, H., Sato, G., Sato, K., Sato, R., Sawada, M., Schartel, N., Serlemitsos, P., Seta, H., Shidatsu, M., Simionescu, A., Smith, R., Soong, Y., Stawarz, L., Sugawara, Y., Sugita, S., Szymkowiak, A., Tajima, H., Takahashi, H., Takahashi, T., Takeda, S., Takei, Y., Tamagawa, T., Tamura, K., Tamura, T., Tanaka, T., Tanaka, Y., Tanaka, Y., Tashiro, M., Tawara, Y., Terada, Y., Terashima, Y., Tombesi, F., Tomida, H., Tsuboi, Y., Tsujimoto, M., Tsunemi, H., Tsuru, T., Uchida, H., Uchiyama, H., Uchiyama, Y., Ueda, S., Ueda, Y., Ueno, S., Uno, S., Urry, M., Ursino, E., de Vries, C., Watanabe, S., Werner, N., Wik, D., Wilkins, D., Williams, B., Yamada, S., Yamaguchi, H., Yamaoka, K., Yamasaki, N. Y., Yamauchi, M., Yamauchi, S., Yaqoob, T., Yatsu, Y., Yonetoku, D., Yoshida, A., Yuasa, T., Zhuravleva, I., & Zoghbi, A. 2016, *Nature*, 535, 117
- Colless, M., Dalton, G., Maddox, S., Sutherland, W., Norberg, P., Cole, S., Bland-Hawthorn, J., Bridges, T., Cannon, R., Collins, C., Couch, W., Cross, N., Deeley, K., De Propriis, R., Driver, S. P., Efstathiou, G., Ellis, R. S., Frenk, C. S., Glazebrook, K., Jackson, C., Lahav, O., Lewis, I., Lumsden, S., Madgwick, D., Peacock, J. A., Peterson, B. A., Price, I., Seaborne, M., & Taylor, K. 2001, *Monthly Notices of the Royal Astronomical Society*, 328, 1039
- Cora, S. A. 2006, *Monthly Notices of the Royal Astronomical Society*, 368, 1540
- Cora, S. A., Tornatore, L., Tozzi, P., & Dolag, K. 2008, *Monthly Notices of the Royal Astronomical Society*, 386, 96
- D'Abrusco, R., Cantiello, M., Paolillo, M., Pota, V., Napolitano, N. R., Limatola, L., Spavone, M., Grado, A., Iodice, E., Capaccioli, M., Peletier, R., Longo, G., Hilker, M., Mieske, S., Grebel, E. K., Lisker, T., Wittmann, C., van de Ven, G., Schipani, P., & Fabbiano, G. 2016, *The Astrophysical Journal*, 819, L31
- Dasadia, S., Sun, M., Sarazin, C., Morandi, A., Markevitch, M., Wik, D., Feretti, L., Giovannini, G., Govoni, F., & Vacca, V. 2016, *The Astrophysical Journal*, 820, L20
- De Grandi, S., Eckert, D., Molendi, S., Girardi, M., Roediger, E., Gaspari, M., Gastaldello, F., Ghizzardi, S., Nonino, M., & Rossetti, M. 2016, *Astronomy & Astrophysics*, 592, A154
- De Grandi, S. & Molendi, S. 2001, *The Astrophysical Journal*, 551, 153
- De Lucia, G. & Blaizot, J. 2007, *Monthly Notices of the Royal Astronomical Society*, 375, 2
- de Vaucouleurs, G. 1953, *Monthly Notices of the Royal Astronomical Society*, 113, 134
- De Young, D. S. 1978, *The Astrophysical Journal*, 223, 47
- Deshev, B., Finoguenov, A., Verdugo, M., Ziegler, B., Park, C., Hwang, H. S., Haines, C., Kamphuis, P., Tamm, A., Einasto, M., Hwang, N., & Park, B.-G. 2017, *Astronomy & Astrophysics*, 607, A131
- Diaferio, A. 1999, *Monthly Notices of the Royal Astronomical Society*, 309, 610
- Dicke, R. H., Peebles, P. J. E., Roll, P. G., & Wilkinson, D. T. 1965, *The Astrophysical Journal*, 142, 414
- Dimotakis, P. E., Miake-Lye, R. C., & Papantoniou, D. A. 1983, *Physics of Fluids*, 26, 3185
- Dolag, K., Vazza, F., Brunetti, G., & Tormen, G. 2005, *Monthly Notices of the Royal Astronomical Society*, 364, 753

- Domainko, W., Mair, M., Kapferer, W., van Kampen, E., Kronberger, T., Schindler, S., Kimeswenger, S., Ruffert, M., & Mangete, O. E. 2006, *Astronomy & Astrophysics*, 452, 795
- Donahue, M., Mack, J., Voit, G. M., Sparks, W., Elston, R., & Maloney, P. R. 2000, *The Astrophysical Journal*, 545, 670
- Donnert, J., Dolag, K., Lesch, H., & Müller, E. 2009, *Monthly Notices of the Royal Astronomical Society*, 392, 1008
- Dotter, A., Chaboyer, B., Jevremović, D., Baron, E., Ferguson, J. W., Sarajedini, A., & Anderson, J. 2007, *The Astronomical Journal*, 134, 376
- Dressler, A. 1980, *The Astrophysical Journal*, 236, 351
- Drinkwater, M. J., Gregg, M. D., & Colless, M. 2001, *The Astrophysical Journal*, 548, L139
- Dubois, Y. & Teyssier, R. 2008, *Astronomy & Astrophysics*, 482, L13
- Ebeling, H., Stephenson, L. N., & Edge, A. C. 2014, *The Astrophysical Journal*, 781, L40
- Eckert, D., Gaspari, M., Owers, M. S., Roediger, E., Molendi, S., Gastaldello, F., Paltani, S., Etori, S., Venturi, T., Rossetti, M., & Rudnick, L. 2017, *Astronomy & Astrophysics*, 605, A25
- Eckert, D., Jauzac, M., Vazza, F., Owers, M. S., Kneib, J.-P., Tchernin, C., Intema, H., & Knowles, K. 2016, *Monthly Notices of the Royal Astronomical Society*, 461, 1302
- Eckert, D., Molendi, S., Owers, M., Gaspari, M., Venturi, T., Rudnick, L., Etori, S., Paltani, S., Gastaldello, F., & Rossetti, M. 2014, *Astronomy & Astrophysics*, 570, A119
- Etori, S. & Fabian, A. C. 2000, *Monthly Notices of the Royal Astronomical Society*, 317, L57
- Fabian, A. C. 1994, *Annual Review of Astronomy and Astrophysics*, 32, 277
- Fabian, A. C., Reynolds, C. S., Taylor, G. B., & Dunn, R. J. H. 2005, *Monthly Notices of the Royal Astronomical Society*, 363, 891
- Fabian, A. C., Sanders, J. S., Allen, S. W., Crawford, C. S., Iwasawa, K., Johnstone, R. M., Schmidt, R. W., & Taylor, G. B. 2003, *Monthly Notices of the Royal Astronomical Society*, 344, L43
- Fabian, A. C., Sanders, J. S., Taylor, G. B., Allen, S. W., Crawford, C. S., Johnstone, R. M., & Iwasawa, K. 2006, *Monthly Notices of the Royal Astronomical Society*, 366, 417
- Fadda, D., Biviano, A., Marleau, F. R., Storrie-Lombardi, L. J., & Durret, F. 2008, *The Astrophysical Journal*, 672, L9
- Falkovich, G. G. 2011, *Fluid mechanics : a short course for physicists* (Cambridge University Press), 167
- Fall, S. M. & Zhang, Q. 2001, *The Astrophysical Journal*, 561, 751
- Feretti, L., Giovannini, G., Govoni, F., & Murgia, M. 2012, *Astronomy and Astrophysics Review*, 20
- Ferrari, C., Govoni, F., Schindler, S., Bykov, A. M., & Rephaeli, Y. 2008, *Space Science Reviews*, 134, 93
- Forbes, D. A., Grillmair, C. J., Williger, G. M., Elson, R. A. W., & Brodie, J. P. 1998, *Monthly Notices of the Royal Astronomical Society*, 293, 325
- Forman, W. & Jones, C. 1982, *Annual Review of Astronomy and Astrophysics*, 20, 547
- Forman, W., Schwarz, J., Jones, C., Filler, W., & Fabian, A. C. 1979, *The Astrophysical Journal*, 234, 27
- Friedmann, A. 1922, *Zeitschrift für Physik*, 10, 377
- Fryxell, B., Olson, K., Ricker, P., Timmes, F. X., Zingale, M., Lamb, D. Q., MacNeice, P., Rosner, R., Truran, J. W., & Tufo, H. 2000, *The Astrophysical Journal Supplement Series*, 131, 273
- Fukazawa, Y., Makishima, K., Tamura, T., Ezawa, H., Xu, H., Ikebe, Y., Kikuchi, K., & Ohashi, T. 1998, *Publications of the Astronomical Society of Japan*, 50, 187
- Gamow, G. 1948, *Nature*, 162, 680

- Gaspari, M. 2015, *Monthly Notices of the Royal Astronomical Society: Letters*, 451, L60
- Gaspari, M., Brighenti, F., & Ruszkowski, M. 2013, *Astronomische Nachrichten*, 334, 394
- Geller, M. J. & Huchra, J. P. 1983, *The Astrophysical Journal Supplement Series*, 52, 61
- Ghizzardi, S., De Grandi, S., & Molendi, S. 2014, *Astronomy & Astrophysics*, 570, A117
- Giacconi, R., Murray, S., Gursky, H., Kellogg, E., Schreier, E., & Tananbaum, H. 1972, *The Astrophysical Journal*, 178, 281
- Giovannini, G., Tordi, M., & Feretti, L. 1999, *New Astronomy*, 4, 141
- Gisler, G. R. 1976, *Astronomy and Astrophysics*, 51, 137
- Godunov, S. 1959, *Matematicheskii Sbornik*, 89, 271
- Govoni, F., Feretti, L., Giovannini, G., Böhringer, H., Reiprich, T. H., & Murgia, M. 2001, *Astronomy & Astrophysics*, 376, 803
- Gunn, J. E. & Gott, J. R. 1972, *The Astrophysical Journal*, 176, 1
- Guo, F., Oh, S. P., & Ruszkowski, M. 2008, *The Astrophysical Journal*, 688, 859
- Guth, A. H. 1981, *Physical Review D*, 23, 347
- H. S. Wang, Q., Markevitch, M., & Giacintucci, S. 2016, *The Astrophysical Journal*, 833, 99
- Ha, J.-H., Ryu, D., & Kang, H. 2018, *The Astrophysical Journal*, 857, 26
- Halbesma, T. L. R., Donnert, J. M. F., de Vries, M. N., & Wise, M. W. 2019, *Monthly Notices of the Royal Astronomical Society*, 483, 3851
- Hallman, E. J., Alden, B., Rapetti, D., Datta, A., & Burns, J. O. 2018, *The Astrophysical Journal*, 859, 44
- Hallman, E. J. & Markevitch, M. 2004, *The Astrophysical Journal*, 610, 81
- Hernquist, L. 1990, *The Astrophysical Journal*, 356, 359
- Hinshaw, G., Nolta, M. R., Bennett, C. L., Bean, R., Dore, O., Greason, M. R., Halpern, M., Hill, R. S., Jarosik, N., Kogut, A., Komatsu, E., Limon, M., Odegard, N., Meyer, S. S., Page, L., Peiris, H. V., Spergel, D. N., Tucker, G. S., Verde, L., Weiland, J. L., Wollack, E., & Wright, E. L. 2007, *The Astrophysical Journal Supplement Series*, 170, 288
- Hoffer, A. S., Donahue, M., Hicks, A., & Barthelmy, R. S. 2012, *The Astrophysical Journal Supplement Series*, 199, 23
- Huang, J., Greengard, L. 2000, *SIAM. J. Sci. Comput.*, 21, 1551
- Hubble, E. 1926, *The Astrophysical Journal*, 64, 321
- . 1929, *Proceedings of the National Academy of Sciences of the United States of America*, 15, 168
- Hudson, D. S., Mittal, R., Reiprich, T. H., Nulsen, P. E. J., Andernach, H., & Sarazin, C. L. 2010, *Astronomy and Astrophysics*, 513, A37
- Hudson, M. J., Harris, G. L., & Harris, W. E. 2014, *The Astrophysical Journal*, 787, L5
- Hwang, H. S. & Lee, M. G. 2009, *Monthly Notices of the Royal Astronomical Society*, 397, 2111
- Iapichino, L., Federrath, C., & Klessen, R. S. 2017, *Monthly Notices of the Royal Astronomical Society*, 469, 3641
- Ichinohe, Y., Simionescu, A., Werner, N., Fabian, A. C., & Takahashi, T. 2019, *Monthly Notices of the Royal Astronomical Society*, 483, 1744
- Ichinohe, Y., Simionescu, A., Werner, N., & Takahashi, T. 2017, *Monthly Notices of the Royal Astronomical Society*, 467, 3662

- Ichinohe, Y., Werner, N., Simionescu, A., Allen, S. W., Canning, R. E. A., Ehlert, S., Mernier, F., & Takahashi, T. 2015, *Monthly Notices of the Royal Astronomical Society*, 448, 2971
- Iodice, E., Spavone, M., Cantiello, M., D'Abrusco, R., Capaccioli, M., Hilker, M., Mieske, S., Napolitano, N. R., Peletier, R. F., Limatola, L., Grado, A., Venhola, A., Paolillo, M., de Ven, G. V., & Schipani, P. 2017, *The Astrophysical Journal*, 851, 75
- Irwin, J. A. & Sarazin, C. L. 1996, *The Astrophysical Journal*, 471, 683
- Johnson, R. E., Markevitch, M., Wegner, G. A., Jones, C., & Forman, W. R. 2010, *The Astrophysical Journal*, 710, 1776
- Jones, C. & Forman, W. 1984, *The Astrophysical Journal*, 276, 38
- . 1999, *The Astrophysical Journal*, 511, 65
- Jones, C., Stern, C., Forman, W., Breen, J., David, L., Tucker, W., & Franx, M. 1997, *The Astrophysical Journal*, 482, 143
- Kapferer, W., Kronberger, T., Weratschnig, J., Schindler, S., Domainko, W., van Kampen, E., Kimeswenger, S., Mair, M., & Ruffert, M. 2007, *Astronomy & Astrophysics*, 466, 813
- Kempner, J. C. & David, L. P. 2004, *Monthly Notices of the Royal Astronomical Society*, 349, 385
- Khatri, R. & Gaspari, M. 2016, *Monthly Notices of the Royal Astronomical Society*, 463, 655
- Kolmogorov, A. 1941, *The Local Structure of Turbulence in Incompressible Viscous Fluid for Very Large Reynolds' Numbers*, Vol. 30 (Izd-vo Akademii nauk SSSR), 301–305
- Kraft, R. P., Birkinshaw, M., Nulsen, P. E. J., Worrall, D. M., Croston, J. H., Forman, W. R., Hardcastle, M. J., Jones, C., & Murray, S. S. 2012, *The Astrophysical Journal*, 749, 19
- Kraft, R. P., Forman, W. R., Jones, C., Nulsen, P. E. J., Hardcastle, M. J., Raychaudhury, S., Evans, D. A., Sivakoff, G. R., & Sarazin, C. L. 2011, *The Astrophysical Journal*, 727, 41
- Kraft, R. P., Roediger, E., Machacek, M., Forman, W. R., Nulsen, P. E. J., Jones, C., Churazov, E., Randall, S., Su, Y., & Sheardown, A. 2017, *The Astrophysical Journal*, 848, 27
- Krauss, L. M. & Chaboyer, B. 2003, *Science (New York, N.Y.)*, 299, 65
- Kravtsov, A. V. & Borgani, S. 2012a, *Annual Review of Astronomy and Astrophysics*, 50, 353
- . 2012b, *Annual Review of Astronomy and Astrophysics*, 50, 353
- Kunz, M. W., Schekochihin, A. A., Chen, C. H., Abel, I. G., & Cowley, S. C. 2015, *Journal of Plasma Physics*, 81, 325810501
- Kunz, M. W., Schekochihin, A. A., & Stone, J. M. 2014, *Physical Review Letters*, 112, 205003
- Lacey, C. & Cole, S. 1993, *Monthly Notices of the Royal Astronomical Society*, 262, 627
- . 1994, *Monthly Notices of the Royal Astronomical Society*, 271, 676
- Lamb, H. 1945, *Hydrodynamics*
- Landau, L. D. & Lifshitz, E. M. 1959, *Course of theoretical physics*, Oxford: Pergamon Press, 1959
- Larson, R. B. & Dinerstein, H. L. 1975, *Publications of the Astronomical Society of the Pacific*, 87, 911
- Larson, R. B., Tinsley, B. M., & Caldwell, C. N. 1980, *The Astrophysical Journal*, 237, 692
- Lemaître, A. G. 1931, *Monthly Notices of the Royal Astronomical Society*, 91, 483
- Li, H. & Gnedin, O. Y. 2014, *The Astrophysical Journal*, 796, 10
- Lidman, C., Iacobuta, G., Bauer, A. E., Barrientos, L. F., Cerulo, P., Couch, W. J., Delaye, L., Demarco, R., Ellingson, E., Faloon, A. J., Gilbank, D., Huertas-Company, M., Mei, S., Meyers, J., Muzzin, A., Noble, A., Nantais, J., Rettura, A., Rosati, P., Sánchez-Janssen, R., Strazzullo, V., Webb, T. M. A., Wilson, G., Yan, R., & Yee, H. K. C. 2013, *Monthly Notices of the Royal Astronomical Society*, 433, 825

- Liu, A., Tozzi, P., Yu, H., De Grandi, S., & Ettori, S. 2018, *Monthly Notices of the Royal Astronomical Society*, 481, 361
- Liu, F. S., Lei, F. J., Meng, X. M., & Jiang, D. F. 2015, *Monthly Notices of the Royal Astronomical Society*, 447, 1491
- Liu, F. S., Mao, S., Deng, Z. G., Xia, X. Y., & Wen, Z. L. 2009, *Monthly Notices of the Royal Astronomical Society*, 396, 2003
- Lucero, D. M., Young, L. M., & van Gorkom, J. H. 2005, *The Astronomical Journal*, 129, 647
- Lyskova, N., Churazov, E., Zhang, C., Forman, W., Jones, C., Dolag, K., Roediger, E., & Sheardown, A. 2019, *Monthly Notices of the Royal Astronomical Society*, 485, 2922
- Machacek, M., Dosaj, A., Forman, W., Jones, C., Markevitch, M., Vikhlinin, A., Warmflash, A., & Kraft, R. 2005, *The Astrophysical Journal*, 621, 663
- Machacek, M., Jones, C., Forman, W. R., & Nulsen, P. 2006, *The Astrophysical Journal*, 644, 155
- Machado, R. E. G. & Neto, G. B. L. 2013, *Monthly Notices of the Royal Astronomical Society*, Volume 430, Issue 4, p.3249-3260, 430, 3249
- MacNeice, P., Olson, K. M., Mobarrry, C., de Fainchtein, R., & Packer, C. 2000, *Computer Physics Communications*, 126, 330
- Marín-Franch, A., Aparicio, A., Piotto, G., Rosenberg, A., Chaboyer, B., Sarajedini, A., Siegel, M., Anderson, J., Bedin, L. R., Dotter, A., Hempel, M., King, I., Majewski, S., Milone, A. P., Paust, N., & Reid, I. N. 2009, *The Astrophysical Journal*, 694, 1498
- Markevitch, M., Gonzalez, A. H., David, L., Vikhlinin, A., Murray, S., Forman, W., Jones, C., & Tucker, W. 2002, *The Astrophysical Journal*, 567, L27
- Markevitch, M., Govoni, F., Brunetti, G., & Jerius, D. 2004, *The Astrophysical Journal*, 627, 733
- Markevitch, M., Ponman, T. J., Nulsen, P. E. J., Bautz, M. W., Burke, D. J., David, L. P., Davis, D., Donnelly, R. H., Forman, W. R., Jones, C., Kaastra, J., Kellogg, E., Kim, D. W., Kolodziejczak, J., Mazzotta, P., Pagliaro, A., Patel, S., VanSpeybroeck, L., Vikhlinin, A., Vrtilik, J., Wise, M., & Zhao, P. 2000, *The Astrophysical Journal*, 541, 542
- Markevitch, M. & Vikhlinin, A. 2007, *Physics Reports*, 443, 1
- Martel, H., Robichaud, F., & Barai, P. 2014, *The Astrophysical Journal*, 786, 79
- Mather, J. C., Cheng, E. S., Cottingham, D. A., Eplee, R. E., J., Fixsen, D. J., Hewagama, T., Isaacman, R. B., Jensen, K. A., Meyer, S. S., Noerdlinger, P. D., Read, S. M., Rosen, L. P., Shafer, R. A., Wright, E. L., Bennett, C. L., Boggess, N. W., Hauser, M. G., Kelsall, T., Moseley, S. H., J., Silverberg, R. F., Smoot, G. F., Weiss, R., & Wilkinson, D. T. 1994, *The Astrophysical Journal*, 420, 439
- Mathews, W. G. & Brighenti, F. 2003, *Annual Review of Astronomy and Astrophysics*, 41, 191
- Mathis, H., Lavaux, G., Diego, J. M., & Silk, J. 2005, *Monthly Notices of the Royal Astronomical Society*, 357, 801
- McCarthy, I. G., Balogh, M. L., Babul, A., Poole, G. B., & Horner, D. J. 2004, *The Astrophysical Journal*, 613, 811
- McCarthy, I. G., Bower, R. G., Balogh, M. L., Voit, G. M., Pearce, F. R., Theuns, T., Babul, A., Lacey, C. G., & Frenk, C. S. 2007, *Monthly Notices of the Royal Astronomical Society*, 376, 497
- McCarthy, I. G., Frenk, C. S., Font, A. S., Lacey, C. G., Bower, R. G., Mitchell, N. L., Balogh, M. L., & Theuns, T. 2008, *Monthly Notices of the Royal Astronomical Society*, 383, 593
- McPartland, C., Ebeling, H., Roediger, E., & Blumenthal, K. 2016, *Monthly Notices of the Royal Astronomical Society*, 455, 2994
- Medezinski, E., Umetsu, K., Okabe, N., Nonino, M., Molnar, S., Massey, R., Dupke, R., & Merten, J. 2016, *The Astrophysical Journal*, 817, 24

- Meidinger, N., Nandra, K., Plattner, M., Rau, A., Barbera, M., Emberger, V., Fuermetz, M., Manhart, M., Müller-Seidlitz, J., & Treberspurg, W. 2017, in *UV, X-Ray, and Gamma-Ray Space Instrumentation for Astronomy XX*, ed. O. H. Siegmund, Vol. 10397 (SPIE), 32
- Mernier, F., de Plaa, J., Pinto, C., Kaastra, J. S., Kosec, P., Zhang, Y.-Y., Mao, J., & Werner, N. 2016, *Astronomy & Astrophysics*, 592, A157
- Merten, J., Coe, D., Dupke, R., Massey, R., Zitrin, A., Cypriano, E. S., Okabe, N., Frye, B., Braglia, F. G., Jiménez-Teja, Y., Benítez, N., Broadhurst, T., Rhodes, J., Meneghetti, M., Moustakas, L. A., Sodré Jr, L., Krick, J., & Bregman, J. N. 2011, *Monthly Notices of the Royal Astronomical Society*, 417, 333
- Mewe, R. 1999, *X-Ray Spectroscopy in Astrophysics, Lectures held at the Astrophysics School X.*, 520, 109
- Mitchell, N. L., McCarthy, I. G., Bower, R. G., Theuns, T., & Crain, R. A. 2009, *Monthly Notices of the Royal Astronomical Society*, 395, 180
- Mitchell, R. J., Culhane, J. L., Davison, P. J. N., & Ives, J. C. 1976, *Monthly Notices of the Royal Astronomical Society*, 175, 29P
- Mittal, R., Hudson, D. S., Reiprich, T. H., & Clarke, T. 2009, *Astronomy & Astrophysics*, 501, 835
- Mohr, J. J., Mathiesen, B., & Evrard, A. E. 1999, *The Astrophysical Journal*, 517, 627
- Molendi, S., Tozzi, P., Gaspari, M., De Grandi, S., Gastaldello, F., Ghizzardi, S., & Rossetti, M. 2016, *Astronomy & Astrophysics*, 595, A123
- Moll, R., Schindler, S., Domainko, W., Kapferer, W., Mair, M., van Kampen, E., Kronberger, T., Kimeswenger, S., & Ruffert, M. 2007, *Astronomy & Astrophysics*, 463, 513
- Molnar, S. M. 2016, *Frontiers in Astronomy and Space Sciences*, 2, 7
- Monaghan, J. J. 1992, *Annual Review of Astronomy and Astrophysics*, 30, 543
- Moore, B., Katz, N., Lake, G., Dressler, A., & Oemler, A. 1996, *Nature*, 379, 613
- More, S., Diemer, B., & Kravtsov, A. V. 2015, *The Astrophysical Journal*, 810, 36
- Mori, M. & Burkert, A. 2000, *The Astrophysical Journal*, 538, 559
- Moster, B. P., Macciò, A. V., Somerville, R. S., Naab, T., & Cox, T. J. 2011, *Monthly Notices of the Royal Astronomical Society*, 415, 3750
- Mukhanov, V. 2005, *Physical Foundations of Cosmology* (Cambridge University Press), 442
- Mulchaey, J. S. 2000, *Annual Review of Astronomy and Astrophysics*, 38, 289
- Mulchaey, J. S., Davis, D. S., Mushotzky, R. F., & Burstein, D. 1996, *The Astrophysical Journal*, 456, 80
- Murakami, H., Komiyama, M., Matsushita, K., Nagino, R., Sato, T., Sato, K., Kawaharada, M., Nakazawa, K., Ohashi, T., & Takei, Y. 2011, *Publications of the Astronomical Society of Japan*, 63, S963
- Nagai, D. & Kravtsov, A. V. 2003, *The Astrophysical Journal*, 587, 514
- Navarro, J. F., Frenk, C. S., & White, S. D. M. 1996, *The Astrophysical Journal*, 462, 563
- Neumann, D. M., Lumb, D. H., Pratt, G. W., & Briel, U. G. 2003, *Astronomy & Astrophysics*, 400, 811
- Nulsen, P. E. J. 1982, *Monthly Notices of the Royal Astronomical Society*, 198, 1007
- Nulsen, P. E. J., McNamara, B. R., Wise, M. W., & David, L. P. 2005, *The Astrophysical Journal*, 628, 629
- Oesch, P. A., Brammer, G., van Dokkum, P. G., Illingworth, G. D., Bouwens, R. J., Labbé, I., Franx, M., Momcheva, I., Ashby, M. L. N., Fazio, G. G., Gonzalez, V., Holden, B., Magee, D., Skelton, R. E., Smit, R., Spitler, L. R., Trenti, M., & Willner, S. P. 2016, *The Astrophysical Journal*, 819, 129
- O'Sullivan, E., David, L. P., & Vrtilik, J. M. 2013, *Monthly Notices of the Royal Astronomical Society*, 437, 730

- Ota, N., Fukazawa, Y., Fabian, A. C., Kanemaru, T., Kawaharada, M., Kawano, N., Kelley, R. L., Kitaguchi, T., Makishima, K., Matsushita, K., Murase, K., Nakazawa, K., Ohashi, T., Sanders, J. S., Tamura, T., & Urata, Y. 2007, *Publications of the Astronomical Society of Japan*, 59, S351
- Owers, M. S., Nulsen, P. E. J., & Couch, W. J. 2011a, *The Astrophysical Journal*, 741, 122
- Owers, M. S., Randall, S. W., Nulsen, P. E. J., Couch, W. J., David, L. P., & Kempner, J. C. 2011b, *The Astrophysical Journal*, 728, 27
- Pakmor, R., Springel, V., Bauer, A., Mocz, P., Munoz, D. J., Ohlmann, S. T., Schaal, K., & Zhu, C. 2016, *Monthly Notices of the Royal Astronomical Society*, 455, 1134
- Pandge, M. B., Bagchi, J., Sonkamble, S. S., Parekh, V., Patil, M. K., Dabhade, P., Navale, N. R., Raychaudhury, S., & Joe, J. 2016, *Monthly Notices of the Royal Astronomical Society*, 472, 2042
- Paolillo, M., Fabbiano, G., Peres, G., & Kim, D. 2002, *The Astrophysical Journal*, 565, 883
- Parrish, I. J., Quataert, E., & Sharma, P. 2009, *The Astrophysical Journal*, 703, 96
- Paterno-Mahler, R., Blanton, E. L., Randall, S. W., & Clarke, T. E. 2013, *The Astrophysical Journal*, 773, 114
- Paul, S., Iapichino, L., Miniati, F., Bagchi, J., & Mannheim, K. 2011, *The Astrophysical Journal*, 726, 17
- Paul, S., John, R. S., Gupta, P., & Kumar, H. 2017, *Monthly Notices of the Royal Astronomical Society*, 471, 2
- Peng, E. W., Ferguson, H. C., Goudfrooij, P., Hammer, D., Lucey, J. R., Marzke, R. O., Puzia, T. H., Carter, D., Balcells, M., Bridges, T., Chiboucas, K., del Burgo, C., Graham, A. W., Guzmán, R., Hudson, M. J., Matković, A., Merritt, D., Miller, B. W., Mouhcine, M., Phillipps, S., Sharples, R., Smith, R. J., Tully, B., & Verdoes Kleijn, G. 2011, *The Astrophysical Journal*, 730, 23
- Peng, Y., Maiolino, R., & Cochrane, R. 2015, *Nature*, 521, 192
- Penzias, A. A. & Wilson, R. W. 1965, *The Astrophysical Journal*, 142, 419
- Perlmutter, S., Aldering, G., Valle, M. D., Deustua, S., Ellis, R. S., Fabbro, S., Fruchter, A., Goldhaber, G., Groom, D. E., Hook, I. M., Kim, A. G., Kim, M. Y., Knop, R. A., Lidman, C., McMahon, R. G., Nugent, P., Pain, R., Panagia, N., Pennypacker, C. R., Ruiz-Lapuente, P., Schaefer, B., & Walton, N. 1998, *Nature*, 391, 51
- Peterson, J. & Fabian, A. 2006, *Physics Reports*, 427, 1
- Peterson, J. R., Kahn, S. M., Paerels, F. B. S., Kaastra, J. S., Tamura, T., Bleeker, J. A. M., Ferrigno, C., & Jernigan, J. G. 2003, *The Astrophysical Journal*, 590, 207
- Planelles, S. & Quilis, V. 2009, *Monthly Notices of the Royal Astronomical Society*, 399, 410
- Poole, G. B., Babul, A., McCarthy, I. G., Fardal, M. A., Bildfell, C. J., Quinn, T., & Mahdavi, A. 2007, *Monthly Notices of the Royal Astronomical Society*, 380, 437
- Poole, G. B., Babul, A., McCarthy, I. G., Sanderson, A. J. R., & Fardal, M. A. 2008, *Monthly Notices of the Royal Astronomical Society*, 391, 1163
- Poole, G. B., Fardal, M. A., Babul, A., McCarthy, I. G., Quinn, T., & Wadsley, J. 2006, *Monthly Notices of the Royal Astronomical Society*, 373, 881
- Pota, V., Romanowsky, A. J., Brodie, J. P., Peñarrubia, J., Forbes, D. A., Napolitano, N. R., Foster, C., Walker, M. G., Strader, J., & Roediger, J. C. 2015, *Monthly Notices of the Royal Astronomical Society*, 450, 3345
- Press, W. H. & Schechter, P. 1974, *The Astrophysical Journal*, 187, 425
- Price, D. J. 2008, *Journal of Computational Physics*, 227, 10040
- Price, D. J. & Federrath, C. 2010, *Mon. Not. R. Astron. Soc.*, 406, 1659
- Ramos, F., Coenda, V., Muriel, H., & Abadi, M. 2015, *The Astrophysical Journal*, 806, 242

- Randall, S., Nulsen, P., Forman, W. R., Jones, C., Machacek, M., Murray, S. S., & Maughan, B. 2008a, *The Astrophysical Journal*, 688, 208
- Randall, S. W., Markevitch, M., Clowe, D., Gonzalez, A. H., & Bradač, M. 2008b, *The Astrophysical Journal*, 679, 1173
- Randall, S. W., Sarazin, C. L., & Irwin, J. A. 2004, *The Astrophysical Journal*, 600, 729
- Rangarajan, F. V. N., Fabian, A. C., Forman, W. R., & Jones, C. 1995, *Monthly Notices of the Royal Astronomical Society*, 272, 665
- Rees, M. J. & Ostriker, J. P. 1977, *Monthly Notices of the Royal Astronomical Society*, 179, 541
- Regev, O., Umurhan, O. M., & Yecko, P. 2016, *Modern Fluid Dynamics for Physics and Astrophysics* (Springer, New York, NY), 706
- Reiprich, T. H., Sarazin, C. L., Kempner, J. C., & Tittley, E. 2004, *The Astrophysical Journal*, 608, 179
- Ricciardone, A. 2017, *Journal of Physics: Conference Series*, 840, 012030
- Ricker, P. M. 2008, *The Astrophysical Journal Supplement Series*, 176, 293
- Ricker, P. M. & Sarazin, C. L. 2001, *The Astrophysical Journal*, 561, 621
- Roediger, E. & Brüggen, M. 2008, *Monthly Notices of the Royal Astronomical Society*, 388, 465
- Roediger, E., Brüggen, M., Rebusco, P., Böhringer, H., & Churazov, E. 2007, *Monthly Notices of the Royal Astronomical Society*, 375, 15
- Roediger, E., Brüggen, M., Simionescu, A., Böhringer, H., Churazov, E., & Forman, W. R. 2011, *Monthly Notices of the Royal Astronomical Society*, 413, 2057
- Roediger, E., Brüggen, M., Simionescu, A., Böhringer, H., Heinz, S., Heinz, S., & Wilcots, E. 2009in (*American Institute of Physics*), 317–320
- Roediger, E., Kraft, R. P., Forman, W. R., Nulsen, P. E. J., & Churazov, E. 2013a, *The Astrophysical Journal*, 764, 60
- Roediger, E., Kraft, R. P., MacHacek, M. E., Forman, W. R., Nulsen, P. E., Jones, C., & Murray, S. S. 2012, *Astrophysical Journal*, 754, 147
- Roediger, E., Kraft, R. P., Nulsen, P., Churazov, E., Forman, W., Brüggen, M., & Kokotanekova, R. 2013b, *Monthly Notices of the Royal Astronomical Society*, 436, 1721
- Roediger, E., Kraft, R. P., Nulsen, P. E. J., Forman, W. R., Machacek, M., Randall, S., Jones, C., Churazov, E., & Kokotanekova, R. 2015a, *The Astrophysical Journal*, 806, 103
- . 2015b, *The Astrophysical Journal*, 806, 104
- Roettiger, K., Burns, J., & Loken, C. 1993, *The Astrophysical Journal*, 407, L53
- Roettiger, K., Loken, C., & Burns, J. O. 1997, *The Astrophysical Journal Supplement Series*, 109, 307
- Roncarelli, M., Gaspari, M., Etori, S., Biffi, V., Brighenti, F., Bulbul, E., Clerc, N., Cucchetti, E., Pointecouteau, E., & Rasia, E. 2018, *Astronomy & Astrophysics*, 618, A39
- Rossetti, M., Eckert, D., De Grandi, S., Gastaldello, F., Ghizzardi, S., Roediger, E., & Molendi, S. 2013, *Astronomy & Astrophysics*, 556, A44
- Rosswog, S. 2015, *Monthly Notices of the Royal Astronomical Society*, 448, 3628
- Rubin, V. C. & Ford, K. W. 1970, *The Astrophysical Journal*, 159, 379
- Russell, H. R., Sanders, J. S., Fabian, A. C., Baum, S. A., Donahue, M., Edge, A. C., McNamara, B. R., & O’Dea, C. P. 2010, *Monthly Notices of the Royal Astronomical Society*, 406, 1721
- Ryu, D., Kang, H., Cho, J., & Das, S. 2008, *Science* (New York, N.Y.), 320, 909
- Ryu, D., Schleicher, D. R. G., Treumann, R. A., Tsagas, C. G., & Widrow, L. M. 2012, *Space Science Reviews*, 166, 1

- Sarazin, C. L. 1986, *Reviews of Modern Physics*, 58, 1
- . 2002, in *Merging Processes in Galaxy Clusters* (Dordrecht: Springer Netherlands), 1–38
- Sasaki, T., Matsushita, K., Sato, K., & Okabe, N. 2016, *Publications of the Astronomical Society of Japan*, 68, 85
- Schaal, K. & Springel, V. 2015, *Monthly Notices of the Royal Astronomical Society*, 446, 3992
- Scharf, C. A., Zurek, D. R., & Bureau, M. 2005, *The Astrophysical Journal*, 633, 154
- Schekochihin, A. A. & Cowley, S. C. 2006, *Physics of Plasmas*, 13, 056501
- Schellenberger, G. & Reiprich, T. H. 2015, *Astronomy & Astrophysics*, 583, L2
- Schenck, D. E., Datta, A., Burns, J. O., & Skillman, S. 2014, *The Astronomical Journal*, 148, 23
- Schindler, S. & Mueller, E. 1993, *Astronomy and Astrophysics*, 272, 137
- Seyfert, C. K. 1943, *The Astrophysical Journal*, 97, 28
- Sharma, P., McCourt, M., Quataert, E., & Parrish, I. J. 2012, *Monthly Notices of the Royal Astronomical Society*, 420, 3174
- Sheardown, A., Fish, T. M., Roediger, E., Hunt, M., ZuHone, J., Su, Y., Kraft, R. P., Nulsen, P., Churazov, E., Forman, W., Jones, C., Lyskova, N., Eckert, D., & De Grandi, S. 2019, *The Astrophysical Journal*, 874, 112
- Sheardown, A., Roediger, E., Su, Y., Kraft, R. P., Fish, T., ZuHone, J. A., Forman, W. R., Jones, C., Churazov, E., & Nulsen, P. E. J. 2018, *The Astrophysical Journal*, 865, 118
- Sheen, Y.-K., Smith, R., Jaffé, Y., Kim, M., Yi, S. K., Duc, P.-A., Nantais, J., Candlish, G., Demarco, R., & Treister, E. 2017, *The Astrophysical Journal*, 840, L7
- Silva, D. R. & Bothun, G. D. 1998, *The Astronomical Journal*, 116, 85
- Simionescu, A., Allen, S. W., Mantz, A., Werner, N., Takei, Y., Morris, R. G., Fabian, A. C., Sanders, J. S., Nulsen, P. E. J., George, M. R., & Taylor, G. B. 2011, *Science*, 331, 1576
- Simionescu, A., Roediger, E., Nulsen, P. E. J., Brüggén, M., Forman, W. R., Böhringer, H., Werner, N., & Finoguenov, A. 2009, *Astronomy & Astrophysics*, 495, 721
- Slipher, V. M. 1917, *Proceedings of the American Philosophical Society*, 56, 403
- Smith, S. & Sinclair. 1936, *The Astrophysical Journal*, 83, 23
- Sod, G. A. 1978, *Journal of Computational Physics*, 27, 1
- Spitzer, L. 1962, *Physics of Fully Ionized Gases*, 2nd edn. (New York)
- Spitzer, L. & L. 1956, *Physics of Fully Ionized Gases* (New York: Interscience Publishers)
- Springel, V. 2010, *Monthly Notices of the Royal Astronomical Society*, 401, 791
- Springel, V. & Farrar, G. R. 2007, *Monthly Notices of the Royal Astronomical Society*, 380, 911
- Springel, V. & Hernquist, L. 2002, *Monthly Notices of the Royal Astronomical Society*, 333, 649
- Springel, V., White, S. D. M., Jenkins, A., Frenk, C. S., Yoshida, N., Gao, L., Navarro, J., Thacker, R., Croton, D., Helly, J., Peacock, J. A., Cole, S., Thomas, P., Couchman, H., Evrard, A., Colberg, J., & Pearce, F. 2005, *Nature*, 435, 629
- St-Onge, D. A. & Kunz, M. W. 2018, *The Astrophysical Journal*, 863, L25
- Stevens, I. R., Acreman, D. M., & Ponman, T. J. 1999, *Monthly Notices of the Royal Astronomical Society*, 310, 663
- Strang, G. 1968, *SIAM Journal on Numerical Analysis*, 5, 506
- Su, Y., Gu, L., White III, R. E., & Irwin, J. 2014, *The Astrophysical Journal*, 786, 152

- Su, Y., Kraft, R. P., Nulsen, P. E. J., Jones, C., Maccarone, T. J., Mernier, F., Lovisari, L., Sheardown, A., Randall, S. W., Roediger, E., Fish, T. M., Forman, W. R., & Churazov, E. 2019, *The Astronomical Journal*, 158, 6
- Su, Y., Kraft, R. P., Nulsen, P. E. J., Roediger, E., Forman, W. R., Churazov, E., Randall, S. W., Jones, C., & Machacek, M. E. 2017a, *The Astrophysical Journal*, 835, 19
- Su, Y., Kraft, R. P., Roediger, E., Nulsen, P., Forman, W. R., Churazov, E., Randall, S. W., Jones, C., & Machacek, M. E. 2017b, *The Astrophysical Journal*, 834, 74
- Su, Y., Nulsen, P. E. J., Kraft, R. P., Forman, W. R., Jones, C., Irwin, J. A., Randall, S. W., & Churazov, E. 2017c, *The Astrophysical Journal*, 847, 94
- Su, Y., Nulsen, P. E. J., Kraft, R. P., Roediger, E., ZuHone, J. A., Jones, C., Forman, W. R., Sheardown, A., Irwin, J. A., & Randall, S. W. 2017d, *The Astrophysical Journal*, 851, 69
- Sunyaev, R. A. & Zeldovich, Y. B. 1972, *Comments on Astrophysics and Space Physics*, 4, 173
- . 1980, *Monthly Notices of the Royal Astronomical Society*, 190, 413
- Takeda, H., Nulsen, P. E. J., & Fabian, A. C. 1984, *Monthly Notices of the Royal Astronomical Society*, 208, 261
- Takizawa, M., Nagino, R., & Matsushita, K. 2010, *Publications of the Astronomical Society of Japan*, 62, 951
- Thorpe, S. A. 1971, *Journal of Fluid Mechanics*, 46, 299
- Toniazzo, T. & Schindler, S. 2001, *Monthly Notices of the Royal Astronomical Society*, 325, 509
- Tully, R. B. & Brent, R. 1987, *The Astrophysical Journal*, 321, 280
- Turk, M. J., Smith, B. D., Oishi, J. S., Skory, S., Skillman, S. W., Abel, T., & Norman, M. L. 2011, *Astrophysical Journal, Supplement Series*, 192, 9
- Tytler, D., O'Meara, J. M., Suzuki, N., & Lubin, D. 2000, *Physica Scripta Volume T*, 85, 12
- Ueda, S., Ichinohe, Y., Kitayama, T., & Umetsu, K. 2019, *The Astrophysical Journal*, 871, 207
- van Dyke, M. & White, F. M. 1982, *Journal of Fluids Engineering*, 104, 542
- Vazza, F., Dolag, K., Ryu, D., Brunetti, G., Gheller, C., Kang, H., & Pfrommer, C. 2011, *Monthly Notices of the Royal Astronomical Society*, 418, 960
- Vikhlinin, A., Burenin, R. A., Ebeling, H., Forman, W. R., Hornstrup, A., Jones, C., Kravtsov, A. V., Murray, S. S., Nagai, D., Quintana, H., & Voevodkin, A. 2009a, *The Astrophysical Journal*, 692, 1033
- Vikhlinin, A., Kravtsov, A. V., Burenin, R. A., Ebeling, H., Forman, W. R., Hornstrup, A., Jones, C., Murray, S. S., Nagai, D., Quintana, H., & Voevodkin, A. 2009b, *The Astrophysical Journal*, 692, 1060
- Vikhlinin, A., Markevitch, M., & Murray, S. S. 2001a, *The Astrophysical Journal*, 551, 160
- . 2001b, *The Astrophysical Journal*, 549, L47
- Vikhlinin, A. A. & Markevitch, M. L. 2002, *Astronomy Letters*, 28, 495
- Vitvitska, M., Klypin, A. A., Kravtsov, A. V., Wechsler, R. H., Primack, J. R., & Bullock, J. S. 2002, *The Astrophysical Journal*, 581, 799
- Vogelsberger, M., Genel, S., Springel, V., Torrey, P., Sijacki, D., Xu, D., Snyder, G., Nelson, D., & Hernquist, L. 2014, *Monthly Notices of the Royal Astronomical Society*, 444, 1518
- Voigt, L. M. & Fabian, A. C. 2004, *Monthly Notices of the Royal Astronomical Society*, 347, 1130
- Voit, G. M. 2005, *Reviews of Modern Physics*, 77, 207
- Wadsley, J., Stadel, J., & Quinn, T. 2003, *New Astronomy*, Volume 9, Issue 2, p. 137-158., 9, 137
- Wadsley, J. W., Keller, B. W., & Quinn, T. R. 2017, *Monthly Notices of the Royal Astronomical Society*, 471, 2357

- Wadsley, J. W., Veeravalli, G., & Couchman, H. M. P. 2008, *Monthly Notices of the Royal Astronomical Society*, 387, 427
- Walker, S., Simionescu, A., Nagai, D., Okabe, N., Eckert, D., Mroczkowski, T., Akamatsu, H., Etori, S., & Ghirardini, V. 2019, *Space Science Reviews*, 215, 7
- Walker, S. A., Hlavacek-Larrondo, J., Gendron-Marsolais, M., Fabian, A. C., Intema, H., Sanders, J. S., Bamford, J. T., & van Weeren, R. 2017, *Monthly Notices of the Royal Astronomical Society*, 468, 2506
- Weinberg, S. 2008, *Cosmology* (Oxford University Press), 593
- West, M. J., Jordán, A., Blakeslee, J. P., Côté, P., Gregg, M. D., Takamiya, M., & Marzke, R. O. 2011, *Astronomy & Astrophysics*, 528, A115
- White, S. D. M. & Rees, M. J. 1978, *Monthly Notices of the Royal Astronomical Society*, 183, 341
- Wood, R. A., Jones, C., Machacek, M. E., Forman, W. R., Bogdan, A., Andrade-Santos, F., Kraft, R. P., Paggi, A., & Roediger, E. 2017, *The Astrophysical Journal*, 847, 79
- York, D. G., Adelman, J., Anderson, Jr., J. E., Anderson, S. F., Annis, J., Bahcall, N. A., Bakken, J. A., Barkhouser, R., Bastian, S., Berman, E., Boroski, W. N., Bracker, S., Briegel, C., Briggs, J. W., Brinkmann, J., Brunner, R., Burles, S., Carey, L., Carr, M. A., Castander, F. J., Chen, B., Colestock, P. L., Connolly, A. J., Crocker, J. H., Csabai, I., Czarapata, P. C., Davis, J. E., Doi, M., Dombeck, T., Eisenstein, D., Ellman, N., Elms, B. R., Evans, M. L., Fan, X., Federwitz, G. R., Fiscelli, L., Friedman, S., Frieman, J. A., Fukugita, M., Gillespie, B., Gunn, J. E., Gurbani, V. K., de Haas, E., Haldeman, M., Harris, F. H., Hayes, J., Heckman, T. M., Hennessy, G. S., Hindsley, R. B., Holm, S., Holmgren, D. J., Huang, C.-h., Hull, C., Husby, D., Ichikawa, S.-I., Ichikawa, T., Ivezić, Ž., Kent, S., Kim, R. S. J., Kinney, E., Klaene, M., Kleinman, A. N., Kleinman, S., Knapp, G. R., Korienek, J., Kron, R. G., Kunszt, P. Z., Lamb, D. Q., Lee, B., Leger, R. F., Limmongkol, S., Lindenmeyer, C., Long, D. C., Loomis, C., Loveday, J., Lucinio, R., Lupton, R. H., MacKinnon, B., Mannery, E. J., Mantsch, P. M., Margon, B., McGehee, P., McKay, T. A., Meiksin, A., Merelli, A., Monet, D. G., Munn, J. A., Narayanan, V. K., Nash, T., Neilsen, E., Neswold, R., Newberg, H. J., Nichol, R. C., Nicinski, T., Nonino, M., Okada, N., Okamura, S., Ostriker, J. P., Owen, R., Pauls, A. G., Peoples, J., Peterson, R. L., Petravick, D., Pier, J. R., Pope, A., Pordes, R., Prosapio, A., Rechenmacher, R., Quinn, T. R., Richards, G. T., Richmond, M. W., Rivetta, C. H., Rockosi, C. M., Ruthmansdorfer, K., Sandford, D., Schlegel, D. J., Schneider, D. P., Sekiguchi, M., Sergey, G., Shimasaku, K., Siegmund, W. A., Smee, S., Smith, J. A., Snedden, S., Stone, R., Stoughton, C., Strauss, M. A., Stubbs, C., SubbaRao, M., Szalay, A. S., Szapudi, I., Szokoly, G. P., Thakar, A. R., Tremonti, C., Tucker, D. L., Uomoto, A., Vanden Berk, D., Vogeley, M. S., Waddell, P., Wang, S.-i., Watanabe, M., Weinberg, D. H., Yanny, B., & Yasuda, N. 2000, *The Astronomical Journal*, 120, 1579
- Yu, H., Diaferio, A., Agulli, I., Aguerri, J. A. L., & Tozzi, P. 2016, *The Astrophysical Journal*, 831, 156
- Zhang, C., Yu, Q., & Lu, Y. 2016, *The Astrophysical Journal*, 820, 85
- Zhu, L., Romanowsky, A. J., van de Ven, G., Long, R. J., Watkins, L. L., Pota, V., Napolitano, N. R., Forbes, D. A., Brodie, J., & Foster, C. 2016, *Monthly Notices of the Royal Astronomical Society*, 462, 4001
- Zhuravleva, I., Churazov, E., Schekochihin, A. A., Allen, S. W., Arévalo, P., Fabian, A. C., Forman, W. R., Sanders, J. S., Simionescu, A., Sunyaev, R., Vikhlinin, A., & Werner, N. 2014, *Nature*, 515, 85
- ZuHone, J. & Markevitch, M. 2009in (*American Institute of Physics*), 383–386
- ZuHone, J. A. 2011, *The Astrophysical Journal*, 728, 54
- ZuHone, J. A. & Kowalik, K. 2016, 9
- ZuHone, J. A., Markevitch, M., & Johnson, R. E. 2010, *The Astrophysical Journal*, 717, 908
- ZuHone, J. A., Markevitch, M., & Lee, D. 2011, *The Astrophysical Journal*, 743, 16
- ZuHone, J. A., Markevitch, M., Ruszkowski, M., & Lee, D. 2013, *The Astrophysical Journal*, 762, 69
- Zuhone, J. A., Ricker, P. M., Lamb, D. Q., & Karen Yang, H. Y. 2009, *Astrophysical Journal*, 699, 1004
- ZuHone, J. A. & Roediger, E. 2016, *Journal of Plasma Physics*, 82, 535820301
- Zwicky, F. 1933, *Helvetica Physica Acta*, 6, 110



# Appendix A

## Characteristics of Fluid Flow

In this section, aspects of fluid flow which are directly related to the flows in the ICM are summarised. For a comprehensive description of hydrodynamics see Lamb (1945), or Regev et al. (2016) which provides a more modernised take and also provides context to astrophysics. The aspects of fluid flow summarised here are:

- Reynold's number,  $Re$
- turbulence
- supersonic motion and bow shocks
- Rayleigh Taylor and Kelvin Helmholtz instability
- flow around a blunt body

Earning its name from the British physicist Osborne Reynolds, the Reynold's number,  $Re$ , is a dimensionless number that determines the ratio of viscous and inertial forces, which is dependent on the material properties of the fluid and the geometry of the flow. It essentially describes the behaviour of the fluid, providing a distinction between laminar and turbulent flow. Mathematically the Reynold's number is defined as,

$$Re = \frac{\rho v L}{\mu} \quad (\text{A.1})$$

where  $\rho$  is the density of the fluid,  $v$  is the velocity of the fluid flow,  $L$  is the characteristic length scale of the fluid and  $\mu$  is the dynamic viscosity of the fluid (Regev et al., 2016). Importantly, the Reynold's number only describes the global behaviour of the fluid flow. On small local scales, in sufficiently large fluid volumes which exhibits laminar flow, pockets of turbulent can still exist, therefore the length scale is important when characterising the behaviour of a fluid. An important characteristic of the Reynold's number is its role as a similarity parameter for viscosity. Similarity parameters are ratios of the magnitude of the forces present and are crucial in modelling as they allow one to scale experiments or simulations. If the similarity parameters are the same in experiment and reality, then forces can then be considered to be correctly modelled. In scenarios of vastly different length

scales, the flow patterns are similar as long as the  $Re$  is similar. This notion is important as wind tunnel experiments can be done with small models of planes or cars which can be used to determine the flow patterns past the full scale versions.



**Fig. A.1:** Taken from *The Album of Fluid Motion* by van Dyke & White (1982), Fig. 24, photographed by Sadatoshi Taneda. An example of Laminar flow around a sphere at a Reynold's number of 1.54. The flow shows the smoothness of the streamlines around the sphere characteristic of laminar flow.

For low Reynold's numbers, the nature of the flow is dominated by the viscosity of the fluid, resulting in a flow that is laminar. This type of flow is called a laminar flow or is also known as a streamline flow. Laminar flows typically have  $Re < \sim 100$ , characterised by small velocities or high viscosity's. In this flow regime, viscous forces dominate the flow dynamics with high momentum diffusion. The fluid flows in layers parallel to each other with no disturbance between them, i.e. no lateral mixing between the layers (see Fig. A.1). Therefore, flow properties, such as the velocity and pressure remain constant at every point. For laminar flows, the Navier-Stokes equations must be used to described the flow due to the significant impact of viscosity.

In contrast, for high Reynold's numbers, typically  $Re > \sim 2000$ , inertial forces now take a dominant role over viscosity, resulting in a fluid flow which is chaotic (see Fig. A.2). These types of flows are termed turbulent flows and can be considered inviscid such that Euler's equations of hydrodynamics can be applied as viscosity is negligible. Turbulent flow is a dissipative process as the kinetic energy of the flow is converted into heat. Therefore, to be sustained, turbulent flows require a source of energy. Deterministic approaches to turbulence are extremely difficult, thus modelling of turbulence is done with statistics. In a turbulent flow, there is fast lateral mixing between fluid layers thus turbulent flows are incredibly diffuse, with increased rates of mass, heat and momentum transfer (Lamb, 1945; Regev et al., 2016). This causes rapid variations in the pressure and velocity of the flow. Further, turbulent flows are rotational with significant fluctuations in vorticity, causing fluid particle paths to become unpredictable and irregular, leading to the production of eddies. Vorticity is a vector field that measures the rotation at any point in a fluid and can help to characterise the evolution of flow (it is important to note that it is only a measure of the local rotation and not the overall rotation of the fluid). Essentially it



**Fig. A.2:** Taken from Dimotakis et al. (1983). Turbulent Flow from a water jet with Reynold's number  $\sim 2300$  revealing the formation and decaying of eddies.

describes the tendency of a point in a fluid to rotate and can be thought of as a measure of the local angular velocity. Mathematically, vorticity is a pseudovector field and in three dimensions is defined as:

$$\vec{\omega} = \nabla \times \vec{v} \quad (\text{A.2})$$

where  $\omega$  is the vorticity and  $v$  is the flow velocity. Evidently, the vorticity will be perpendicular to the fluid flow if the flow itself is two dimensional. If the vorticity in any region of a fluid is zero, then it is irrotational, and is therefore characterised as an irrotational flow. As a turbulent flow progresses, the large turbulent eddies become unstable and decay into smaller eddies, transferring their energy in the process. The smaller eddies undergo the same process and decay into even smaller eddies producing a cascade of energy. The cascade continues until a critical length scale is reached known as the Kolomogorov length scale where viscous forces take over and can effectively dissipate the kinetic energy into internal energy. This turbulent energy cascade is described by Kolmogorov Theory (Kolmogorov, 1941). Eddies (eddy for singular) are a significant phenomenon of turbulent flow, producing fluctuations in the flow velocity causing the fluid to swirl and reverse current. For example, this would be the case as a flow moves past a blunt object. An eddy is formed once fluid flow attains a critical velocity which is enough to produce a lower pressure behind the object downstream, creating a void of space. At this point, the fluid in the downstream region flows into the void which is then followed by a brief reverse flow upstream that generates the swirling motion, this action can also produce sound waves due to pressure disturbances.

As the velocity of a flow increases, moving from laminar flow to turbulent flow, there is a transitional regime termed transitory flow. This flow occurs at intermediate Reynold's numbers and the flow is essentially a mixture of laminar and turbulent. This is a direct result of the Reynold's number being proportional to the velocity of flow and inversely proportional to viscosity.

An important quantity of fluid dynamics which is used to describe the velocity of an object through a fluid is the Mach number,  $M$ , named after the Austrian physicist Ernst Mach who correctly predicted that a conical shock wave should be produced when an object travels faster than the local speed of sound. The Mach number is a dimensionless quantity and is the ratio of the speed of a fluid to the speed of sound in that fluid.

$$M = \frac{v}{c} \quad (\text{A.3})$$

where  $v$  is the velocity of the fluid and  $c$  is the speed of sound in that fluid. For values of  $M < 1$ , this corresponds to subsonic motion. For values of  $M > 1$ , this pertains to supersonic motion meaning that a shock wave is produced. For values of  $M$  around 1, this motion is described as transonic where the motion has both subsonic and supersonic elements. In a galaxy cluster, the infall of a galaxy or subcluster has typical speeds on order of  $\sim 1000 \text{ km s}^{-1}$  which is supersonic, i.e.  $M > 1$ , therefore a bow shock will lead in front of the infalling galaxy or subcluster.

Fluid flows can be subjected to instabilities, these are small perturbations which grow extracting energy from the fluid. There are many different types of fluid instabilities, but only the Rayleigh-Taylor instability (RTI) and Kelvin-Helmholtz instability (KHI) will be discussed here. The RTI arises when two fluids of different densities share an

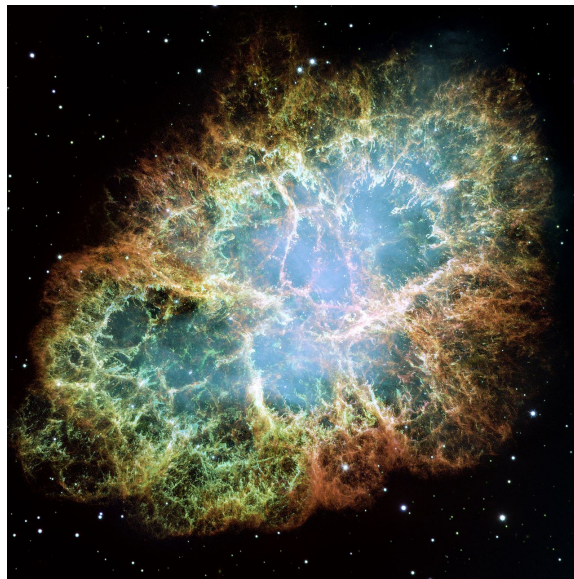


**Fig. A.3:** Optical image of the Crab Nebula demonstrating the effect of the Rayleigh-Taylor Instability (RTI). Obtained from <https://www.eso.org/public/images/eso9948f/>. Credit: ESO.

interface resulting in the lighter fluid pushing against the denser fluid. For example, if the heavier fluid sits on top of the lighter fluid in a gravitational field, the lighter fluid will push upwards, rising and mixing with the heavier fluid producing plumes that flow upwards; this is essentially driven by buoyancy. In this situation, it is the potential energy in the gravitational field which is being extracted by the instability. The RTI is known to occur on astrophysical scales, as for example, the interstellar gas being pushed out of a galaxy due to cosmic rays or due to a pulsar generating an expanding wind nebula that collects remnants of a supernova explosion, this is a famous example of the Crab nebula (see: Fig.

A.3). The KHI is a wave-like perturbation that occurs at the the interface between parallel shear flows - these are layers of fluid which move at different parallel velocities. The KHI's kinetic energy from the average flow and grow in size. The waves become rolled over producing vortex-like structures as the shear flow induces vorticity as can be seen in Figure A.4. This essentially produces a shearing layer that is a vortex sheet which overturns and spirals in motion leading to mixing of the fluid. Therefore, the KHI plays an important role in the production of turbulence in a fluid. As mentioned, in the conditions of the ICM, the flow can be stabilised against the instability by the presence of magnetic fields or viscosity (Chandrasekhar, 1961).

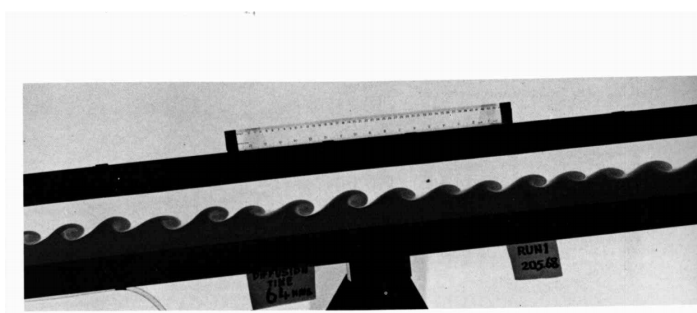


**Fig. A.4:** Image taken from Thorpe (1971). The Kelvin-Helmholtz Instability of stratified shear flow.

When a blunt object, such as a sphere or a circular cylinder is placed in the path of a fluid, a boundary layer of fluid forms around the blunt body which detaches and forms a wake. The wake forms directly behind the object where the fluid becomes disturbed and sees the production of eddies and vortices. The flow past a circular cylinder at  $Re = 2000$  is shown Fig. A.5 which demonstrates the disturbed flow in the wake region behind the circular cylinder. From the onset of the fluid flow, directly in front of the blunt body where the boundary layer is smallest, a stagnation point is formed where the local flow velocity is zero. Directly behind the blunt body, in the near wake, is a deadwater region where the average velocity of the flow is directed upstream. Only in the far wake region the average flow velocity is directed downstream. At high Reynolds numbers, i.e. low viscosities, the wake becomes highly turbulent and harvests large eddy motions (Landau & Lifshitz, 1959). For a galaxy moving through the ICM, Roediger et al. (2015a) find that even with a turbulent wake, the average flow will still follow a torus-like pattern. This is such that the outer part of the torus flows away downstream in contrast to the inner part of the torus where the flow is directed upstream, this is the deadwater region. As mentioned, the flow around a blunt body creates sees the production of vortices in the near wake. At high Reynold's numbers (values around 100), a rather aesthetic consequence arises as the unsteady separation of flow around the blunt object causes the vortices to become unstable. At a critical point, the vortices detach alternately at a constant frequency and drift downstream giving a cyclonic appearance, this is known as a von Karman vortex street. An example of the von Karman vortex street is shown in Figure A.6.

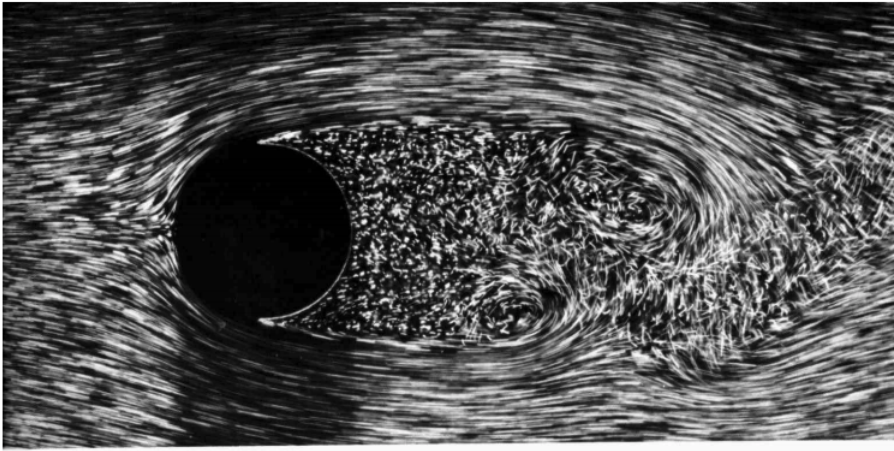


**Fig. A.5:** Image taken from van Dyke & White (1982) showing the flow past a circular cylinder at  $Re = 2000$ . The disturbed flow behind the circular cylinder characterises the wake region where eddies and vortices are produced.

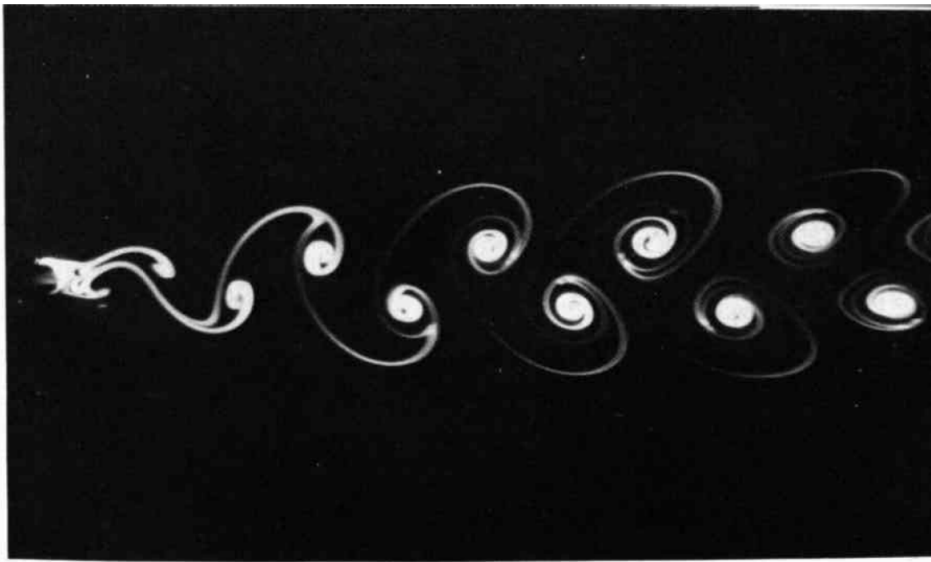


**Fig. A.6:** Image taken from Fig. 105 from van Dyke & White (1982), image photographed by Sadatoshi Taneda. The formation of a von Karman vortex behind a circular cylinder at  $Re = 105$ .